DAMAGE MECHANICS AND CONDITION MONITORING OF WIND TURBINE GEARBOX MATERIALS

by

Valter Luiz Jantara Junior

A thesis submitted to the University of Birmingham for the degree of DOCTOR OF PHILOSOPHY

School of Metallurgy and Materials
College of Engineering and Physical Sciences
University of Birmingham

March 2019

ABSTRACT

The wind energy industry has been suffering from premature wind turbine gearbox failures since its inception. These components are designed to last 20-25 years. However, they rarely survive more than 7 years without being refurbished or replaced. The aim of this study is to better understand wind turbine gearbox failures and increase the reliability of this component. Failed samples were retrieved from the field. Thorough failure analysis revealed that misalignments, poor lubrication, and the presence of MnS inclusions can severely reduce the lifetime of wind turbine gearboxes. Rolling contact fatigue tests reiterate these findings. Acoustic emission monitoring was employed during laboratory tests. This condition monitoring technique was able to detect damage nucleation and propagation accurately during fatigue crack growth and rolling contact fatigue testing. Finally, finite element analysis was coupled with a constitutive model to quantify and predict damage in wind turbine gearboxes, while also testing for different service conditions. It was found that angular misalignment was the most detrimental service condition, followed by radial misalignment, and lack of lubrication. Additionally, an estimation of the remaining useful lifetime of the component was generated, further assisting wind turbine farm operators to move towards the implementation of a true predictive maintenance approach.

To my wife and my family

ACKNOWLEDGEMENTS

I would like to thank the National Council of Technological and Scientific Development (CNPq), for the scholarship under the Science without Borders program and for the financial support.

I also want to express my gratitude towards my supervisors: Dr Mayorkinos Papaelias, Professor Hanshan Dong, and Dr Hector Basoalto, for the countless meetings and guidance. Their support, friendship, and knowledge were crucial for the development of this work.

I would like to thank all Surface Engineering members, especially Dr Mario Coseglio, Mr James Alexander, Dr Xiaoying Li, and Dr Jun Zhou for the valuable discussions and comments. I also want to thank Mr Behnam Dashtbozorg for the help with experiments and proofreading.

I would also like to thank Ms Yana Liang, for the XRD testing, Mr David Price for the help with the tensile testing, and Dr Tim Doel for the help with fatigue crack growth testing. I also want to express my gratitude to all the staff at the School of Metallurgy and Materials.

I would like to thank Dr Evaldo Toniolo Kubaski and MSc Selauco Vurobi Júnior. Without their confidence and inspiration, this journey would have ended before it even began.

Finally, I want to thank my wife, Giana Thomaz, for the confidence deposited in me throughout all these years, for proofreading and commenting on my work, and for putting up with me talking about wind turbines in my sleep.

PUBLICATIONS AND AWARDS

Journal Papers

Jantara Junior, V., Basoalto, H., Dong, H., Marquez, F.P.G., Papaelias, M., 2018. *Evaluating the challenges associated with the long-term reliable operation of industrial wind turbine gearboxes.* IOP Conference Series: Materials Science and Engineering, 454(1), pp.12094. DOI: https://doi.org/10.1088/1757-899X/454/1/012094

Jantara Junior, V., Zhou, J., Roshanmanesh, S., Hayati, F., Hajiabady, S., Li, X.Y., Dong, H. and Papaelias, M., 2017. *Evaluation of damage mechanics of industrial wind turbine gearboxes.* Insight-Non-Destructive Testing and Condition Monitoring, 59(8), pp.410-414. DOI: https://doi.org/10.1784/insi.2017.59.8.410

Zhou, J., Roshanmanesh, S., Hayati, F., **Jantara Junior, V.**, Wang, T., Hajiabady, S., Li, X.Y., Basoalto, H., Dong, H. and Papaelias, M., 2017. *Improving the reliability of industrial multi-MW wind turbines.* Insight-Non-Destructive Testing and Condition Monitoring, 59(4), pp.189-195. DOI: https://doi.org/10.1784/insi.2017.59.4.189

Conference Papers

Graham, K., Kerkyras, S., Tzaferis, K., **Jantara Junior, V.**, Papaelias, M. *Inspection and evaluation of hydrogen-induced defects in SA516GR steel plate.* First International Conference on Welding & NDT of the Hellenic Society of NDT and the Welding Greek Institute. Athens, Greece, October 2018.

Papaelias, M., Amini, A., Culwick, R., Heesom, J., Huang, Z., **Jantara Junior, V.**, Kaenwunruen, S., Kerkyras, S., Kongpuang, M., Garcia Marquez, F.P., Shi, S., Upton, A., Vallely, P. *Advanced remote condition monitoring of railway infrastructure and rolling stock.* First International Conference on Welding & NDT of the Hellenic Society of NDT and the Welding Greek Institute. Athens, Greece, October 2018.

Zhou, J., Roshanmanesh, S., Hayati, F., **Jantara Junior, V.**, Wang, T., Hajiabady, S., Li, X.Y., Dong, H. and Papaelias, M., 2016. *Increasing the reliability of industrial multi-MW wind turbines.* NDT 2016 - 55th Annual Conference of the British Institute of Non-Destructive Testing, 2016, Nottingham, UK.

Jantara Junior, V., Zhou, J., Roshanmanesh, S., Hayati, F., Hajiabady, S., Li, X.Y., Dong, H. and Papaelias, M., 2017. *Evaluation of damage mechanics of industrial wind turbine gearboxes.* First World Congress on Condition Monitoring, 2017, London, UK.

Awards

Second best presentation on the 8th BEAR PGR Conference, for the presentation entitled *"Wind turbine gearbox damage simulation"*, February 2018.

The Len Gelman Award for the best paper in the Proceedings of the First World Congress on Condition Monitoring by a person in the early stages of their career, July 2017.

Best presentation on the National Student Conference in Metallic Materials 2017, for the presentation entitled *"Initial steps towards damage prediction of wind turbine gearboxes"*, July 2017.

Second best poster on the Materials Forum 2017 at the University of Birmingham, January 2017.

Contents

List of Figures

List of Tables

List of Abbreviations and Symbols

Abbreviations

a-C:H Amorphous hydrocarbon coatings, page 41

AE Acoustic Emission, page 30

AGMA American Gear Manufacturers Association, page 8

ANSI American National Standards Institute, page 8

ASPN Active Screen Plasma Nitriding, page 40

ASTM American Society for Testing and Materials, page 102

CAD Computer Aided Design, page 190

CDM Continuum Damage Mechanics, page 61

DCPD Direct Current Potential Drop, page 88

DCPN Direct Current Plasma Nitriding, page 40

DLC Diamond-like carbon, page 41

EDS Energy Dispersive Spectroscopy, page 68

EHL Elastohydrodynamics, page 22

EU European Union, page 1

FEA Finite Element Analysis, page 198

FFT Fast Fourier Transform, page 27

FZG "Forschungsstelle fur Zahnrader und Getriebebau", a type wear test for gears, page 65

GTN Gurson-Tvergaad-Needleman, page 63

HV Hardness Vickers, page 8

IEC International Electrotechnical Commission, page 8

ISO International Organization for Standardization, page 8

LCOE Levelised Cost of Electricity, page 2

MC/a-C:H Amorphous hydrocarbon coatings with metal carbides, page 41

MIO A colloidal suspension of molybdenum disulphide, page 11

PAC Physiycal Acoustics Corporation, page 86

RCF Rolling contact fatigue, page 9

S-N Stress-cycles, page 222

SCADA Supervisory control and data acquisition, page 25

SEM Scanning Electron Microscope, page 68

SI International System of Units, page 18

US United States, page 189

WC/a-C:H Amorphous hydrocarbon coatings with tungsten carbides, page 42

WC Tungsten carbide, page 112

WEA White etching area, page 13

WTG Wind turbine gearbox, page 2

XRD X-Ray Diffraction, page 68

Greek Symbols

β Constant reflecting statistical nature of the process, see equation (7.23), page 165

$\boldsymbol{\varepsilon}$ True strain tensor, see equation (2.32), page 49

$\boldsymbol{\sigma}$ Stress tensor, see equation (2.11), page 45

δ_{ij} Kronecker delta, see equation (2.16), page 45

$\dot{\boldsymbol{\sigma}}$ Stress rate tensor, see equation (7.10), page 163

$\dot{\rho}$ Rate of change of dislocation density, see equation (7.23), page 165

$\dot{\sigma}^{ks}$ Rate of change of substructural stress, see equation (7.23), page 165

$\dot{\varepsilon}^{p}$ Plastic strain rate, see equation (2.78), page 63

$\dot{\varepsilon}_{0}^{''}$ Model parameter, see equation (7.23), page 165

η	Specific film thickness, see equation (2.3), page 23
λ	Stretch ratio, see equation (2.38), page 50
ν	Poisson's ratio, see equation (2.55), page 54
ν_i	Poisson's ratio of the indenter, see equation (3.3), page 83
ω	Rotational speed, see equation (5.1), page 112
$\overline{\sigma}$	Von Mises stress, see equation (2.65), page 58
$\overline{\varepsilon}^p$	Equivalent plastic strain, see equation (2.75), page 62
$\overset{\triangledown}{\boldsymbol{\sigma}}$	Jaumann stress rate tensor, see equation (7.9), page 163
Φ	Gurson's flow rule, see equation (2.77), page 63
π	Mathematical constant. Ratio of the circumference of a circle to its diameter
Ψ	Kachanov's damage variable, see equation (2.70), page 61
ρ	Mobile dislocation density, see equation (7.23), page 165
ρ^{ss}	Steady state mobile dislocation density, see equation (7.23), page 165
σ	Stress, see equation (2.8), page 43
σ^p	Obstacle strength parameter, see equation (7.23), page 165
σ^{is}	Isotropic strength parameter, see equation (7.23), page 165
σ^{ks}	Substructural kinematic stress, see equation (7.23), page 165
σ^{or}	Orowan stress, see equation (7.23), page 165
σ_0	Yield stress, see equation (2.61), page 56
σ_b	Bending stress, see equation (7.176), page 199
σ_c	Contact stress, see equation (7.177), page 200
σ_m	Mean Stress, see equation (2.16), page 45
σ_{cr}	Composite roughness of oil layer, see equation (2.3), page 23
σ_{eff}	Effective stress, see equation (2.72), page 61

σ_{pr} Principal stress, see equation (2.12), page 45

τ Yield strength in shear, see equation (2.63), page 57

τ_{max} Maximum shear stress, see equation (2.62), page 57

θ Pressure angle of a gear, see equation (2.2), page 19

ε_N Strain where half of the inclusions are broken, see equation (2.82), page 64

Roman Symbols

$\boldsymbol{D}$ Total strain rate tensor, see equation (7.5), page 162

$\boldsymbol{D}^e$ Elastic strain rate tensor, see equation (7.7), page 162

$\boldsymbol{D}^p$ Plastic strain rate tensor, see equation (7.7), page 162

$\boldsymbol{S}$ Deviatoric stress tensor, see equation (7.8), page 162

$\boldsymbol{W}$ Total spin tensor, see equation (7.5), page 162

$\boldsymbol{W}^e$ Elastic spin tensor, see equation (7.7), page 162

$\boldsymbol{W}^p$ Plastic spin tensor, see equation (7.7), page 162

$\dot{\psi}$ Rate of change of damage, see equation (7.23), page 165

$\dot{f}$ Rate of change of voids, see equation (2.81), page 64

$\mathbf{B}$ Right Cauchy-Green tensor, see equation (2.29), page 48

$\mathbf{C}$ Elastic coefficient tensor, see equation (2.49), page 53

$\mathbf{E}$ Green-Lagrange strain tensor, see equation (2.36), page 49

$\mathbf{e}$ Almansi strain tensor, see equation (2.31), page 49

$\mathbf{F}^e$ Elastic deformation gradient tensor, see equation (7.1), page 161

$\mathbf{F}^p$ Plastic deformation gradient tensor, see equation (7.1), page 161

$\mathbf{F}$ Deformation gradient tensor, see equation (2.21), page 47

$\mathbf{G}$ Left Cauchy-Green tensor, see equation (2.25), page 48

$\mathbf{I}$ Identity tensor, see equation (2.30), page 49

$\mathbf{L}$ Velocity gradient tensor, see equation (7.2), page 162

A	Area of a section, see equation (2.8), page 43
a	Crack length, see equation (4.1), page 88
a_0	Initial crack length, see equation (4.1), page 88
A_d	Area of microvoids or microcracks, see equation (2.70), page 61
a_e	Semi-minor axe of the ellipse, see equation (5.8), page 115
a_g	Addendum of a gear, page 19
A_v	Dynamic factor parameter, see equation (7.179), page 201
b	Dedendum of a gear, page 19
b_e	Semi-major axe of the ellipse, see equation (5.9), page 116
B_v	Dynamic factor parameter, see equation (7.180), page 201
b_v	Burger's vector, see equation (7.23), page 165
C	Material constant, see equation (4.2), page 89
c	Clearance of a gear, page 19
C^1	Constant, see equation (7.23), page 165
C^2	Constant, see equation (7.23), page 165
C^3	Constant, see equation (7.23), page 165
C^4	Constant, see equation (7.23), page 165
c_1	Lamè constant, see equation (2.55), page 54
c_2	Lamè constant (modulus of rigidity), see equation (2.56), page 54
c_d	Centre distance between gears, see equation (7.175), page 192
C_e	Mesh alignment correction factor, see equation (7.182), page 202
C_{ma}	Mesh alignment factor, see equation (7.182), page 202
C_{mc}	Lead correction factor, see equation (7.182), page 202
C_{pf}	Pinion proportion factor, see equation (7.182), page 202
C_{pm}	Pinion proportion modifier, see equation (7.182), page 202

CP_{max}	Maximum contact pressure, see equation (5.10), page 116
d_g	Diameter of the pitch circle of the gear, see equation (2.1), page 18
d_p	Diameter of the pitch circle of the pinion, see equation (7.175), page 192
E	Young's modulus, see equation (2.55), page 54
E_i	Elastic modulus of the indenter, see equation (3.3), page 83
E_r	Reduced elastic modulus, see equation (3.2), page 83
F	Force, see equation (2.8), page 43
f	Gurson's damage variable, see equation (2.77), page 63
f_*	GTN parameter for void volume fraction, see equation (2.80), page 64
f_N	Volume fraction of inclusions at which damage can be nucleated, see equation (2.82), page 64
f_R	Void volume fraction at fracture, see equation (2.80), page 64
F_w	Face width of a gear, page 19
G	Shear modulus, see equation (7.23), page 165
g	Slip ratio, see equation (5.1), page 112
H	Hardness, see equation (3.1), page 83
h	Film thickness of oil layer, see equation (2.3), page 23
h^s	Effective modulus of the hard phase, see equation (7.23), page 165
H^*	Maximum possible stress that can be redistributed, see equation (7.23), page 165
h_t	Tooth height, page 19
I	Stress invariant, see equation (2.15), page 45
K	Stress intensity factor, see equation (4.2), page 89
k	Boltzmann constant, see equation (7.23), page 165
k^D	Model parameter, see equation (7.23), page 165

K_B	Rim-thickness factor, see equation (7.176), page 199
k_e	Ellipticity parameter, see equation (5.6), page 115
K_f	Fatigue stress concentration factor, see equation (7.186), page 203
K_H	Load distribution factor, see equation (7.176), page 199
K_o	Overload factor, see equation (7.176), page 199
K_s	Size factor, see equation (7.176), page 199
K_v	Dynamic factor, see equation (7.176), page 199
L	Load, see equation (4.3), page 89
l	Length, see equation (2.38), page 50
M	Taylor factor, see equation (7.23), page 165
m	Material constant, see equation (4.2), page 89
m_B	Backup ratio, see equation (7.183), page 202
m_g	Module of a gear, see equation (2.1), page 18
m_s	Gear speed ratio, see equation (7.188), page 204
m_t	Transverse metric module, see equation (7.176), page 199
N	Number of cycles, see equation (4.2), page 89
N_g	Number of gear teeth, see equation (2.1), page 18
P	Pressure, see equation (2.64), page 57
p	Circular pitch, see equation (2.2), page 18
Q	Slope of the unloading curve, see equation (3.2), page 83
q_1	GTN model parameter, see equation (2.79), page 63
q_2	GTN model parameter, see equation (2.79), page 63
Q_v	AGMA transmission accuracy level, see equation (7.181), page 201
$Q_{j/v}$	Diffusion activation energy, see equation (7.23), page 165
R	Gas constant, see equation (7.23), page 165

r	Radius of a circumference, see equation (2.38), page 50
S	Deviatoric stress, see equation (2.16), page 45
S_e	Elliptic integral of the second kind, see equation (5.7), page 115
S_N	Standard deviation for nucleation strain, see equation (2.82), page 64
T	Temperature, see equation (7.23), page 165
t	Time, see equation (7.27), page 169
T_q	Torque, see equation (7.178), page 200
t_R	Rim thickness, see equation (7.183), page 202
U	Electric potential, see equation (4.1), page 88
U_0	Initial electric potential, see equation (4.1), page 88
V	Pitch line velocity, see equation (7.179), page 201
W	Width, see equation (4.1), page 88
W_t	Tangential transmitted load, see equation (7.176), page 199
Y	Adapted Lewis form factor, see equation (7.186), page 203
y	Half of the distance of the DCPD sensors, see equation (4.1), page 88
Y_j	Geometry factor for bending strength, see equation (7.176), page 199
Z_e	Elastic coefficient, see equation (7.177), page 200
Z_I	Geometry factor for pitting resistance, see equation (7.177), page 200
Z_r	Surface condition factor, see equation (7.177), page 200

CHAPTER 1

INTRODUCTION

1.1 INDUSTRIAL CHALLENGES

Renewable energy sources have been expanding continuously since the signing of the Kyoto Protocol in 1997. The Kyoto Protocol established the initial targets for the reduction of greenhouse gas emissions for industrialised countries [1]. Additionally, the European Union (EU) countries are required to achieve a contribution of at least 20% of their total energy mix using renewable energy sources by 2020 according to the requirements of the Renewable Energy Directive [2].

Wind power plays a major role amongst utility-scale renewable energy power generation, experiencing an average annual growth rate of 23% over the last decade. The total global installed capacity has reached 539 GW as of 2017, contributing more than 5% of the total global electricity demand [3].

At the same time, the rated power capacity of wind turbines has greatly increased from 15 kW in the 1980s to around 10 MW in 2018 (VESTAS V-164 upgraded model) [4] whilst 12MW models are being designed [5]. To enable the production of higher power output, the diameter of the rotor has increased as well, reaching lengths up to 164 m. Historical trends imply that power capacity and size of wind turbines will keep increasing with 20 MW models being quite possible in the mid-term future [6].

However, the expansion of wind power capacity has been restricted due to a number of operational challenges which are yet to be addressed. The most important of these challenges appear to be the reliability of the wind turbine gearbox (WTG). WTGs are currently unable to survive their predicted design lifetime of 20-25 years. Most of them hardly reach a useful operational lifetime of more than 7 years without serious refurbishment or replacement. In offshore wind turbines, failure occurs even earlier due

to the highly variable loads experienced, resulting in rapid structural degradation. Early and unexpected gearbox failures can result in additional expenditure due to the loss of production as well as associated corrective maintenance costs. Gearbox failures can be related to gear, bearing, or shaft failures. In the United Kingdom, it is estimated that 20% of the Levelised Cost of Electricity (LCOE) produced by offshore wind farms arises due to operation and repairs [7].

1.2 AIMS AND OBJECTIVES

The aim of this study is to contribute towards a better understanding of the failure mechanisms of WTG components. In order to achieve this, the combination of mechanical tests, advanced condition monitoring, surface engineering, and micromechanical damage modelling was employed in this multi-disciplinary study. The main objectives of this study have been:

1. To carry out failure analysis of WTG components provided by wind farm operators, in order to better understand their root cause and failure mechanisms;

2. To develop a reliable and accurate finite element model coupled with a micromechanical damage evolution law that simulates failure in WTG components;

3. To study material damage initiation and propagation under rolling contact fatigue conditions similar to those experienced by WTGs, and evaluate the influence of different surface engineering methods;

4. To monitor rolling contact fatigue and mechanical tests via advanced acoustic emission monitoring, in order to evaluate and quantify damage initiation and propagation.

Finally, these data were combined to drive forward the understanding of failure of WTGs and its components, while presenting modelling and condition monitoring solutions to increase their reliability.

CHAPTER 2

LITERATURE REVIEW

2.1 WIND TURBINES

A precursor to the first horizontal-axis wind turbine, similar to the ones used nowadays, was built in 1931 in Yalta, former Soviet Union. Its tower was 30 m high and had a capacity of 100 kW [8]. The horizontal-axis design with three blades is currently the most common wind turbine configuration. The main components of this configuration are shown in Figure 2.1 [9, 10].

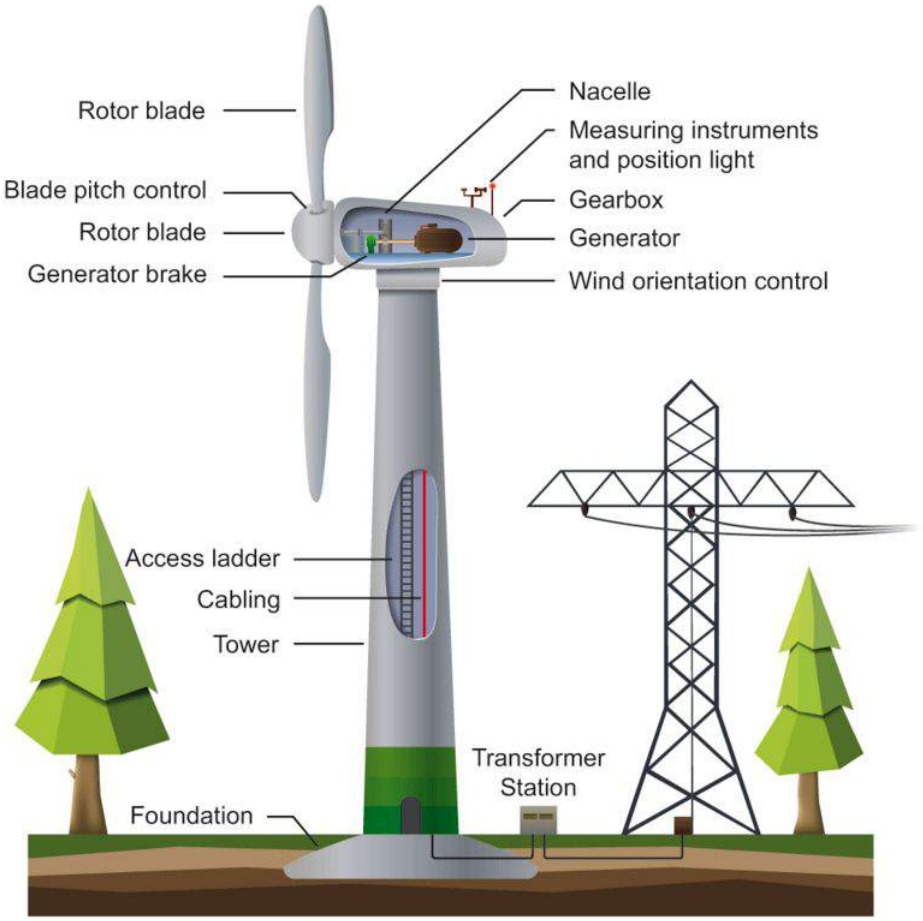

Figure 2.1: Main components of a three-bladed wind turbine. Source: [11].

The rotor blades are connected to each other through the hub and turn as air particles impact on their surface due to kinetic energy of the wind. In geared wind turbine designs, the gearbox acts by multiplying the rotational speed of the rotor in the generator up to the speed required for electrical power generation. The yaw system rotates the nacelle and rotor at the top of the tower according to the direction of the wind. The position of the blades is adjusted by the pitch mechanism. The pitch mechanism, when required, can also act as an aerodynamic brake, controlling the amount of kinetic energy harvested by the blades [9, 12].

The energy capacity of wind turbines has been increasing in the last decades, from 15 kW machines in the late 1990s to 10 MW machines at present [4, 6]. Even bigger wind turbines, up to 20 MW, are now under development [13]. Although wind turbines continue to be produced in small, medium and large sizes, wind turbines above 1 MW have become commonplace for utility-scale power generation. This is because wind turbine costs per rated kW usually decrease as machine size increases [10, 14]. In 2013, the average energy capacity of installed wind turbines was 1.93 MW, against an average of 1.34 MW for all turbines operating worldwide [15]. This shows an increasing trend for larger wind turbines being preferred by manufacturers and operators.

In order to be cost-effective, wind turbines must achieve their intended design lifetime, while generating enough electricity to offset the initial capital and maintenance costs required. Although wind turbines are typically designed to last at least 20 years, this is rarely the case. WTG designs have improved over recent years but they have not achieved yet their intended desired lifetime goals. Given that gearboxes are amongst the most expensive sub-systems of utility-scale wind turbines, their premature failure increases the cost of wind energy production considerably [9, 10, 16]. Direct-driven design configurations also exist and have been developed to remove the need of a gearbox. However, direct-drive designs are heavier and more expensive when compared to geared wind turbine models [17]. Tavner et al. [18] discussed that the failure rate of the power electronics in direct-drive wind turbines is significant, resulting in high cumulative down-

times which are comparable with those caused by gearbox failures. In wind farms with poor accessibility, the frequent failure of the wind turbine power electronics can result in significant operational downtimes throughout long-term use. Consequently, this can adversely impact the financial success of the wind turbine.

2.2 GEARBOX

Approximately 75% of all wind turbines are based on geared designs. However, in the case of offshore wind farms, there is an increasing tendency to employ direct-drive designs to overcome the reliability issues of current gearbox designs [10].

Most geared wind turbines employ a two or three-stage gear set, as shown in Figure 2.2. The most significant advantage of using a planetary stage gear set is the high gear ratio achieved while maintaining a reasonably light and compact design configuration. Additionally, the planetary set can handle high torque loads, which is the main reason of being installed at the low-speed shaft. Another great benefit of geared wind turbines is that the high speed required by the generator allows the use of a smaller and more compact generator in comparison with direct-drive wind turbines, saving in total weight and cost of a wind turbine [10, 19, 20]. Apart from the aforementioned configurations, new drive-train designs such as the medium-speed drive-train have been under development [10, 21].

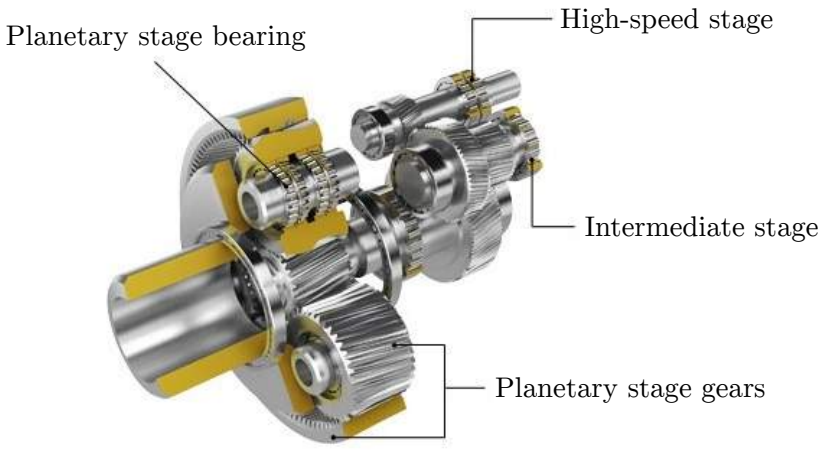

Figure 2.2: Schematic diagram of a wind turbine gearbox. Source: [22].

The conditions in which WTGs operate are different from other gearboxes used in conventional steady-state applications. The loads under which they are submitted vary with the aerodynamic torque applied on the blades. Other external electromechanical failures can also generate shock loads and lateral loads that can be transferred to the gearbox. The lack of satisfactory understanding of the stochastic and dynamic loads, as well as misalignment of the high-speed shaft, and lack of proper lubrication are some of the causes of premature gearbox failures. The failure mechanics are also not fully understood as of yet [10, 23].

Numerous authors have suggested that the leading factor of WTG failures is bearing damage, particularly in the high-speed shaft. The damage in bearings then subsequently progresses into the gear teeth as excess clearance and wear debris produce misalignment and surface wear [16, 24, 25]. A study by Kotzalas and Doll [26] has concluded that the wear suffered by the main bearings reduces their lifetime, leading to wind turbine downtime as long as 600h [25]. This level of downtime associated with the gearbox replacement is related with the difficulty of accessing the nacelle as well as the wind farm site itself [9, 27]. Additionally, gearbox replacement requires special equipment. In the case of offshore wind farms, special jack-up vessels carrying such equipment may not be readily available or adverse weather conditions may prevent the deployment of the maintenance crews on site. Apart from the costs associated with the loss of energy production, maintenance equipment and personnel, the gearbox itself is one of the most expensive wind turbine subsystems. It accounts for a significant percentage of the overall wind turbine capital cost which can be as high as 20% of the total wind turbine cost. Figure 2.3 shows that even though the gearbox is among the components that fail less frequently, it has the second highest downtime of all [28].

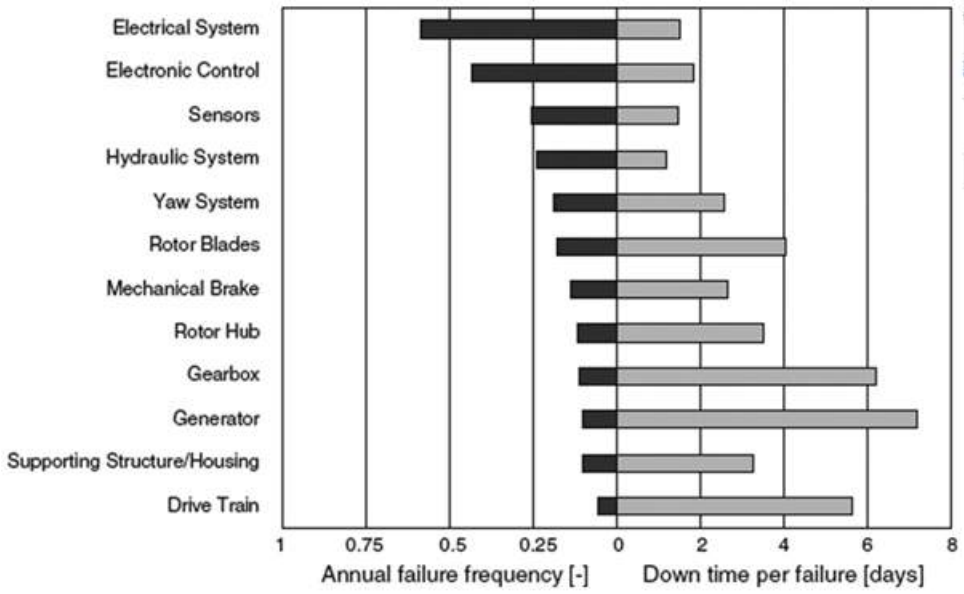

Figure 2.3: Downtime and annual failure frequency of several wind turbine components and subsystems. Source: [28].

2.2.1 Gearbox materials

Ferrous alloys are usually first choice of the the designer when it comes to power transmission gears [29]. Gears for this kind of application generally use high chromium steel grades that produce a soft yet tough core, in order to accommodate the bending on the base of the gear tooth [30]. Table 2.1 shows data on different materials and treatments used for gear design.

Table 2.1: Material data for gear design. Adapted from: [31].

Condition or treatment	**Material**	**Surface hardness (HV)**	**Tensile strength of core (MN/m^2)**	**Allowable contact fatigue stress (MN/m^2)**	**Allowable bending fatigue stress (MN/m^2)***
Normalised	0.4% C steel	165	530	10	145
Through hardened	C-Mn, Mn-Mo, 3% Ni	200	695	12.5	159
	1% Cr-Mo, 3% Ni-Cr, 3% Cr-Mo	250	850	21.5	214
	1% Cr-Mo, 2.5% Ni-Cr-Mo	270	925	23.5	221
	3% Ni-Cr-Mo	365	1230	26	234
Carburised	C case hardening steels	800	495	65.5	214
	2% Ni-Mo	725	750	69	255
	3% Ni-Cr-Mo	750	950	75.5	283
	4.25% Ni-Cr, 4.15% Ni-Cr-Mo	710	1250	89.5	345
Nitrided	3% Cr-Mo	850	800	55	179
	3% Cr-Mo-V	850	1250	69	283

* These values do not include stress concentration factors at the tooth roots.

According to the WTG design recommended by the American Gear Manufacturers Association (AGMA) [32], the core hardness of external gears must be in the range of 290-450 hardness Vickers (HV). In order to improve their durability, gear components are also surface hardened [30]. All gear materials must follow the ISO 6336-5 standard [33]. The allowable contact fatigue stress and the allowable bending fatigue stress, as well as the effective case depth, also need to be in accordance with the IEC 61400 standard [34].

Grade 2 material in the ANSI/AGMA classification or MQ material in the ISO 6336 classification are generally used in the making of wind turbine gears [35]. Therefore, wind turbine gears are often manufactured from low carbon, high chromium and molybdenum steel grades such as 4320, 4820, 9310, and 18CrNiMo7-6 [36]. For carburised gears, nickel and molybdenum in the right combination can increase the maximum toughness of the material. They also improve the resistance to grain coarsening during austenitising [37].

On a WTG, the contact stresses are typically between 1.0 and 2.1 GPa. The bending stresses are usually in the range of 345 to 483 MPa. However, external factors such as braking events and misalignments can increase these stresses up to 10 times [37].

WTG designs have been improving over the years resulting in the continuous revision of the IEC-61400 international standard, which outlines the minimum requirements for the specification, design and verification of gearboxes in wind turbines [34]. Despite these continuous improvements, several technical challenges remain that have yet to be overcome, especially in the case of offshore wind farms.

2.2.2 Gearbox failures

WTGs are exposed to a range of damage mechanisms that can affect them. Such damage mechanisms can include rolling contact fatigue, abrasive wear, micropitting, scuffing, white etching area cracks, false brinelling, and fretting corrosion. The most common faults observed are related to gear and bearing damage. Bearing failures are found to be the root cause of the majority of these failures [26, 38]. A brief explanation for some of the mentioned failure modes is provided below.

Rolling contact fatigue (RCF) is one of the main causes for failure of components that experience rolling/sliding contact. RCF is caused by alternating stress fields either at the surface or subsurface of the material. This leads to the initiation of cracks that eventually grow due to cyclic loading, leading to material removal as micropitting or spalling [39]. Catastrophic failure then occurs as a result of misalignment or debris within the contact region. RCF failures are usually classified as having originated from the surface or subsurface regions.

When the contacting elements are lubricated properly, the crack typically starts as a subsurface crack which then propagates towards the surface. An example of RCF subsurface cracks can be seen in Figure 2.4. Since these subsurface cracks usually initiate around inclusions, the cleanliness of the steel plays a major role in minimizing RCF and prolonging the life of the component [40]. RCF lifetime can also be impacted by other factors such as the material microstructure, residual stress, contact pressure, operating temperature and work-hardening response [40, 41]. RCF occurs in a small amount of material, due to the stress field being highly localised. Contact widths are usually between 200 µm to 1000 µm [40].

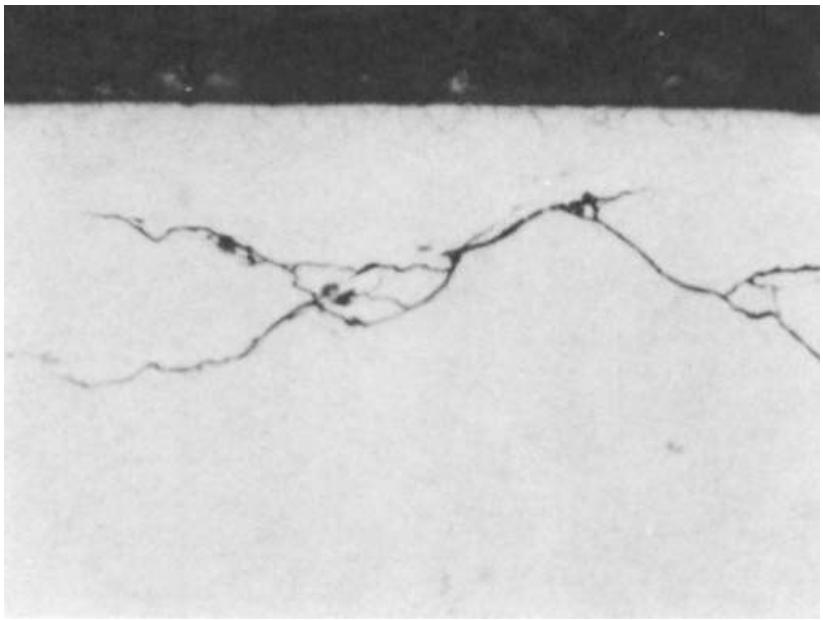

Figure 2.4: Gear tooth section showing RCF subsurface cracks. Source: [39].

The material response under RCF can be related to either perfectly elastic, elastic shake-

down, plastic shakedown, or ratcheting, as shown in Figure 2.5 [42].

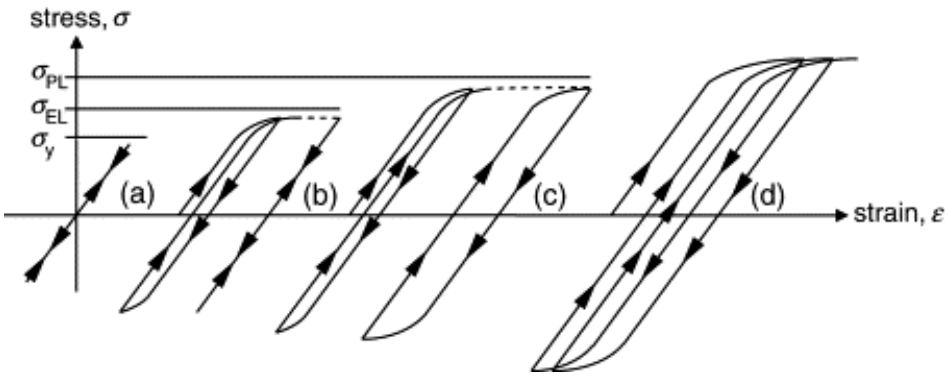

Figure 2.5: Possible material responses under RCF: perfectly elastic (a), elastic shakedown (b), plastic shakedown (c), and ratcheting (d). Source: [42].

The perfectly elastic response occurs when the plastic yield of the material is never reached during RCF. The elastic shakedown occurs when the plastic yield of the material is reached in the first few cycles, and the combined effect of the residual stresses with the plastic-hardening brings the material to an elastic state. Plastic shakedown occurs when the applied load is higher so that the cyclic stress-strain curve of the material behaves as a loop. Finally, ratcheting occurs when the material accumulates plastic deformation at every loop until the ductility limit is reached [42].

Way [43] was the first to reproduce RCF in laboratory conditions by using a twin-disc machine where two steel disks would rotate against one another under a specified load. A great number of experiments have since been carried out, including setups where contact is made between a cylinder and another cylinder, cylinder against ball, multiple balls against one cylinder, among others. Other parameters that are usually examined as part of RCF tests are the rolling/sliding ratio, contact stress, operating temperature, rotational speed of the specimens, and lubrication regime [44].

However, even though RCF has been extensively studied [39], investigations regarding intermittent lubrication are scarce. This is a particularly important area for WTGs since instant misalignments created by sudden wind gusts, for example, might squeeze the lubricant film away from the contacting teeth. Tyfour et al. [45] used a twin disc machine to study the effect of a brief dry period of contact followed by a water

lubricated period on RCF of pearlitic rail steels. It was found that 500 dry cycles reduced the fatigue life of the specimens by 40%, at a Hertzian contact pressure of 1.5 GPa. Fletcher and Beynon [46] ran similar tests at the same contact pressure and 500 dry cycles, followed by a lubricated period. They investigated the effects of two different lubricants: water and a colloidal suspension of molybdenum disulphide in an oil carrier fluid (MIO lubricant). They found the specimens tested with the MIO lubricant lead to a rapid mode of surface failure, which was not observed during the water lubricated tests. Faccoli et al. [47] compared the RCF of two rail steel grades under dry, lubricated, and intermittent lubrication conditions, using water as the lubricant. For both materials, the addition of water after a dry testing period accentuated the propagation of cracks, leading to a worse RCF life when compared to fully dry tests.

Micropitting (Figure 2.6a) is normally a precursor to greater surface failures and affects both gears and bearings. This type of failure is related to tangential shear stress caused by rolling and sliding contact. Micropitting often occurs when the oil layer does not have enough thickness in order to separate the contact surfaces, causing them to slide against one another [20, 26]. Micropitting is particularly damaging to bearings as it changes the geometry of raceways and rollers. These changes may result in an increase of the internal clearance, generating edge stresses which can evolve into macro-pitting, subsequently resulting in bearing failure [48].

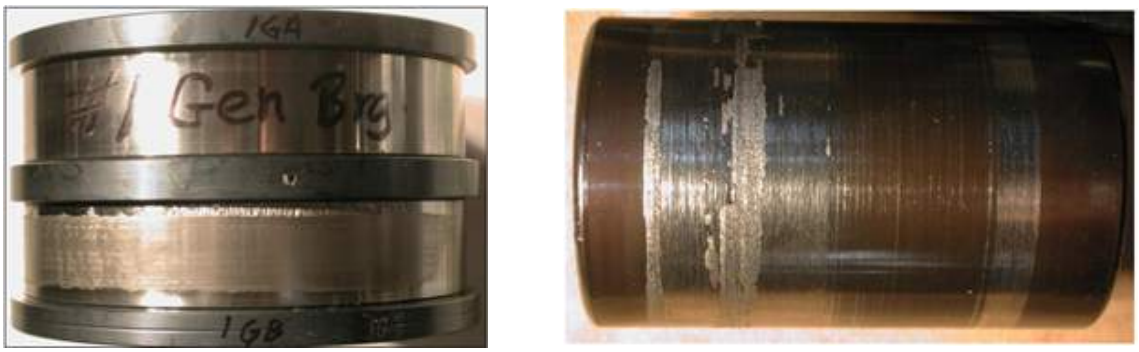

(a) (b)

Figure 2.6: Micropitting in the inner race of a bearing (a). Scuffing in bearing roller (b). Source: [49].

Scuffing, shown in Figure 2.6b, is normally caused by overheating. Overheating can arise when the thickness of the lubrication film in between the contact surfaces is inadequate (generally due to high loads or increased speed). This causes local frictional heating at the surface, which is the main cause for scuffing. The first signs of scuffing are the sudden increase in vibration, followed by a progressive temperature rise. If no action is taken, dramatic effects, such as smoke from the overheating lubricant or even sparks may be generated. Severe scuffing can eventually lead to gear tooth fracture. Once scuffing begins, it is difficult to re-establish an appropriate oil film condition to prevent further degradation [20, 26].

False brinelling (Figure 2.7a) and **fretting corrosion** (Figure 2.7b) are wear mechanisms that are also common in WTGs. Even though these terms are often used interchangeably, they depict two different wear mechanisms. Both are caused by relatively small motions, which may occur when wind turbines are parked but are vibrating due to the wind [20]. The difference between these modes is explained by Errichelo in ref. [50]. False brinelling occurs under boundary lubrication due to mild wear adhesion and produces magnetite debris. It generates noise and reduces the lifetime of bearings due to the creation of stress concentrators that eventually lead to fatigue failure. Fretting corrosion occurs under unlubricated conditions and is related to fretting damage followed by corrosion. Due to lack of lubricant severe adhesion takes place, resulting in the removal of the original oxide layer. Fretting corrosion produces hematite debris. The best solution for preventing false brinelling and fretting corrosion is to minimise the vibration of the components using vibration isolators or by tightening the contact surfaces. Additionally, appropriate surface engineering treatment or solid lubricants can be used to keep the surfaces separated. Incorporating anti-wear additives in the oil is also beneficial, leading to reduced wear rate.

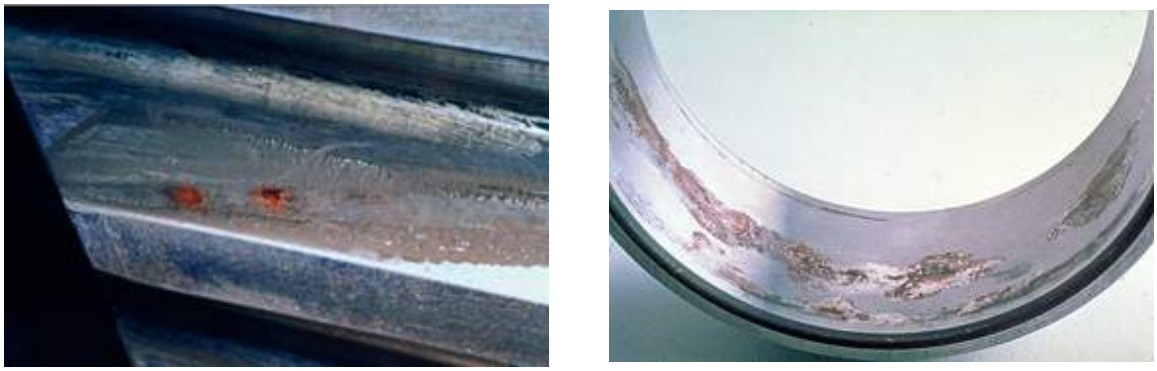

(a) (b)

Figure 2.7: False brinelling of planet gear teeth (a), source: [50]. Fretting corrosion of bearing inner ring (b), source: [51].

White etching area (WEA) cracking is the most common type of failure of WTG bearings. Its formation mechanism has not been particularly well explained yet, despite great research efforts [7]. WEA cracking is a type of rolling contact damage that has the appearance of a crack or macro-pitting on gear and bearing surfaces. Cracks propagating from WEAs may generate flaking-type wear of bearing raceways. Hydrogen embrittlement produces a similar type of wear. Due to this, several studies suggested the diffusion of hydrogen from the oil could potentially be the reason for WEAs on WTG bearings [7, 20]. Another reason could be the debonding of non-metallic inclusions, which was found to have an effect on the initiation of WEAs [52]. WEAs have this name because they appear white after etching in nital, as shown in Figure 2.8.

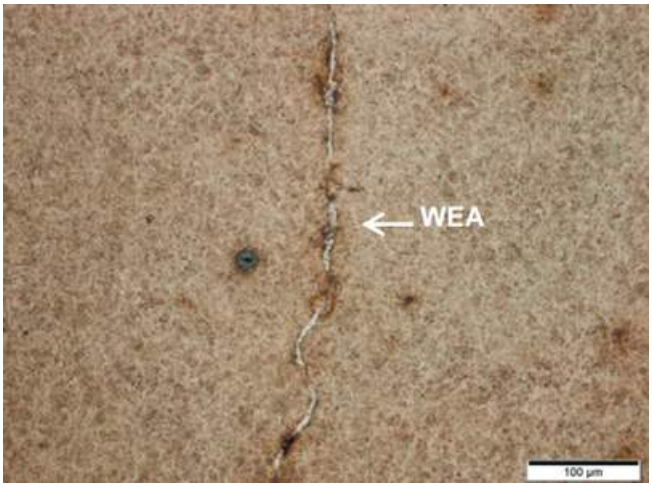

Figure 2.8: Optical micrograph image of white etching areas. Source: [20].

Tooth bending fatigue, shown in Figure 2.9, is another common WTG failure mechanism. Depending on its design and loading conditions, high-stress concentrations are usually present at the root radius of the gear tooth. Due to the dynamic load variability that is pertinent to gear movement, the tooth root radius becomes a preferential site for crack nucleation. The crack path resembles that of the letter "L" with the crack initially growing inwards, towards the zero-stress point. However, as the crack propagation continues, the zero-stress point shifts laterally, until reaching a position at the root of the opposite side, eventually leading to tooth fracture. Due to overloading, it is also commonly found that adjacent teeth also break. Tooth bending fatigue can be caused by poor design, overloads, incorrect assembly or misalignment [53].

Figure 2.9: Tooth bending fatigue crack of a spur gear. Source: [54].

Contamination in the gearbox oil is a problem that has been investigated in numerous studies [27, 28, 55]. Particle contamination can cause abrasive wear and initiate surface fatigue spalling, as well as reduce the service life of gear lubricants [26, 56]. Impurities are capable of entering the gearbox during manufacturing, assembly or maintenance, produced by wear, or admitted by breathers and seals. The use of smooth surfaces, surface-hardened gears and high viscosity lubricants can minimise the internal generation of wear debris [55].

As already mentioned, several failure modes such as micropitting and scuffing

arise from unsatisfactory lubrication film thickness [26]. Water contamination is one of the roots of these failures since it can be a catalyst of micropitting [27]. It causes the effective viscosity of the lubricant to change, consequently changing the ability of film generation in the contact surfaces [26, 57].

Another reason for gearbox failure is the operational environment under which they operate, and the lack of understanding of the dynamic stochastic loads. In a wind turbine, the torque level will be in the range of zero and the standard torque due to the wind velocity. Sometimes, the torque can be even higher than the standard torque due to slow pitch responses. Moreover, due to braking events, occasional larger torques of short duration may exist [58]. Due to the large amounts of torque to which they are submitted, wind turbine drive-train components need to be significant in size. These drive-train components experience instant and long-term misalignments of the gear mesh, as well as bending of the gearbox casings and shafts. Wind turbines also experience abrupt changes in velocity due to connection and disconnection of the power grid generators, which can release potential energy that leads to high amplitude torque reversals [26]. Tavner et al. [59] showed a strong correlation between failure rate and weather conditions. They found the temperature and humidity play an important role in WTG failures.

2.3 GEAR DESIGN

Gears are toothed wheels used for transmitting motion or torque between machinery mechanisms. Gears have been used for more than 3000 years and are currently employed in the majority of machinery. They come in a great variety of sizes and shapes and are generally attached to a spinning shaft and used in couples. Several categories of gears exist, each more appropriate for a specific application [60].

2.3.1 Types of gears

Spur gears (Figure 2.10) are cylindrical gears and have teeth whose edges are parallel to its axis of rotation. Spur gears are employed to transfer torque among parallel shafts. They are the most basic kind of gear form and the other types of gears are based on its

format. Spur gears are usually employed when machine noise is not a detrimental factor [61].

Figure 2.10: Spur gear with 55 teeth.

Helical gears (Figure 2.11) have teeth whose edges are not parallel to the axis of rotation but inclined at an angle instead. Even though they can be employed for similar uses as spur gears, helical gears are more silent due to the steady engagement of the teeth during meshing [61]. They are usually employed in high-speed applications and are generally more expensive than spur gears [62]. Helical gears can also be used to transfer torque among non-parallel shafts.

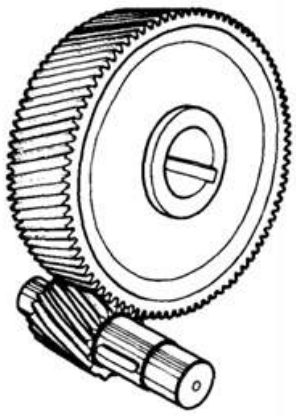

Figure 2.11: Helical gear pair. Source: [63].

Bevel gears are conical instead of cylindrical and are employed for the transmission of rotation between nonparallel shafts, usually perpendicular. They are employed in vehicles, helicopters and mills [60]. Figure 2.12 displays a couple of straight tooth bevel gears.

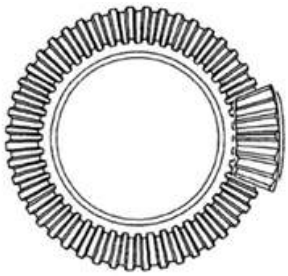

Figure 2.12: Straight-tooth bevel gear pair. Source: [63].

A worm gear is a type of helical gear which may have one or more threads resembling a screw. The edges of the worm are cut in order to guarantee that they will mesh with the edges of the worm gear. Worm gear sets are able to deliver high-speed reduction and can be used in high load applications. The frictional heat generation in a worm gear set is high, hence continuous lubrication is required [62]. Figure 2.13 shows a worm gear set.

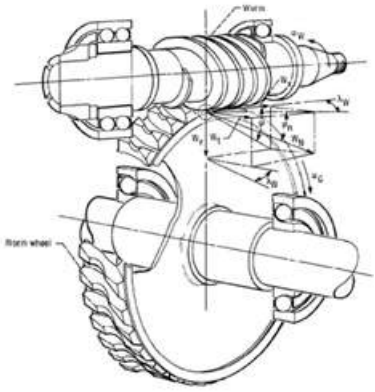

Figure 2.13: Worm gear pair. Source: [63].

2.3.2 Spur gears nomenclature

The nomenclature for several parts of a spur gear is shown in Figure 2.14. Whenever a couple of gears is meshing, the smaller gear is named the "pinion", while the bigger is named "gear wheel" or only "gear" [61, 62].

The pitch circle is a conceptual circle on which most gear designs are based. The diameter of the pitch circle (d_p) is named pitch diameter and is given in mm [61].

The module (m_g) is the pitch diameter divided by the number of teeth (N_g), as shown in equation 2.1, and is also given in mm [61]. In the SI, the gears are indexed

by its module. Typically, the height of a tooth is 2.25 times the module [62]. Figure 2.15 shows the relationship between gear tooth and module.

$$m_g = \frac{d_p}{N_g} \tag{2.1}$$

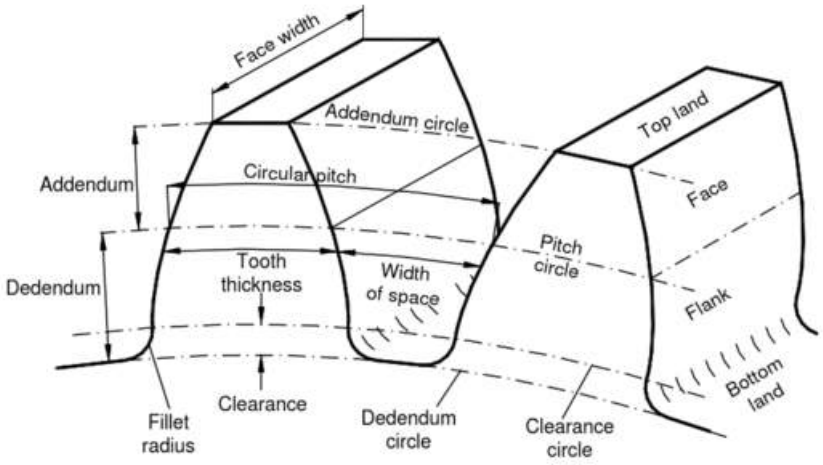

Figure 2.14: Schematic diagram of spur gear showing the main gear geometry. Source: [62].

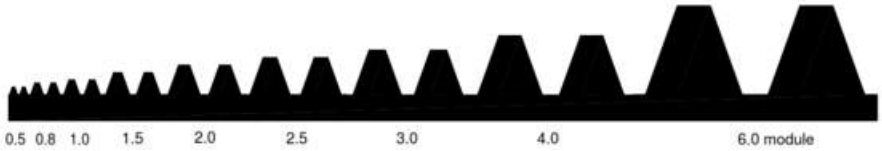

Figure 2.15: Relationship between gear tooth size and module. Source: [62].

The circular pitch (p) is the length between a point in one tooth to a corresponding point of a subsequent tooth along the pitch circle and can be calculated by the formula on equation 2.2 [62].

$$p = \pi m_g = \frac{\pi d_g}{N_g} \tag{2.2}$$

The addendum (a_g) is the distance between the addendum circle and pitch circle. The dedendum (b) is the distance between the dedendum circle and pitch circle. The tooth height (h_t) is equal to the sum of the addendum and the dedendum [61]. The addendum

is usually equal to the module, while the dedendum is usually 1.25 times the module. The width of the gear is named face width (F_w).

The clearance (c) is the difference between the dedendum and the addendum, and the clearance circle is a theoretical circle that will be tangent to the addendum of the coupling gear [61].

The pressure angle is the angle θ between the pressure line and the tangent of the pitch circle through the pitch point P [61] as shown in Figure 2.16. The resultant force vector between two mating gears has the same direction as the pressure line. The resultant design of the gear will depend on the pressure angle of choice [62]. The current standard pressure angle is 20°, however, angles between 14.5° and 25° are used occasionally, depending on the application.

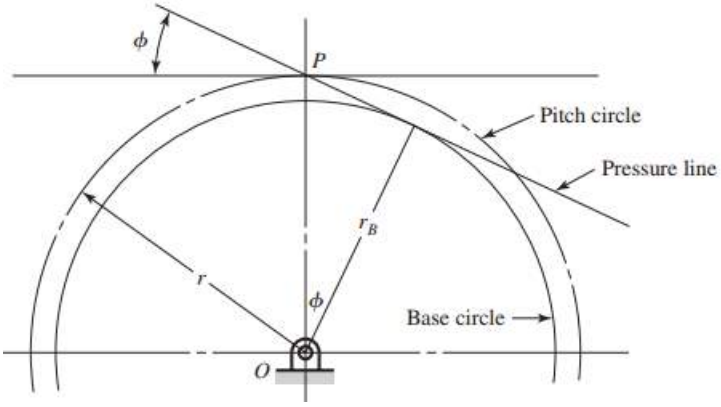

Figure 2.16: Illustration of pressure angle and pressure line. Source: [61].

2.3.3 Involute profile

The most commonly employed tooth design is the full depth involute profile. Whenever involute shaped gears are mating, the velocity ratio between them is constant. This means that from the moment of the first contact until disengagement, the gear speed is constant and proportional to the pinion speed. This causes a smooth action and avoids accelerations and decelerations that would be present whether the velocity was not constant, which would generate vibrations and potentially damaging torsional oscillations [62].

An involute can be described by the path performed by unwinding a ball tied

to a string wrapped around a cylinder, as seen in Figure 2.17.

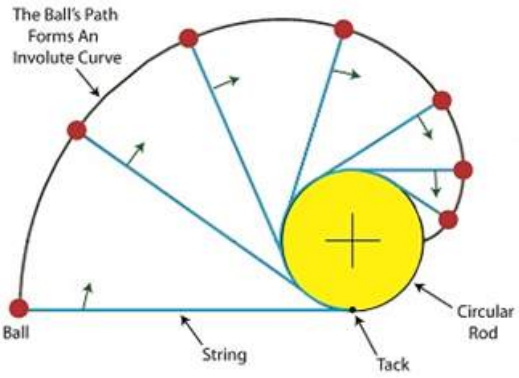

Figure 2.17: Generation of an involute curve. Source: [64].

2.4 LUBRICATION

With no lubrication, most machines would have a brief operating life. Insufficient lubrication is a serious problem since it generates excessive wear. The machine can then reach a point, usually after a short time, in which its components will not be able to operate properly and the device must be removed from service and refurbished. Insufficient lubrication causes frictional forces to be generated among the surfaces in contact. These forces may overload the drive engines. Additionally, insufficient lubrication causes machinery to be noisy and run inefficiently [65].

Machinery components are usually lubricated by fluid layers or films that are interposed between surfaces in motion. These layers reduce the interaction between the surfaces, and thus the frictional forces between them are reduced as well [65].

Three different regimes of lubrication can occur whenever a fluid is used: boundary lubrication, mixed film lubrication and hydrodynamic lubrication, as shown in Figure 2.18.

Hydrodynamic lubrication is sometimes called fluid-film or thick-film lubrication and is the most advantageous type of lubrication. In this regime, the coefficient of friction is governed only by the bulk viscosity of the lubricant [66]. Additionally, the interacting surfaces are entirely separated from each other and the contact load is maintained by the lubricant layer alone [67] since the height of the lubricating layers are usually many

times bigger than the height of the asperities of the mating surface [68].

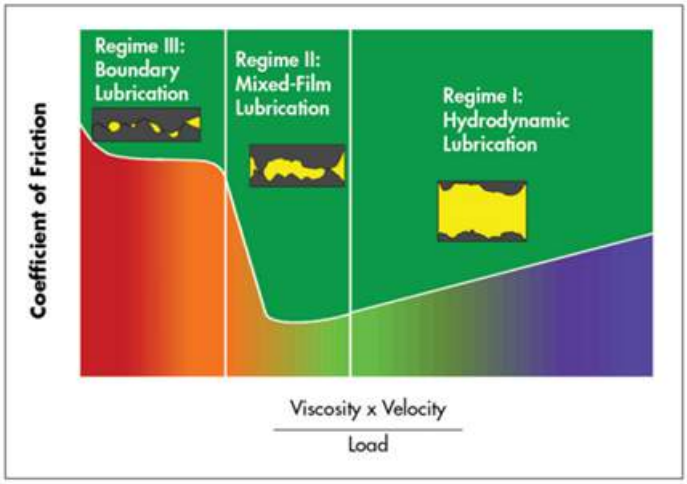

Figure 2.18: Stribeck curve showing three lubrication regimes. Source: [67].

Mixed lubrication occurs when the surfaces are not totally separated. Part of the load is supported by surface irregularities while the balance of the load is supported by the lubricant layer [67]. The friction coefficient is governed by the surface roughness, the material properties of the interacting parts, and the material properties of the lubricant [66]. Usually, due to the excessive loads, increase in temperature, slow-speeds, start operations or run-in of new machinery, the lubricant film will break down and the parts it used to separate will interact with each other. The breakdown of the mixed film regime leads to boundary lubrication [65]. In a simplified view, mixed lubrication can be expressed as a mixture of hydrodynamic and boundary lubrication [66].

As the load increases in magnitude, a speed or viscosity reduction in the Stribeck curve occurs, and the friction coefficient can rise to higher levels. This regime is known as boundary lubrication. In this regime, the solid interacting parts are completely in contact. The lubricant layer becomes so thin (usually thinner than the height of some asperities) that its properties are now different than the bulk, and its viscosity has little influence on wear and friction behaviour. At this stage, what dominates the physical properties of the lubricant films are their melting point, shear strength and hardness [68]. To diminish the erosion and friction under boundary conditions, the introduction of additives that offer superior properties may be needed. Breakdown of the boundary lubrication regime may

be caused by corrosive and adhesive wear [65].

Lubricant layer thickness is influenced by numerous aspects, such as the applied load, and speed and design of the interacting surfaces. However, the viscosity of the oil is the most important factor. An increase in viscosity causes the thickness of the lubricant layer to increase. If the reduction in the viscosity (due to the increase of the temperature, for example) is sufficiently high, it can alter the lubrication regime of the gearbox, reducing its lifetime. Moreover, a higher temperature of the oil can accelerate the rate of oxidation, reducing its useful life [67].

Nevertheless, the lubricant film thickness between the tooth flanks of gearboxes cannot be calculated using the classical hydrodynamic lubrication theory. Effects of pressure viscosity of the oil, as well as elasticity of the tooth flanks also need to be taken into account in order to estimate the contact film thickness. The regime where these parameters are accounted for is called elastohydrodynamics (EHL) [69].

2.4.1 Elastohydrodynamics

EHL is a subgroup of hydrodynamic lubrication where the elastic deformation of the contacting parts has an important participation. In this regime, the contacting surfaces may deform with the objective of increasing the area that supports the load, as shown in Figure 2.19. The EHL layer thickness is smaller than that of the conventional hydrodynamic lubrication, but the lubricant layer is still sustaining most of the load. In some areas, however, irregularities can be in contact with each other [68].

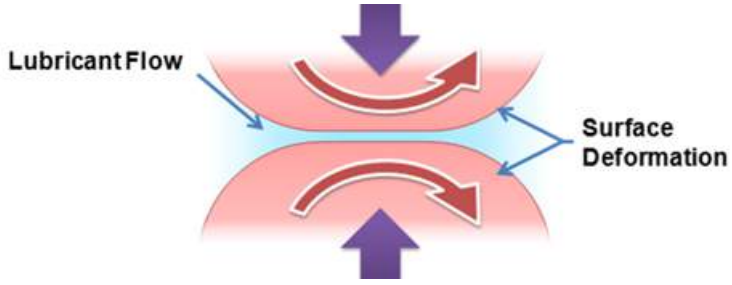

Figure 2.19: Schematic diagram of two surfaces under EHL lubrication. Source: [70].

EHL is mostly severely induced in heavily loaded contacts, where loads act over relatively

small contact areas, such as gear teeth or bearings (Figure 2.20). The high pressures generated by these heavily loaded contacts may progress to viscosity variations of the oil as well as elastic deformation of the interacting parts, therefore changing the geometry of the parts surrounded by the oil layer. Due to this, the hydrodynamic solutions had to be modified in order to account for the effects of the wear rate and temperature [68].

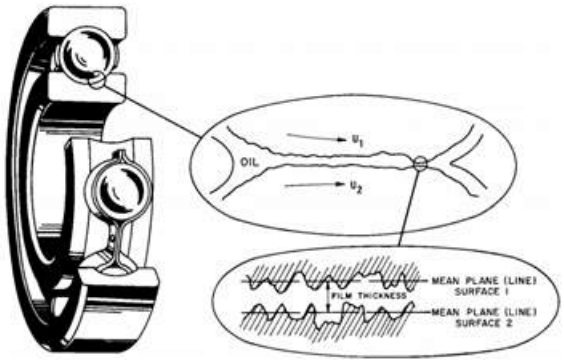

Figure 2.20: Representation of the contact area between ball and inner race of a bearing. Source: [65].

If the asperities in Figure 2.20 were higher, they would probably touch beyond the oil layer. Therefore, surface roughness and film thickness are vital to EHL. The specific film thickness (η) is given by the film thickness (h) divided by the composite roughness (σ_{cr}) of the two interacting parts, as shown in equation 2.3 [65]. The specific film thickness is associated with the capability of the oil layer to avoid or diminish wear or scuffing. If η is smaller than 1, the boundary lubrication regime will prevail and the interacting surfaces will be in contact most of the time, and under severe wear conditions. When η is between 1 and 1.5, the regime of lubrication that prevails is the mixed lubrication, and therefore, η above 1.5 is preferred for optimum bearing life [71].

$$\eta = \frac{h}{\sigma_{cr}} \tag{2.3}$$

2.5 CONDITION MONITORING

Condition monitoring systems are instruments used to verify the condition and quantify the reliability of an in-service system. They consist of several detectors and processing tools in order to deliver a non-stop evaluation of the conditions of components. Examples of condition monitoring methods are vibration analysis, oil analysis, acoustic emission, thermography, and generator current analysis [12]. The main concept behind condition monitoring is to choose a quantifiable parameter that changes as the condition of the device or component deteriorates [72].

In the early days, industrial wind turbines were only monitored during regular inspections carried out by maintenance personnel attending them. However, in order to realistically reduce the breakdown rate and address insurance requirements, more effective inspection procedures based on the efficient use of remote condition monitoring had to be implemented. The application of remote condition monitoring systems aims to identify faults as early as possible, preventing the likelihood of catastrophic failure and unnecessary loss of production, and consequently define repairs in time [12]. As wind turbines become larger and more expensive, the need to monitor their performance and predict damage initiation and rate of propagation has increased. Hence, remote condition monitoring systems have become standard in order to improve the protection of these expensive assets and maximise the potential of wind energy production by reducing downtime and maximising availability and capacity factor [25].

Figure 2.21 shows a schematic diagram of a condition monitoring system, which comprises of parts for detecting (transformation of physical indicators, typically to electric signals), data acquirement (transmission from the detectors to processing computer), feature extraction (treatment of the unprocessed data), pattern organisation (analysis of fault type and its gravity) and life prediction (projection of residual service lifespan of the monitored structure) [73].

In wind turbines, remote condition monitoring systems are often installed on

the drive-train, in order to determine the actual condition of its subcomponents (main bearing, gearbox components, generator bearings). Currently, vibration analysis is the most popular technique for monitoring onshore and offshore wind turbines [74–77]. However, the capability of remote condition monitoring systems relies both on the number and type of sensors, as well as the extraction and analysis methods [12].

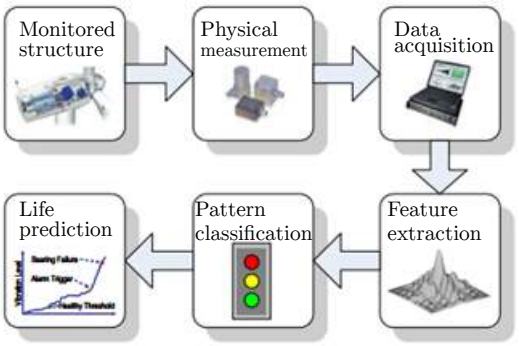

Figure 2.21: Schematic diagram of a condition monitoring system. Source: [78].

Even though the installation of a condition monitoring system may be costly at first, it will rapidly pay back by directly reducing operation and maintenance costs and growing the production rates. Additionally, the forewarn provided by the system on future faults allows the operator time to plan and order the parts that need to be replaced [79].

Supervisory control and data acquisition (SCADA) systems are incorporated in modern wind farms with the responsibility of connecting the wind farm and meteorological stations at the wind farm site to the dispatch centre of the wind farm operator [80]. These systems usually monitor parameters like temperature, lubricating oil health, as well as the vibration levels of the drive-train [81]. Garcia Marquez et al. reviewed the latest condition monitoring systems for wind turbines in ref. [12]. Salameh et al. reviewed condition monitoring techniques for WTG in ref. [82].

Because several types and configurations of gearboxes exist, the determination of their health, wear and failures have been limited to measure some basic fault symptoms which are common to almost every configuration [72].

Degradation or damage to the gearbox may manifest in several forms, such as

debris, vibration, additional heating or acoustic emission. Therefore, vibration analysis, oil debris analysis and acoustic emission monitoring can be used to effectively monitor the gearbox condition [80]. Nevertheless, no single technique can detect all possible failure modes since each has its own strengths and limitations [78]. Some of the condition monitoring techniques applied to gearboxes are discussed in the next subsections.

2.5.1 Vibration analysis

Vibration analysis is the most widely used condition monitoring technique [72, 83]. Most machines vibrate, and therefore, they will possess a vibration degree that can be considered natural. In general, excessive vibrations usually arise from mechanical problems such as imbalance, rubbing, bent shafts, worn gears, and torque variations, to name a few, and each of these flaws produces vibration and noise in an exclusive way. To better analyse the vibration signals, the original vibration state of the healthy components needs to be obtained and understood. Thus, vibration measurements should be trended over time. This is more important when the severity of a defect needs to be ascertained rather than just identifying the nature of the defect itself. Spectral analysis of these signals is able to provide an indication of gearbox components anomalies in detail [72, 76, 80, 83].

Vibration is caused by the rotational movement of individual components. As the rotational velocity of the components varies, the direction or amplitude of the forces responsible for causing the vibration changes. The consequence is that most of the vibration discrepancies will possess frequencies that correlate to the rotational velocity. Having knowledge of the characteristic frequencies of these components at a particular rotational speed from the gearbox manufacturer can help inspection engineers identify the defective component by performing spectral analysis on the raw vibration signals acquired [83]. Table 2.2 shows the most usual vibration frequencies and how they are related to rotational velocity, as well as the probable causes for each problem.

In order to capture the vibration response of gearbox components, industrial piezoelectric accelerometers are employed. The accelerometers used need to be carefully selected to ensure that their operating frequency range is appropriate for the rotational

speed of the components being monitored. The acquired signals are then analysed using a variety of distinct techniques, such as spike energy, kurtosis, spectrum analysis, cepstral analysis and envelope detection [84].

Table 2.2: Vibration frequencies and its most probable causes. Adapted from [72].

Frequency in terms of rpm	**Most probable causes**	**Other possible causes and remarks**
1 x rpm	Imbalance	Eccentric journals, gears or pulleys Misalignment or bent shaft Bad belts Resonance Reciprocating forces Electrical problems
2 x rpm	Mechanical looseness	Misalignment Reciprocating forces Resonance Bad belts
3 x rpm	Misalignment	Generally a mixture of misalignment and excessive axial clearances
Less than 1 x rpm	Oil whirl	Bad drive belts Background vibration Sub-harmonic resonance Beat vibration

The vibration signature from a component is made of complex signals, being a combination of sinusoidal waveforms of different amplitudes, frequencies and phase differences, all related to original rotational speed. In order to analyse the spectrum or the frequency distribution, it is necessary to transform the vibration signature from the time domain to the frequency domain. This is usually accomplished with the use of Fast Fourier Transform (FFT). The FFT is the relationship between the amplitude of vibration to the frequency function [72, 83].

Spectral analysis is a common method of processing the data, where the spectrum range of the vibration signal is presented. Usually, different components of the same

system will generate noise at different frequencies, making spectral analysis a capable method. Gearboxes, for instance, will produce vibration at both the fundamental and the harmonics frequencies of the mating gears, with each couple of gears usually having its unique frequency. Therefore, the variations in the spectrum can often be mapped to a unique component. This analysis, however, becomes harder as the complexity of the system increases [85].

The cepstrum is an anagram of the spectrum, and in essence, it is the spectrum of a spectrum. The advantage of using cepstral analysis is the ability to detect periodic harmonics even when they are covered in a high noise level. These periodicities could, for example, be the result of a fault in a ball bearing. However, the cepstral analysis does not work well for more than two signals at the same time domain. In these cases, it is necessary to turn to different signal analysis techniques [72].

Even though vibration analysis is a reliable and standardised technique (e.g. ISO 10816 standard), the variability of the loading conditions associated with wind turbine operation makes the evaluation of data quite challenging [76, 86]. The fact that the wind turbine drive-train consists of multiple components rotating at different speeds, ranging from low to high, adds to the complexity of the analysis. In addition, certain defect types may mask other defects which can evolve rapidly and subsequently cause failure [87]. Generally, it is important to understand that vibration analysis is used to detect the result of damage to a component giving rise to characteristic vibration signatures. Therefore, small defects, particularly damage initiation and propagation are not possible to be detected through vibration analysis. Thus it is common to couple vibration analysis with other condition monitoring techniques, such as oil analysis or acoustic emission monitoring in order to increase sensitivity, especially when damage levels are still low [25].

2.5.2 Oil analysis

Monitoring of the lubricating oil flow for metallic debris is a more direct method for the detection of wear and surface fatigue faults in gearboxes. Oil-related condition monitoring

tools are roughly divided into two subgroups: oil condition monitoring and wear debris analysis [88]. The oil condition monitoring focuses on the evaluation of the properties of the lubricant, such as acidity, viscosity, temperature and chemical composition. These measurements assess the oil quality and whether it needs to be replaced or not [84, 89]. Wear debris analysis, on the other hand, evaluates the amount of debris generated by wear of the rotating components that are present in the oil samples, as well as particle composition, size, concentration and morphology. These data can provide information about the different modes, rate and severity of wear incurring in the gearbox [80]. Table 2.3 relates the shapes of the debris found in the oil with their probable causes. Nonetheless, while oil analysis may be used as a pro-active maintenance plan, wear debris analysis can be employed to monitor wear in a reactive way only [83].

Two different monitoring approaches are commonly applied: the offline or real-time methods. In the offline method, oil and debris samples are collected at scheduled time intervals and referred to a laboratory for examination. In the real-time method, sensors are installed usually on the filtration loop, either inline or online, and collect data continuously. Even though offline methods are able to evaluate the oil condition, they can only be carried out once the gearbox is opened. Therefore, the presence of maintenance personnel is required in order to physically obtain the samples. The online sensors remove this requirement and can actually provide useful information regarding the degradation of rotating components and oil quality in real time. This information can be used to plan maintenance activities far more effectively. Offline oil analysis cannot prevent catastrophic failure since certain defects might develop and rapidly evolve between two periods of oil sample collection. [88].

Real-time oil analysis is therefore particularly useful in detecting and verifying lubricant and component deterioration due to either loss of additives, contamination, or metal wear. Additionally, it can provide early warning of incipient failures, particularly during early failure stages of damage evolution. Real-time oil analysis is becoming more and more important and cost-efficient, especially since online sensors have been available

at an acceptable cost [12].

Table 2.3: Particle shape of debris related to its most probable causes. Adapted from [72].

Particle shape	**Probable causes**
Spheres	Metal fatigue
	Welding sparks
	Glass peening beads
Pebbles and smooth voids	Quarry dust
	Atmosphere dust
Chunks and slabs	Metal fatigue
	Bearing pitting
	Rock debris
Platelets and flakes	Running-in metal wear
	Paint or rust
Curls, spirals and silvers	Machining debris produced at high temperature
Rolls	Probably similar to platelets but in a rolled form
Strands and fibres	Polymers
	Cotton and wood fibre
	Occasionally metal

A variety of methods are available for examining the condition of the lubricant and any wear elements that may be existent, such as photoacoustic spectroscopy, solid-state viscometry, ferrography, among others [72, 89].

2.5.3 Acoustic emission

Acoustic emissions (AEs) are transient elastic waves produced by a quick release of strain energy due to a distortion or fault inside a material [90]. Currently, a recognised point of view is that acoustic emission accompanies almost all physical phenomena in solids and their surfaces, with the possibility of registering this emission depending only on the sensitivity of the measuring equipment [91].

Unlike vibration analysis, acoustic emission can identify faults characterised by high frequencies in the range of 20 kHz to 1 MHz [92]. Piezoelectric transducers and

optical fibre-based displacement detectors are usually employed in this method, converting energy into a voltage. This voltage is electrically amplified and further processed as acoustic emission data, with the help of timing circuits [89, 93, 94].

AE techniques can be divided into two subgroups: signal-based and parameter-based. The signal-based technique records the full waveform, and thus requires a large amount of storage space. However, it captures more information and is more useful for statistical analysis, for example. The parameter-based technique records and stores only the most important characteristics of the signal, such as amplitude, duration, root mean square value, energy, kurtosis, crest factor, counts and events. These parameters are defined by the operator [95]. The AE energy (also referred to as "PAC energy") is defined as the area of the rectified voltage signal over the duration of the AE signal and is measured in $\mu V \cdot s$ [96].

Examples of sources of acoustic emission in rotating equipment include cyclic fatigue, material loss, crack initiation and propagation, delamination, among others [89, 90]. Such emissions spread to the exterior of the component as Rayleigh waves, which are a mixture of longitudinal and transverse waves. The displacement of these waves is measured with an acoustic emission sensor [90]. The quantity of acoustic emission energy released, as well as the amplitude of the resultant wave, will depend on both the speed and the size of the originating event. Therefore, an abrupt crack will cause a bigger signal than a slow-moving crack, when all other parameters are maintained. One popular theory is that the amount of emission energy is related to the area of the new surface created [94].

The acoustic emission process is illustrated in Figure 2.22. The process starts with a stimulus acting on a component, and the resulting stress is what causes the acoustic emission, by deforming the material. The stress acts locally on it, producing local plastic deformation, which generates the acoustic emission waves. These waves travel through the material from the originating event in all directions, transmitted through the component until arriving at the sensor. As a reaction to the mechanical displacement, an electric

signal is produced by the sensor and is then passed to electronic equipment for further processing [94].

The signal detected by the sensor is amplified and filtered. Amplifiers increase the signal voltage in order to promote it to an optimum measurement level. Along with amplifiers, frequency filters are incorporated into the acoustic emission equipment, in order to define the frequency range and attenuate low-frequency background noise. These processes of amplification and filtering are called signal conditioning since they "clean" the signal and prepare it for the detection and measurement process [94].

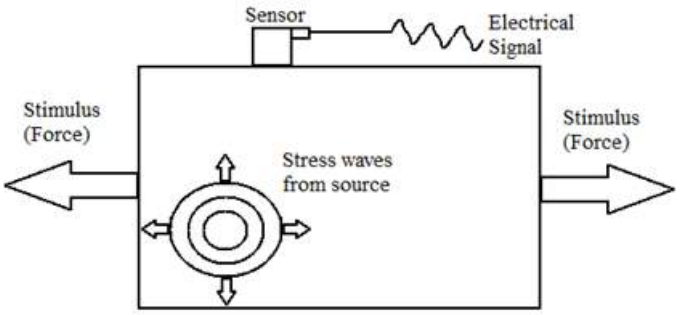

Figure 2.22: Schematic diagram of the acoustic emission process. Adapted from [94].

Two particular features of acoustic emission are the Kaiser effect and the Felicity effect [94], as shown in Figure 2.23. The Kaiser effect signifies the fact that acoustic emission activity will only resume when the previous maximum load has been exceeded once the original loading condition has been removed [93]. The Felicity effect, on the other hand, is the behaviour observed by the generation of acoustic emission at a stress level below the previous maximum. Usually, small defects lean towards the Kaiser effect, whereas structurally significant defects lean towards the Felicity effect [94]. These effects are often used in structural health monitoring analysis to understand the severity of damage sustained by a structure.

The biggest difference between the AE technique and other non-destructive techniques is that the first one is passive while most of the others are active. Active techniques are so called because, in order to create an effect in the material and detect a signal, external energy must be applied. Conversely, acoustic emission detects energy

that is generated from within the material being monitored [94].

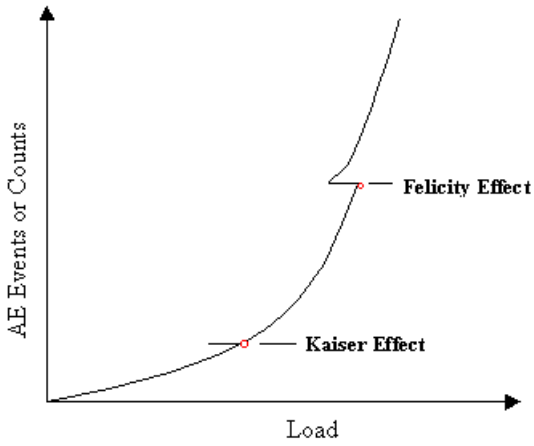

Figure 2.23: AE events versus load illustrating the Kaiser effect and Felicity effect. Adapted from [97].

An advantage of the acoustic emission method versus other non-destructive methods is that the failure and fracture processes can be monitored during all the component operating life, without causing any disruption. Moreover, acoustic emission is usually employed to detect damage in its early stage, and hence long before the component fails catastrophically [98].

The limitations of the acoustic emission technique are due to the difficulties associated with treating and analysing the acquired data, due to the high sampling rate required for some applications.

The main difference between acoustic emission over vibration is the detection of noise variations as the contact surfaces of rotating components degrade due to damage or lubrication irregularities. Vibration arises from the response of the structure itself. Therefore, the two different types of sensors capture distinctly different phenomena. For the vibrational response of a structure to change, damage needs to be more severe in comparison with acoustic emission, which focuses on the detection of noise changes produced by the contact surfaces of the rolling elements instead.

Several authors have been studying the relationship between acoustic emission and the initiation and propagation of defects and failures [92, 99, 100]. Al-Ghamd et al. [101] have found that due to the sensitivity of acoustic emission to surface roughness, the

length of the defect can be estimated from the AE spectrum.

Miettinen and Pataniitty [93] conducted acoustic emission measurements in order to detect the fault of rolling bearings with low rotation speeds, from 0.5 to 5 rpm. AE was found to detect defects in the slowest rotational speed, whereas vibration analysis methods could only identify the fault when the rotation speed remained in the range of 10 to 20 rpm.

Studies by Toutountzakis and Mba [99] and Elforjani and Mba [102] demonstrated that the acoustic emission values increased with the initiation of defects, thus demonstrating the applicability of acoustic emission to gear and bearing health diagnosis. The same behaviour was demonstrated by Sentoku [100], which linked tooth surface damage, such as pitting, to acoustic emission generation. They reached the conclusion that with increasing pitting, the energy and amplitude increased as well.

Although acoustic emission testing has greatly evolved over the last decade, deeper research is needed in order to use this technique for monitoring gearboxes on the wind turbine industry.

2.6 SURFACE ENGINEERING

The term surface engineering involves all methods and processes that are used to induce, modify or improve the performance of the surface of engineering materials [103] by altering its chemical and/or topographical properties [26]. Metallic and non-metallic surface coatings have been developed by surface engineering. Metallic coatings can be divided into hard or soft. Soft layers, like silver, act as a solid lubricant, accommodating the motion of moving parts. Hard layers resist well to corrosion and abrasive wear, however, they are still vulnerable to adhesion wear. Non-metallic coatings may reduce fretting origination by reducing the microwelding of irregularities. Moreover, they are corrosion and abrasion resistant. The downside of this type of coating is that they break down due to fracture and delamination when submitted to high frequency and highly loaded contacts [104].

Gear failures characterised by superficial flaws are common and intricate, due to contact fatigue and complex loading conditions. In order to achieve a long lifetime, gears must have a tough core to withstand fatigue bending and impact stresses. At the same time, they must have a hard surface and fatigue strength to reduce the damage caused by wear and sub-superficial cyclic loading. Such versatile mechanical properties can be achieved by employing appropriate effective surface engineering processes, such as carburising and nitriding. Both surface treatment methods generate residual compressive stresses in the most superficial layers, increasing the endurance limit for cyclic stresses [105]. Duplex surface engineering is also an alternative way of achieving the required properties by combining two or more surface treatment processes.

2.6.1 Carburising

Carburising is a thermochemical surface treatment process in the presence of a carbon-rich environment or atmosphere, such as charcoal or carbon monoxide. This treatment is conducted above the austenitic transformation temperature of the steel, due to the high carbon solubility of austenite. After being held at the treatment temperature for sufficient time, which will be dependent on the composition of the material and the intended case depth, the steel is quenched to create a martensitic microstructure [106]. After quenching, the steel is often tempered to relieve residual stresses that build up due to the dimensional changes arising from the transformation of the face centred cubic austenite to the body centred tetragonal martensite and increase toughness. Hardness values will be higher at the surface of the steel and will decrease with increasing depth in the carburised zone [105]. Several carburising methods have been developed and used in industry, such as pack carburising, gas carburising, vacuum carburising, plasma carburising and salt bath carburising. In gas carburising, which is the most used form of carburising commercially, the carbon source is a furnace atmosphere generated from gaseous hydrocarbons such as methane, propane and butane [106].

Carburising itself produces a carbon diffusion layer, and quenching must be achieved by post heat treatment to produce martensite. The quenching method depends

on the grade of steel used, carbon content in the carburised layer, as well as carburising temperature. The resultant surface layer is strong and wear-resistant [106].

After being treated, gears need subsequent grinding since the high temperatures of this process inevitably cause deformations [105]. Currently, carburising is the most employed treatment of WTGs. However, further research and enhanced surface treatments are required in order to reach the needs of modern industry [107].

In pack carburising, the source of carbon is so rich that at the surface of the steel the limit of solubility of carbon in austenite is reached, and some carbides may form at the surface. Moreover, such atmospheres can also deposit soot on the components within the furnace. Pack carburising is still in use in some parts of the world where the resources are limited, but the current practice has a goal of controlling the carbon content of the furnaces so that sooting is minimised and the final carbon concentration of the surface is below the solubility limit in austenite [106]. This has been obtained with the use of gas carburising.

The controlled carburising atmospheres are produced by mixing an enriching gas, which serves as the source of carbon, with a carrier gas. The latter, usually an endothermic gas, is mainly composed of CO, N_2, H_2, CO_2, and H_2O, where only the N_2 acts as a diluent. The enriching gas is usually methane or propane. The endothermic gas plays a role in accelerating the carburising reaction at the surface of the parts. The proportion of enriching and carrier gas will depend on the carbon demand, which is the rate at which carbon is absorbed by the material [106].

Carbon can be added or removed rapidly from steel by the following reversible reactions:

$$2\ CO \leftrightarrow C + CO_2 \tag{2.4}$$

and

$$CO + H_2 \leftrightarrow C + H_2O \tag{2.5}$$

However, a carburisation process based purely on the decomposition of CO would require large flow rates of atmosphere gas to produce substantial carburising. Therefore, the carrier gas provides carbon for the process by reactions such as:

$$CH_4 + CO_2 \leftrightarrow 2\ CO + 2\ H_2 \tag{2.6}$$

and

$$CH_4 + H_2O \leftrightarrow CO + 3\ H_2 \tag{2.7}$$

These chemical reactions regenerate CO and H_2, thereby directing equations 2.4 and 2.5 to the right, accelerating the carburising process [106, 108].

The composition of the furnace gas may be analysed to estimate the potential carbon, by measuring the dew point of the gas, which is the temperature where water droplets are deposited from the gas. This is determined by the water content in the furnace. The carbon potential can also be estimated by measuring the concentration of CO_2 in the furnace [106].

2.6.2 Nitriding

Nitriding is a surface treatment process usually performed in iron-based materials and is characterised by diffusing atomic nitrogen through the material. Since nitriding is a diffusion governed method, several reactions are involved both at the surface and subsurface. Nitriding can be achieved in a variety of ways and with different atmospheres, such as gas mixtures, salt baths or plasmas [109].

Depending on the nitriding "power" of the nitriding atmosphere, a nitride zone, which can be subdivided into a compound layer and a diffusion zone will be formed. The compound layer thickness can reach several µm and is largely composed of iron nitrides [109]. The compound zone, however, is not always present and will be dependent on a variety of factors, such as the amount of the alloying elements present and the time and temperature to which the treated part will be exposed [110]. The diffusion zone, of a thickness up to several hundredths of µm, is usually composed of iron nitrides in

carbon steels, or other types of nitrides in cases where the steel has alloying elements with affinity for nitrogen, such as aluminium or chromium [109]. The microhardness profile of a nitrided steel can be seen in Figure 2.24.

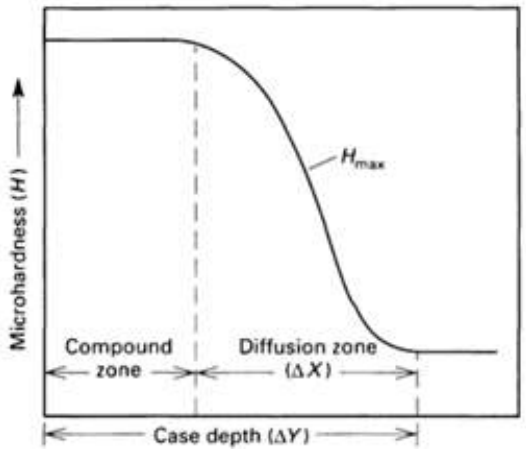

Figure 2.24: Microhardness profile of a nitrided steel. Source: [110].

The technological importance of nitriding is mostly due to the great increase of the fatigue resistance, wear, and corrosion provided by the external layer [109]. In nitriding, the surface hardness achieved is usually higher than in carburising, between 900 HV and 1200 HV. Moreover, since it does not cause significant deformation, nitriding can be done on the finished component [105].

At first, gear manufacturers were unwilling to use nitriding, because the gas nitriding processes employed at the time resulted in the production of a brittle and porous layer consisting of iron nitrides. Due to the thickness of this layer, a final grinding had to be incorporated into the process. However, at the end of the 1960s, a new process called plasma nitriding was developed and introduced. Plasma nitriding solved the problems associated with the generation of the brittle and porous layer. The introduction of plasma nitriding processing stimulated research and the development of a finer process, with the possibility of controlling the compound layer thickness and treating the whole component uniformly [111].

Plasma nitriding (also called ion nitriding or glow discharge nitriding), is a surface treatment method that uses glow discharge technology in order to insert atomical

nitrogen into the component for later diffusion. The method of plasma nitriding may be split into the following stages: air removal, heating, glow-discharge, and cooling [110].

Air removal is performed to get rid of the majority of the previous air and impurities. Even though low levels of pressure can be reached, they are usually not needed. After air removal, the temperature is increased before the glow discharge. The pressure is also increased to reduce the glow seam thickness and avoid overheating [110].

After heating the components, the process gas, usually a combination of nitrogen, hydrogen, and sometimes, small quantities of methane, is admitted. The gas is then ionised by the employment of an electric field, entering the plasma state. The components to be treated are then coupled to the cathode, whereas the compartment itself acts as the anode. During the process, the ions are accelerated towards the cathode by the electric field. Close to the component, the positive nitrogen ion obtains an electron from the cathode, emitting a photon in the process. This emission is the visible glow discharge that names the method. The ions then impact on the surface of the component with high kinetic energy, raising its temperature due to the release of energy upon striking. Therefore, no external heating is needed, since the temperature is dependent on the voltage and gas pressure, and the gas composition can be modified in order to control the nitriding potential. Finally, the gas circulation and voltage are shut down, and the temperature of the components is brought down by the flow of inert gas [110, 112].

In this technique, the accelerated ions hit the surface of the material uninterruptedly, providing a new and energetic surface for nitriding reactions, therefore eliminating the passivation issues which sometimes happens in other nitriding techniques. When compared with gas nitriding, plasma nitriding offers several benefits, for example, reduction in processing time, lower part distortion [110], among others [112].

Even though plasma nitriding is superior to other nitriding methods, especially regarding gas and energy consumption, there are still some disadvantages to it. For example, the normal direct current plasma nitriding (DCPN) technique brings the components to be treated to a high cathodic potential, so that plasma can be formed, leading to heat-

ing and nitriding. This, however, creates some difficulties, such as the "edging effect", "hollow cathode effect", damage by arcing, and unstable chamber temperature [113–115].

The active screen plasma nitriding (ASPN) technique was created in order to overcome some of these challenges. In this technique, the components to be nitrided are surrounded by a hollowed metal cage to which a high cathodic potential is applied. The components are electrically insulated from the worktable and held at a floating potential. The plasma is then formed on the metal cage, rather than directly at the surface of the components. This plasma then heats the cage and consequently the components inside, while also ionising the gas, electrons, and other active nitriding species surrounding it. The ASPN technique allows components with complex shapes to be nitrided, while maintaining a stable chamber temperature and eliminating arcing damage and "edge effects" [113–117]. Figure 2.25 shows a comparison between the DCPN and ASPN techniques.

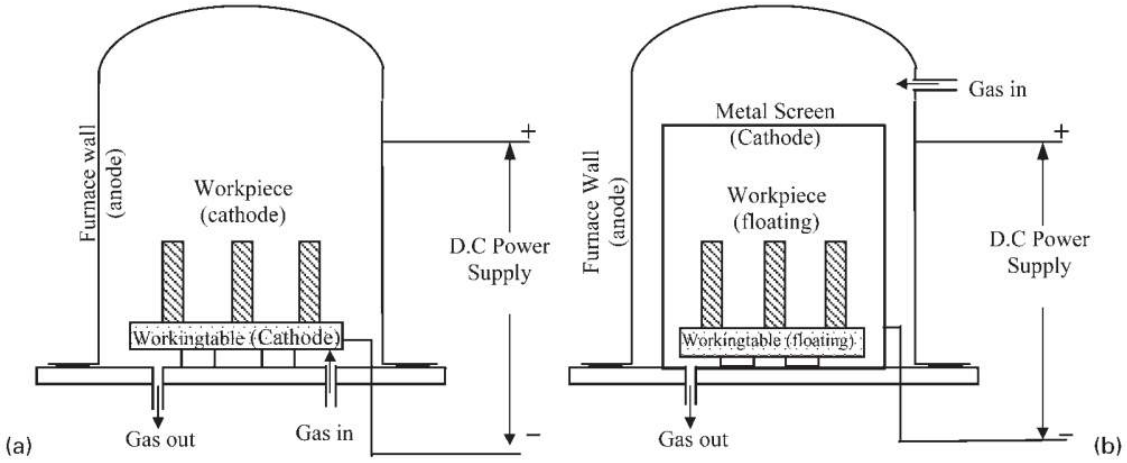

Figure 2.25: Schematic diagrams of: DCPN technique (a), ASPN technique (b). Source: [117].

2.6.3 Duplex and composite coatings

Gears used in high-performance applications, such as WTGs, are required to operate under challenging conditions, which can hardly be reached solely by carburising or nitriding alone [118]. Several studies [118–120] concluded that the duplex treatment can enhance the technical properties of components.

Duplex surface engineering is characterised by the consecutive application of

two or more surface treatments, in order to generate a composite surface with mixed properties that is impossible to be obtained by any surface treatment alone. Duplex surface engineering can be subdivided into two groups (type I and type II), according to the interactions and resulting properties of the composite layer. Processes that complement one another, and in which the resultant properties arise from both processes, fall into the type I category. Processes that enhance another, fulfilling the role of a pre- or post-treatment, fall into the type II category. The final properties of type II are usually a function of only one process [118].

Duplex surface systems are not merely the combination of surface treatments processes that separately have the desired properties. This is due to the fact that the final result of a duplex system will be dependent of the synergy of the two separate properties, instead of just the sum of the effect delivered by separate treatment processes. Incorrect combinations can lead to even worse properties than the component would experience with only one or even no surface treatment at all [118].

Finite element analysis demonstrated that when the plastic shear strain at the interaction between the coatings surpasses a critical value, an interface crack can be initiated in between layers [121]. Since the shear stress and strain along boundaries are expressively dependent on the friction content, coatings with a small friction coefficient used as the outer layer in a duplex system will reduce the interfacial shear stress and also increase wear resistance, therefore reducing the tendency of failure of upper coatings. In this matter, diamond-like carbon (DLC or a-C:H) coatings are efficient since they exhibit low friction against most types of contact surfaces [118]. However, they also tend to be brittle and are not suitable for high load applications [122, 123]. DLC coatings are distinguished by their high residual stress levels and low adhesion when coated on most materials. Dong and Bell [120] overcame the adhesion problem by applying a coating in-between the DLC and the substrate.

Carbon-based coatings are frequently strengthened with metal carbides precipitates (MC/a-C:H), forming nanocomposites that can typically be placed below the

tempering temperatures of steels [104]. These coatings are usually three times harder than steel and possess low friction coefficients. This is achieved by combining the wear resistance of the carbides with the elastic properties of the matrix. However, the lifespan of these coatings depends significantly on their processing circumstances and microstructure [26, 104]. A long-lasting WC/a-C:H layer along with a super finished surface may greatly reduce the formation of micropitting in bearings [26].

Evans et al. [124] conducted wear tests with different surface treatments in order to assess their impact on friction and wear of WTG bearings. Only the surface with a WC/a-C:H coating endured the toughest friction and wear conditions when compared to isotropically finished surfaces coated with black oxide.

In order to increase the wear protection, a hard coating that can also act as a solid lubricant, such as graphite or molybdenum disulphide (MoS_2), is a great advantage. MoS_2 coatings can be improved with the addition of Cr or Ti [125]. MoS_2/Ti coatings are even harder and less sensitive to water vapour than MoS_2. Martins et al. [122] showed they significantly increase the scuffing load capacity of gears while reducing their coefficient of friction. Moreover, the coating also improved the efficiency of the tested gearbox by 0.5%.

2.7 MECHANICS OF DEFORMATION

In continuum mechanics, deformation is a mapping from an original configuration to a new (final) configuration. A configuration is a set that contains the positions of all particles in a body. When a material deforms under a small stress, the deformation will probably be elastic. Elastic deformation is reversible, meaning that whenever a body deforms elastically under a load, it will return to its previous configuration when the load is removed. A larger stress, however, may cause plastic deformation. Plastic deformation is not reversible, and thus the body will not return to its previous shape once the stress is removed [126].

The amount of deformation a body undergoes is named strain. Strain is de-

scribed in terms of relative displacement in a body, excluding rigid-body motions [126]. Stress is a measure of force intensity, which can act either within a body or at the surface of a body subjected to loads. A body is then considered free of stress if the interatomic forces are the only forces acting on it. Stresses are, therefore, the result of the forces applied by an external agent [127].

The concepts of stress and strain, along with elasticity and plasticity will be explored in the next subsections.

2.7.1 Stress and strain

Stress can be defined as the intensity of force at a point, and is given by the ratio $\Delta F/\Delta A$, as the limit of ΔA tends to zero:

$$\sigma_{ij} = \lim_{\Delta A_i \to 0} \frac{\Delta F_j}{\Delta A_i} \tag{2.8}$$

Where F is a force and A is an area. To define a stress, two subscripts are necessary. The first one, i, refers to the normal of the plane where the force is acting, whereas j denotes the direction of the force. Normal stresses, compressive or tensile, are denoted by repeated indexes. For example, σ_{yy} indicates a force in the y-direction is acting on a plane normal to y. Shear stresses, on the contrary, are defined by two different indexes. A shear force in the z-direction acting on a plane perpendicular to x would be expressed as σ_{xz} [126]. In order to fully describe a stress state, nine stress components are necessary, which makes it a second rank tensor. Figure 2.26 shows the nine components of stress.

In tensor notation, σ_{ij} can be expressed as:

$$\sigma_{ij} = \begin{bmatrix} \sigma_{xx} & \sigma_{xy} & \sigma_{xz} \\ \sigma_{yx} & \sigma_{yy} & \sigma_{yz} \\ \sigma_{zx} & \sigma_{zy} & \sigma_{zz} \end{bmatrix} \tag{2.9}$$

where i and j are iterated over x, y, and z. Since the stress tensor is symmetric [128], it

can be rewritten to:

$$\sigma_{ij} = \begin{bmatrix} \sigma_{xx} & \sigma_{xy} & \sigma_{xz} \\ \sigma_{xy} & \sigma_{yy} & \sigma_{yz} \\ \sigma_{xz} & \sigma_{yz} & \sigma_{zz} \end{bmatrix} \tag{2.10}$$

which means that actually only six components are needed to describe the stress state.

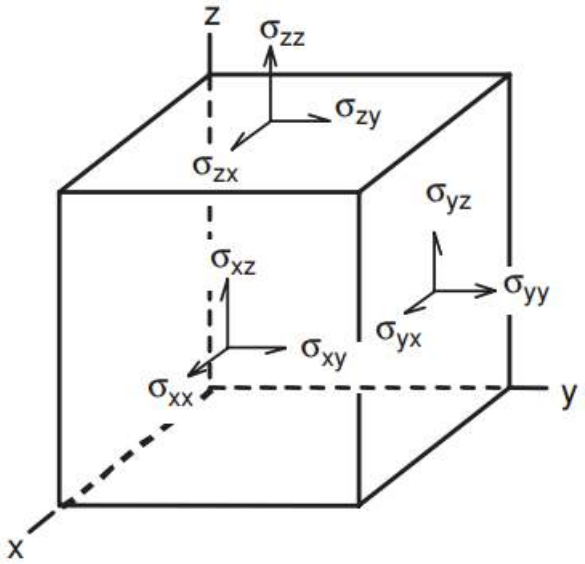

Figure 2.26: All the nine components of stress acting on a component. Source: [126].

The Voigt notation is used to simplify the writing of second-order tensors, by transforming them into vectors. It also transforms fourth-order tensors into matrices. The stress state can be written in Voigt notation as:

$$\boldsymbol{\sigma} = \begin{bmatrix} \sigma_{xx} \\ \sigma_{yy} \\ \sigma_{zz} \\ \sigma_{xy} \\ \sigma_{xz} \\ \sigma_{yz} \end{bmatrix} = \begin{bmatrix} \sigma_{11} \\ \sigma_{22} \\ \sigma_{33} \\ \sigma_{12} \\ \sigma_{13} \\ \sigma_{23} \end{bmatrix} \tag{2.11}$$

Where x = 1, y = 2 and z = 3. It is always possible to find a set of axes (x', y', z') where all the shear stress components will be zero. When this is the case, the normal stresses σ_{xx}, σ_{yy}, and σ_{zz} are called principal stresses, and x', y' and z' are the principal axes. The magnitudes of the principal stresses σ_{pr} are the roots of the following cubic equation [126]:

$$\sigma_{pr}^3 - I_1\sigma_{pr}^2 - I_2\sigma_{pr} - I_3 = 0 \tag{2.12}$$

where I_1, I_2, and I_3 are not dependent on the axes' orientation and so called stress invariants. They are given by:

$$I_1 = \sigma_{11} + \sigma_{22} + \sigma_{33} = \sigma_{ii} = tr(\boldsymbol{\sigma}) \tag{2.13}$$

$$I_2 = \sigma_{11}\sigma_{22} + \sigma_{22}\sigma_{33} + \sigma_{11}\sigma_{33} - \sigma_{12}^2 - \sigma_{23}^2 - \sigma_{13}^2 = \frac{1}{2}\,\sigma_{ii}\sigma_{jj} - \sigma_{ij}\sigma_{ji} \tag{2.14}$$

$$I_3 = det(\sigma_{ij}) = \sigma_{11}\sigma_{22}\sigma_{33} + 2\,\sigma_{12}\sigma_{23}\sigma_{13} - \sigma_{12}^2\sigma_{33} - \sigma_{23}^2\sigma_{11} - \sigma_{13}^2\sigma_{22} \tag{2.15}$$

Where tr is the trace, $det(\sigma_{ij})$ is the determinant of the stress tensor, and repeated indexes such as σ_{ii} represent summation, as per the Einstein summation convention.

It is often convenient to decompose the stress into a sum of two tensors. One of them is the mean hydrostatic stress tensor (also called volumetric stress tensor or mean normal stress tensor), which changes the volume of the stressed body and is given by $\sigma_m\delta_{ij}$; the other being the deviatoric component (S_{ij}), named stress deviator tensor, which distorts the body. Therefore:

$$\sigma_{ij} = S_{ij} + \sigma_m\delta_{ij} \tag{2.16}$$

Where δ_{ij} is the Kronecker delta operator, which is equal to 0 if $i \neq j$ and equal to 1 if

$i = j$, while σ_m is the mean stress given by:

$$\sigma_m = \frac{1}{3}\,\sigma_{ii} = \frac{\sigma_{11} + \sigma_{22} + \sigma_{33}}{3} = \frac{1}{3}\,I_1 \tag{2.17}$$

And the deviatoric stress tensor can be calculated by subtracting the mean stress from the stress tensor:

$$S_{ij} = \sigma_{ij} - \sigma_m \delta_{ij} \tag{2.18}$$

$$\begin{bmatrix} S_{xx} & S_{xy} & S_{xz} \\ S_{xy} & S_{yy} & S_{yz} \\ S_{xz} & S_{yz} & S_{zz} \end{bmatrix} = \begin{bmatrix} \sigma_{xx} - \sigma_m & \sigma_{xy} & \sigma_{xz} \\ \sigma_{xy} & \sigma_{yy} - \sigma_m & \sigma_{yz} \\ \sigma_{xz} & \sigma_{yz} & \sigma_{zz} - \sigma_m \end{bmatrix} \tag{2.19}$$

As bodies deform, they can experience stretch, rigid body rotation and translation. The stretch provides the shape change, whereas the rigid body rotation does not contribute to shape changes nor the internal stress. Translation does not change the stress state [129].

In order to understand deformation, let us have a look at a piece of material in the undeformed configuration, as shown in Figure 2.27. A load is applied to the material in the state A so that it deforms into the state B. Consider now an infinitesimal line, $\overline{PQ}$, or vector, $d\boldsymbol{X}$, which is in the material original configuration. The position of point P is given by the vector $\boldsymbol{X}$, relative to the origin of the coordinate system [129].

As the body deforms from state A to state B, the line $\overline{PQ}$ is also deformed and is now given by $\overline{P'Q'}$, or vector, $d\boldsymbol{x}$. The position of the point P' relative to the origin coordinate system is now given by the vector $\boldsymbol{x}$, and since the point P has been translated by the vector $\boldsymbol{u}$ to point P', the vector $\boldsymbol{x}$ can be calculated by [129]:

$$\boldsymbol{x} = \boldsymbol{X} + \boldsymbol{u} \tag{2.20}$$

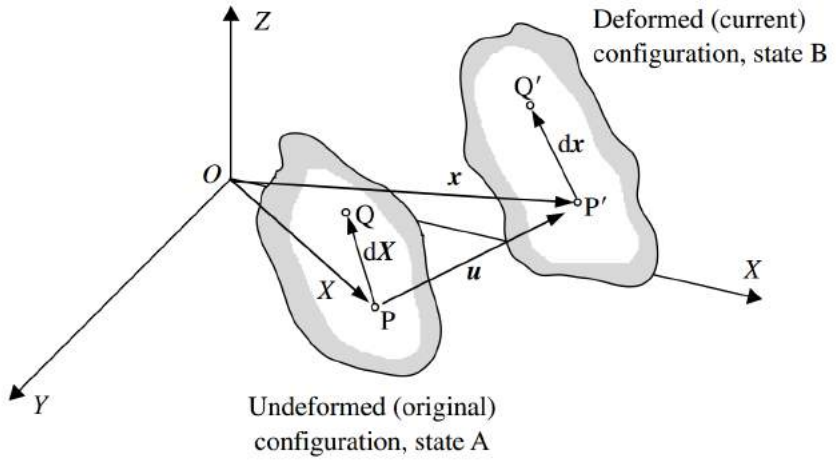

Figure 2.27: Body in undeformed state A undergoing deformation to the deformed state B. Source: [129].

The infinitesimal vector $d\boldsymbol{X}$ is transformed to its deformed state, $d\boldsymbol{x}$, by the deformation gradient, $\boldsymbol{F}$, where [129]:

$$d\boldsymbol{x} = \boldsymbol{F}\ d\boldsymbol{X} \tag{2.21}$$

Which can also be written as:

$$\begin{bmatrix} dx \\ dy \\ dz \end{bmatrix} = \begin{bmatrix} F_{xx} & F_{xy} & Fxz \\ F_{yx} & F_{yy} & Fyz \\ F_{zx} & F_{zy} & Fzz \end{bmatrix} \begin{bmatrix} dX \\ dY \\ dZ \end{bmatrix} = \begin{bmatrix} \frac{\partial x}{\partial X} & \frac{\partial x}{\partial Y} & \frac{\partial x}{\partial Z} \\ \frac{\partial y}{\partial X} & \frac{\partial y}{\partial Y} & \frac{\partial y}{\partial Z} \\ \frac{\partial z}{\partial X} & \frac{\partial z}{\partial Y} & \frac{\partial z}{\partial Z} \end{bmatrix} \begin{bmatrix} dX \\ dY \\ dZ \end{bmatrix} \tag{2.22}$$

or:

$$\boldsymbol{F} = \frac{\partial \boldsymbol{x}}{\partial \boldsymbol{X}} \tag{2.23}$$

The deformation gradient describes the deformation process fully, meaning that it includes stretch as well as rigid body rotation. For problem-solving, it is important to separate the stretch from the rigid body rotation. A strain-dependent measure on rigid body rotation would not be ideal since it would give a different measure of strain depending on the orientation of the body. If only the length is considered, ds, of the line $d\boldsymbol{x}$ in the

deformed configuration, one can write [129]:

$$ds^2 = d\boldsymbol{x} \cdot d\boldsymbol{x} = (\boldsymbol{F}\ d\boldsymbol{X}) \cdot (\boldsymbol{F}\ d\boldsymbol{X}) = d\boldsymbol{X}^T\ \boldsymbol{F}^T\ \boldsymbol{F}\ d\boldsymbol{X} = d\boldsymbol{X}^T\ \boldsymbol{G}\ d\boldsymbol{X} \tag{2.24}$$

so that:

$$\boldsymbol{G} = \boldsymbol{F}^T\boldsymbol{F} \tag{2.25}$$

Where $\boldsymbol{G}$ is the left Cauchy-Green tensor. If the length dS of the $d\boldsymbol{X}$ line is taken into account, then:

$$dS^2 = d\boldsymbol{X}^T d\boldsymbol{X} \tag{2.26}$$

From equation 2.23:

$$d\boldsymbol{X} = \boldsymbol{F}^{-1}\ d\boldsymbol{x} \tag{2.27}$$

Substituting equations 2.21 and 2.27 into equation 2.26:

$$dS^2 = (\boldsymbol{F}^{-1}\ d\boldsymbol{x})^T\ \boldsymbol{F}^{-1}\ d\boldsymbol{x} = d\boldsymbol{x}\ (\boldsymbol{F}^{-1})^T\ \boldsymbol{F}^{-1}\ d\boldsymbol{x} = d\boldsymbol{x}\ \boldsymbol{B}^{-1}\ d\boldsymbol{x} \tag{2.28}$$

where

$$\boldsymbol{B}^{-1} = (\boldsymbol{F}^{-1})^T\ \boldsymbol{F}^{-1} \tag{2.29}$$

and is called the right Cauchy-Green tensor. A measure of stretch is given by the difference in length of $\overline{PQ}$ and $\overline{P'Q'}$, which can be written as:

$$ds^2 - dS^2 = d\boldsymbol{x} \cdot d\boldsymbol{x} - d\boldsymbol{x} \cdot \boldsymbol{B}^{-1}\ d\boldsymbol{x} = d\boldsymbol{x} \cdot (\boldsymbol{I} - \boldsymbol{B}^{-1})d\boldsymbol{x} \tag{2.30}$$

In which $\boldsymbol{I}$ is the identity tensor. If ds and dS are the same length, there is no stretch and therefore $\boldsymbol{B}$ must be equal to $\boldsymbol{I}$, meaning that in such case the deformation gradient consists only of rigid body rotation. The right Cauchy-Green tensor could be itself a measure of strain, since it does not depend on rigid body rotation but depends on the stretch. However, even when the stretch is zero, it contains non-zero components (since it would be equal to the identity tensor). A way of overcoming this is by using a strain measure called Almansi strain, given by [129]:

$$\boldsymbol{e} = \frac{1}{2}(\boldsymbol{I} - \boldsymbol{B}^{-1}) \tag{2.31}$$

Which is zero when the stretch is zero. Another measure of strain is the true strain, or logarithmic strain, given by

$$\boldsymbol{\varepsilon} = \frac{1}{2}\ln \boldsymbol{B}^{-1} \tag{2.32}$$

Which is also zero when the stretch is zero. A different approach to calculating the change in length of the $\overline{PQ}$ line was to work with the original configuration, for example:

$$ds^2 - dS^2 = d\boldsymbol{x}d\boldsymbol{x} - d\boldsymbol{X}d\boldsymbol{X} = (\boldsymbol{F}d\boldsymbol{X})(\boldsymbol{F}d\boldsymbol{X}) - d\boldsymbol{X}d\boldsymbol{X} \tag{2.33}$$

$$= d\boldsymbol{X}\boldsymbol{F}^T\boldsymbol{F}d\boldsymbol{X} - d\boldsymbol{X}d\boldsymbol{X} = d\boldsymbol{X}(\boldsymbol{F}^T\boldsymbol{F} - \boldsymbol{I})d\boldsymbol{X} \tag{2.34}$$

$$= d\boldsymbol{X}(\boldsymbol{G} - \boldsymbol{I})d\boldsymbol{X} = d\boldsymbol{X}(2\boldsymbol{E})d\boldsymbol{X} \tag{2.35}$$

where

$$\boldsymbol{E} = \frac{1}{2}(\boldsymbol{G} - \boldsymbol{I}) = \frac{1}{2}(\boldsymbol{F}^T\boldsymbol{F} - \boldsymbol{I}) \tag{2.36}$$

$\boldsymbol{E}$ is the large strain, also called the Green-Lagrange strain tensor [129]. To exemplify the meaning of these different strain measures, consider the case of uniaxial stress of a circular rod in the y-direction. This is shown in Figure 2.28.

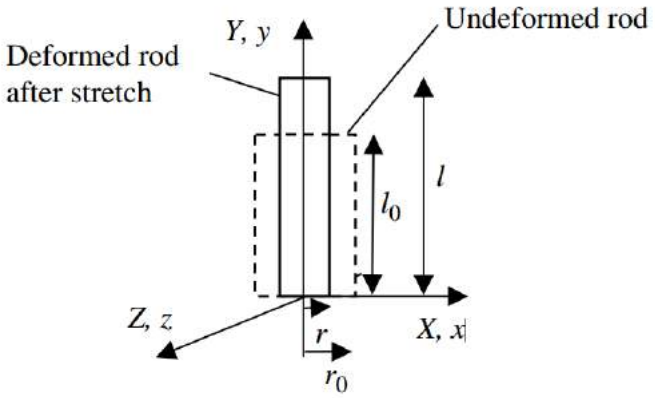

Figure 2.28: Uniaxial deformation of circular rod in the y-direction. Source: [129].

The stretch ratios λ for this case are given by:

$$\lambda_x = \frac{r}{r_0} = \lambda_z \tag{2.37}$$

$$\lambda_y = \frac{l}{l_0} \tag{2.38}$$

If the case of large strains is considered, the elastic strains can be ignored. The incompressibility condition can then be written in terms of the stretches as:

$$\lambda_x \lambda_y \lambda_z = 1 \tag{2.39}$$

Since λ_x is equal to λ_z, then:

$$\lambda_x = \lambda_z = \frac{1}{\sqrt{\lambda_y}} = \left(\frac{l}{l_0}\right)^{-1/2} \tag{2.40}$$

Considering the stretch along the z-axis, any point Z in the original state then becomes the point $z = \lambda_z Z$ in the deformed configuration. Thus:

$$\frac{\partial x}{\partial X} = \lambda_x \tag{2.41}$$

$$\frac{\partial y}{\partial Y} = \lambda_t \tag{2.42}$$

$$\frac{\partial z}{\partial Z} = \lambda_z \tag{2.43}$$

and

$$\frac{\partial x}{\partial Y} = \frac{\partial x}{\partial Z} = \frac{\partial y}{\partial X} = \frac{\partial y}{\partial Z} = \frac{\partial z}{\partial X} = \frac{\partial z}{\partial Y} = 0 \tag{2.44}$$

It is now possible to write the deformation gradient, using equation 2.23:

$$\boldsymbol{F} = \frac{\partial \boldsymbol{x}}{\partial \boldsymbol{X}} = \begin{bmatrix} \frac{\partial x}{\partial X} & \frac{\partial x}{\partial Y} & \frac{\partial x}{\partial Z} \\ \frac{\partial y}{\partial X} & \frac{\partial y}{\partial Y} & \frac{\partial y}{\partial Z} \\ \frac{\partial z}{\partial X} & \frac{\partial z}{\partial Y} & \frac{\partial z}{\partial Z} \end{bmatrix} = \begin{bmatrix} \lambda_x & 0 & 0 \\ 0 & \lambda_y & 0 \\ 0 & 0 & \lambda_z \end{bmatrix} = \begin{bmatrix} \left(\frac{l}{l_0}\right)^{-1/2} & 0 & 0 \\ 0 & \left(\frac{l}{l_0}\right) & 0 \\ 0 & 0 & \left(\frac{l}{l_0}\right)^{-1/2} \end{bmatrix} \tag{2.45}$$

Since $\boldsymbol{F}$ is a symmetric matrix, its transpose is equal to itself, as in $\boldsymbol{F}^T = \boldsymbol{F}$. The inverse of $\boldsymbol{F}$ is:

$$\boldsymbol{F}^{-1} = \begin{bmatrix} \left(\frac{l}{l_0}\right)^{1/2} & 0 & 0 \\ 0 & \left(\frac{l}{l_0}\right)^{-1} & 0 \\ 0 & 0 & \left(\frac{l}{l_0}\right)^{1/2} \end{bmatrix} \tag{2.46}$$

And one can now look at all the different measures of strain. The left Cauchy-Green tensor for this uniaxial case will be:

$$\boldsymbol{B}^{-1} = (\boldsymbol{F}^{-1})^T \boldsymbol{F}^{-1} = \boldsymbol{F}^{-1}\boldsymbol{F}^{-1} = \begin{bmatrix} \frac{l}{l_0} & 0 & 0 \\ 0 & \left(\frac{l}{l_0}\right)^{-2} & 0 \\ 0 & 0 & \frac{l}{l_0} \end{bmatrix} \tag{2.47}$$

And the true plastic strain will be given by:

$$\boldsymbol{\varepsilon} = -\frac{1}{2}\ln \boldsymbol{B}^{-1} = \begin{bmatrix} -\frac{1}{2}\ln\frac{l}{l_0} & 0 & 0 \\ 0 & ln\frac{l}{l_0} & 0 \\ 0 & 0 & -\frac{1}{2}\ln\frac{l}{l_0} \end{bmatrix} \tag{2.48}$$

As expected for uniaxial plasticity conditions, we can see that $\varepsilon_{xx} = \varepsilon_{zz} = -\frac{1}{2}\varepsilon_{yy}$ [129]. This is an example in which stretch takes place exclusively since no rigid body rotation has taken place.

2.7.2 Elasticity

Constitutive relationships relate the stress to the strain while also defining some material properties which are needed in order to capture the behaviour of the material accurately [128]. The elastic behaviour is a material property which is characterised by the complete recovery to an original shape upon the removal of the applied forces acting on it. The elastic behaviour may be linear or non-linear, as shown in Figure 2.29 [127].

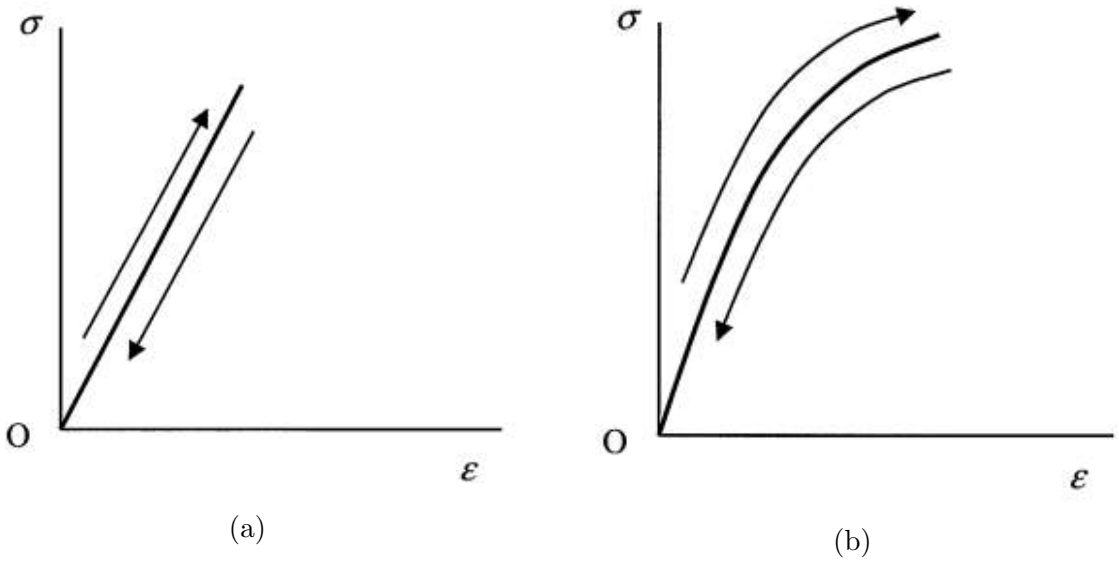

Figure 2.29: Linear elastic behaviour (a), and non-linear elastic behaviour (b). The arrows represent loading and unloading. Source: [127].

The linear elastic behaviour occurs if the deformations in a material increase proportionally upon the increase of the applied load. The linear elastic behaviour was first noticed

by Robert Hooke and is named after him as "Hooke's Law". Thomas Young was then the first to divide the applied load by the area and the deflection of the tested specimen, thereby relating normal stress to normal strain in the same direction by the proportionality constant E, named after him [128].

We can write the constitutive equation for linear behaviour as:

$$\sigma_{ij} = C_{ijkl}\ \varepsilon_{kl} \quad \text{or} \quad \boldsymbol{\sigma} = \boldsymbol{C}\ \boldsymbol{\varepsilon} \tag{2.49}$$

Where the tensor of elastic coefficients $\boldsymbol{C}$ is a fourth-order tensor and has 81 components. However, due to symmetry of the stress and strain tensors, we can write:

$$C_{ijkl} = C_{jikl} = C_{ijlk} \tag{2.50}$$

Reducing the number of components from 81 to 36. The coefficients of $\boldsymbol{C}$ may depend on temperature. However, if these coefficients are constants, the material is said to be homogeneous. For convenience, we will now write the equation 2.49 in Voigt notation:

$$\begin{bmatrix} \sigma_1 \\ \sigma_2 \\ \sigma_3 \\ \sigma_4 \\ \sigma_5 \\ \sigma_6 \end{bmatrix} = \begin{bmatrix} C_{11} & C_{12} & C_{13} & C_{14} & C_{15} & C_{16} \\ C_{21} & C_{22} & C_{23} & C_{24} & C_{25} & C_{26} \\ C_{31} & C_{32} & C_{33} & C_{34} & C_{35} & C_{36} \\ C_{41} & C_{42} & C_{43} & C_{44} & C_{45} & C_{46} \\ C_{51} & C_{52} & C_{53} & C_{54} & C_{55} & C_{56} \\ C_{61} & C_{62} & C_{63} & C_{64} & C_{65} & C_{66} \end{bmatrix} \begin{bmatrix} \varepsilon_1 \\ \varepsilon_2 \\ \varepsilon_3 \\ \varepsilon_4 \\ \varepsilon_5 \\ \varepsilon_6 \end{bmatrix} \tag{2.51}$$

If a material can be described by the same $\boldsymbol{C}$ coefficients in every set of reference axes, such material is called isotropic. The constitutive equation for isotropic materials only possesses two constants. Isotropy requires the elastic tensor $\boldsymbol{C}$ to be isotropic. The components of an isotropic tensor do not change by any orthogonal transformation. For example, zero-order tensors and scalars are always isotropic, however, there is no isotropic vector (first-order tensor). The only isotropic second-order tensor is the identity tensor $\boldsymbol{I}$

(and any multiples of it). The fourth-order isotropic tensor can be written as [127]:

$$C_{ijkl} = c_1\delta_{ij}\delta_{kl} + c_2(\delta_{ik}\delta_{jl} + \delta_{il}\delta_{jk}) + c_3(\delta_{ik}\delta_{jl} - \delta_{il}\delta_{jk}) \tag{2.52}$$

Where c_1, c_2, and c_3 are constants. But for the given symmetry of the stress and strain tensors, c_3 must be equal to zero. The equation 2.49 can then be written as:

$$\sigma_{ij} = (c_1\delta_{ij}\delta_{kl} + c_2\delta_{ik}\delta_{jl} + c_2\delta_{il}\delta_{jk})\ \varepsilon_{kl} \tag{2.53}$$

And by the substitution property of δ_{ij}, we can reduce the expression to:

$$\sigma_{ij} = c_1\delta_{ij}\varepsilon_{kk} + 2\ c_2\varepsilon_{ij} \tag{2.54}$$

Which is Hooke's Law for isotropic linear behaviour. The constants c_1 and c_2 are known as the Lamè constants. These constants are given by the combination of two engineering constants: the Young's modulus, E, and the Poisson's ratio, ν.

The c_1 constant can be written as:

$$c_1 = \frac{\nu E}{(1+\nu)(1-2\nu)} \tag{2.55}$$

The c_2 constant, called modulus of rigidity, or shear modulus, is given by:

$$c_2 = \frac{E}{2\ (1+\nu)} \tag{2.56}$$

In the case of uniaxial tension, already shown in Figure 2.28, we can write:

$$\varepsilon_{yy} = \frac{\sigma_{yy}}{E} \tag{2.57}$$

$$\varepsilon_{xx} = \varepsilon_{zz} = -\nu\ \varepsilon_{yy} \tag{2.58}$$

The Poisson's ratio is, therefore, the ratio between the lateral contraction over the longi-

tudinal strain [127].

A material that possesses elastic symmetry in three mutually perpendicular planes is named an orthotropic material, and its $\boldsymbol{C}$ matrix has only 12 non-zero coefficients [127]:

$$C_{ij} = \begin{bmatrix} C_{11} & C_{12} & C_{13} & 0 & 0 & 0 \\ C_{21} & C_{22} & C_{23} & 0 & 0 & 0 \\ C_{31} & C_{32} & C_{33} & 0 & 0 & 0 \\ 0 & 0 & 0 & C_{44} & 0 & 0 \\ 0 & 0 & 0 & 0 & C_{55} & 0 \\ 0 & 0 & 0 & 0 & 0 & C_{66} \end{bmatrix} \tag{2.59}$$

Finally, the Hooke's law (equation 2.51) can be rewritten as:

$$\begin{bmatrix} \sigma_1 \\ \sigma_2 \\ \sigma_3 \\ \sigma_4 \\ \sigma_5 \\ \sigma_6 \end{bmatrix} = \begin{bmatrix} c_1 + 2c_2 & c_1 & c_1 & 0 & 0 & 0 \\ c_1 & c_1 + 2c_2 & c_1 & 0 & 0 & 0 \\ c_1 & c_1 & c_1 + 2c_2 & 0 & 0 & 0 \\ 0 & 0 & 0 & c_2 & 0 & 0 \\ 0 & 0 & 0 & 0 & c_2 & 0 \\ 0 & 0 & 0 & 0 & 0 & c_2 \end{bmatrix} \begin{bmatrix} \varepsilon_1 \\ \varepsilon_2 \\ \varepsilon_3 \\ \varepsilon_4 \\ \varepsilon_5 \\ \varepsilon_6 \end{bmatrix} \tag{2.60}$$

2.7.3 Plasticity

Plasticity, in metals, is described as the time-independent permanent deformation beyond the elastic limit. Ideally, there is a stress threshold separating the elastic limit from the inelastic, and that is called the yield stress (σ_0) [130], show in Figure 2.30.

If a material is loaded from point O to point C, unloaded, and then reloaded, permanent deformation will only occur at a stress level that is past σ_C. This behaviour is known as work hardening or strain hardening. It means that the stress for a material to undergo plastic flow will be higher if it has already undergone a certain amount of plastic deformation.

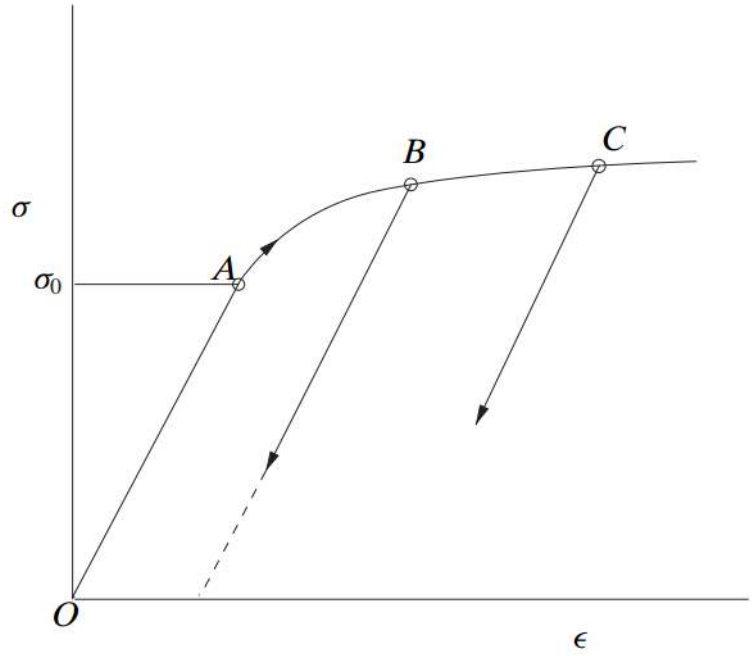

Figure 2.30: Example of a stress-strain curve of a metal. Source: [130].

Another characteristic of metal deformation is that it is dependent on the loading path. Beyond the yielding point of the material, a loading reversal will cause the compressive yield stress to be different from the tensile stress and vice versa. Usually, the yield stress in the reverse direction is lower than the yield stress in the pre-strain direction. This effect is known as the Bauschinger effect [126, 130].

An elastic perfectly plastic material is shown in Figure 2.31. The material follows the Hooke's Law up to σ_0, and flows if the applied stress is equal or higher than σ_0. The meaning of "perfectly plastic" refers to the absence of work hardening.

Plasticity theory deals with the yielding of materials under complex states of stress. A yield criterion mathematically describes the yielding of materials under complex stress conditions. For an isotropic material, the yield criterion can be expressed in terms of principal stresses [126]:

$$f(\sigma_1, \sigma_2, \sigma_3) = \sigma_0 \tag{2.61}$$

where σ_0 is the tensile yield strength in a uniaxial test.

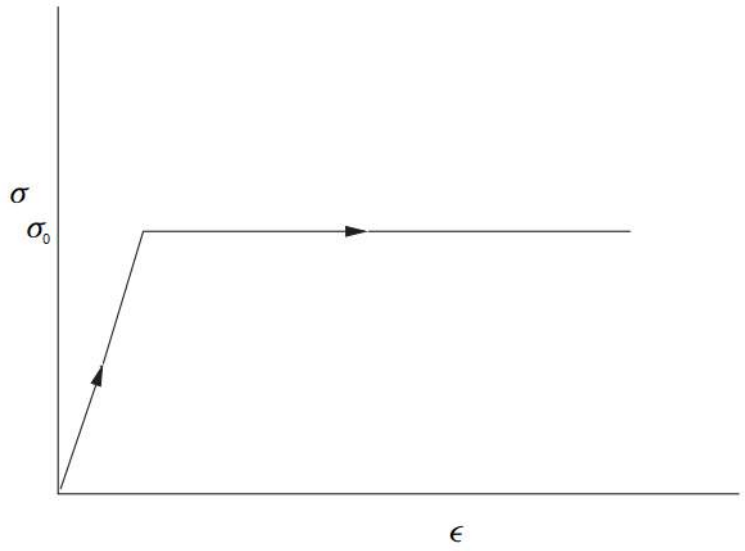

Figure 2.31: Stress-strain curve of an elastic perfectly plastic material. Source: [130].

One of the first yield criteria was proposed by Tresca [126], and its condition for yielding is that the largest shear stresses must surpass a critical value. For this reason, it is also called "the maximum shear stress criterion". The largest shear stress, given by τ_{max} is:

$$\tau_{max} = \frac{\sigma_{max} - \sigma_{min}}{2} \tag{2.62}$$

In terms of principal stresses, the Tresca criterion is given by:

$$\frac{1}{2}\max(|\sigma_1 - \sigma_2|,\ |\sigma_2 - \sigma_3|,\ |\sigma_3 - \sigma_1|) = \frac{1}{2}\sigma_0 = \tau \tag{2.63}$$

Where τ is the yield strength in shear. We can quickly reach the conclusion that this yield criterion does not predict failure under hydrostatic stress, since in such conditions:

$$\sigma_1 = \sigma_2 = \sigma_3 = P \tag{2.64}$$

Where P is the pressure. Such condition would lead to a zero value on equation 2.63, resulting in no plastic flow.

Another yield criterion, and the most commonly used yield criterion, particularly in computational analysis, is the Von Mises criterion, which is also called equivalent

stress or maximum distortion energy criterion. It was first developed by Von Mises, without a physical interpretation. However, it is currently accepted that it expresses the critical value of the shear component of the deformation energy of a body. According to this criterion, a body will yield once the shear deformation of a complex state of stress is equivalent to that of a body under uniaxial stress. Additionally, it is also called the J_2 theory, because the equivalent stress is given by the second invariant of the stress deviator tensor [131].

The equivalent stress, $\overline{\sigma}$ is given by:

$$\overline{\sigma} = \sqrt{\frac{(\sigma_1 - \sigma_2)^2 + (\sigma_2 - \sigma_3)^2 + (\sigma_3 - \sigma_1)^2}{3}} \tag{2.65}$$

Which can also be written in a reduced form, using the stress deviator tensor S_{ij} given by equation 2.18:

$$\overline{\sigma} = \sqrt{\frac{3}{2} S_{ij} \cdot S_{ij}} \tag{2.66}$$

In the Von Mises criterion, the material will yield if the equivalent stress $\overline{\sigma}$ is higher than the yield stress in uniaxial conditions, σ_0. Similarly to the Tresca criterion, the Von Mises criterion does not predict yielding for hydrostatic stress conditions.

Let us now compare the two yield criteria, in a state of plane stress, where $\sigma_3 = 0$, as shown in Figure 2.32.

According to the Tresca criterion, the material yields when:

$$\tau_{max} = \frac{\sigma_0}{2} \tag{2.67}$$

In the first quadrant, we have $\sigma_1 > 0$ and $\sigma_2 > 0$. Two situations are possible: when σ_1 is greater than σ_2, we have $\sigma_1 = \sigma_0$. Conversely, when σ_2 is greater than σ_1, we have $\sigma_2 = \sigma_0$.

In the second quadrant, $\sigma_1 < 0$ and $\sigma_2 > 0$. We then have:

$$\sigma_1 - \sigma_2 = \sigma_0 \tag{2.68}$$

The equation 2.68 is the equation of a line, intersecting the x-axis at $-\sigma_0$ and the y-axis at σ_0. The third and fourth quadrants can be worked out in a similar manner to the first and second quadrants.

For the Von Mises criterion, in plane stress condition, we can write:

$$\sigma_1^2 + 2\sigma_1\sigma_2 + \sigma_2^2 = \sigma_0^2 \tag{2.69}$$

The equation 2.69 is the equation of an ellipse. We can then plot both the Tresca and the Von Mises criterion on the plane stress plane, as shown in Figure 2.32.

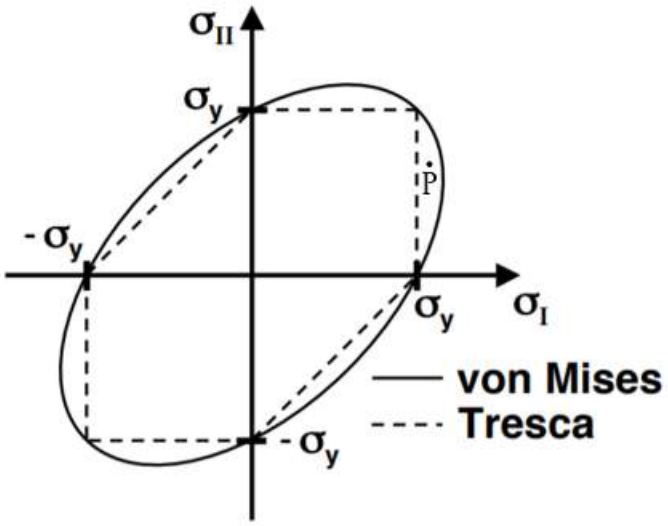

Figure 2.32: Comparison between Tresca and Von Mises yielding criteria in a plane state of stress. Souce: [132].

We can see that both criteria are fairly close, however, the Tresca criterion is more conservative. For point P, for example, the Tresca criterion would predict plastic flow, whereas Von Mises would not. Another important conclusion that can be drawn is that for the second and fourth quadrants, where the material is submitted to a mix of tensile and compressive stresses, plastic flow may occur even if both stresses are lesser than σ_0.

When a material deforms plastically and hardens, the stress required for it to flow increases. This means that the yield surface should expand. When this expansion is uniform in all directions of the stress space, the hardening effect is called isotropic. The isotropic hardening can be applied to anisotropic materials and does not imply that the material itself is isotropic [126, 129].

The isotropic hardening, however, cannot explain some effects such as the Bauschinger effect, where a material pre-strained in one direction will usually have a lower yield stress in the reverse direction. This can be explained by kinematic hardening, where the yield surface, instead of expanding, is translated along the stress space, without changing shape or size. The kinematic model is better used for describing small strains after a change in the loading path, whereas the isotropic model is useful for describing large strains. Figure 2.33 shows a comparison between both models [126].

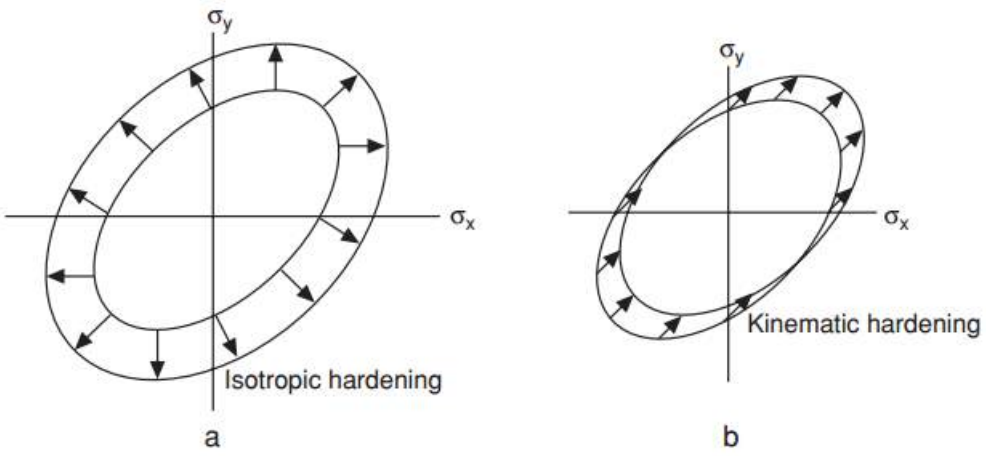

Figure 2.33: Isotropic hardening expanding the yield surface (a), and kinematic hardening translating the yield surface (b). Source: [126]

2.8 CONTINUUM DAMAGE MECHANICS

Modern engineering materials subjected to external loads often suffer irreversible changes of their microscopic internal structures, besides macroscopic deformation. These microstructural changes impair the mechanical properties of these materials and thus are named damage [133, 134].

At the mesoscale level, damage is due to the initiation and growth of microcracks

or microvoids. These defects can grow and coalesce, evolving to macrocracks that eventually lead to failure, while also damaging material properties such as fracture toughness, strength, and remaining lifetime. Continuum damage mechanics (CDM) is the branch of continuum mechanics that investigates the mechanical behaviour of damaged materials, as well as the initiation and propagation of damage itself [134, 135].

The notion of damage mechanics was first proposed by Kachanov [136]. He introduced a scalar damage variable Ψ such that $\Psi = 1$ for the undamaged material and $\Psi = 0$ for the fully damaged material. An interpretation of this damage variable is shown in equation 2.70, which is basically the ratio between the area of microvoids or microcracks (A_D) of a given section, and the total area of the section (A):

$$\Psi = \frac{A_D}{A} \quad where\ 0 < \Psi < 1 \tag{2.70}$$

Rabotnov [137] then introduced the concept of effective stress. If we consider the case of the uniaxial stress of a circular rod, we can write the stress as:

$$\sigma = \frac{F}{A} \tag{2.71}$$

Where F is the force applied to the rod, and A is the area of the section of the rod which is perpendicular to F. However, if the defects present in the material, such as microvoids or microcracks are open, we can represent the area of these defects by A_D. The effective stress σ_{eff} can then be written, and is basically related to the surface that actually bears the applied load, as shown in equation 2.73:

$$\sigma_{eff} = \frac{F}{A - A_D} \tag{2.72}$$

We can then combine this approach with Kachanov's definition of damage (equation 2.70) and get to:

$$\sigma_{eff} = \frac{\sigma}{1 - \Psi} \tag{2.73}$$

The Kachanov-Rabotnov approach considers that due to the cavities present, the effective stress (σ_{eff}) acting locally is actually higher than the stress being applied (σ), as shown in equation 2.73. The elastic modulus of a damaged material is lowered as damage progresses and can be defined as [138]:

$$E_{eff} = E(1 - \Psi) \tag{2.74}$$

2.8.1 Micromechanical modelling of ductile damage

The first micromechanical models to describe ductile damage were developed by McClintock [139] and Rice and Tracey [140]. They outlined the evolution of pre-existing voids of different shapes contained in a rigid plastic material. Both studies correlated the effect of the mean stress and the plastic strain on the void size evolution. For spherical voids, the growth rate of a void with a radius R can be given by [140]:

$$\frac{dR}{R} = g \exp\left(\frac{3}{2}\frac{\sigma_m}{\sigma_0}\right)\overline{\varepsilon}^p \tag{2.75}$$

Where g is a constant, $\overline{\varepsilon}^p$ is the equivalent strain, σ_0 is the yield stress and σ_m is the mean stress. A simple failure criterion can then be defined, which states that failure occurs when the normalised void radius reaches a critical value [141]:

$$\left(\frac{R}{R_0}\right) = \left(\frac{R}{R_0}\right)_c \tag{2.76}$$

Where R_0 is the initial void radius, R can be obtained by integrating equation 2.75, and the ratio $(R/R_0)_c$ is a material parameter representing the maximum possible value before failure.

These models, however, do not take into the account the behaviour of the material due to the growth of voids. The first model to take into the account the softening generated by the interactions between the voids and the matrix was a model developed by Gurson [142]. Gurson analysed a finite sphere, rigid and perfectly plastic with a spherical

void contained in it. He then introduced his damage variable, f, which is the ratio between the volume of the void and the volume of the sphere itself. He then derived a flow rule, Φ, incorporating the damage variable f:

$$\Phi = \frac{\overline{\sigma}^2}{\sigma_0^2} + 2f \cosh\left(\frac{1}{2}\frac{\sigma_{kk}}{\sigma_0}\right) - 1 - f^2 \tag{2.77}$$

Where $\overline{\sigma}$ is the effective stress, σ_0 is the yield stress, and σ_{kk} is the trace of the stress tensor. This predicts that the material will yield under hydrostatic pressure, as long as the material is voided, i.e, $f > 0$. If a material consists of voids completely, what would be an ideal condition for failure, $f = 1$. The rate of growth of voids is given by $\dot{f}_{growth}$:

$$\dot{f}_{growth} = (1 - f)\ \dot{\varepsilon}^p_{kk} \tag{2.78}$$

Where $\dot{\varepsilon}^p_{kk}$ is the trace of the plastic strain rate tensor. Similarly to the models of McClintock and Rice and Tracy, the Gurson model does not account for the nucleation of voids, but only for the growth of pre-existing voids.

The modelling of void nucleation is much more challenging than modelling void growth. This is because of the need for specifying material properties for the inclusions and sometimes even for the interfaces between the matrix and the inclusion. Additionally, since the particle sizes can greatly vary, both the dislocation scale and the continuum mechanics scale must be considered, for small and large particles, respectively. The models must also account for particle cracking and particle decohesion [143].

Tvergaad and Needleman [144] then modified the Gurson model in order to account for fracture and coalescence. The resulting model is known as the Gurson-Tvergaad-Needleman model, or GTN model. The new proposed flow rule can be written as:

$$\Phi = \frac{\overline{\sigma}^2}{\sigma_0^2} + 2q_1 f_* \cosh\left(\frac{q_2}{2}\frac{\sigma_{kk}}{\sigma_0}\right) - 1 - (q_1 f_*)^2 \tag{2.79}$$

The parameters q_1 and q_2 are used to better describe the void growth behaviour. Values of $q_1 = 1.5$ and $q_2 = 1.0$ are often used. The term f_* is dependant on the void volume

fraction f. Its objective is to model the coalescence of the voids, once the void volume fraction reaches a critical value f_c:

$$f_* = \begin{cases} f, & \text{if } f \leq f_c \\ f_c + \left(\frac{1}{q_1} - f_c\right) \frac{f - f_c}{f_R - f_c}, & \text{otherwise} \end{cases} \tag{2.80}$$

Where f_R is the void volume fraction at fracture. Rupture occurs at $f_* = 1/q_1$. The void volume fracture increment in the GTN model is given by the sum of the rate of growth and the rate of nucleation:

$$\dot{f} = \dot{f}_{growth} + \dot{f}_{nucleation} \tag{2.81}$$

The rate of growth of voids employed in the GTN model is the same used by Gurson (equation 2.78). The rate of nucleation of voids was developed by Chu and Needleman [145] and takes the form of a Gaussian function:

$$\dot{f}_{nucleation} = \frac{f_N}{S_N \sqrt{2\pi}} \exp\left[-\frac{1}{2}\left(\frac{\overline{\varepsilon}^p - \varepsilon_N}{S_N}\right)^2\right] \tag{2.82}$$

Where f_N is the volume fraction of inclusions at which damage can be nucleated, ε_N is the strain where half of the inclusions are broken, S_N is the standard deviation for the nucleation strain and $\overline{\varepsilon}^p$ is the equivalent plastic strain of the matrix.

2.8.2 Continuum damage mechanics applied to gearboxes

Pandkar et al. [146] studied the contribution of hard particles in bearing steels subjected to rolling contact fatigue. A non-linear model with isotropic and kinematic hardening was used. They concluded that the particles, acting as stress concentrators, introduce shear stresses which generates ratcheting in the metal matrix. Other heterogeneities, such as pores, inclusions and dislocations might also generate the same effect.

Osman and Velex [147] took into account the influence of dynamic loading conditions on pitting formation on gears. The dynamic loads were found to influence

damage depending on the speed range, with higher speeds being more detrimental than lower speeds. It was also found that the tip relief on both gears and pinions are an important factor in reducing the fatigue damage in the engagement area.

Franulovic et al. [148] used a non-linear kinematic hardening model in order to predict low-cycle fatigue in the tooth root of gears due to short-time overloads. Even though a good agreement was found, the model lacks the ability to predict other types of damage, such as rolling contact fatigue, and, more importantly, any type of damage that develops after the low-cycle fatigue stage.

Brandao et al. [149, 150] used a numerical model to predict micropitting and mass loss of a spur gear. The model is dependant on roughness data, which was obtained from FZG tests (a rig where one gear is loaded against another by an electric motor). The model showed an accurate prediction of the mass loss of the gear, however, the predicted roughness evolution did not correlate well with the laboratory tests.

Yazici et al. [151] used both the Gurson and the Gologanu models to investigate the rolling process and surface densification of powder manufactured gears. While the Gurson model considers the porosities to be spherical, the Gologanu model accounts for different pore shapes, as well as for the evolution of these shapes. It was found that the final profile of the manufactured gears is mostly dependant on the tool shape and that the final porosity at the approach side is slightly lower than on the trail side. Even though the work focuses on the closing of existing pores from the sintering process, both models can be used in damage prediction if we account for the porosity as a measure of damage.

Li and Choi [152], and Li and Lee [153] coupled the use of a Paris-Erdogan law model with a 2D finite element analysis to the evolution of a crack in a gear tooth. Stress and strain fields were calculated based on different parameters such as geometry, load and material properties.

Glodez et al. [154] employed finite element analysis in order to determine the service life of a high strength alloy steel gear subjected to tooth bending fatigue. The analysis was divided in two steps: crack initiation, which assumed that the crack would

initiate where the principal stress is at a maximum; and crack growth, which is based on the displacement correlation method.

2.9 SUMMARY

Even though the wind energy industry has been expanding greatly over the past decade, certain reliability issues are yet to be resolved. Operation and maintenance can make up to 30% of the overall levelised cost of electricity [155]. WTGs are the component with the highest downtime, and its failure mechanisms are still not fully understood.

Typical WTG failures include scuffing, fretting corrosion, micropitting, WEA cracking and tooth bending fatigue. They are usually related to poor lubrication, lubricant contamination, misalignments, overloading, and the highly variable loading conditions to which these components are subjected to.

This chapter provided a detailed review of important aspects of WTGs, such as materials and failures, gear design, and lubrication. Additionally, it provides the reader with the background for the subsequent chapters of the thesis, especially on condition monitoring, surface engineering and continuum damage mechanics, which are the focus for increasing the reliability of this component.

.

CHAPTER 3

CHARACTERISATION

3.1 MATERIALS AND PROCEDURES

EN24T and EN40B were the steel grades chosen as reference materials in this research study. Their chemical compositions are given in Table 3.1. The EN24T is a medium-carbon alloy steel, usually used in components such as gears and shafts. The EN40B exhibits high wear resistance together with great toughness and good ductility. The EN40B is also known for its suitability for nitriding [156].

Both materials were procured as a round bar of 45 mm diameter. Prior to characterisation, the materials were prepared by standard cutting, grinding, and polishing procedures.

Table 3.1: Chemical composition in weight of the EN24T and EN40B [157, 158].

Material	**Composition (wt%)**								
	C	Si	Mn	Cr	Ni	Mo	S	P	Fe
EN24T	0.35 - 0.45	0.10 - 0.35	0.45 - 0.70	0.90 - 1.40	1.30 - 1.80	0.20 - 0.35	0.00 - 0.05	0.00 - 0.05	Balance
EN40B	0.20 - 0.30	0.10 - 0.35	0.40 - 0.65	2.90 - 3.50	0.00 - 0.40	0.40 - 0.70	0.00 - 0.05	0.00 - 0.05	Balance

In order to investigate the microstructural homogeneity, samples were cut in both the longitudinal and the transverse directions. The samples were then labelled as shown in Table 3.2.

Table 3.2: Sample labels for different steel grades and directions.

Material	**Direction**	**Sample label**
EN24T	Transverse	24T
EN24T	Longitudinal	24L
EN40B	Transverse	40T
EN40B	Longitudinal	40L

The microstructure of the working materials was assessed with an Axioscope 2 optical microscope manufactured by Carl Zeiss Ltd, equipped with an AxioCam MR digital camera. Secondary and backscattered electron micrographs were captured using a JEOL 6060, a Philips XL 30, and a JEOL 7000 secondary electron microscope (SEM). Energy-dispersive X-ray spectroscopy (EDS) chemical analyses were performed on an Oxford Inca EDS coupled to each SEM. Prior to microstructure observation, the samples were etched with 2% nital.

The X-ray diffraction (XRD) tests were performed in X'Pert Philips XRD instrument with Cu Kα (k = 0.145 nm) radiation. The 2θ range was measured from 30° to 110°.

A Mitutoyo MVK-H1 hardness testing machine with a Vickers diamond indenter was used to evaluate the microhardness of the samples.

Nanoindentation using a Nano Vantage (Micro Material, UK) machine was used to characterise the hardness of the DLC coatings. The depth of each indent was controlled to 100 nm.

A laser Raman spectroscope, containing a Renishaw InVia reflex spectrometer was used to analyse the DLC coatings. The laser used had a wavelength of 488 nm and a power of 2 mW. The measurements were performed in an Instec HCS621V cell with a pressure and flow of argon gas of 1 bar and 100 ml/min, respectively.

3.2 UNTREATED MATERIALS

3.2.1 EN24T

The EN24T steel was characterised by optical and scanning electron microscopes, microhardness, XRD and EDS. The microstructure of the EN24T steel is tempered martensite, as seen in Figures 3.1, 3.2b and 3.3b, and is confirmed by the XRD diffractogram (Figure 3.5), showing no other phases are present. Additionally, several inclusions were found in the microstructure. In the 24T samples, the inclusions have a round shape (Figure 3.2a), whilst they are elongated in the 24L samples (Figure 3.3a). The 24L sample is aligned with the rolling direction of the bar, which explains the shapes of the inclusions. Figure 3.4 shows the finely dispersed carbides in the tempered martensite matrix.

By using the EDS, it was possible to determine that the inclusions were MnS, as shown in Figure 3.6 and Table 3.3. The carbon content is much higher than what was expected (Table 3.1). This is probably due to hydrocarbon contamination in the SEM chamber [159]. Another possible explanation is that X-rays generated by light elements are difficult to measure reliably [160]. All the other elements are within the specified range.

The microhardness profile of both 24T and 24L samples can be seen in Figure 3.7. The hardness is constant throughout the cross-section of both samples, and they also exhibit similar hardness values, as was expected from the similar grain structure obtained from the micrographs. The average microhardness for the 24T sample is 317.0 $\pm$ 15.0 HV 0.05 and for the 24L is 325.8 $\pm$ 19.5 HV 0.05. The microhardness of the EN24T is therefore in the range required by the AGMA for external gears, which is between 290 to 450 HV [32].

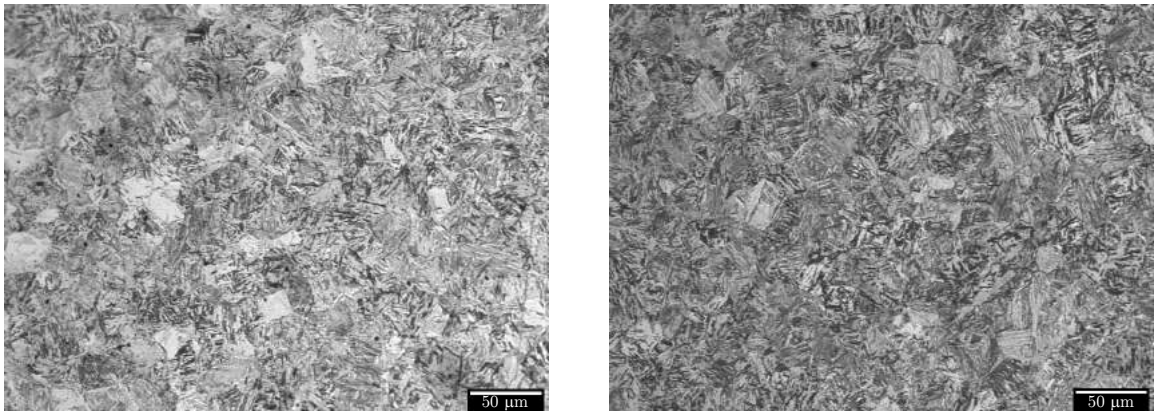

(a) (b)

Figure 3.1: Optical micrographs of the 24T (a) and 24L (b) samples, etched with 2% nital.

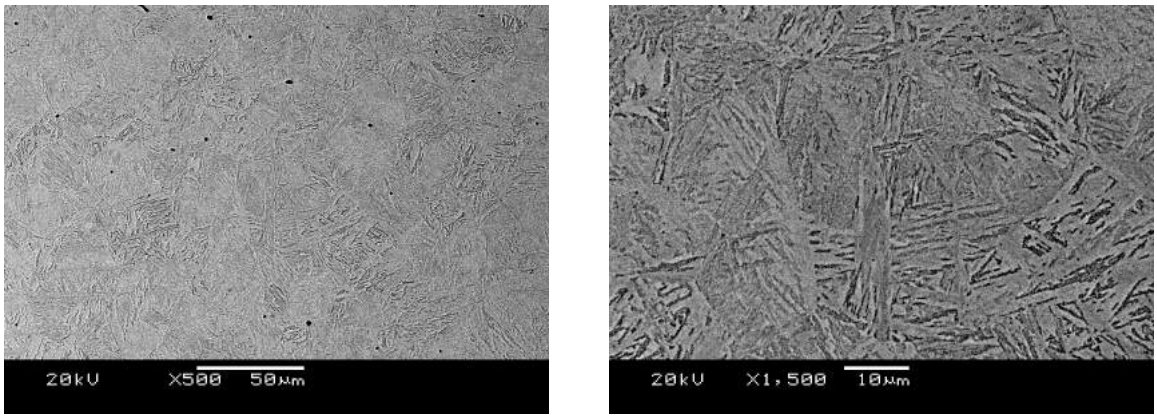

(a) (b)

Figure 3.2: SEM micrographs of the 24T samples etched with 2% nital.

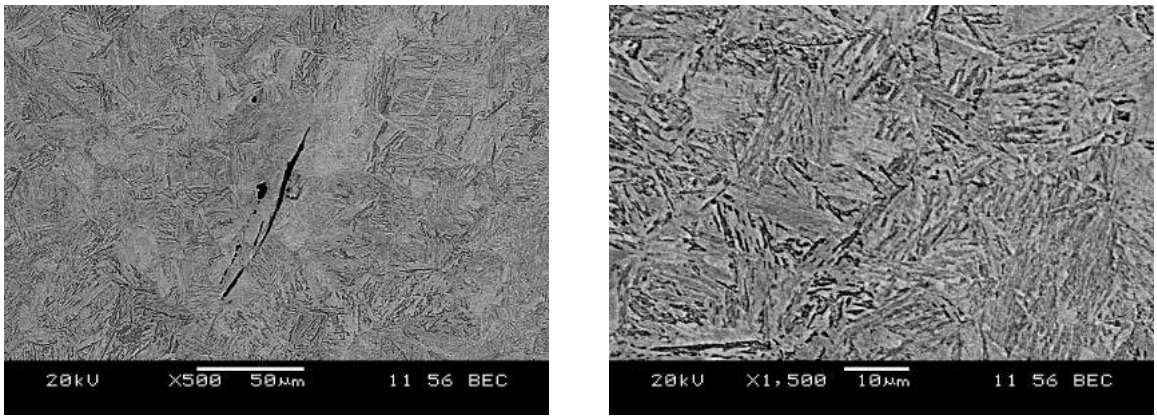

(a) (b)

Figure 3.3: SEM micrographs of the 24L samples etched with 2% nital.

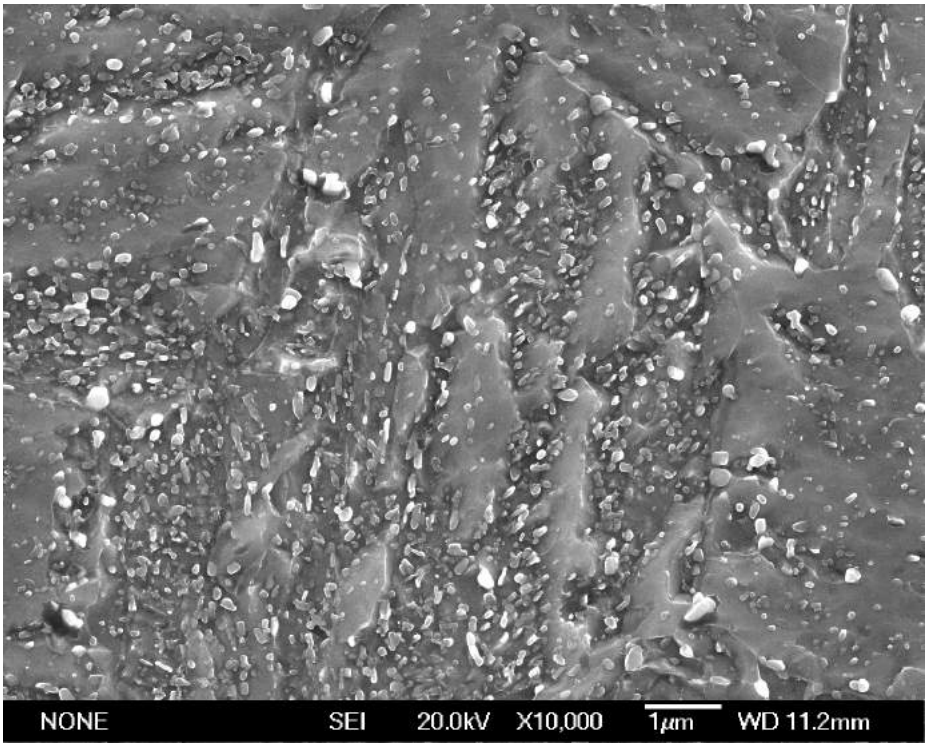

Figure 3.4: SEM micrographs of the 24L sample etched with 2% nital showing the finely dispersed carbides.

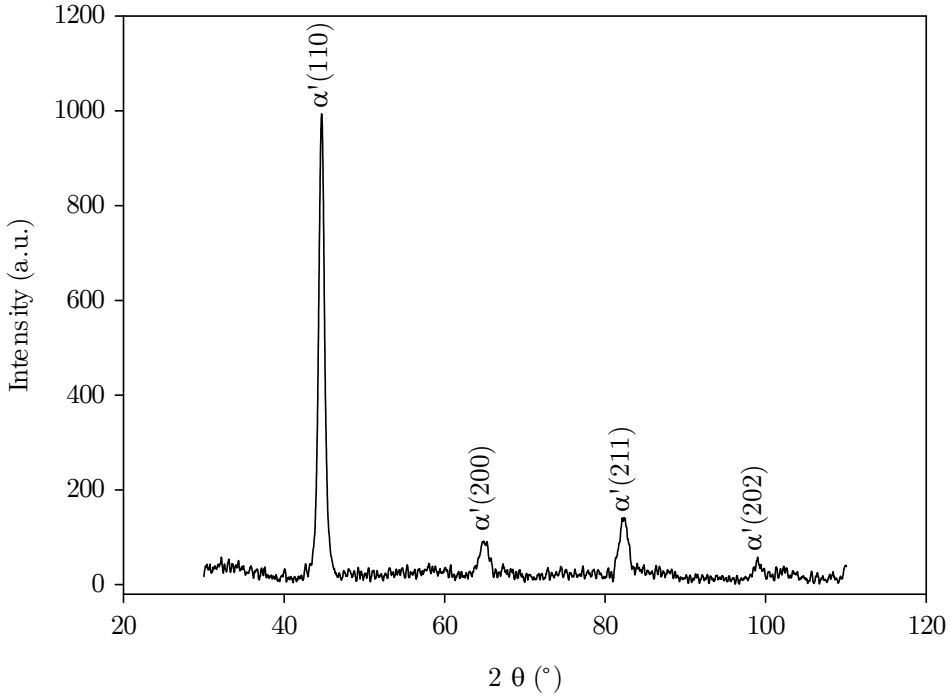

Figure 3.5: X-ray diffractogram of the EN24T steel, showing martensite peaks.

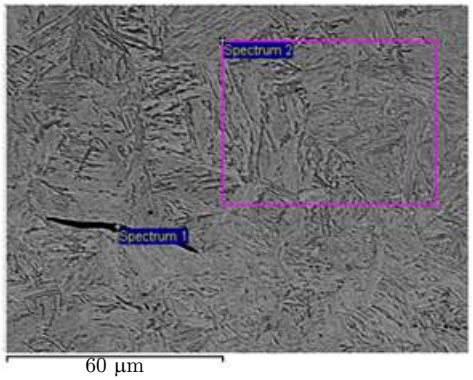

Figure 3.6: SEM micrographs of EDS locations. Etched with 2% nital.

Chemical element	**Spectrum 1 (wt%)**	**Spectrum 2 (wt%)**
C	2.4	1.8
Si	0.2	0.3
S	25.8	-
Cr	0.5	1.4
Mn	51.9	0.7
Ni	-	1.3
Mo	-	0.3
Fe	19.2	94.2

Table 3.3: EDS results of the locations in Figure 3.6.

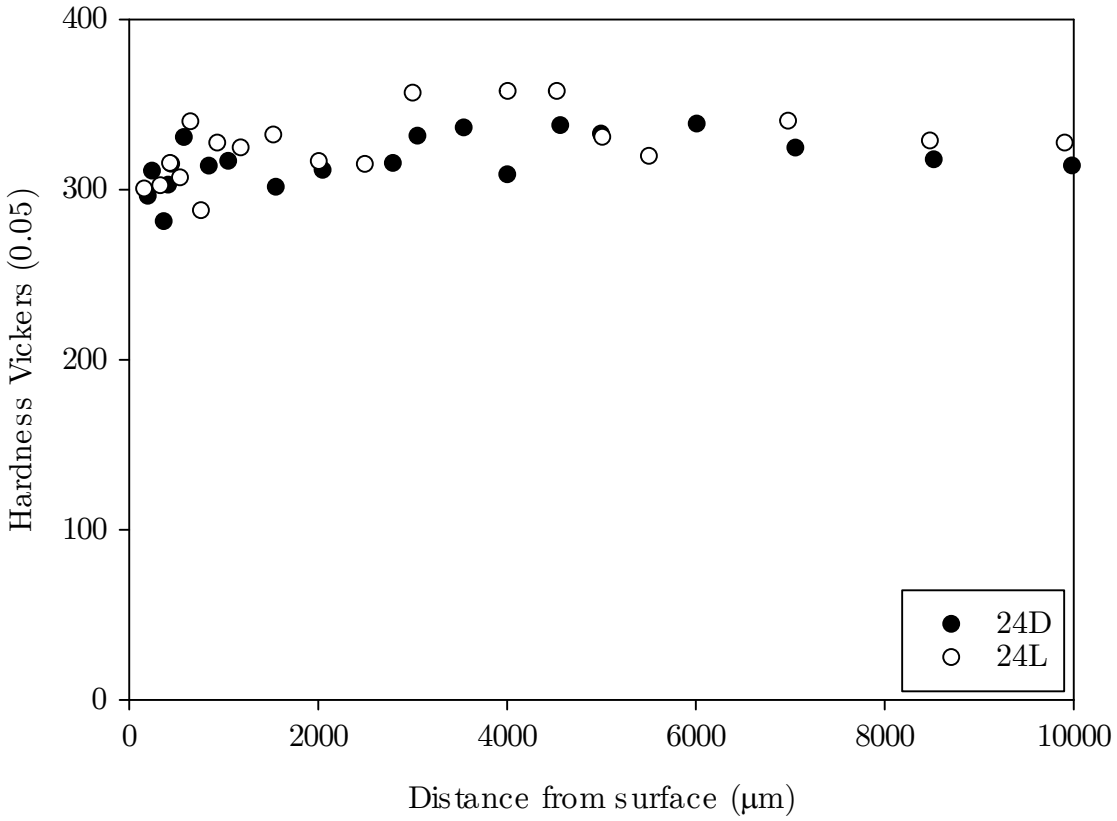

Figure 3.7: Microhardness profile of 24T and 24L samples.

3.2.2 EN40B

Similarly to the EN24T steel, the EN40B microstructure is also tempered martensite, as Figures 3.8, 3.9b and 3.10b show, and is confirmed by the XRD diffractogram (Figure 3.13). The inclusions are also round for the 40T sample (Figure 3.9a) and elongated for the 40L sample (Figure 3.10a), which is parallel to the rolling direction. The inclusions were also found to be MnS, as shown in the EDS analysis (Figure 3.11 and Table 3.4). The compositions are as expected, except for the carbon content. Figure 3.12 shows the finely dispersed carbides in the tempered martensite matrix.

The microhardness profile of the 40T and 40L samples can be seen in Figure 3.14. In the same way as the 24T and 24L samples, the microhardness remains constant throughout both cross-sections. Both samples have similar hardness values. The average microhardness for the 40T sample is 329.6 ± 10.2 HV 0.05 and for the 40L is 325.9 ± 19.6 HV 0.05, meaning that they are in the range required by the AGMA as well.

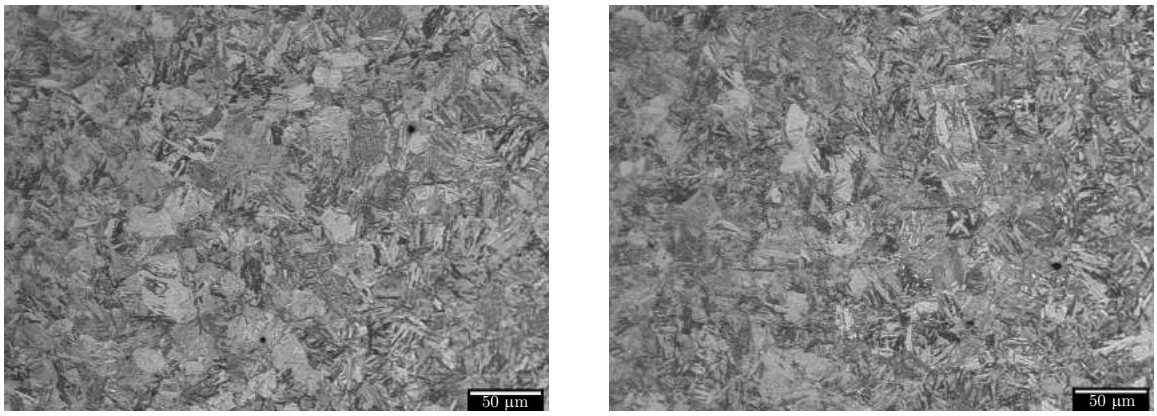

(a) (b)

Figure 3.8: Optical micrographs of the 40T (a) and 40L (b) samples, etched with 2% nital.

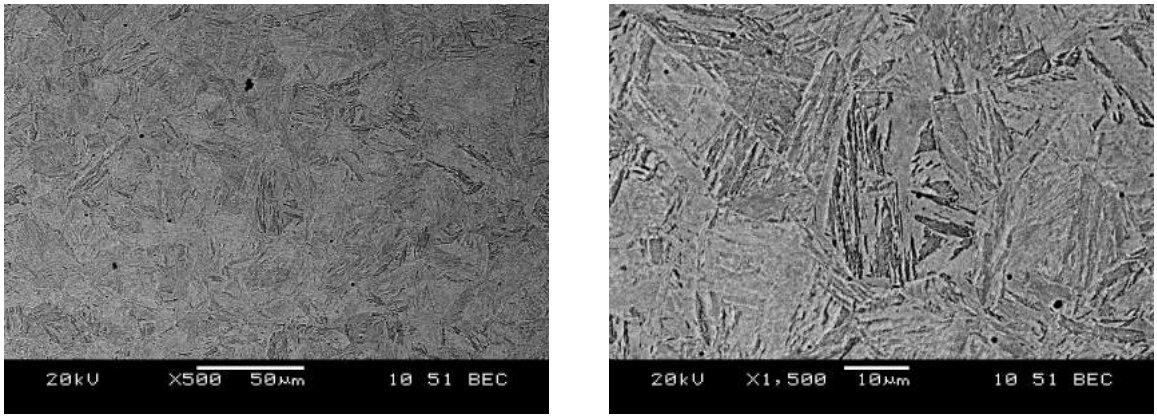

(a) (b)

Figure 3.9: SEM micrographs of the 40T samples etched with 2% nital.

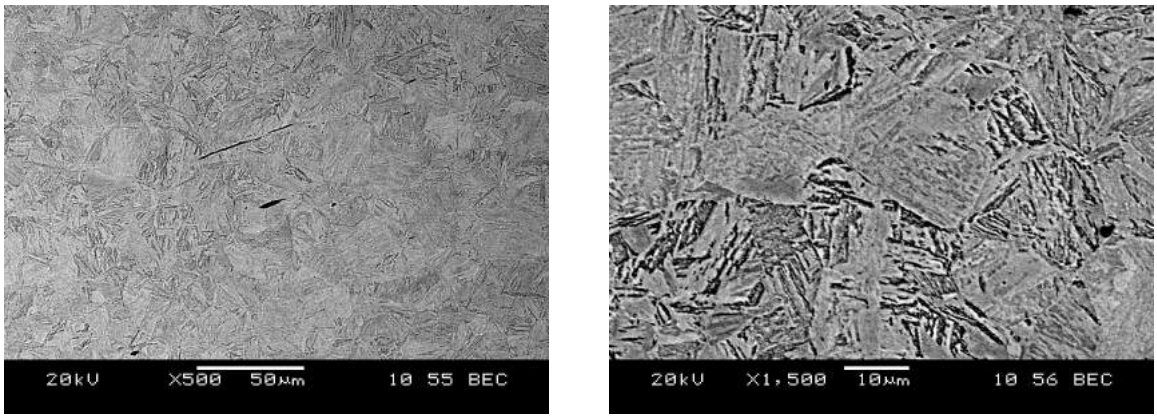

(a) (b)

Figure 3.10: SEM micrographs of the 40L samples etched with 2% nital.

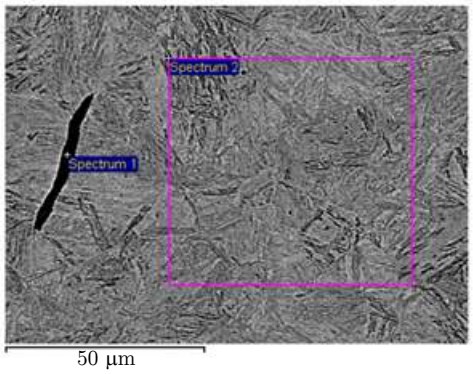

Figure 3.11: SEM micrographs of EDS locations. Etched with 2% nital.

Chemical element	**Spectrum 1 (wt%)**	**Spectrum 2 (wt%)**
C	3.8	1.9
Si	-	0.2
S	28.5	-
Cr	2.7	3.3
Mn	53.1	0.6
Mo	-	0.5
Fe	11.9	93.5

Table 3.4: EDS results of the locations in Figure 3.11.

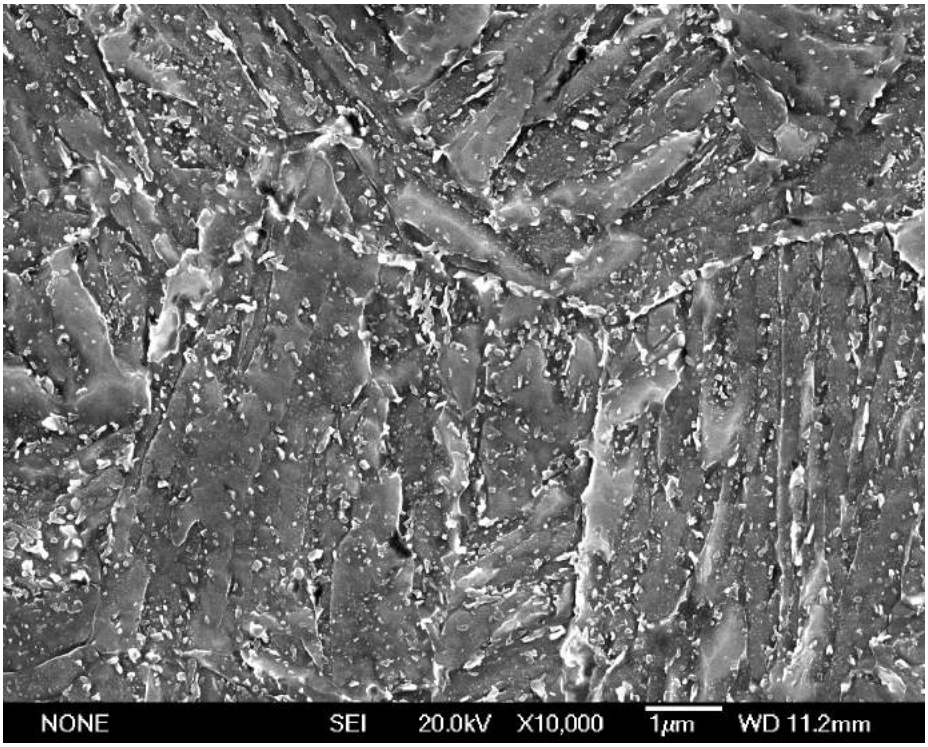

Figure 3.12: SEM micrograph of the 40L sample etched with 2% nital showing the finely dispersed carbides.

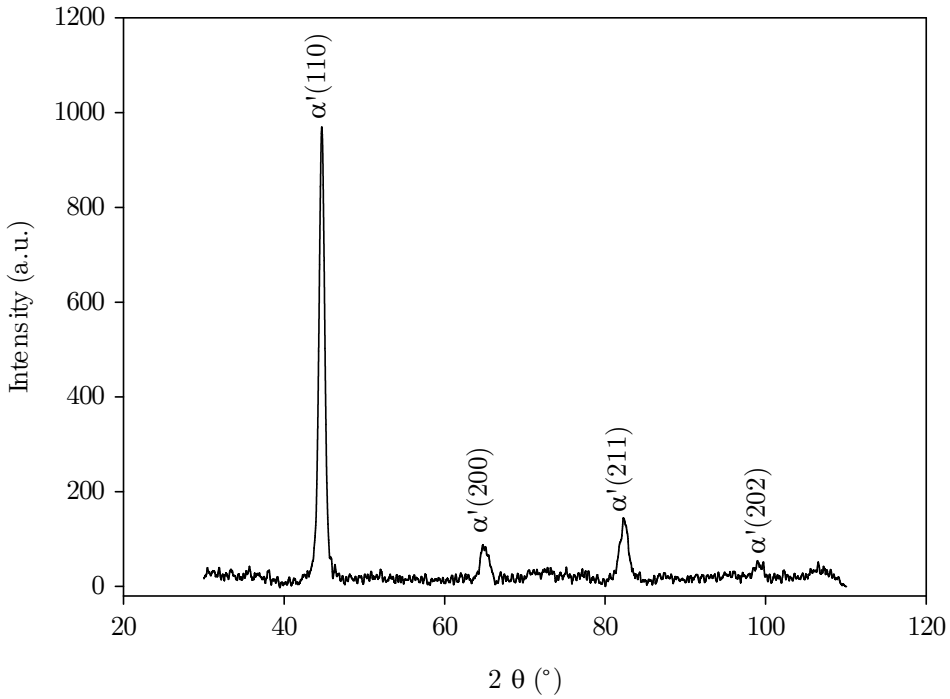

Figure 3.13: X-ray diffractogram of the EN40B steel, showing martensite peaks.

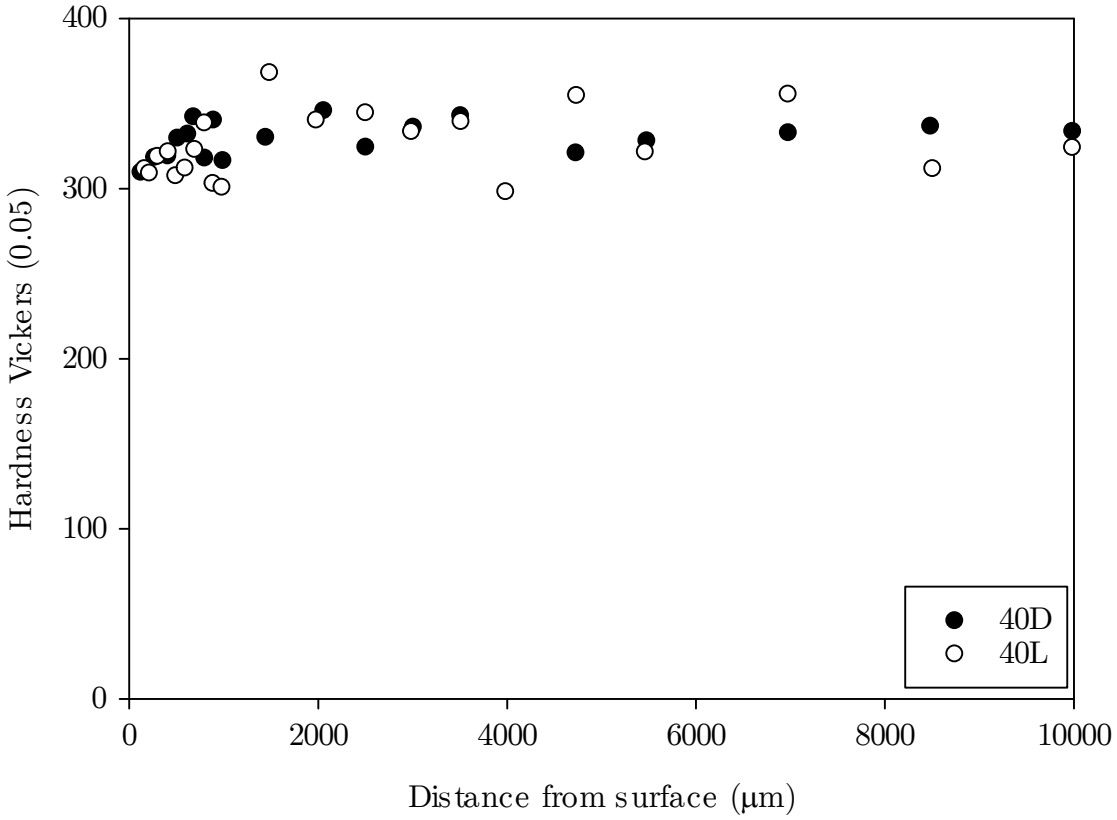

Figure 3.14: Microhardness profile of 40T and 40L samples.

3.3 SURFACE TREATED MATERIALS

The surface treatment processes carried out in this project are summarised in Table 3.5. The EN24T was coated with DLC, whereas the EN40B was nitrided, DLC-treated, and duplex treated in a combination of nitriding and DLC.

The DLC coating chosen for this work was BALINIT ®C, available from Oerlikon Balzers Coatings Ltd, due to its good surface fatigue resistance and self-lubricating properties. BALINIT ®C is a WC/a-C:H coating. A thin Cr interlayer is used to increase the adhesion to the substrate.

Table 3.5: Surface treatments performed.

Material	Treatment	Label
EN24T	Untreated	24U
	DLC only	24U-DLC
EN40B	Untreated	40U
	DLC only	40U-DLC
	Nitriding only	40N
	Nitriding and DLC	40N-DLC

The EN40B was active screen plasma nitrided using a Klockner Ionon 60 kVA plasma nitriding machine at the School of Metallurgy and Materials in the University of Birmingham. The treatment was performed at 550°C for 20 hours, in a working gas atmosphere of 25% N_2 and 75% H_2. The treatment temperature was achieved with an atmosphere of H_2. The pressure of the gas mixture was 4 mbar.

3.3.1 EN40B nitrided

A cross-section of the nitrided EN40B steel can be seen in Figure 3.15. The overall diffusion layer can be seen in Figure 3.15c. A closer look of the nitriding layer surface (3.15a) shows a thin compound layer, which can be seen in more detail in Figure 3.15b. The compound layer is brittle and can have an adverse effect to the wear resistance of nitrided steels [161]. It is also softer than the nitrided layer [162]. More often, the compound layer is formed from a mixture of γ'-Fe_4N and ϵ-$Fe_{2-3}N$ phases. In the nitrided EN40B steel, an interface in the compound layer is distinguishable, with a columnar ϵ phase at the top and an angular γ' at the bottom. The existence of both phases is confirmed by the XRD shown in Figure 3.17.

Figures 3.15c and 3.15d show a continuous network of prior austenite grain boundary precipitates. Mridha and Jack [162] found the microstructure of a EN40B nitrided steel evolves due to the formation of fine CrN plates in the nitrided zone. These plates create large compressive stresses parallel to the specimen surface. If following

nitriding, no compound layer is formed, decarburisation is likely to occur. However, as this is not the case for the nitriding used in this study, the released carbon from the cementite is instead driven deeper into the bulk as a result of the nitrogen-rich surface, creating a carbide-enriched sub-layer. Due to the compressive stress, the cementite precipitates in the prior austenite grain boundaries, in a direction parallel to the surface of the specimen. This is confirmed by an EDS line scan of a carbide, as Figure 3.16 shows. This continuous network of carbides is usually detrimental to the ductility of nitrided steels [163].

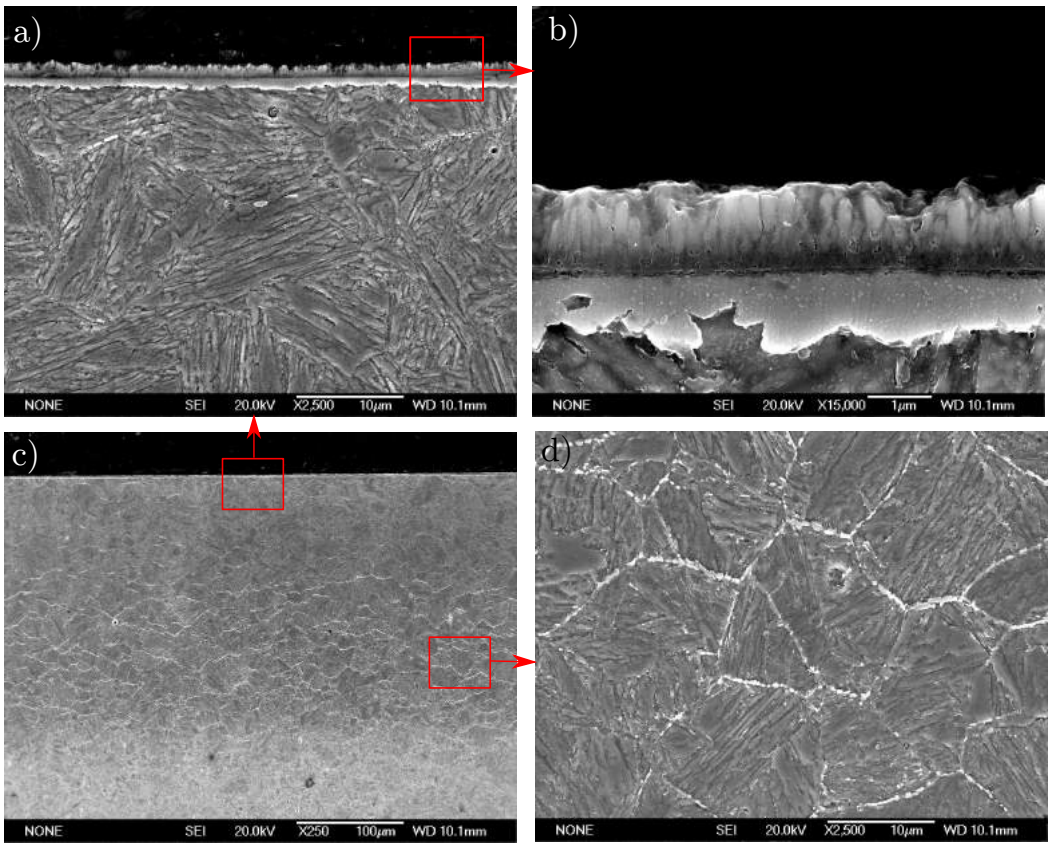

Figure 3.15: SEM micrographs showing the nitrided layer at different regions. Etched with 2% nital.

A microhardness profile of the nitrided EN40B is shown in Figure 3.18. The hardness of the case is 800 HV 0.05, and the case depth, defined as the distance to the surface to a point where the hardness is 400 HV [33], is 300 μm. The hardness decreases at 200 μm, which is comparable with the size of the diffusion zone shown in Figure 3.15c.

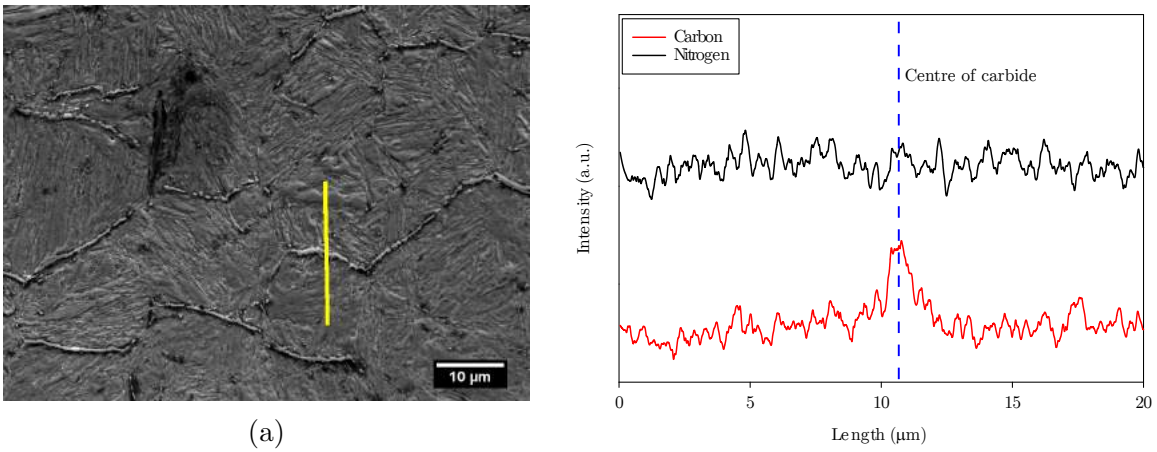

(a) (b)

Figure 3.16: SEM micrograph of the EN40B carbide and the location on the EDS line scan, etched with 2% nital (a), and the results of the EDS line scan for carbon and nitrogen (b).

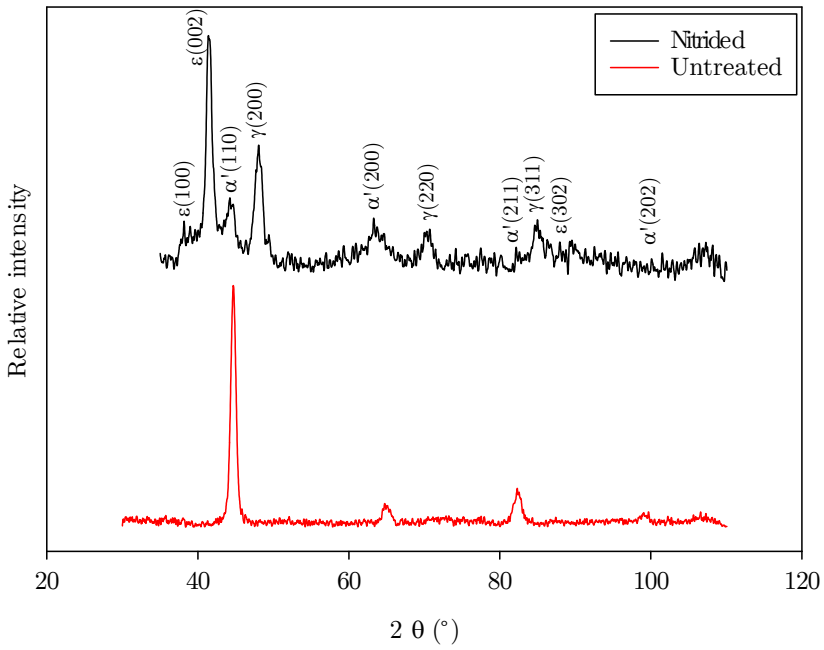

Figure 3.17: X-ray diffractogram of the nitrided EN40B.

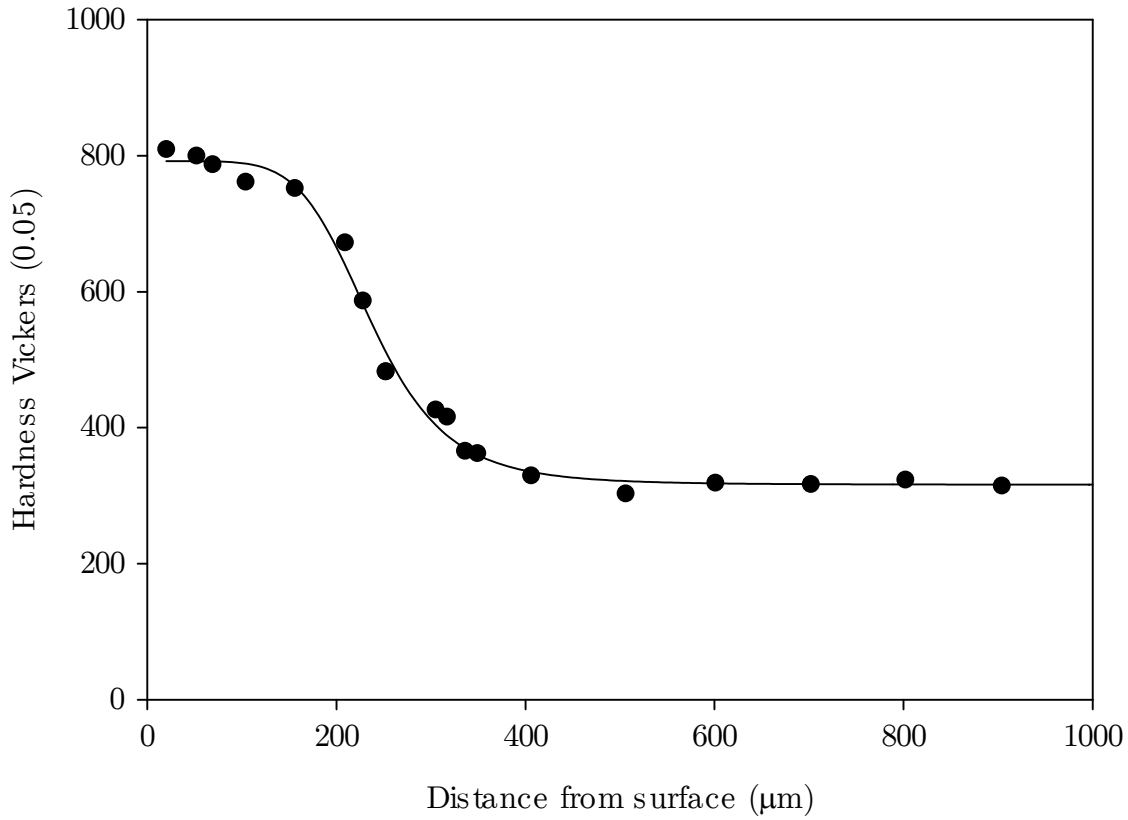

Figure 3.18: Microhardness profile of the nitrided EN40B steel.

3.3.2 DLC treatment

Single surface systems were created by applying DLC coatings to the EN24T and EN40B in the untreated condition (Figure 3.19). A duplex surface system was created by applying DLC coatings to the nitrided EN40B (Figure 3.20).

The DLC layer is distinguishable from the chromium interlayer, which is thinner and acts as a bonding agent between the coating and the substrate. The elements are confirmed by EDS shown in Figure 3.21.

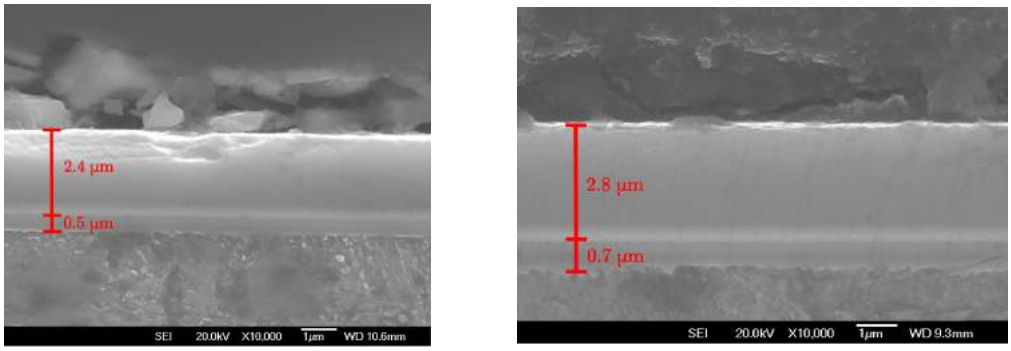

(a) (b)

Figure 3.19: SEM micrographs of the DLC single surface systems showing the EN24T (a), and the EN40B (b), untreated condition. Etched with 2% nital.

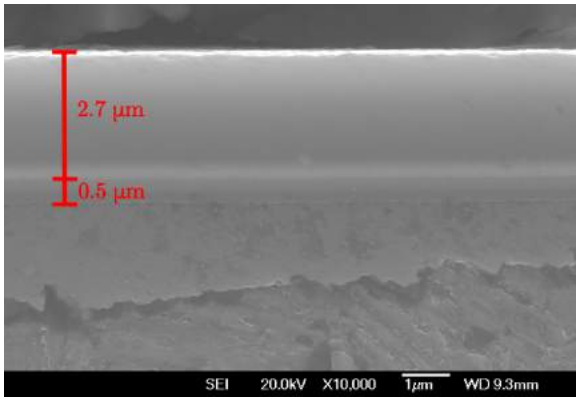

Figure 3.20: SEM micrograph of the nitrided and DLC-treated EN40B. Etched with 2% nital.

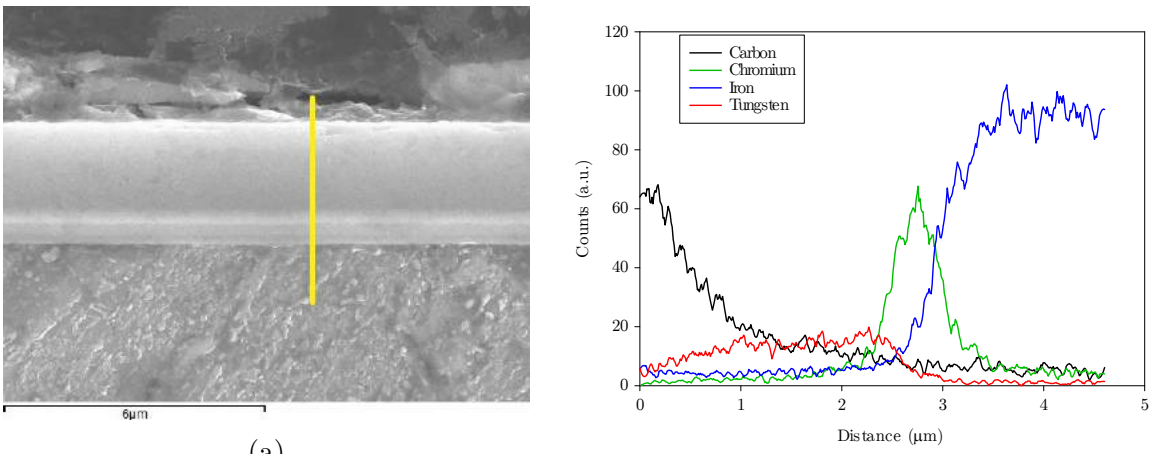

(a) (b)

Figure 3.21: SEM micrograph of the DLC layer for the EN24T sample, etched with 2% nital, with the yellow line showing the position of the EDS line scan (a), and the results of the EDS line scan (b).

Figure 3.22 shows the summarised data for the thickness of the three samples, measured with the ImageJ software. The DLC layer is slightly thinner in the EN24T untreated sample, whereas the chromium layer is slightly thicker in the EN40B untreated sample.

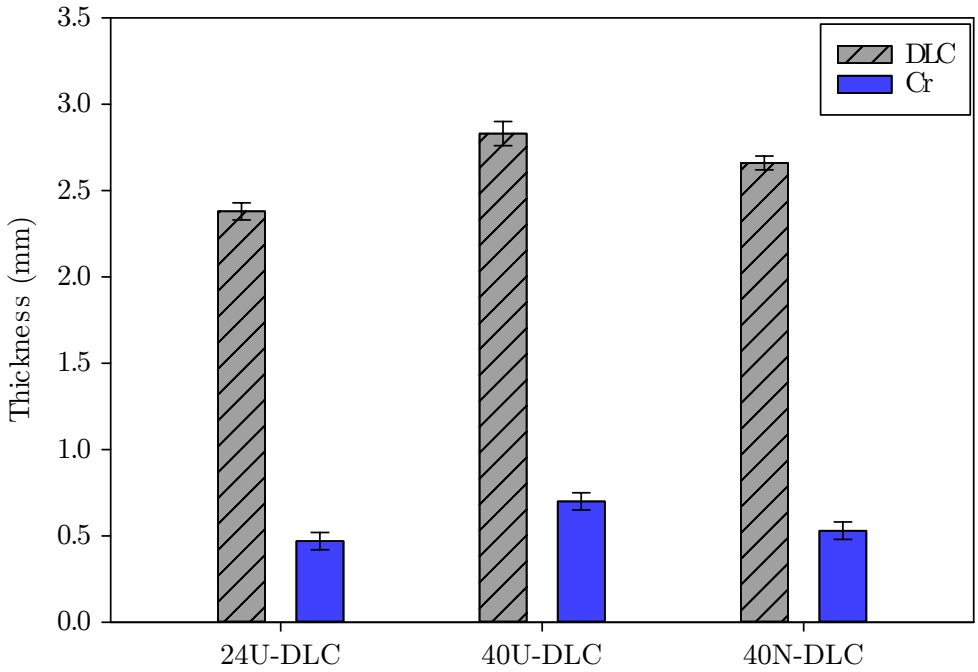

Figure 3.22: DLC and chromium layer thickness of the treated samples.

As a result of the thickness of the DLC coating, nanoindentation was used to measure the hardness of the layer. Nanoindentation uses low loads in order to avoid crack formation. Similar to microhardness testing, nanoindentation also consists of a sharp tip made of a hard material being pressed down onto a sample to create an indent. The area and depth of the indent, as well as the force applied by the indenter, will correlate with the hardness of the tested material.

A nanoindentation load-displacement curve can be seen in Figure 3.23. The tests can be either load or depth controlled. When the value for the chosen parameter is reached, the load is maintained for a small period of time (dwell time) before unloading. During unloading, the material will often experience elastic recovery, which can be observed by the difference between the maximum indentation displacement (h_{max}) and the

final recovery displacement (h_f).

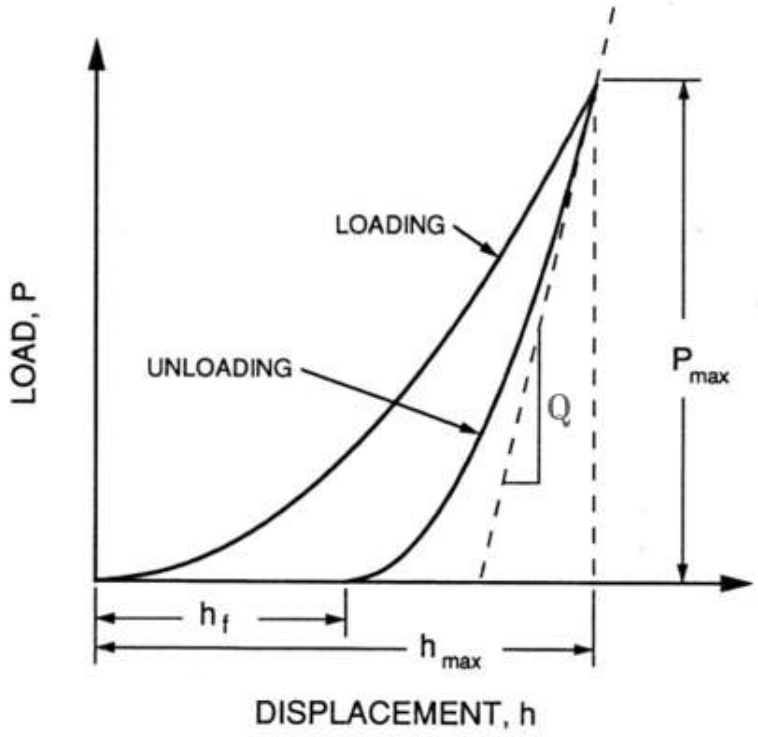

Figure 3.23: Typical load-displacement curve of a nanoindentation test. Source: [164].

The hardness and elastic modulus can then be calculated with equations 3.1 to 3.3 [164]:

$$H = \frac{P_{max}}{A} \tag{3.1}$$

$$Q = \frac{dP}{dH} = \frac{2}{\sqrt{\pi}} E_r \sqrt{A} \tag{3.2}$$

$$\frac{1}{E_r} = \frac{(1-\nu^2)}{E} + \frac{(1-\nu_i^2)}{E_i} \tag{3.3}$$

Where H is the hardness, P_{max} is the maximum load, A is the residual indentation area, Q is the slope of the unloading curve, E_i and ν_i^2 are the elastic modulus and Poisson's ratio of the indenter, and E and ν^2 are the elastic modulus and Poisson's ratio of the sample, respectively. The E_r is the reduced elastic modulus.

Nanoindentation was carried out on the surface of the DLC-treated samples to measure their hardness. Due to the small thickness of the coating, the tests were depth controlled to 100 nm. This guarantees that any results obtained would be solely dependant on the DLC coating, with no effect arising from the underlying Cr interlayer or bulk substrate material.

The nanoindentation results are shown in Figure 3.24. The hardness of the DLC coating on the EN24T steel is slightly higher than the other samples. This can clearly be seen in Figure 3.24b, which shows the EN24T needed a higher force to achieve the same 100 nm depth than the other samples.

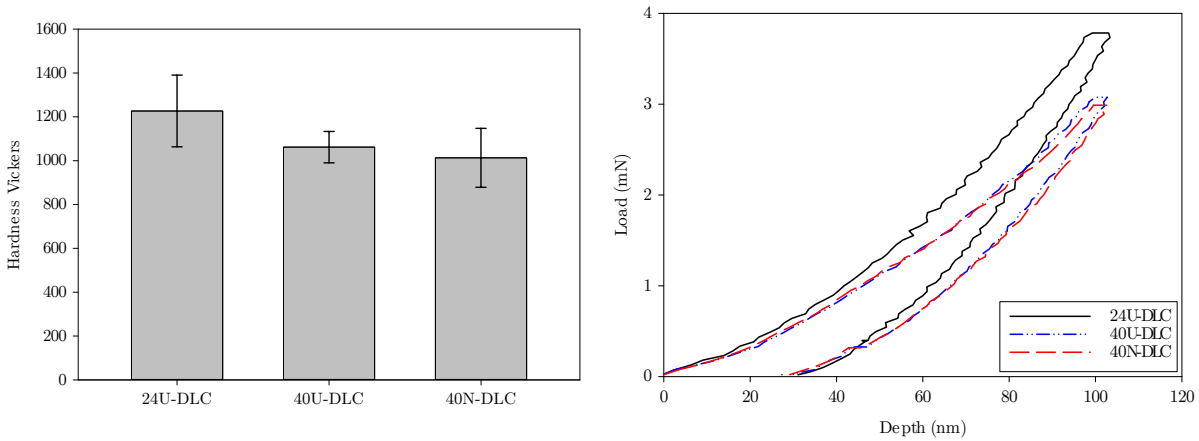

(a) (b)

Figure 3.24: Hardness comparison of all DLC-treated samples (a). Loading and unloading curves of DLC-treated samples (b).

Figure 3.25 shows the Raman spectrum of the DLC coating. Two bands can be distinguished from the spectrum. These are defined as the sp^2 graphite band and the sp^3 disordered band [165]. The disordered peak is located at 1392 cm^{-1} with an intensity of 605, while the graphite peak is located at 1559 cm^{-1} with an intensity of 910. The ratio of the intensity of the disordered peak over the intensity of the graphite peak gives the component ratio of sp^2 and sp^3 clusters, which in this analysed DLC coating is 0.66.

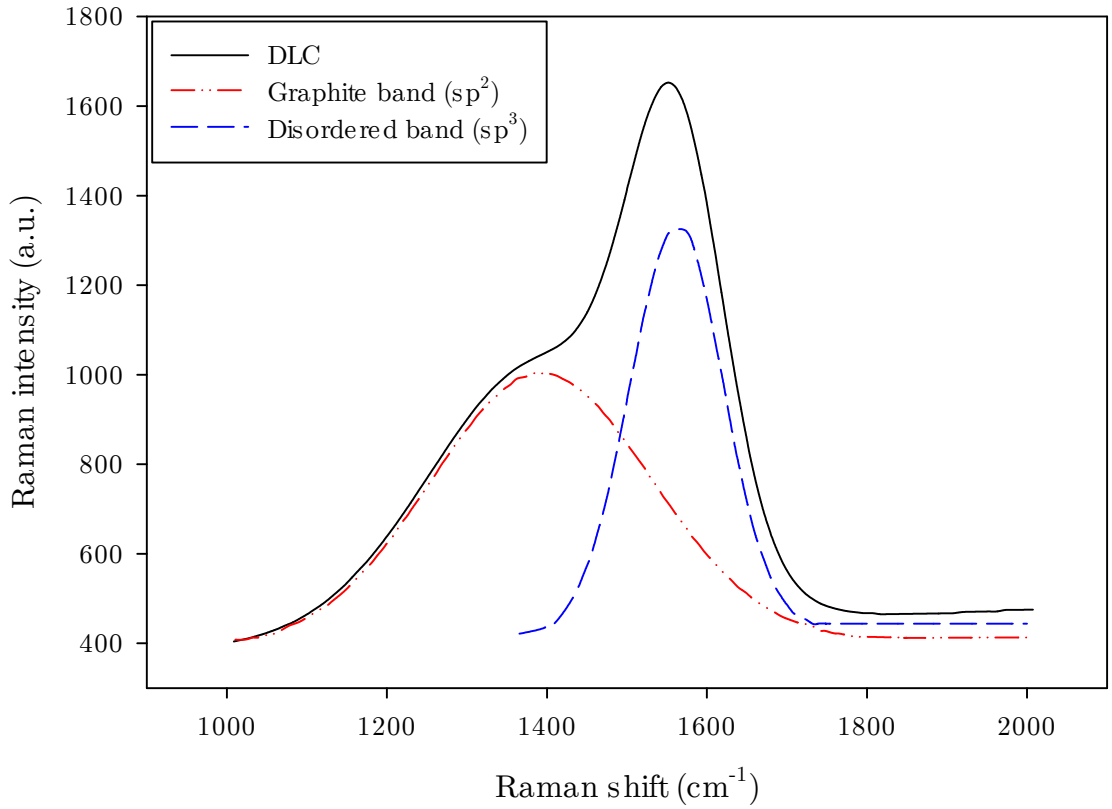

Figure 3.25: Raman spectrum of the DLC coating.

3.4 SUMMARY

Both steel grades selected for the experimental work of this study present a similar microstructure based on tempered martensite. Some elongated MnS inclusions were also identified. The hardness is also similar and around 320 HV 0.05 for both.

Different surface treatments were performed on each steel grade. The EN24T was DLC coated, while the EN40B was plasma nitrided, DLC coated, and also duplex treated, in a combination of plasma nitriding and DLC coating. All treatments yielded the expected hardness and depth. These characterised materials were used throughout the mechanical and rolling contact fatigue testing on the following chapters.

CHAPTER 4

MECHANICAL TESTING

4.1 FATIGUE CRACK GROWTH

Three-point bending fatigue crack growth samples were manufactured according to ISO 12108 [166], as shown in Figure 4.1. The tolerance for the radius at the notch tip was 0.1 mm.

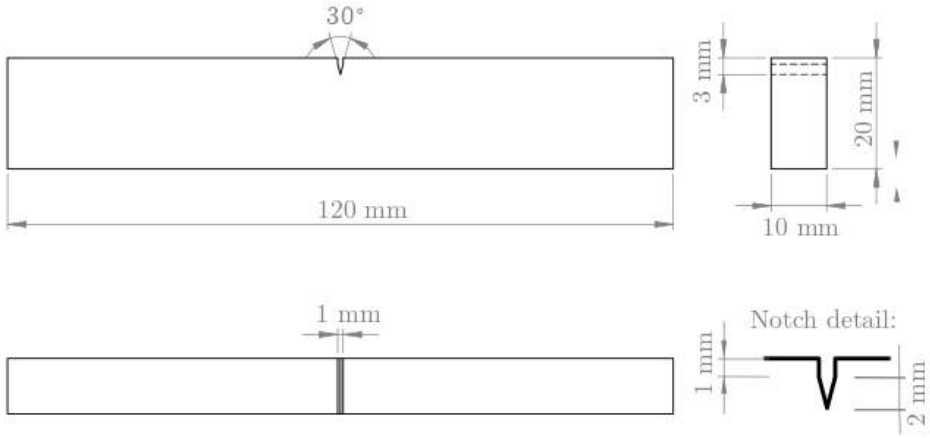

Figure 4.1: Dimensions of the fatigue crack growth samples.

The notch acted as a crack initiation point for the pre-cracking process. The pre-cracking was carried out on an Amsler 20 kN Vibrophore electro-mechanical high-frequency fatigue machine, at a maximum load of 9.0 kN, frequency of 105 Hz, and R-ratio of 0.1. An AE system and plastic replicas were used to monitor the pre-craking process.

The AE signals were detected and recorded using a 4-channel AE system procured from Physical Acoustics Corporation (PAC, now Mistras). The data acquisition was performed using the AEwin software. Two 150-700 kHz PAC R50α piezoelectric AE sensors were connected to PAC model 2/4/6 pre-amplifier and attached to the samples with epoxy adhesive (Araldite®). The same AE system was used during both pre-cracking and fatigue crack growth testing for all samples. Pencil lead break tests were performed

before each test to confirm the acoustic coupling quality consistency.

The acoustic emission parameters were set after preliminary tests had been carried out so that noise could be minimised. The parameters for both the pre-cracking and fatigue crack growth testing are shown in Table 4.1.

Table 4.1: AE parameters of the pre-cracking and fatigue crack growth test.

AE parameter	**Pre-cracking**	**Fatigue crack growth**
Threshold	70 dB	40 dB
Pre-Amplification level	40 dB	40 dB
Analogue filter	0.2 - 1 MHz	0.2 - 1 MHz
Sampling rate	5 MSPS	5 MSPS
Pre-Trigger	256 µs	256 µs
Length	10 k	10 k
Peak Definition Time	600 µs	600 µs
Hit Definition Time	1000 µs	1000 µs
Hit Lockout Time	2000 µs	2000 µs
Duration	25 ms	25 ms

Figure 4.2 shows an example of the acoustic emission activity during the pre-craking process of one of the EN24T steel samples. The sudden increments in the cumulative energy marked by red arrows are showing that cracks are initiating and/or growing.

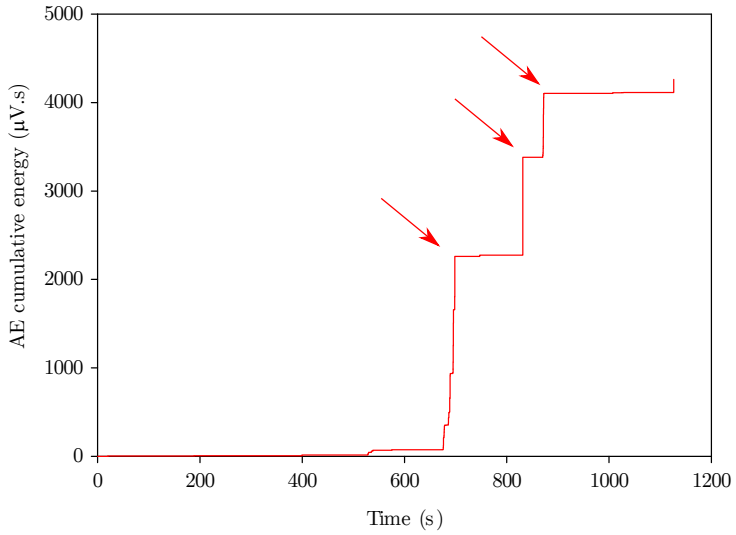

Figure 4.2: Acoustic emission activity during pre-cracking of an EN24T steel sample.

Figure 4.3 shows a crack obtained from the pre-cracking process, where the crack propagating from the notch can be observed.

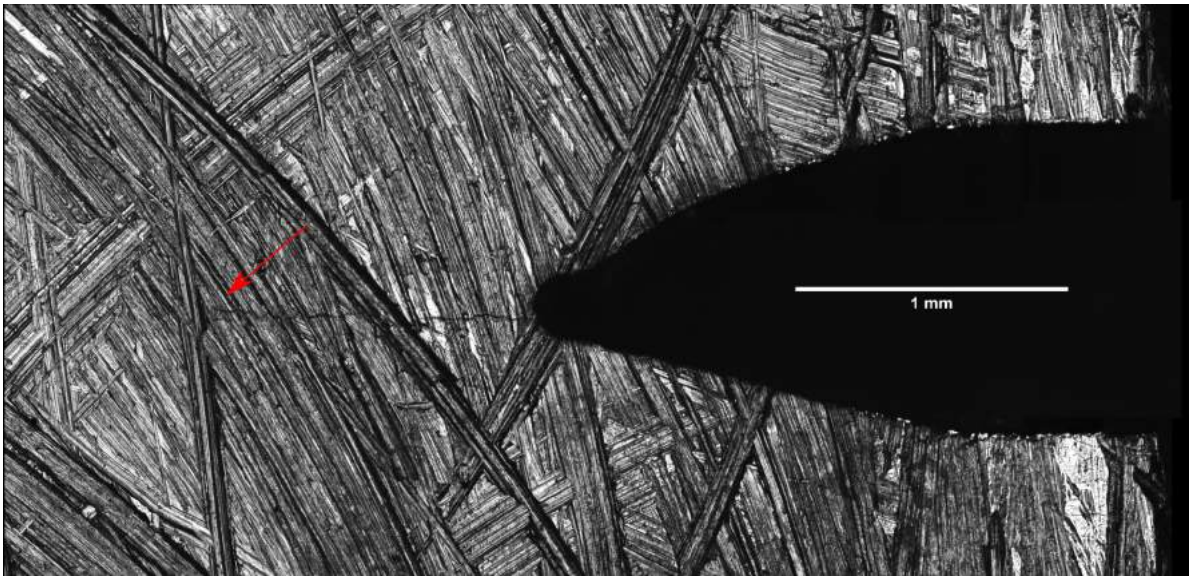

Figure 4.3: Crack obtained from the pre-cracking process. The red arrow marks the end of the crack.

After being pre-cracked, the samples were placed in a Dartec 50 kN Servo-Hydraulic Universal Test Machine. They were subjected to a maximum load of 8 kN and R ratio of 0.1. The wave shape was sinusoidal. Direct current potential drop (DCPD) was employed to monitor the crack size. The current applied through the samples was 20 A. The EN24T samples were tested at both 0.25 Hz and 1 Hz, while the EN40B samples were tested at 1 Hz. A chart recorder was used to extract the DCPD data with a recording speed of 1 mm/min. The number of cycles was calculated from the chart length, whereas the crack size was calculated using Johnson's formula [167], shown in equation 4.1:

$$a = \frac{2W}{\pi} \cos^{-1} \frac{\cosh[(\pi y)/(2W)]}{\cosh\{(U/U_0)\cosh^{-1}[(\cosh(\pi y)/(2W))/(\cos(\pi a_0)/(2W))]\}} \tag{4.1}$$

Where a is crack length, a_0 is the initial crack length, U is the potential, U_0 is the initial potential, y is half of the distance of the DCPD sensors and W is the specimen width.

The Paris-Erdogan law [168] relates the stress intensity factor (K) to the crack

growth rate (da/dN), where da is the infinitesimal crack length growth over a number of cycles (dN) as seen in equation 4.2:

$$\frac{da}{dN} = C(\Delta K)^m \tag{4.2}$$

Where C and m are material constants. The crack growth rate can be calculated from Johnson's formula, and the stress intensity factor for a three-point bend specimen with a single edge notch is given by equation 4.3 [169]:

$$K = \frac{4L}{B}\sqrt{\frac{\pi}{W}}\left[1.6\left(\frac{a}{W}\right)^{1/2} - 2.6\left(\frac{a}{W}\right)^{3/2} + 12.3\left(\frac{a}{W}\right)^{5/2} - 21.2\left(\frac{a}{W}\right)^{7/2} + 21.8\left(\frac{a}{W}\right)^{19/2}\right] \tag{4.3}$$

Where L is the load and B is the thickness. The ΔK from equation 4.2 is given by the difference of K calculated at the maximum and minimum loads during the fatigue cycle.

4.1.1 Paris-Erdogan Law

Three EN24T samples were tested at a frequency of 0.25 Hz and three samples at a frequency of 1 Hz. Another six EN40B samples were tested at a frequency of 1 Hz. A plot of the stress intensity factor versus the crack growth rate for all 12 tested samples can be seen in Figure 4.4.

From Figure 4.4 it is possible to calculate the Paris-Erdogan law parameters C and m, as shown in Table 4.2. It is possible to see that the EN24T steel at 1 Hz has the highest crack growth rate, followed by the EN24T at 0.25 Hz and the EN40B at 1 Hz. At lower stress intensity factor ranges, this effect is less intense, with all three samples having similar values in terms of the crack growth rate. However, as the stress intensity factor increases, the difference in the fatigue crack growth rate between these samples becomes more evident. This behaviour is in line with what was observed by Musuva and Radon [170], which found the frequency to have a low effect on the fatigue crack growth at low-stress ratios.

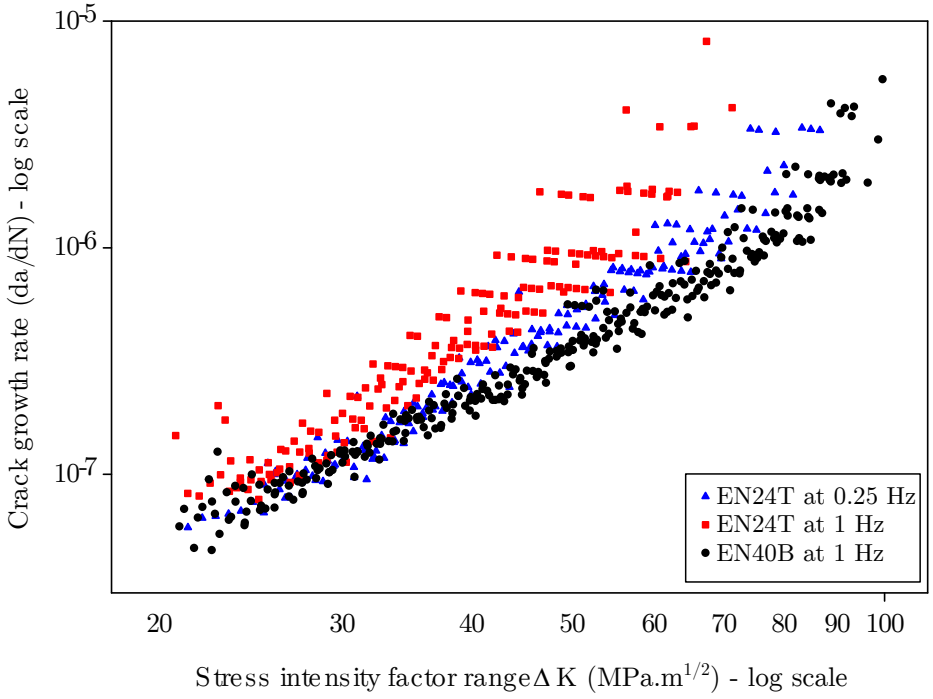

Figure 4.4: Stress intensity factor versus crack growth rate of EN24T and EN40B samples, plotted in logarithmic scale.

Table 4.2: Paris-Erdogan law parameters of the EN24T and EN40B steels.

Material	**Frequency** (Hz)	**m**	**C** $(\mathrm{m}/(\mathrm{cycle}\cdot\mathrm{MPa}\cdot\sqrt{\mathrm{m}}))$
EN24T	1.00	3.20 ± 0.11	$(3.90 \pm 1.13) \times 10^{-12}$
EN24T	0.25	2.86 ± 0.10	$(6.17 \pm 0.45) \times 10^{-12}$
EN40B	1.00	2.36 ± 0.14	$(4.78 \pm 2.62) \times 10^{-11}$

4.1.2 AE monitoring and failure analysis

Figure 4.5 shows one of the EN24T samples after failure. Due to the high toughness of the EN24T steel, the sample did not break completely and had to be cut so the failure surface could be analysed.

Figure 4.5: EN24T steel sample after failure.

A photo of the failure surface is shown in Figure 4.6. The three different zones, initiation, fatigue crack propagation, and catastrophic failure can be easily identified. An SEM micrograph of the fatigue crack propagation zone shows several microcracks. The catastrophic failure area is shown in another SEM micrograph, and several dimples and voids can be seen, characteristic of a ductile fracture.

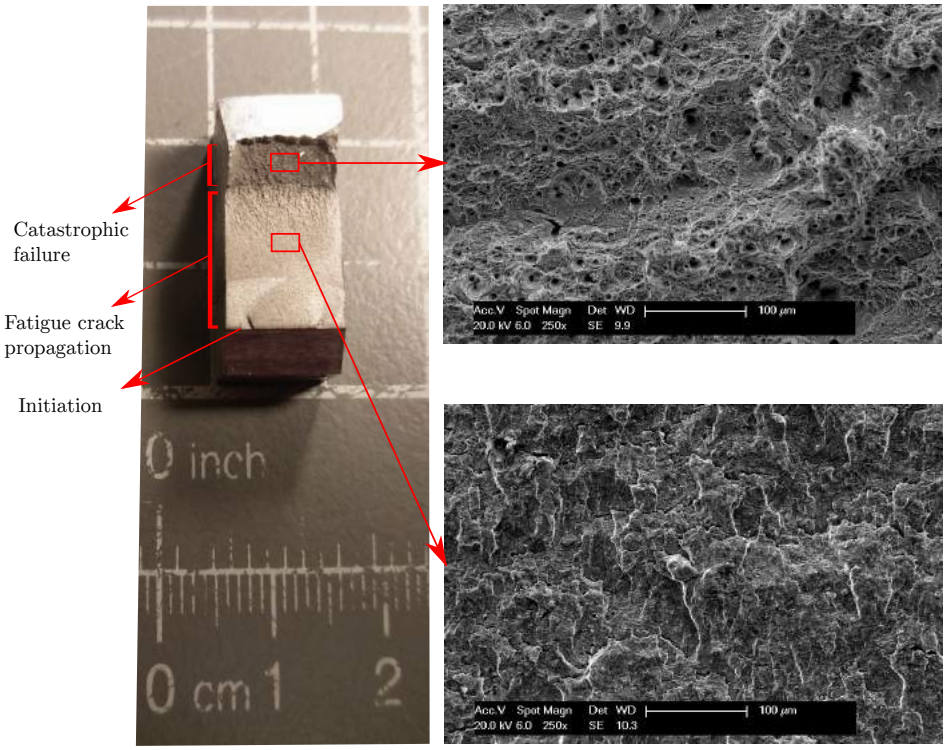

Figure 4.6: Fatigue crack photo and SEM micrographs showing different regions of a EN24T steel sample.

Figure 4.7 shows both the fatigue crack propagation area and the catastrophic failure area in greater detail. From Figure 4.7a, it is possible to identify the striation features and secondary cracking, characteristic of fatigue failure. In the catastrophic area, several dimples can be observed, some containing MnS inclusions. The final mode of failure of all samples was ductile failure.

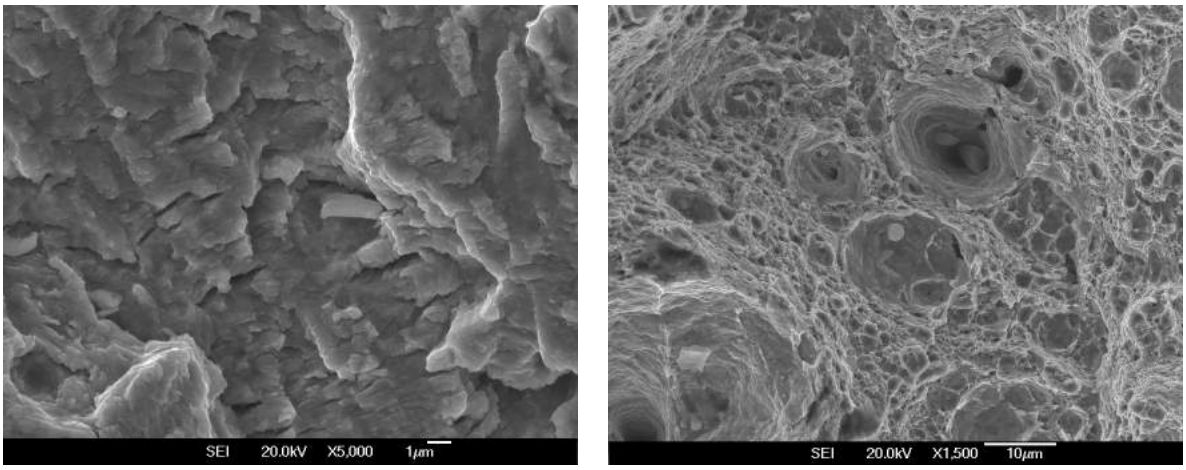

(a) (b)

Figure 4.7: SEM micrographs of: fatigue crack growth area showing striations and secondary cracking (a), and catastrophic failure area showing dimples (b).

- **EN24T steel**

The results of the EN24T steel samples tested at 0.25 Hz are shown in Table 4.3, whereas Table 4.4 shows the results of the samples tested at 1.00 Hz.

Table 4.3: Paris-Erdogan law parameters of the three EN24T steel samples tested at 0.25 Hz.

Sample	**Number of cycles**	**m**	**C** $(\mathrm{m}/(\mathrm{cycle} \cdot \mathrm{MPa} \cdot \sqrt{\mathrm{m}}))$
EN24T-25-1	50,265	2.84	6.47×10^{-12}
EN24T-25-2	35,716	2.98	5.52×10^{-12}
EN24T-25-3	37,702	2.75	2.75×10^{-12}

Table 4.4: Paris-Erdogan law parameters of the three EN24T steel samples tested at 1.00 Hz.

Sample	**Number of cycles**	**m**	**C** $(\mathrm{m}/(\mathrm{cycle}\cdot\mathrm{MPa}\cdot\sqrt{\mathrm{m}}))$
EN24T-100-1	33,065	3.29	4.55×10^{-12}
EN24T-100-2	32,739	3.26	2.32×10^{-12}
EN24T-100-3	35,430	3.04	4.84×10^{-12}

A comparison between crack size, obtained via the DCPD method, versus the cumulative acoustic emission energy of all six samples is shown from Figure 4.8 to Figure 4.10.

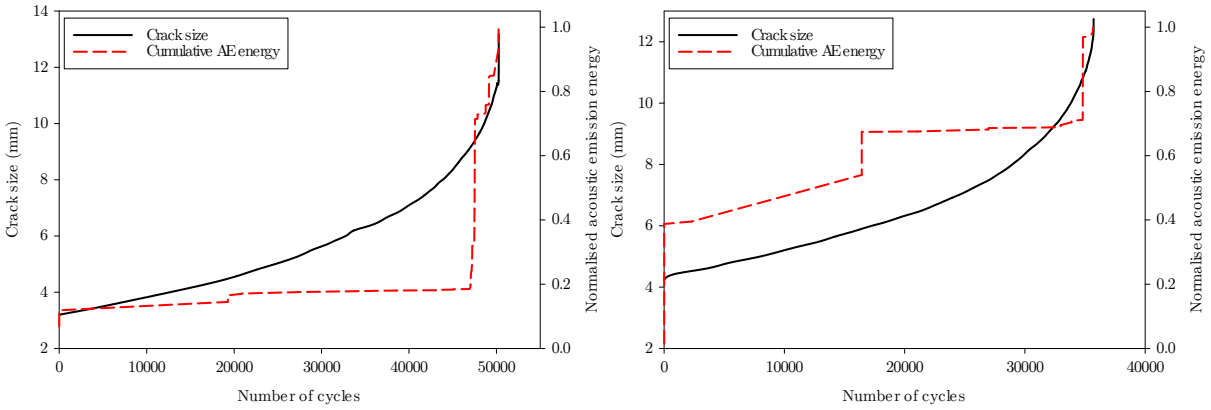

Figure 4.8: Comparison between DCPD and AE energy of sample EN24T-25-1 (a), and sample EN24T-25-2 (b).

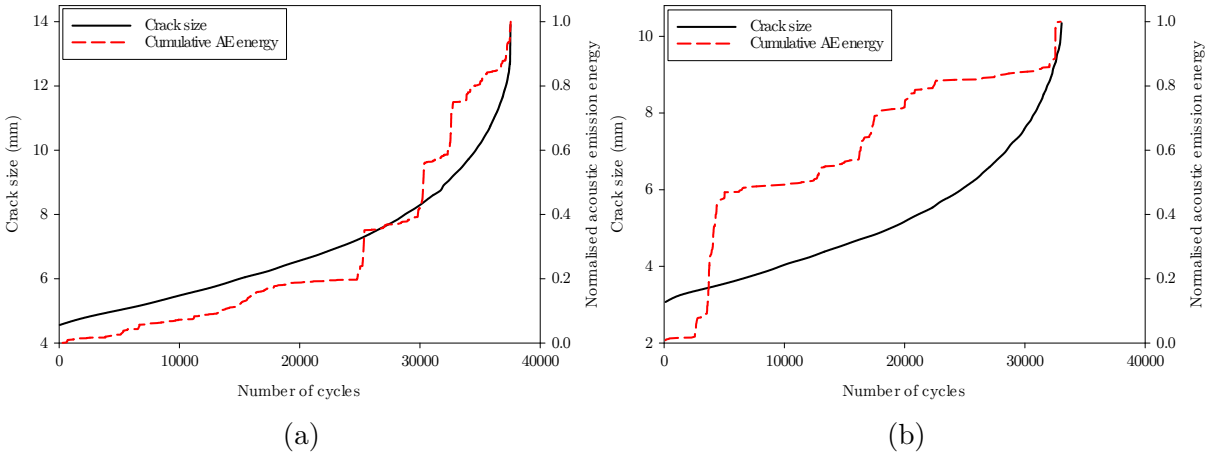

Figure 4.9: Comparison between DCPD and AE energy of sample EN24T-25-3 (a), and sample EN24T-100-1 (b).

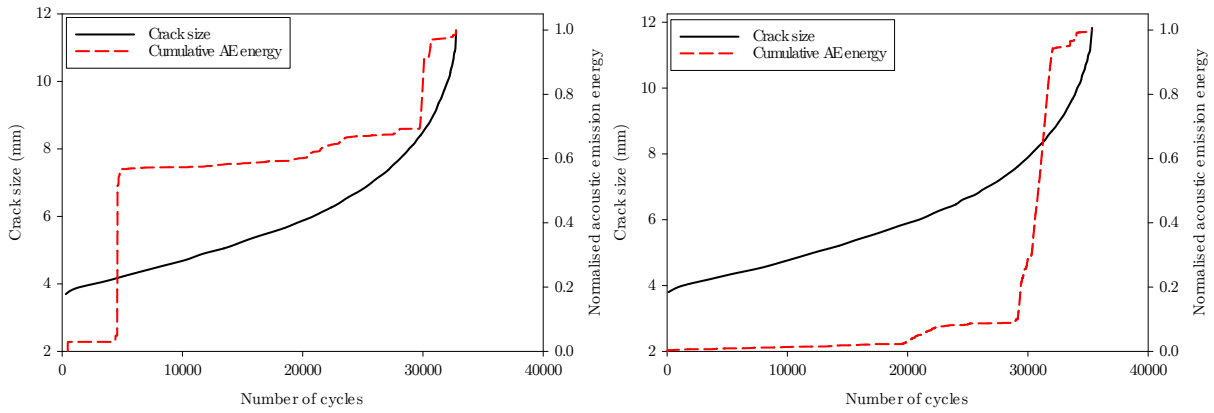

Figure 4.10: Comparison between DCPD and AE energy of sample EN24T-100-2 (a), and sample EN24T-100-3 (b).

Sample EN24T-25-3 shows the best correlation between the crack size and cumulative AE energy. However, this was not the case for the majority of the samples. Some samples, for example EN24T-25-1 and EN24T-100-3, undergo a quiet period for the majority of the test, and most acoustic emission activity is detected close to fracture.

Samples EN24T-25-2, EN24T-100-1 and EN24T-100-2, on the other hand, show a more step-like graph, with alternation of quiet periods and more energetic bursts. With the help of the DCPD data, it was possible to identify the crack size in which these bursts occurred. The fracture surfaces were then inspected with the help of an SEM in order to identify any events that could have been the origin of such bursts.

Figure 4.11 shows the fracture surface of the EN24T-25-3 sample at a crack size of 8 to 10 mm. Two triangular features could be distinguished from the fracture surface of the sample at this point, and are shown in Figure 4.11. These features have a significant crack at the base of the triangle, which could generate strong AE signals. From the DCPD data, the first highlighted signal burst occurs at a crack size of 8.1 mm, whereas the second one occurs at 9.3 mm, meaning they are approximately 1.2 mm apart. From the micrograph at the bottom left of Figure 4.11, the defects are located 1.3 mm from each other, corroborating the fact they could be the source of the AE signal bursts.

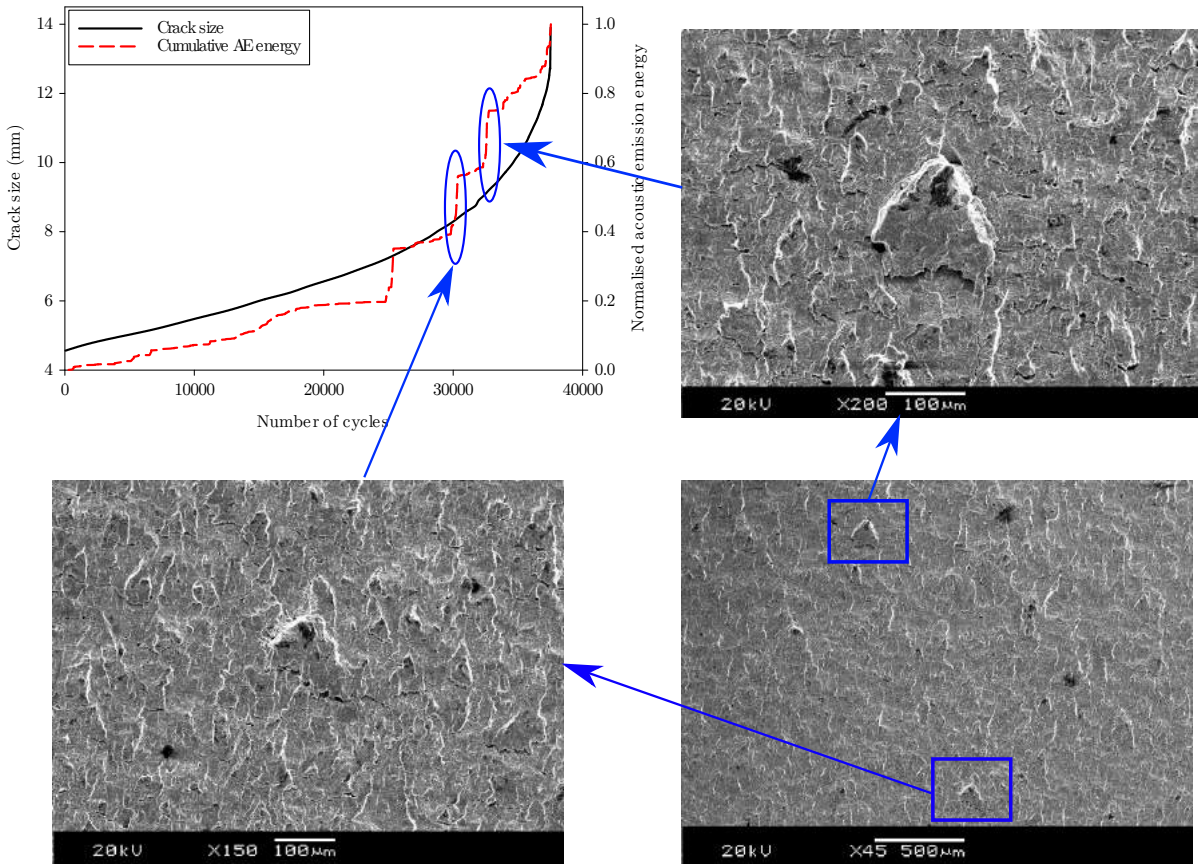

Figure 4.11: SEM micrographs of the fracture surface of sample EN24T-25-3 showing the origin of some of the AE cumulative energy bursts.

A similar defect was also found on sample EN24T-100-2, as shown in Figure 4.12. A triangle shaped feature with a significant crack at the root was found, which can explain the signal burst at 30,000 cycles. The crack is around 300 µm and both sides of the fracture surface are shown in Figure 4.12. It is possible to see that both sides would fit together.

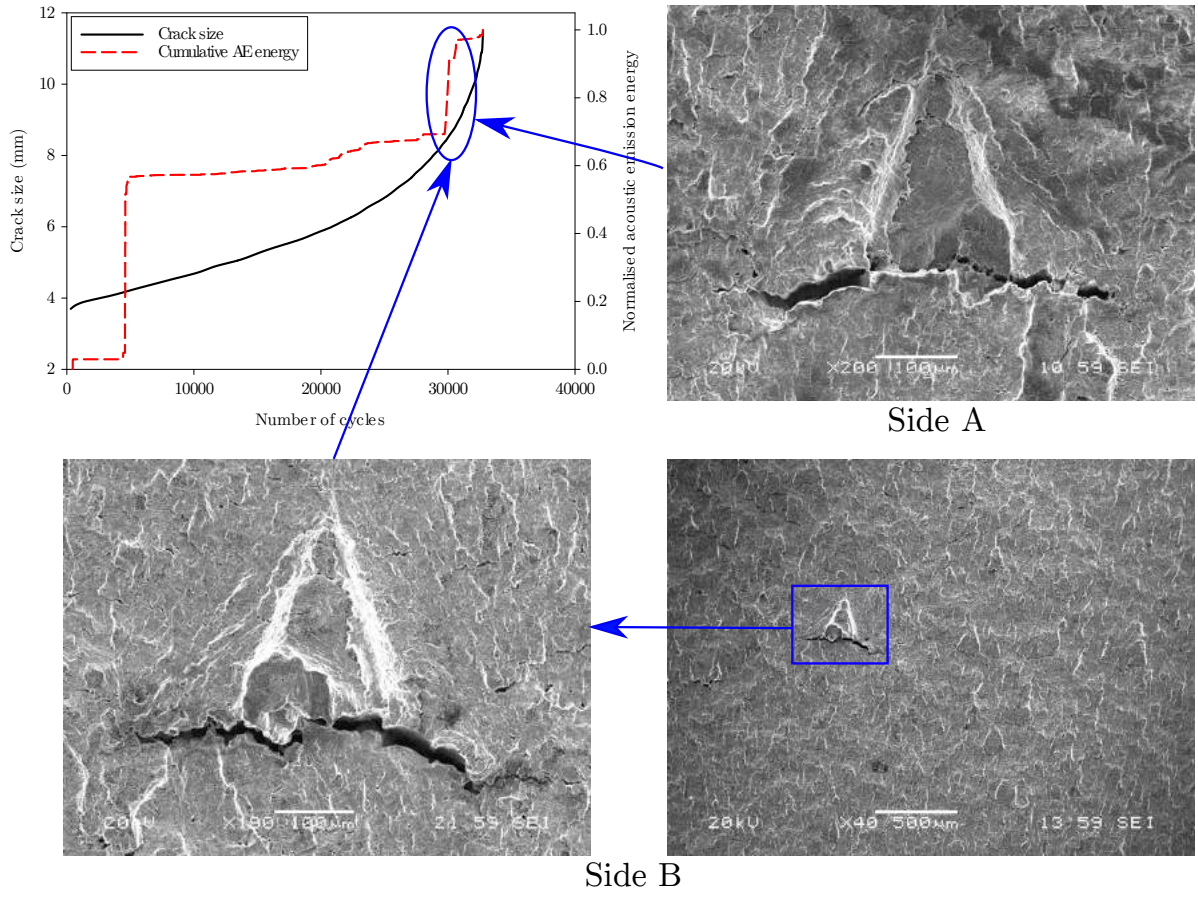

Figure 4.12: SEM micrographs of the fracture surface of sample EN24T-100-2 showing the origin of the AE cumulative energy burst.

For the sample 24-100-3, however, another type of defect was found. Looking at the first micrograph, at the top right of Figure 4.13, it is possible to identify a secondary crack, which appears to initiate at the edge of the sample. Zooming into the fracture surface of this crack, it is possible to notice a cleavage-like fracture surface, which is quite different from the striations that characterise the rest of the fracture surface of the sample. This was the only identifiable defect at this number of cycles and was likely the origin of the AE signals.

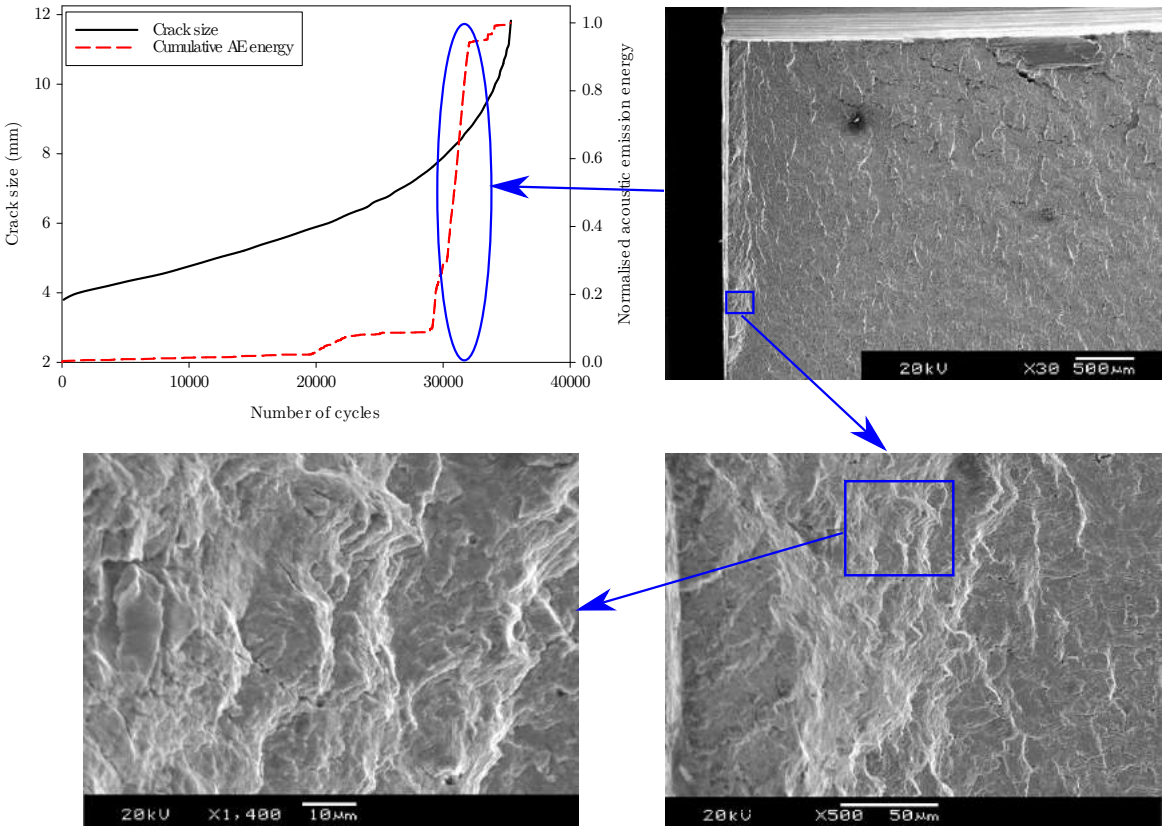

Figure 4.13: SEM micrographs of the fracture surface of sample EN24T-100-3 showing the origin of the AE cumulative energy burst.

The same pattern is seen in sample 24-100-1 (Figure 4.14). The final AE burst can be explained by the presence of a secondary crack growing from the edge of the sample, which also shows a cleavage-like fracture surface.

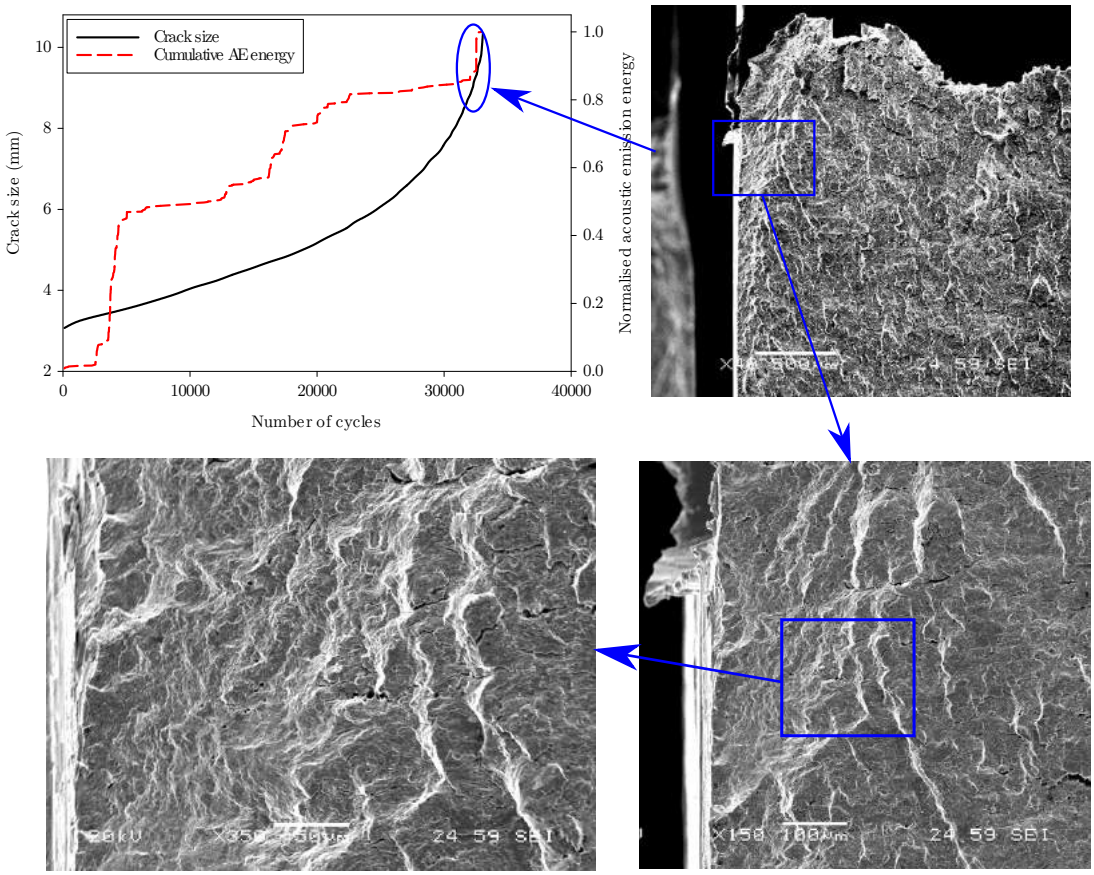

Figure 4.14: SEM micrographs of the fracture surface of sample EN24T-100-3 showing the origin of the AE cumulative energy burst.

- **EN40B steel**

The Paris-Erdogan law values of each one of the tested EN40B are summarised in Table 4.5. Similarly, graphs containing the crack size evolution and cumulative AE energy versus the number of cycles can be seen from Figure 4.15 to Figure 4.17.

Table 4.5: Paris-Erdogan law parameters of all EN40B steel samples tested at 1.00 Hz.

Sample	**Number of cycles**	**m**	**C** $(\mathrm{m}/(\mathrm{cycle}\cdot\mathrm{MPa}\cdot\sqrt{\mathrm{m}}))$
EN40B-100-1	66,840	3.29	2.59×10^{-11}
EN40B-100-2	48,247	3.26	2.17×10^{-11}
EN40B-100-3	60,785	3.04	2.33×10^{-11}
EN40B-100-4	61,884	3.29	2.32×10^{-11}
EN40B-100-5	45,142	3.26	2.26×10^{-11}
EN40B-100-6	59,772	3.04	2.47×10^{-11}

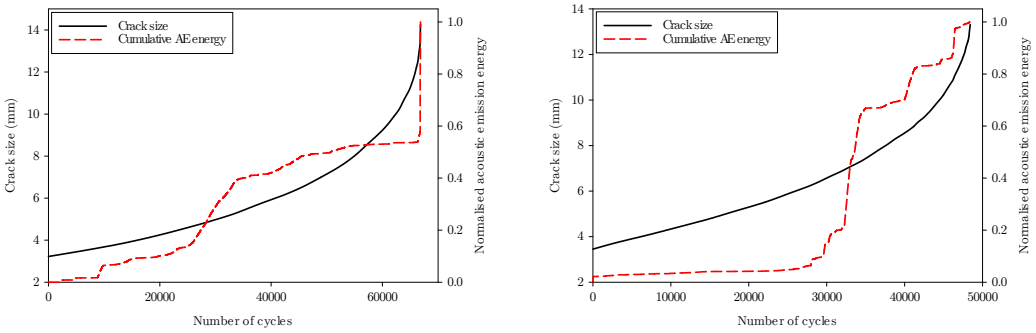

(a) (b)

Figure 4.15: Comparison between DCPD and AE energy of sample EN40B-100-1 (a), and sample EN40B-100-2 (b).

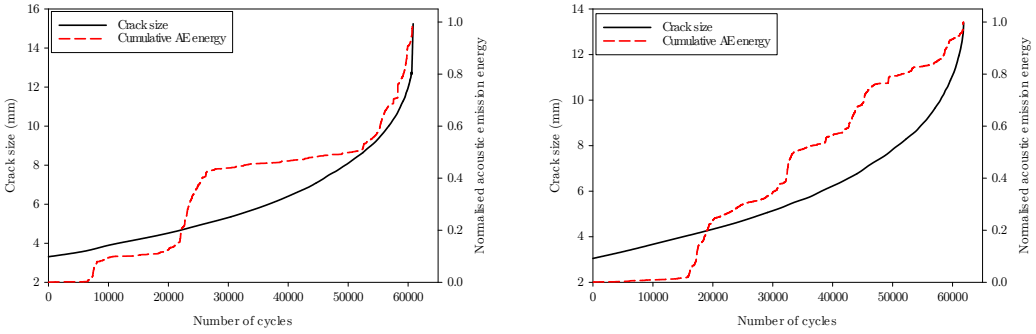

(a) (b)

Figure 4.16: Comparison between DCPD and AE energy of sample EN40B-100-3 (a), and sample EN40B-100-4 (b).

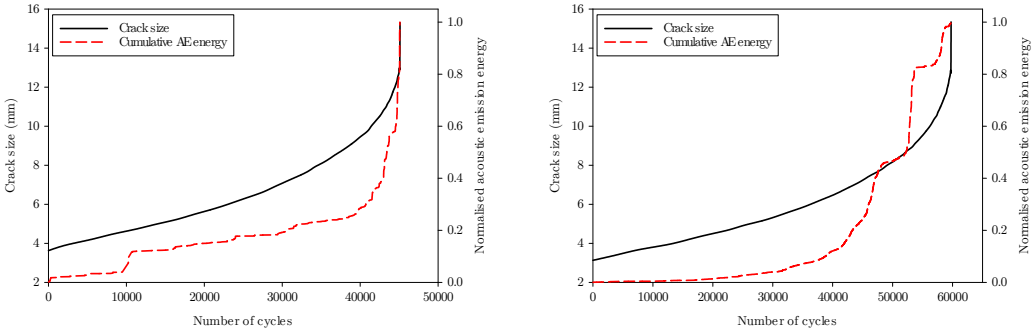

(a) (b)

Figure 4.17: Comparison between DCPD and AE energy of sample EN40B-100-5 (a), and sample EN40B-100-6 (b).

In the case of the EN24T steel, only a few samples presented a good correlation between crack size and cumulative AE energy, namely EN40B-100-1 and EN40B-100-6. The remaining samples either present sudden increases in the cumulative energy or present a more step-like increase, differently from the steady evolution seen in the crack size obtained by DCPD.

The origin of some of the AE bursts is shown in the following SEM micrographs. Sample EN40B-100-1 (Figure 4.18), similarly to sample EN24T-100-1, shows a secondary crack which has an origin at the side of the sample. The surface of this crack also has a cleavage-like fracture surface and is likely the origin of the AE burst.

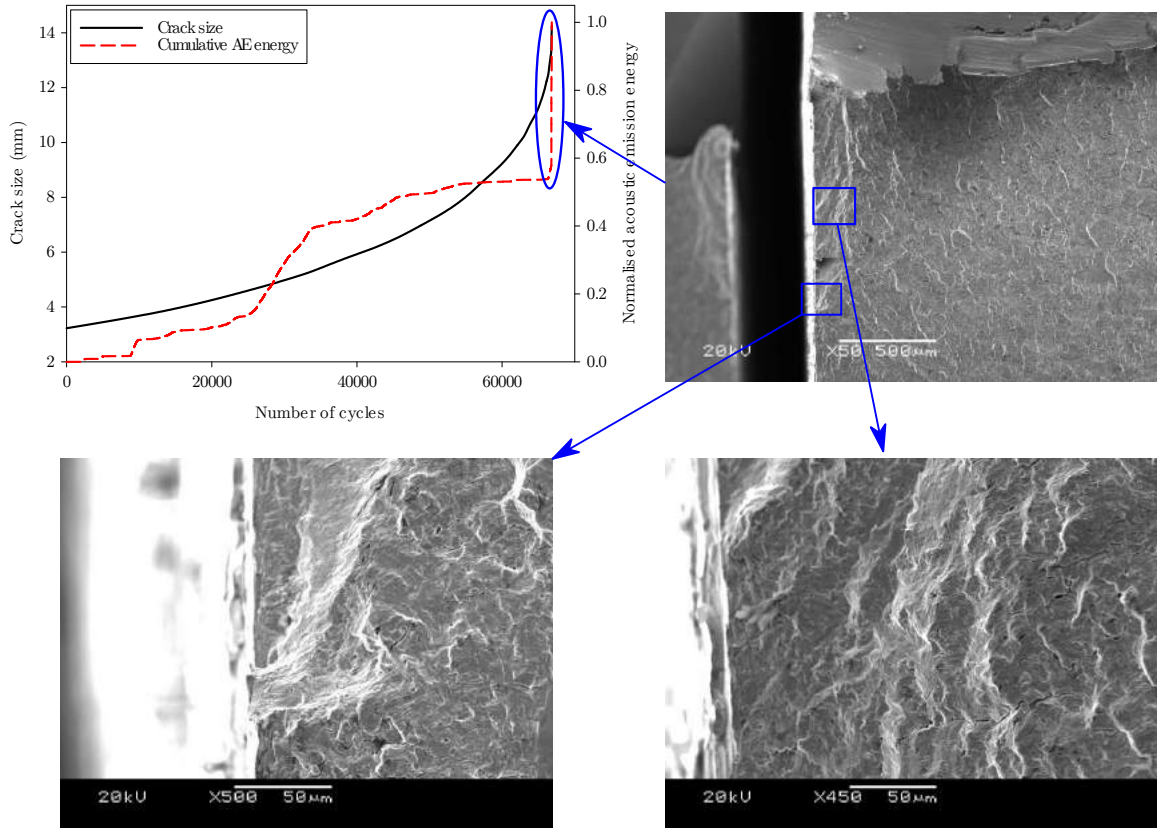

Figure 4.18: SEM micrographs of the fracture surface of sample EN40B-100-1 showing the origin of the AE cumulative energy burst.

On sample EN40B-100-3, only the origin of one AE burst was identified. By comparing the DCPD data and measurements from the image, this was identified as the first AE burst. Its origin is from a crack of a semi-circular shape, as shown in Figure 4.19. The

crack is around 100 µm long and was detected at 10,000 cycles.

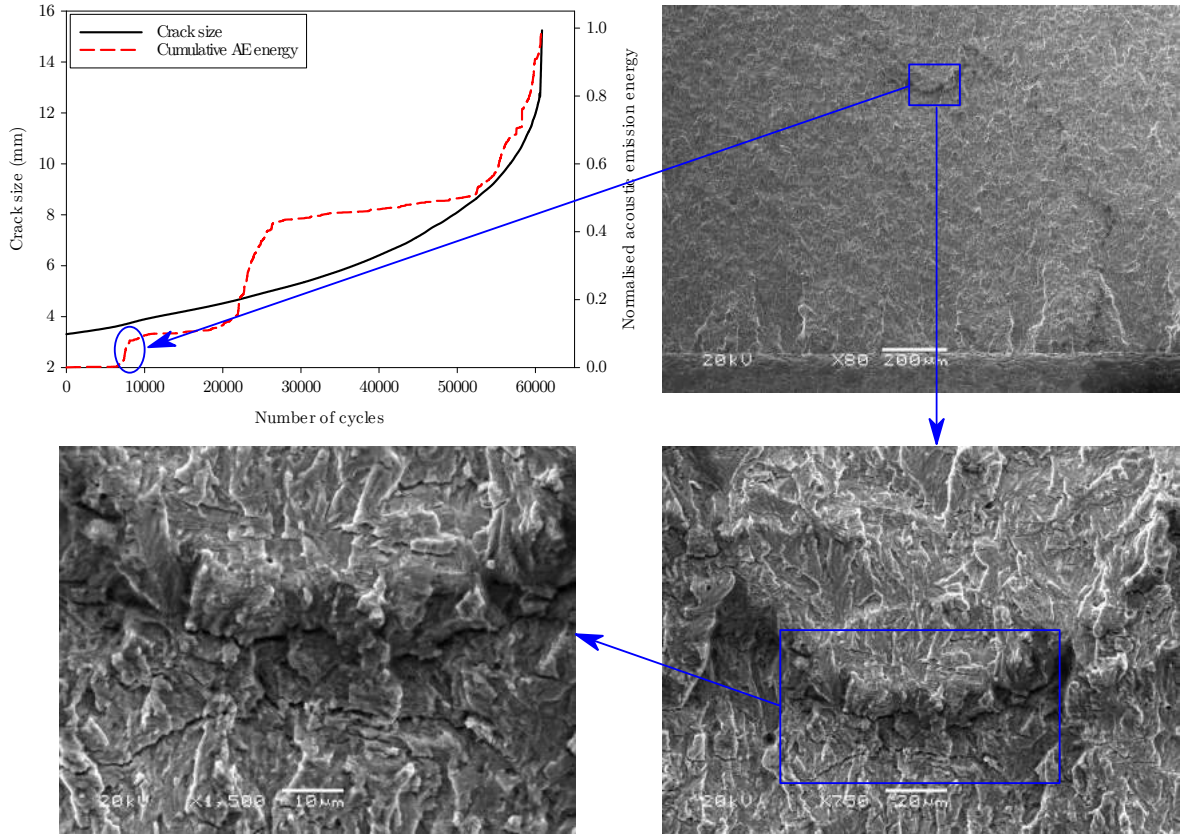

Figure 4.19: SEM micrographs of the fracture surface of sample EN40B-100-3 showing the origin of the AE cumulative energy burst.

More information could be obtained from sample EN40-100-6 (Figure 4.20). The final burst was also identified to be from a side crack with a cleavage-like surface. However, the first burst, at a crack size of around 7.5 mm, was found to be originated by the inclusion in the bottom left SEM micrograph. The EDS revealed it to be mostly iron (52.7%), carbon (25.5%), and chromium (12.4%). Several cracks can be found at the inclusion site. The middle AE burst was identified as a rougher area with cracks around it, similar to the triangular features found on the EN24T samples.

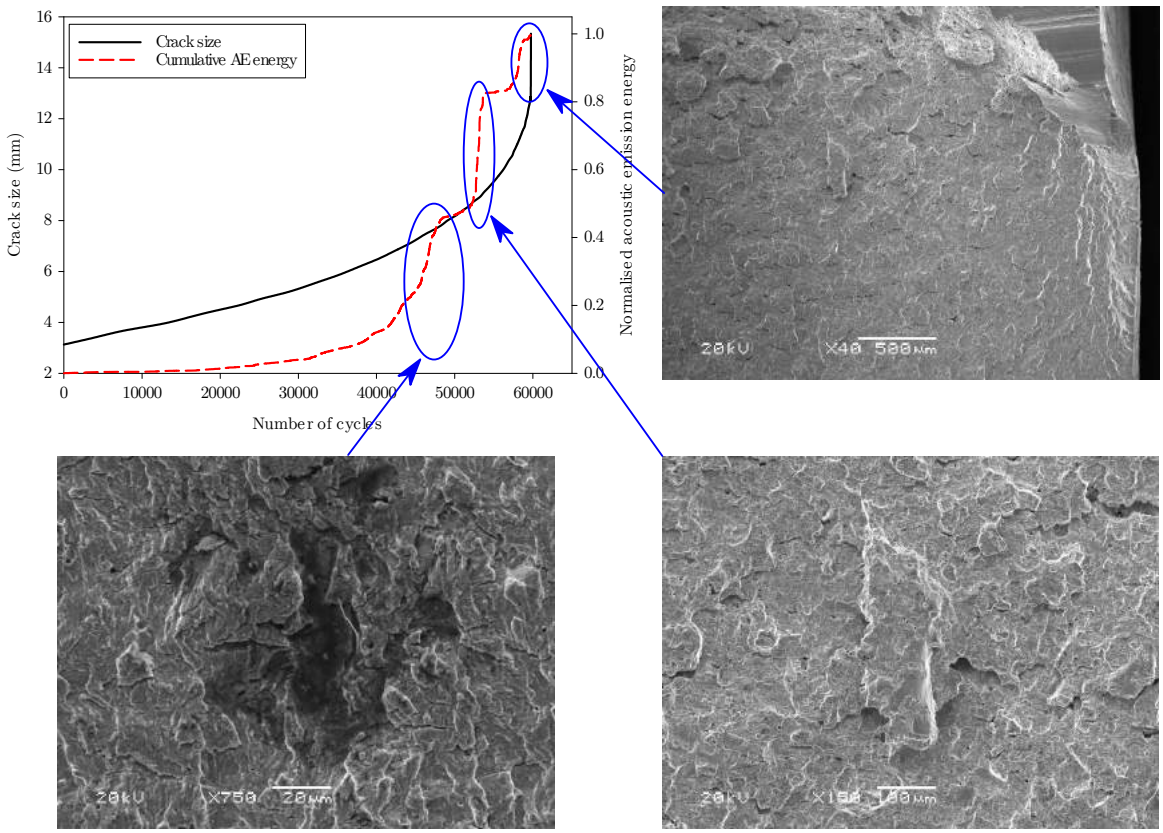

Figure 4.20: SEM micrographs of the fracture surface of sample 100-6 showing the origin of the AE cumulative energy burst.

4.2 TENSILE TESTING

The tensile tests were carried out according to the provisions of the ASTM E8 standard [171]. An electro-mechanical testing machine manufactured by Zwick Roell, model 1484 was employed. Some samples had the acoustic emission activity arising from the testing process monitored using the same PAC AE system as in the fatigue crack growth tests. The only changes applied to the previous setup was the substitution of the R50α sensors with PICO sensors, also manufactured by PAC. The PICO sensors were chosen due to their much smaller diameter of only 5 mm since the R50α sensors would have been too big for the samples and a coupling of satisfactory quality would not have been possible. Unfortunately, due to the small size of the samples used, the extensometer and acoustic emission sensors could not be used at the same time. The AE parameters used during the tensile tests are shown in Table 4.6.

Table 4.6: AE parameters of the tensile test.

AE parameter	**RCF test**
Threshold	40 dB
Pre-Amplification level	40 dB
Analogue filter	0.1 - 1 MHz
Sampling rate	5 MSPS
Pre-Trigger	256 µs
Length	10 k
Peak Definition Time	600 µs
Hit Definition Time	1000 µs
Hit Lockout Time	2000 µs
Duration	25 ms

The samples were manufactured in a cylindrical shape, as shown in Figure 4.21, with a gauge diameter of 4 mm and a gage length of 18 mm. The strain rate was 10^{-3} s^{-1}.

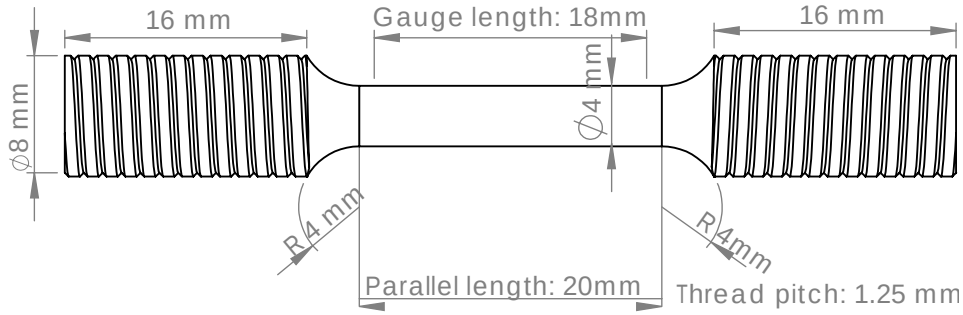

Figure 4.21: Dimensions of tensile test samples.

4.2.1 EN24T

Five samples in the untreated condition of the EN24T steel grade were tested. Of these, two samples (24U1 and 24U2) were tested with acoustic emission sensors mounted on them. The remaining samples (24U3, 24U4, and 24U5) were tested with the use of an extensometer.

Figure 4.22 shows the acoustic emission activity that was captured during the tensile test. As can be clearly seen there is little AE activity, mainly due to the high ductility and hence high level of plastic deformation exhibited by these samples.

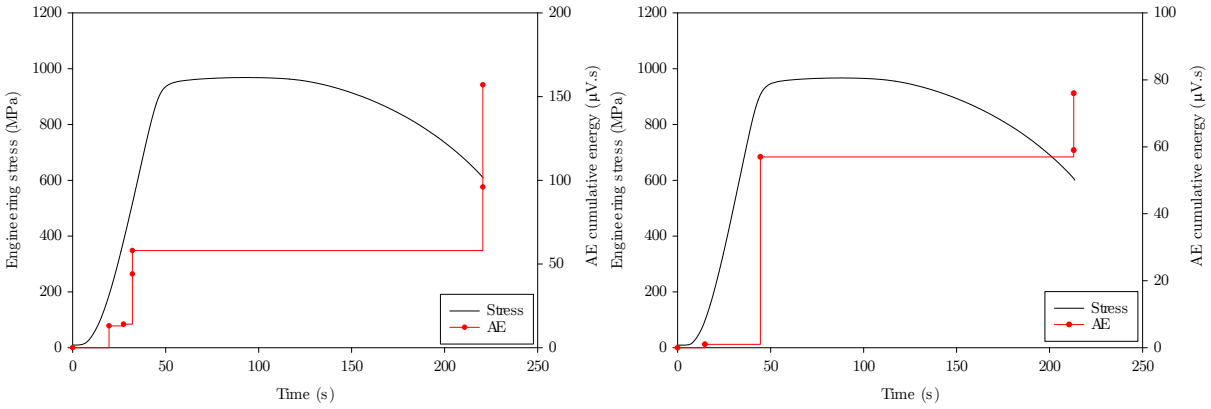

Figure 4.22: Engineering stress and cumulative acoustic emission energy versus time of samples 24U1 (a) and 24U2 (b).

The engineering stress-strain curves are shown in Figure 4.23. A summary of the test results, containing the yield strength of the material, ultimate tensile strength, elongation and elastic modulus is shown in Table 4.7.

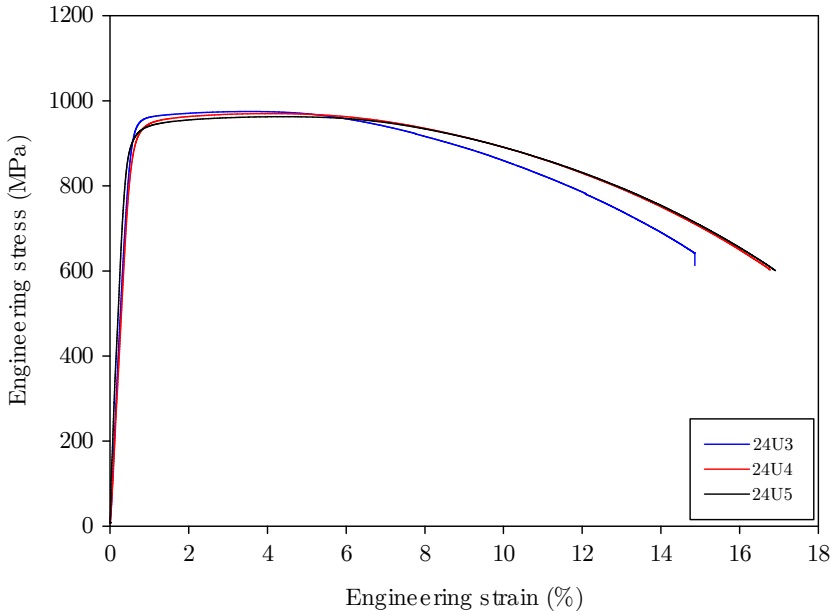

Figure 4.23: Engineering stress-strain curves of the EN24T untreated samples.

Table 4.7: Tensile test results of the untreated samples.

Sample name	**Yield strength (MPa)**		**Ultimate tensile strength (MPa)**	**Elongation (%)**	**Elasticity modulus (GPa)**
	Offset method (0.2%)	Extension-under-load method (0.5%)			
24U1	-	-	968.5	-	-
24U2	-	-	967.1	-	-
24U3	937	852.6	974.9	14.9	181.8
24U4	917	814.4	970.1	16.8	177.2
24U5	913	884.2	962.8	16.9	201.9
Average	**922 ± 10**	**850.4 ± 28.5**	**968.7 ± 3.9**	**16.2 ± 0.9**	**187.0 ± 10.7**

The failure strain of the EN24T was found to be approximately 16%. The ultimate tensile strength was measured to be in the range of 970 MPa. Figure 4.24 shows the ductile fracture of the 24U3 sample, where necking is clearly visible. Overall, the tests had good repeatability.

Figure 4.24: 24U3 sample showing ductile fracture (cup-cone).

Figure 4.25 shows the fracture surfaces at higher magnification. Dimples and voids, typical

of ductile fracture, can be clearly seen in the 24U3 sample.

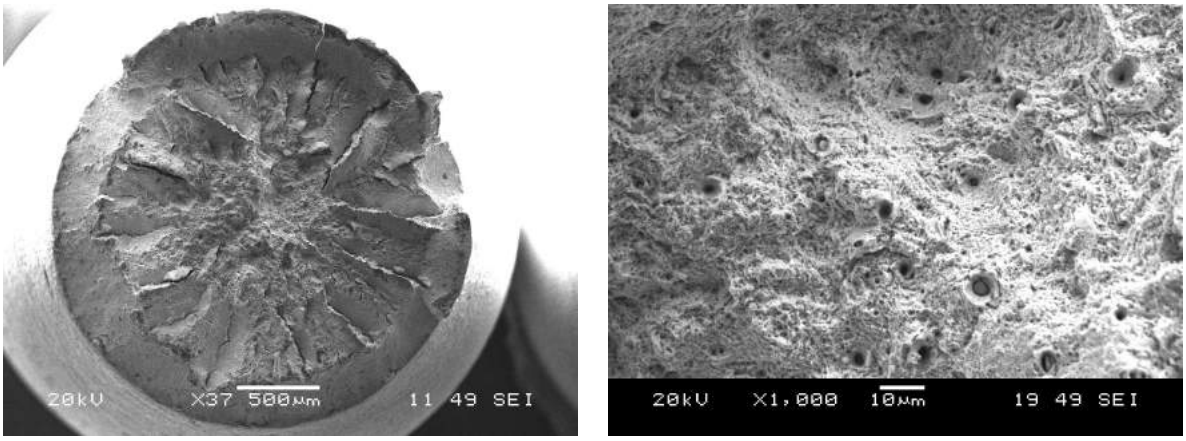

(a) (b)

Figure 4.25: SEM micrographs showing the fracture surfaces of the 24U3 sample at different magnifications.

A great number of voids in the 24U3 sample were created by MnS inclusions. One of them is shown in Figure 4.26. The void was created from the decohesion between the elongated inclusions and the parent metal.

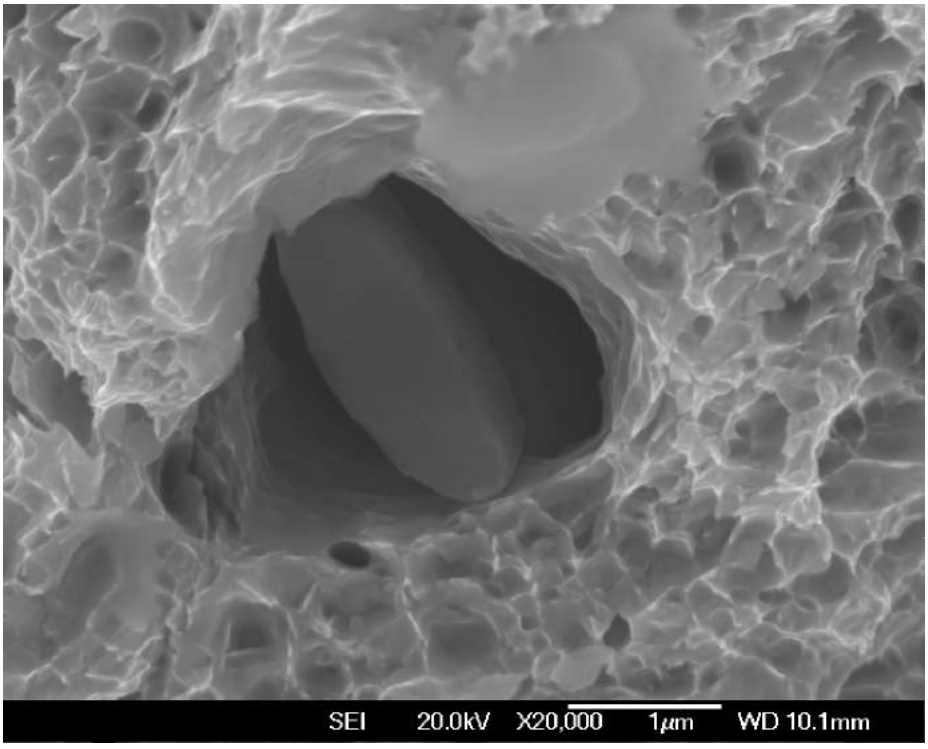

Figure 4.26: SEM micrograph showing a void formed by the decohesion of an MnS inclusion at the fracture surface of the 24U3 sample.

4.2.2 EN40B

Five samples of the EN40B steel grade in the untreated condition were tested. Of these, two samples (40U1 and 40U2) were tested with acoustic emission sensors coupled to them, and the remaining samples (40U3, 40U4, and 40U5) were tested with the use of an extensometer.

Figure 4.27 shows the acoustic emission activity that was captured during the tensile test for the first two samples.

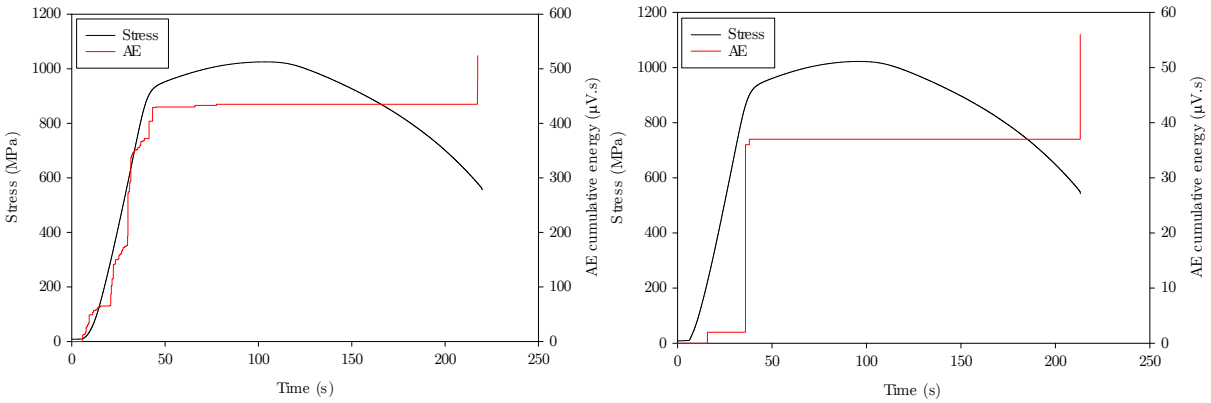

Figure 4.27: Engineering stress and cumulative acoustic emission energy versus time of samples 40U1 (a) and 40U2 (b).

Similarly to the EN24T samples, the untreated EN40B only showed AE activity during elastic deformation and fracture, with no signals being captured during plastic deformation. It is clear from Figure 4.27 that after yielding the next signal emitted by the samples is from the fracture process. This is due to the fact that during plastic deformation no detectable elastic stress waves are generated and hence acoustic emission activity recorded is minimal.

The engineering stress-strain curves for the samples tested with the extensometer are shown in Figure 4.28. A summary of the test results, containing the data for yield strength, ultimate tensile strength, elongation and elastic modulus is shown in Table 4.8.

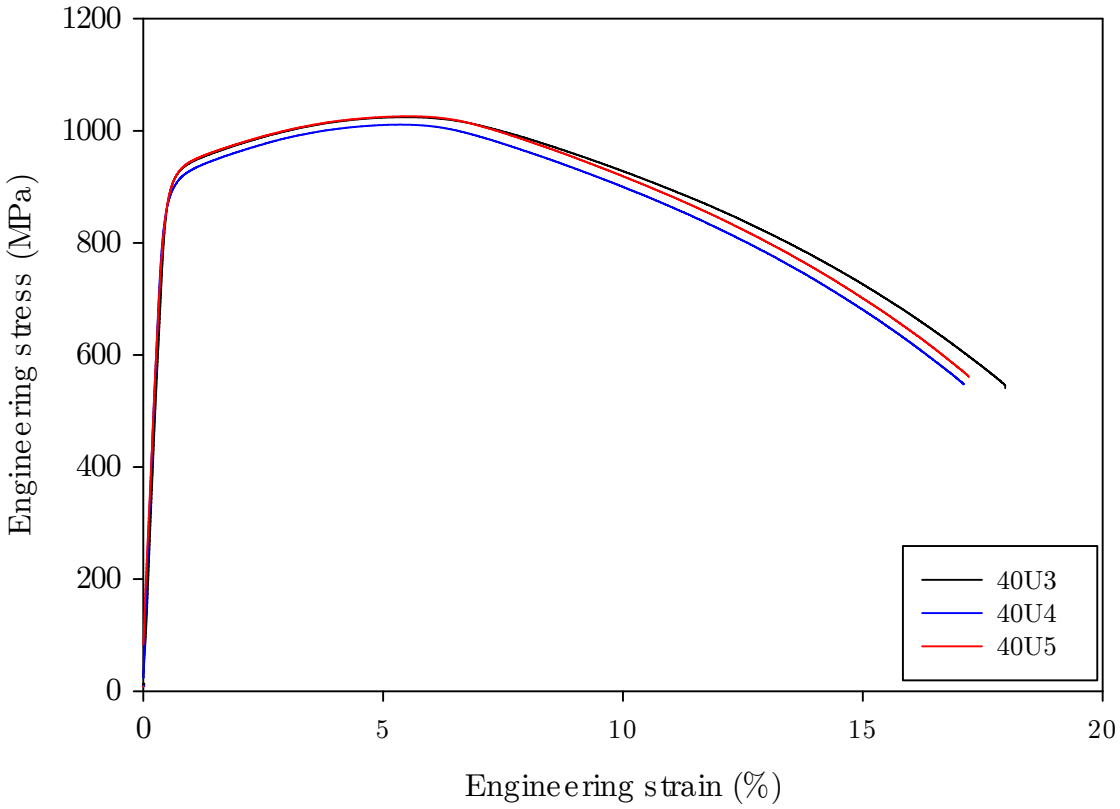

Figure 4.28: Engineering stress-strain curves of the untreated samples.

Table 4.8: Tensile test results of the untreated samples.

Sample name	**Yield strength (MPa)**		**Ultimate tensile strength (MPa)**	**Elongation (%)**	**Elasticity modulus (GPa)**
	Offset method (0.2%)	Extension-under-load method (0.5%)			
40U1	-	-	1025.4	-	-
40U2	-	-	1022.3	-	-
40U3	888	867.3	1024.4	18.0	197.9
40U4	865	866.4	1011.1	17.1	202.7
40U5	874	869.0	1026.0	17.2	188.8
Average	**876 ± 9**	**867.6 ± 1.1**	**1021.8 ± 5.5**	**17.4 ± 0.4**	**196.4 ± 5.7**

Both steel grades presented similar values for the elastic modulus as well for elongation. The EN40B has a higher ultimate tensile strength by approximately 50 MPa when

compared with the EN24T, while the EN24T has a superior yield strength (by the offset method) by approximately 50 MPa. Overall, the tests had good repeatability.

The untreated EN40B also presented necking and the final fracture was a typical cup-cone fracture. The fracture surface of the 40U3 sample can be seen in Figure 4.29a. Similarly to the EN24T steel, several radial cracks can be seen.

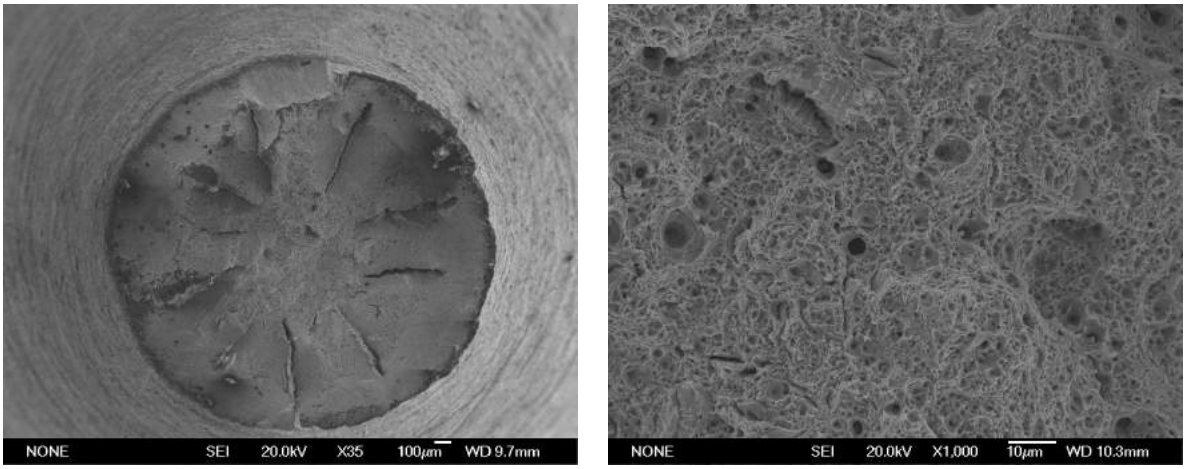

(a) (b)

Figure 4.29: SEM micrographs showing the fracture surfaces of the 40U3 sample.

Figure 4.29b shows the fracture surface at higher magnification. Dimples and voids, typical of ductile fracture, can be seen in the 40U3 sample.

Several voids in the 40U3 sample were created by MnS inclusions likewise the EN24T. Some of them are shown in Figure 4.30. The voids were created from the decohesion between the elongated inclusions and the parent metal.

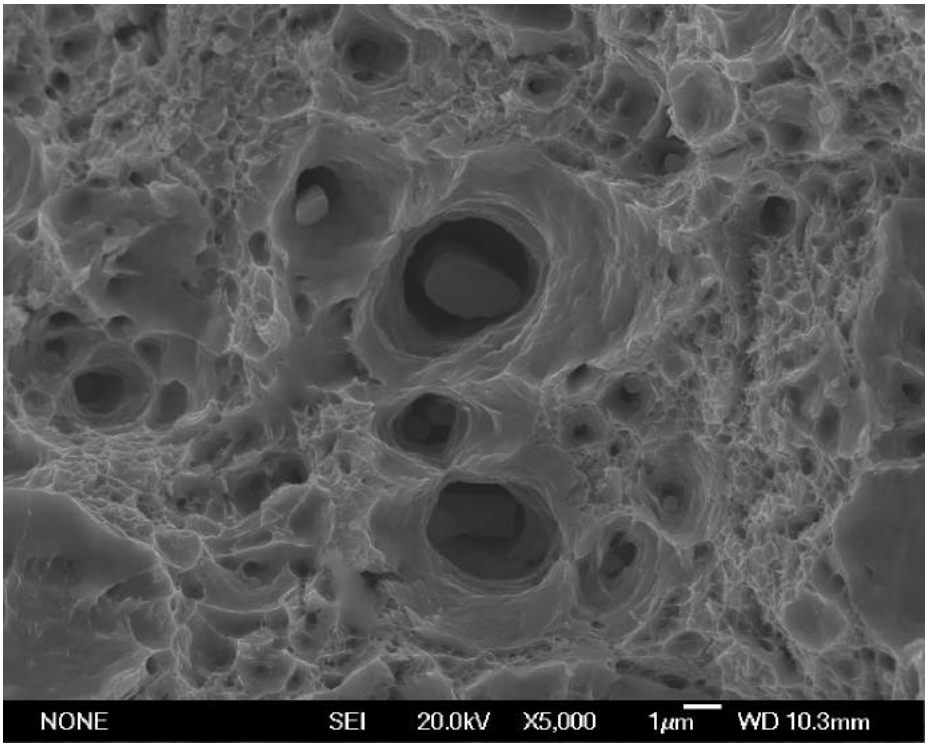

Figure 4.30: SEM micrograph showing voids formed by the decohesion of MnS inclusions at the fracture surface of the 40U3 sample.

4.3 SUMMARY

Both EN24T and EN40B steel grades were found to have similar mechanical properties after mechanical tests were carried out. The EN40B had a slightly lower crack growth rate than the EN24T, however, the results are still comparable. AE monitoring was successfully employed on the the fatigue crack growth samples, but it did not correlate well with the crack size obtained with DCPD. Instead, sharp rises in the AE energy were observed in most tested samples. These could be correlated with defects in the fracture surface most of the time, showing the AE technique is very sensitive to small defects and crack growth.

The tensile tests, on the other hand, did not show much AE activity for the untreated steels. This is mainly because the EN24T and EN40B plastically deformed and failed by void nucleation, in a classic cup-cone fracture. The EN24T and EN40B have similar tensile properties, and the tests had good repeatability.

CHAPTER 5

ROLLING CONTACT FATIGUE

5.1 EXPERIMENTAL

Wheel-on-wheel tests are commonly used to simulate the kinematic conditions of a gear pair in a less complex and inexpensive way when compared with FZG tests. Even though wheel-on-wheel tests do not have the complex geometry of gears, they generally have a good correlation with tests conducted on gears [172].

The tribometer used in this study was an AMSLER A135 wheel-on-wheel universal tribometer. A schematic diagram of the AMSLER A135 device is shown in Figure 5.1.

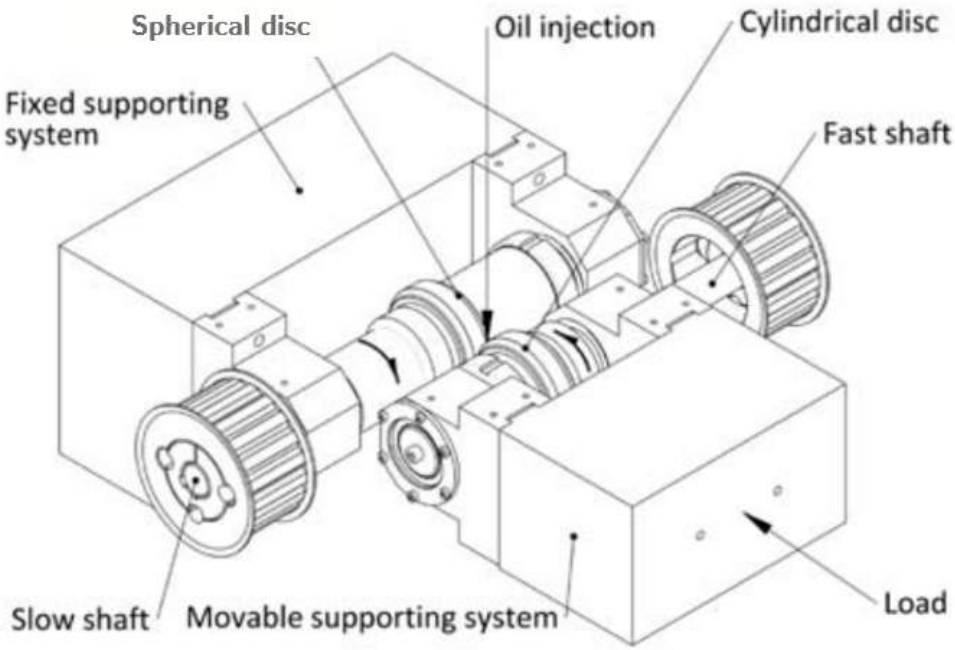

Figure 5.1: Schematic diagram of the AMSLER A135 tribometer. Source: [172].

The test configuration consists of two specimens rotating against one another. The upper specimen rotates with a speed of 360 rpm and the lower specimen at 400 rpm. A load

is then applied to one of the wheels. The test can be run in both dry or lubricated conditions. In the case of lubricated conditions, the steel sample was partially submerged in an oil container.

Zhou [173] used the same machine to test two steel wheels under lubricated conditions, at the maximum load possible, generating 1 GPa of contact stress, for more than 350 hours (or 8.4 million cycles). Little to no wear was observed, hence running the test for longer would make the experiments impractical due to time constraints.

Therefore, to accelerate the damage initiation, the contact stress had to be increased. Since the load was already at maximum, the solution selected to address this problem was to use a counter wheel made of tungsten carbide (WC). WC is an even harder and more wear resistant material than the samples tested. The WC wheel was manufactured having a spherical contour in its surface in order to increase the contact stress, so that the wear could occur at a faster rate. The design of both the WC counter wheel and the steel samples can be seen in Figures 5.2 and 5.3, respectively.

The WC wheel was chosen to be the slowest rotating wheel in order to achieve a slip ratio of 18%. Considering the slip ratios between the flanks of spur gears are usually in between 0% and 20% the slip ratio achieved was within acceptable limits [174]. The slip-ratio (g) can be calculated with the equation 5.1 where r_1 and r_2 are the radii of the wheels, and ω_1 and ω_2 are their rotational speeds.

$$g = 200\frac{(r_1\omega_1 - r_2\omega_2)}{(r_1\omega_1 + r_2\omega_2)} \tag{5.1}$$

In order to make the tests comparable and to achieve the same surface roughness for all tested wheels, each sample was polished to an average roughness of 0.5 µm. Figure 5.4 shows the surface of both wheels before the tests were conducted.

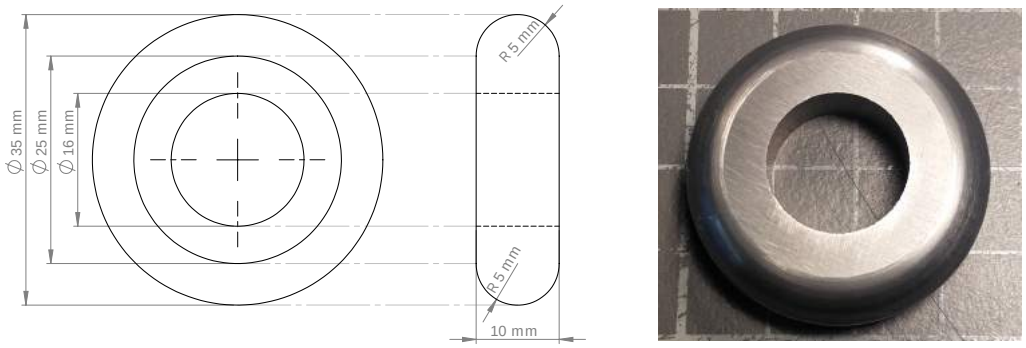

(a) (b)

Figure 5.2: WC carbide wheel drawing (a); WC carbide wheel specimen (b).

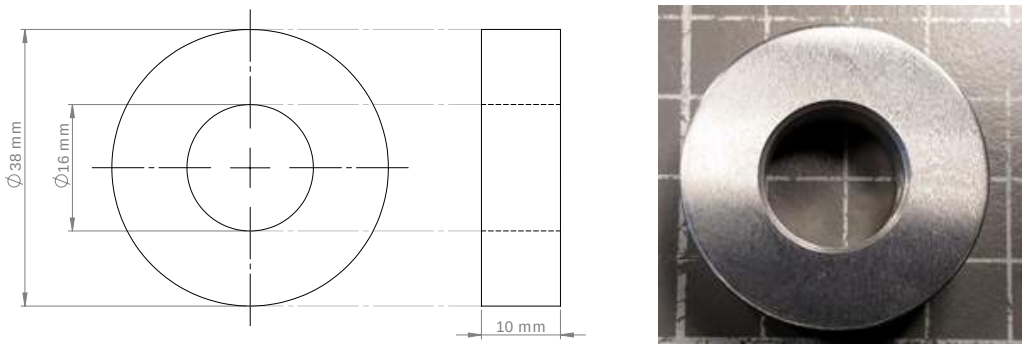

(a) (b)

Figure 5.3: Steel wheel drawing (a); Steel wheel specimen (b).

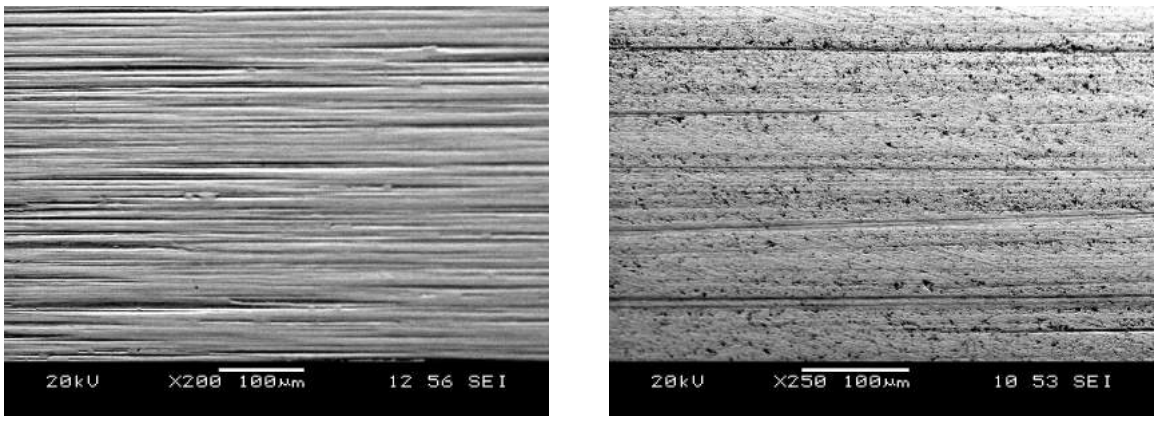

(a) (b)

Figure 5.4: SEM micrographs of the EN24T wheel (a), and WC wheel (b), in their initial condition.

The RCF tests were performed under lubricated conditions, at room temperature and with ambient humidity. For lubrication during testing 15W-40 Shell engine oil was employed.

Before and after each test, the wheels were ultrasonic cleaned, dried and weighed in a balance with a measurement sensitivity of 0.1 mg.

The samples tested were monitored by the same AE system used on the fatigue crack growth and tensile tests, with one R50α sensor coupled to the oil cage of the tribometer. The AE parameters for the RCF tests can be seen in Table 5.1.

Table 5.1: AE parameters of the RCF test.

AE parameter	**RCF test**
Threshold	40 dB
Pre-Amplification level	40 dB
Analogue filter	0.1 - 1 MHz
Sampling rate	1 MSPS
Pre-Trigger	512 µs
Length	10 k
Peak Definition Time	300 µs
Hit Definition Time	600 µs
Hit Lockout Time	4000 µs
Duration	100 ms

The AE threshold was set to 40 dB. However, the noise and vibration level of the machine varied from test to test. The threshold remained unchanged, but whenever noise was detected above 40 dB, the noisy signals were manually discarded during data processing. This was achieved by simply disregarding any signals with an amplitude lower than the new threshold. This new threshold can be identified in the AE graphs as the smallest y-axis value.

The minimal load that can be applied in this tribometer is 200 N, which corresponds to the weight of the components that hold the upper wheel in place. Additional load can be applied up to a maximum of 2000 N.

The resultant contact area of the WC with a spherical contour and the cylindrical steel samples is an ellipse. In order to calculate the contact pressure, the reduced radii in the x and y coordinates must be calculated using equations 5.2 and 5.3, where r_{1x} and r_{1y} refer to the radii of the WC wheel, and r_{2x} and r_{2y} to the steel wheel. The

final reduced radii (r) is given by equation 5.4.

$$\frac{1}{r_x} = \frac{1}{r_{1x}} + \frac{1}{r_{2x}} \tag{5.2}$$

$$\frac{1}{r_y} = \frac{1}{r_{1y}} + \frac{1}{r_{2y}} \tag{5.3}$$

$$\frac{1}{r} = \frac{1}{r_x} + \frac{1}{r_y} \tag{5.4}$$

Additionally, the reduced elasticity modulus (E_r) has to be calculated by equation 5.5, where E_1 and ν_1 are the elasticity modulus and Poisson's ratio for the WC wheel, respectively, and E_2 and ν_2 correspond to the same for the steel wheel.

$$\frac{1}{E_r} = \frac{1-\nu_1^2}{E_1} + \frac{1-\nu_2^2}{E_2} \tag{5.5}$$

The ellipticity parameter is given by k_e (equation 5.6), and S_e is the elliptic integral of the second kind, which can be approximated by equation 5.7. The semi-minor (a_e) and semi-major (b_e) axes of the ellipse can then be calculated by Hertzian contact stress analysis following equations 5.8 and 5.9. The load applied is given by L [175].

$$k_e = 1.0339 \left(\frac{r_y}{r_x}\right)^{0.6360} \tag{5.6}$$

$$S_e = 1.0003 + \frac{0.5968 r_x}{r_y} \tag{5.7}$$

$$a_e = \sqrt[3]{\frac{3k_e^2 S_e L r}{\pi E_r}} \tag{5.8}$$

$$b_e = \sqrt[3]{\frac{3 S_e L r}{\pi k_e E_r}} \tag{5.9}$$

Finally, the maximum contact pressure (CP_{max}) can be calculated by equation 5.10.

$$CP_{max} = \frac{3L}{2\pi a_e b_e} \tag{5.10}$$

By using the values in Table 5.2, the contact pressure can be calculated as a function of the load.

Table 5.2: Parameters used for calculating contact pressure.

Sample	r_x (mm)	r_y (mm)	E (Gpa)	ν (-)
WC	5	17.5	650	0.2
EN24T	∞	19	187	0.3

The widely available finite element code "ABAQUS" was used to create a static finite element model to analyse the stress distributions between the sample and the counter-wheel. To increase computational efficiency, only one-sixth (or 60°) of each wheel was modelled. The steel wheel was fixed in all directions, while the counter-wheel was constrained in all but the y-direction. A reference point for each wheel was created at what would be the centre of the wheel. A coupling constraint was then made between the reference point and the internal surface of the wheel. The load was applied on the y-direction at the reference point of the counter wheel. A frictionless surface-to-surface contact interaction was established. Both wheels were meshed with C3D8 elements, and a mesh convergence analysis was conducted to guarantee the reliability of the results. The Young's modulus and Poisson's ratio used for each wheel can be seen in Table 5.2. The finite element model showing both wheels and the reference point constraints can be seen at Figure 5.5.

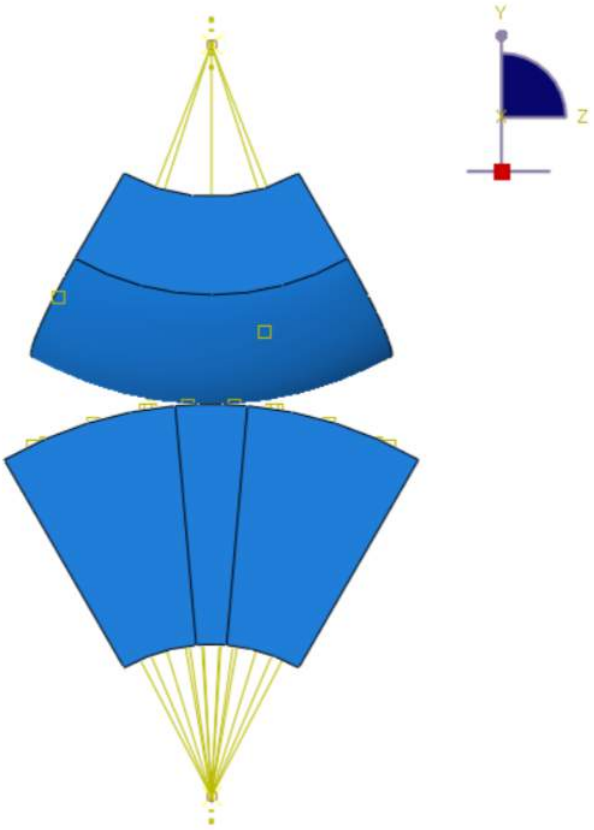

Figure 5.5: Finite element model of the RCF test, front view.

The simulation was run with different loads in the range that can be applied by the tribometer, which is from 200 N to 2000 N. A comparison between the finite element model and the equation 5.10 can be seen in Figure 5.6.

A good agreement between the Hertzian contact pressure equation and the simulation was found. The minimum contact pressure values (Hertzian) that can be achieved by this setup is 2.77 GPa and the maximum contact is 5.97 GPa. Therefore, by changing the applied force, any contact pressure value in this range can be achieved.

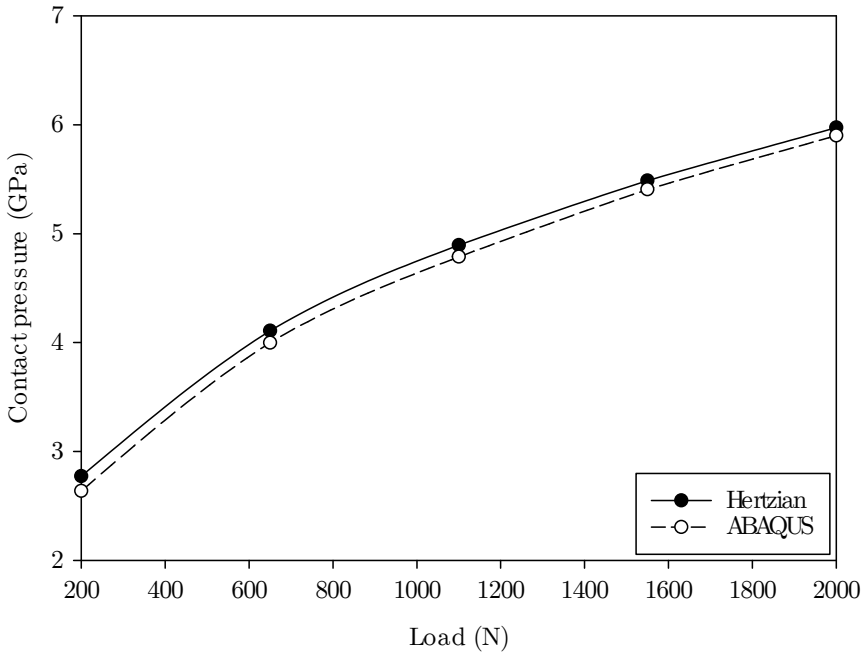

Figure 5.6: Comparison between Hertzian and finite element model contact stress values of an EN24T sample in contact with the WC wheel.

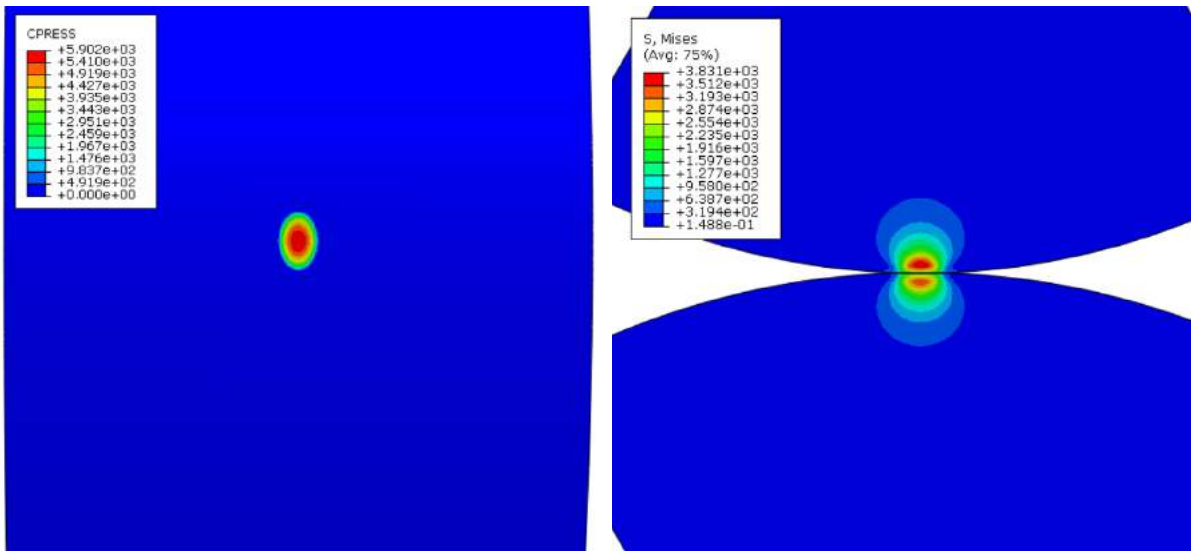

Figure 5.7: Contact stress (MPa) contour plot, top view (left). Von Mises stress (MPa) contour plot, cut from the x plane (right). Both images show the untreated wheel at a load of 2000N.

Figure 5.7 shows the ellipse resultant from the contact between the spherical WC wheel and the cylindrical untreated steel sample. Additionally, it shows the Von Mises stress

contour plot of a transversal cut of the x plane, showing that the highest stress concentrations are at the subsurface, right below the contact point of the wheels.

All samples in this study were tested with a load of 1200 N, which means the samples were subjected to a contact stress of around 5.0 GPa.

5.1.1 Experiment limitations

The WC wheels were manufactured by powder metallurgy in a spherical disc shape. Even with the use of powder densification techniques, there will always be the presence of pores in the finalised material. This is easily proven by comparing the weight of different WC discs. Their weight varies from 97.1 g to 98.1 g. Since powder metallurgy is a net-shape manufacturing process, the weight variation can only be explained by the presence of pores in the samples.

These pores can be seen in Figure 5.8. They are randomly distributed on the surface of the sample and will change the contact stresses and consequently wear behaviour of the tested steel samples. Due to the huge contact stresses to which the samples are subjected (over 5.0 GPa), the effect of these defects are amplified and can produce variations on the tests.

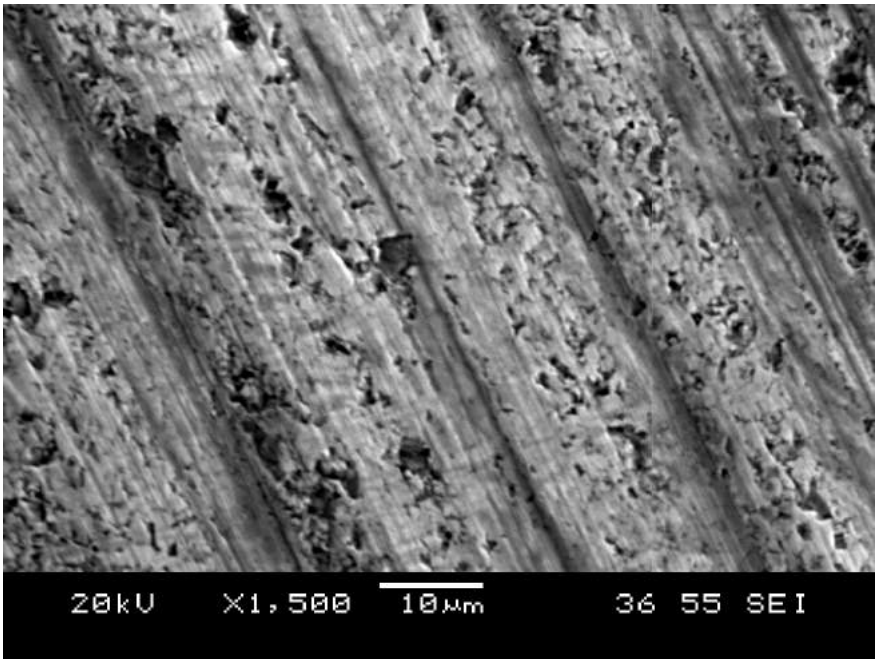

Figure 5.8: SEM micrograph of the WC wheel surface showing pores.

Another complicating factor is that even though the WC wheels are wear resistant, they will still eventually wear, as Figure 5.9 shows. This means that, ideally, new wheels should be used in each test, making experiments expensive. As the aim of the test is to be able to use the acoustic emission monitoring system to be able to detect failures under rolling contact fatigue conditions, WC wheels were reused in some cases. This means that the wear results cannot be quantitatively compared, however, they can still provide useful insight on the damage initiation and propagation.

WTGs can survive millions of cycles in operation, and thus the cut-off value for the RCF test was set to 2 million cycles, or until severe damage was observed. At 400 rpm, however, this is more than 80 hours of testing per sample. As the machine needed to be supervised at all times, the testing of a large number of samples was impractical due to time constraints of the present study. Therefore, the focus of this chapter is not on the quantitative assessment of wear resistance of the different treatments, but instead, on the correlation of the different types of defects detected and evaluated through acoustic emission signals obtained during testing.

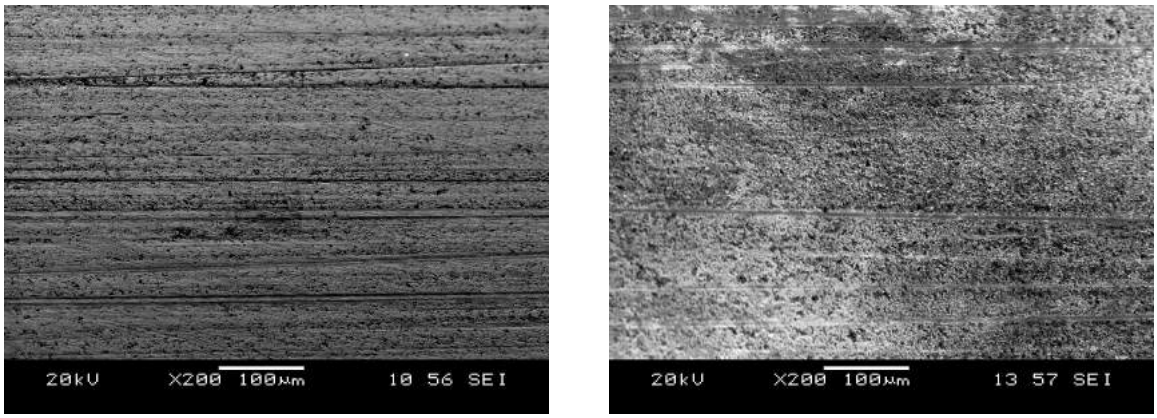

(a) (b)

Figure 5.9: SEM micrographs of the WC wheel before the test (a), and after 4.0 million cycles (b).

Finally, the large stresses generated plastic deformation on the steel samples tested. Such stresses are only commonly observed on wind turbine gears due to misalignment and/or overloading from severe wind gusts.

However, this test setup can still provide valuable information and fulfil the goals of this study, which are: to study the failure mechanisms of different coatings under RCF conditions, and verify if acoustic emission monitoring can be used to monitor and quantify damage evolution under these conditions.

5.2 RESULTS

5.2.1 EN24T untreated

Due to the similar mechanical properties of the EN24T and EN40B steel grades, the EN24T steel grade was randomly chosen to be the untreated steel grade tested. The first test was performed on the untreated EN24T steel under fully lubricated conditions, meaning that the steel samples were lubricated during the entire test. The acoustic emission system was used to monitor defects in the samples. Additionally, the test was also periodically interrupted for weighting and examination. The weight loss as a function of the number of cycles for the fully lubricated sample can be seen in Figure 5.10.

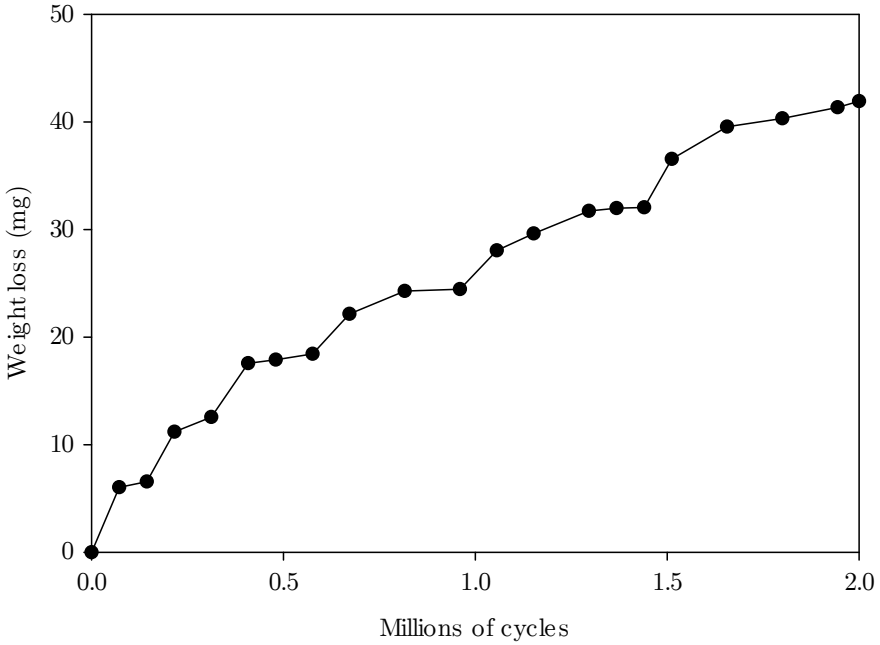

Figure 5.10: Weight loss versus number of cycles of the untreated fully lubricated sample.

It shows a linear relationship between the weight and number of cycles, however, the

amount of wear is negligible considering the sample is being subject to over 2 million cycles under 5 GPa of contact stress. The AE monitoring system, however, shows several signals, especially up to 0.5 million cycles. A more energetic signal was detected just before 1 million cycles, as shown in Figure 5.11. At this point, the test was stopped and the sample was taken to the SEM for examination.

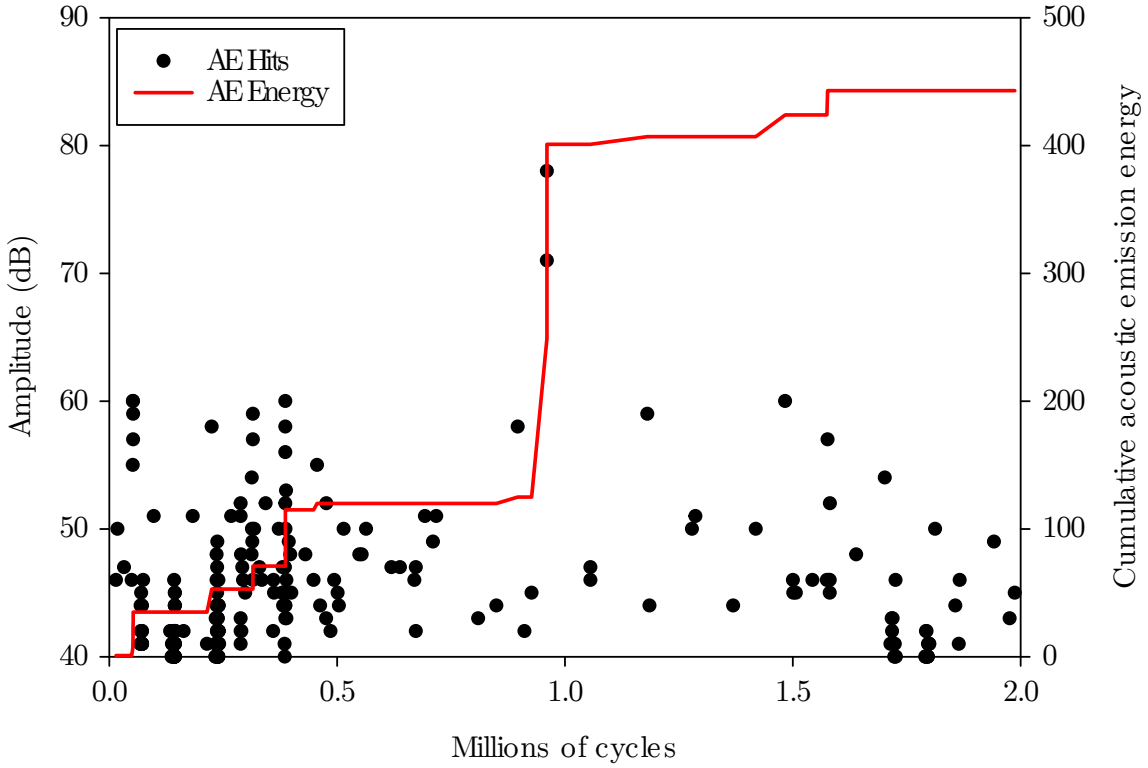

Figure 5.11: AE hits and cumulative energy of the fully lubricated untreated sample as a function of the number of cycles.

The SEM examination at 1 million cycles did not reveal any defects in the sample wear track, and thus, the test was allowed to proceed until its cut-off value of 2 million cycles had been reached. Figure 5.12a shows the sample after the end of the test. The wear track is very distinguishable, due to the depression created by plastic deformation. No defects are visible. The sample was then taken to the SEM, where it was thoroughly inspected, and again, no defects were found (Figure 5.12b).

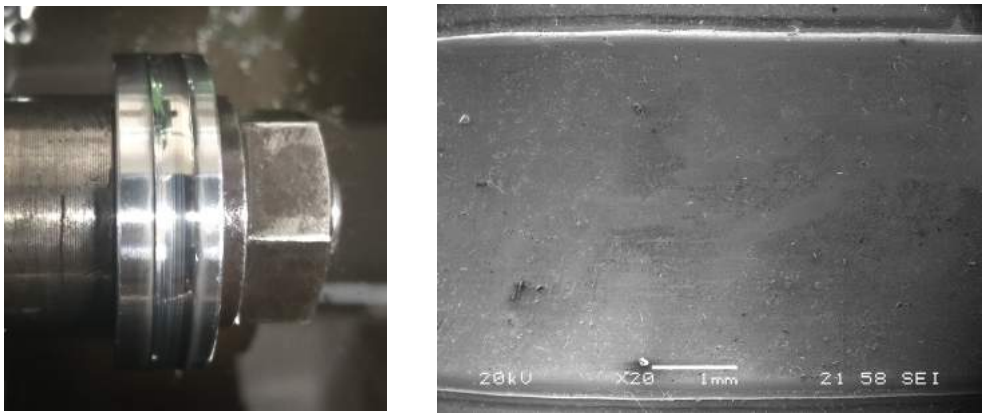

(a) (b)

Figure 5.12: Untreated fully lubricated sample after 2 million cycles (a). SEM micrograph after 2 million cycles (b).

The sample was then cut so that its cross-section could be analysed. Its full cross-section can be seen in Figure 5.13. The compressive forces acting on the wheel pushed some of the material to the sides of the wear track, creating two slopes at both the right and the left of the wear track.

Figure 5.13: Optical micrograph showing cross-section of the wear track of the untreated fully lubricated sample.

SEM micrographs of the cross-section (Figure 5.14), however, show several subsurface cracks. These are the source of the AE signals detected, showing that even small subsurface cracks in the very early stages of initiation can be detected with AE. Additionally, Figure 5.14b shows cracks that could coalesce, eventually resulting in a micropit if the test had been allowed to continued further.

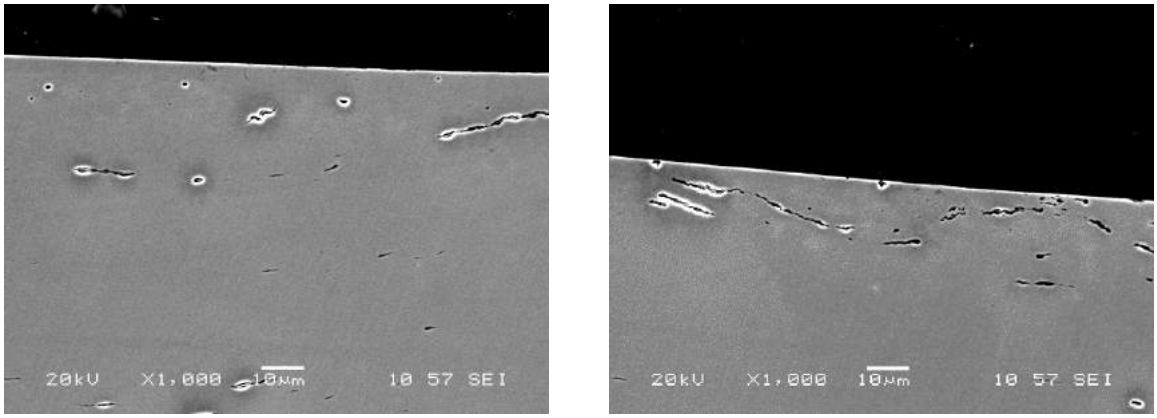

(a) (b)

Figure 5.14: SEM micrographs of the cross-section of the untreated fully lubricated sample.

Since no surface defects were found, and the subsurface cracks detected were still quite small, a more demanding condition was tested on the untreated EN24T steel. Tyfour et al. [45] found that initial dry cycling can greatly reduce RCF life. Therefore, the second test, named "dry-lubricated", was run for 1,500 cycles without lubricant, and then fully lubricated for the remaining of the test, until 2 million cycles were achieved.

The weight loss graph of the dry-lubricated test is shown in Figure 5.15. It is possible to notice a sharp increase in the weight loss at the very beginning of the test, corresponding to the initial dry cycles. After the first 1,500 dry cycles, the wear rate diminishes and follows a linear pattern.

Figure 5.16 shows AE signals and cumulative energy recorded during the test. Several signals were detected at the start of the test, and they are related to the break-in of the WC wheel and the creation of the wear track. The first noticeable sharp increase in AE energy, after the initial signals, was detected at around 1.3 million cycles. After this, the cumulative energy grows in a step-like pattern, until a high energy event happens at 1.8 million cycles.

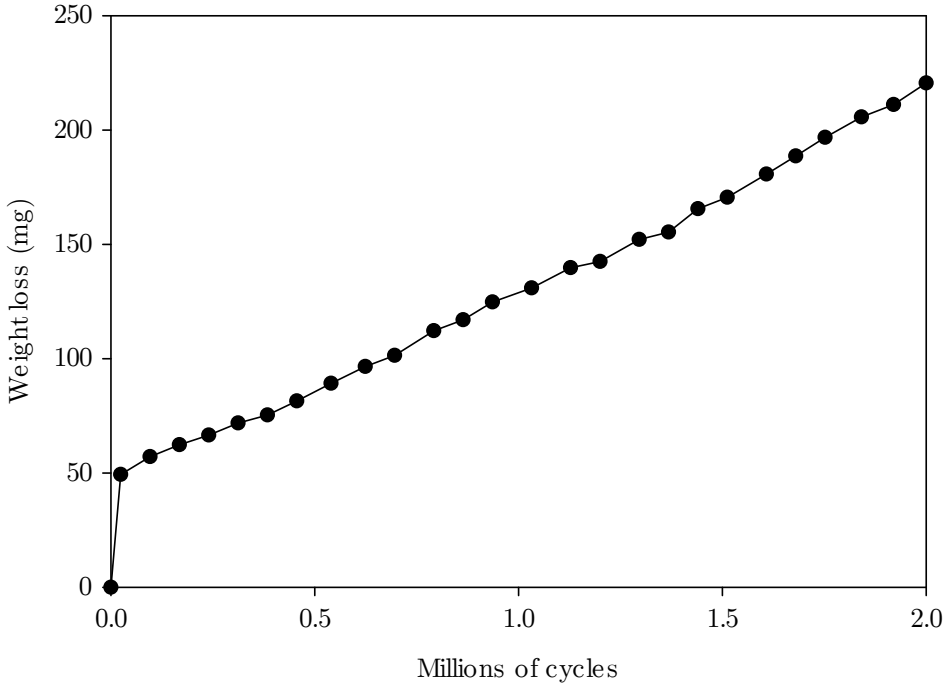

Figure 5.15: Weight loss versus number of cycles of the untreated dry-lubricated sample.

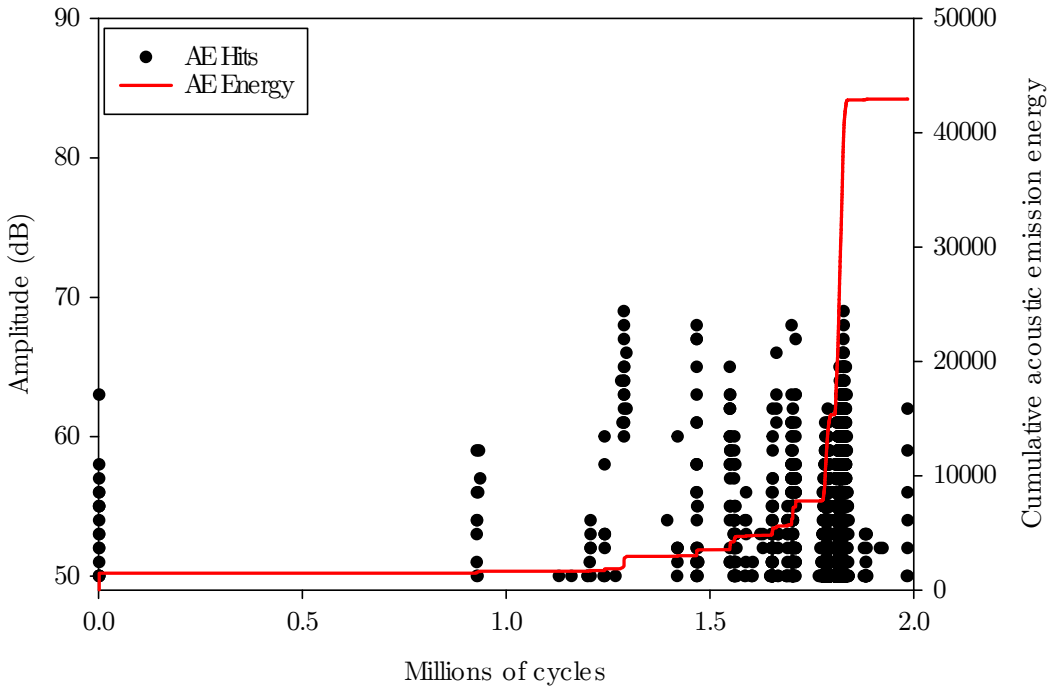

Figure 5.16: AE hits and cumulative energy of the untreated dry-lubricated sample as a function of the number of cycles.

After the signals at 1.3 million cycles were detected, the sample was analysed in the SEM. Figure 5.17 shows two examples of common defects found throughout the sample. Most defects were found near the wear track edges. Cracks up to 1 mm in length were found.

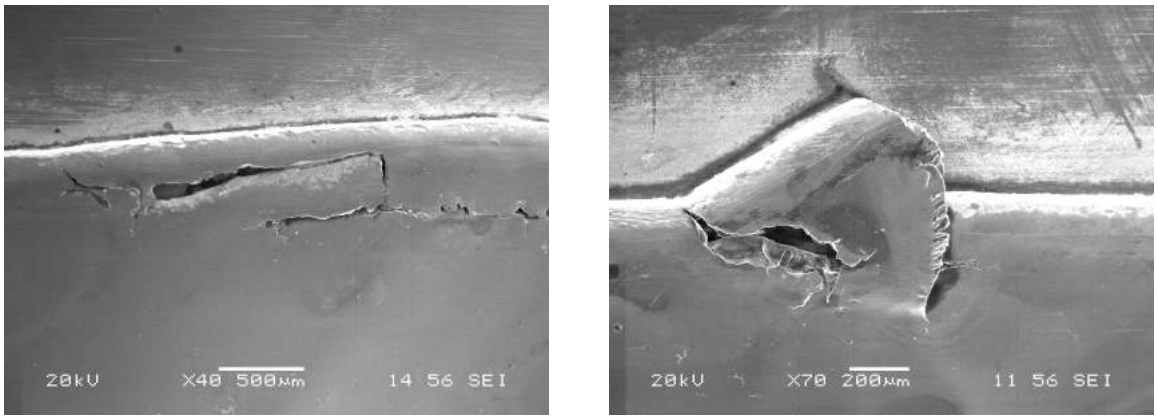

(a) (b)

Figure 5.17: SEM micrographs of the wear track of the untreated dry-lubricated sample after 1.3 million cycles.

The test was resumed and new SEM micrographs were taken at 1.75 million cycles and at the end of the test (2 million cycles). Figure 5.18 shows the size of one of the cracks is around 5 mm. These findings correlate well with the acoustic emission signals detected. Moreover, the occurrence of detectable acoustic emission signals became much more frequent after the 1.3 million cycles margin, indicating crack growth. At the end of the test (Figure 5.19), the crack has grown further, whilst branching can also be seen. At the right end side of the crack, it is possible to see a crater that has originated from material that broke and got removed from the cracked area.

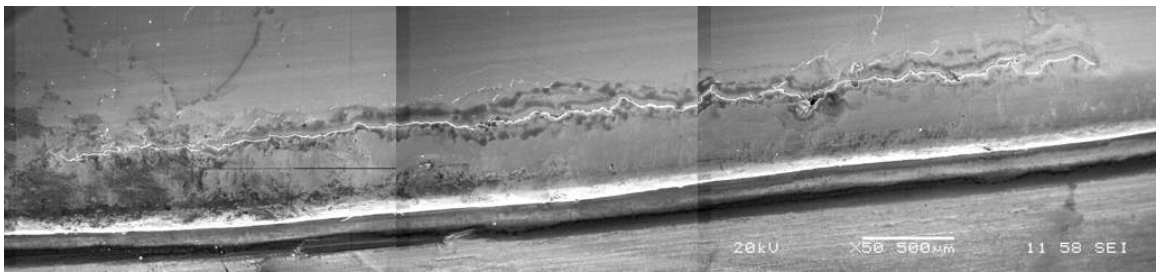

Figure 5.18: SEM micrograph of the wear track of the untreated dry-lubricated sample after 1.75 million cycles.

Figure 5.19: SEM micrograph of the wear track of the untreated dry-lubricated sample after 2 million cycles.

At the end of the test, the surface defects were distinguishable with naked eye, as shown in Figure 5.20. Moreover, material delamination can be seen in Figure 5.20b. The delamination originated from a crack which grew to around one-sixth of the circumference of the wheel.

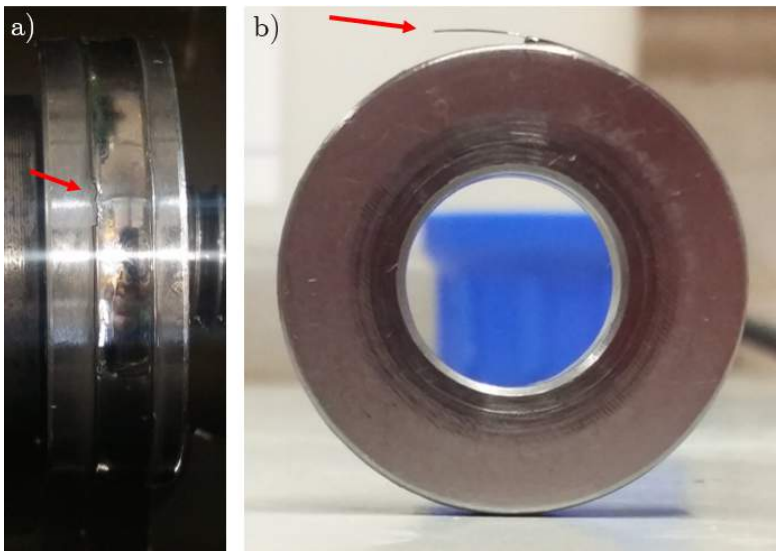

Figure 5.20: Untreated dry-lubricated sample after 2 million cycles, top view (a). Lateral view (b).

Similarly to the fully lubricated sample, the dry-lubricated sample also shows several subsurface cracks (Figure 5.21) with sizes ranging from 10 to 70 µm.

The AE monitoring system was again able to detect defects in the initiation stage. AE signals were first detected at 0.9 million cycles, with stronger and more frequent signals being detected from this point onwards. Subsurface and surface cracking and delamination were the main sources of the signals.

Since WTGs can often oscillate between lubricated and dry periods, mostly due to overloads caused by misalignment or wind gusts, the untreated sample was also tested

under intermittent lubrication conditions, which are scarcely reported in the available literature to date.

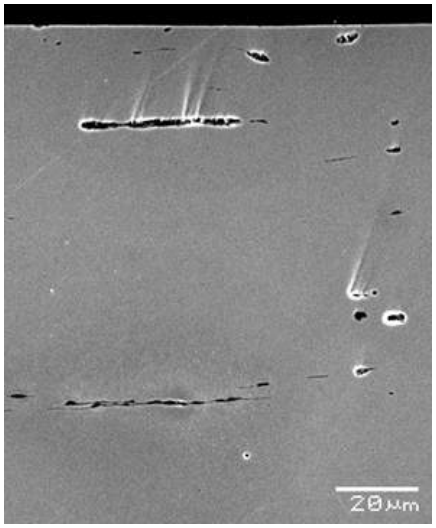

Figure 5.21: SEM micrograph of the cross-section of the untreated dry-lubricated sample.

The intermittent test was also run for 2 million cycles and divided in 72,000 cycles (or 3 hours) increments. The first 800 cycles of each increment were run without lubrication, while the remaining 71,200 cycles were under lubricating conditions. These conditions were repeated until 2 million cycles were reached.

The weight loss of the untreated intermittent sample is shown in Figure 5.22. Two different weight loss rates can be identified for the sample tested under the intermittent conditions. The first one is up to 1.3 million cycles, and not as severe. After this number of cycles was reached, there was a substantial increase in the weight loss rate observed. This happened due to a substantial mass of the material delaminating from the sample surface, similar to the one in the dry-lubricated sample seen in Figure 5.20. In the intermittent test, however, several delaminated areas completely broke off the sample.

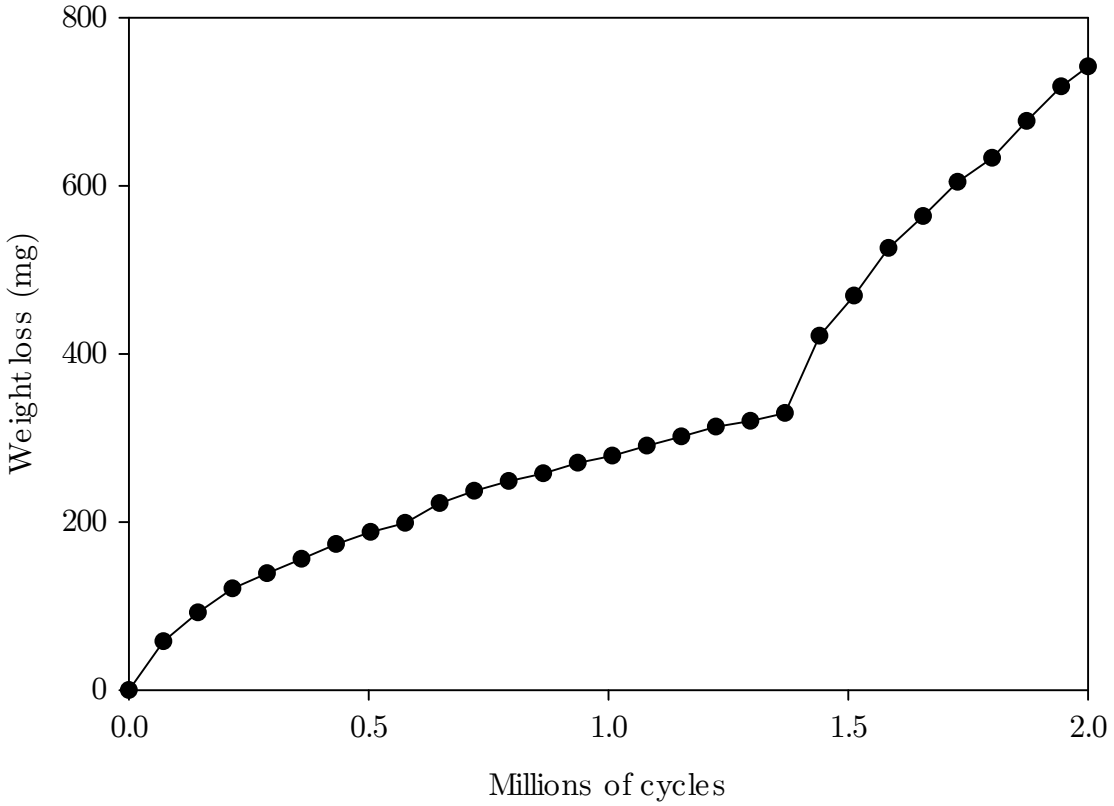

Figure 5.22: Weight loss versus number of cycles of the untreated intermittent sample.

The AE signals of the intermittent test are shown in Figure 5.23. The initial distinguishable feature of this test is the number of signals captured during the first quarter of the test. Most of these signals do not originate from material defects, but instead due to poor coupling between the sensor and the oil container. The coupling between the sensor and oil container degraded over time, and most of the signals up to 0.5 million cycles are due to the sensor wobbling and capturing this movement as signals. However, there are still three distinguishable peaks that are very likely to have originated from growing defects in the material. After the sensor coupling was fixed, at 0.5 million cycles, some signals were captured, but they did not have much energy. This changed at and after 1.2 million cycles when several signals that can be related to defects growing in the material were captured. The signals detected after this point were strong and frequent, clearly indicating damage evolution.

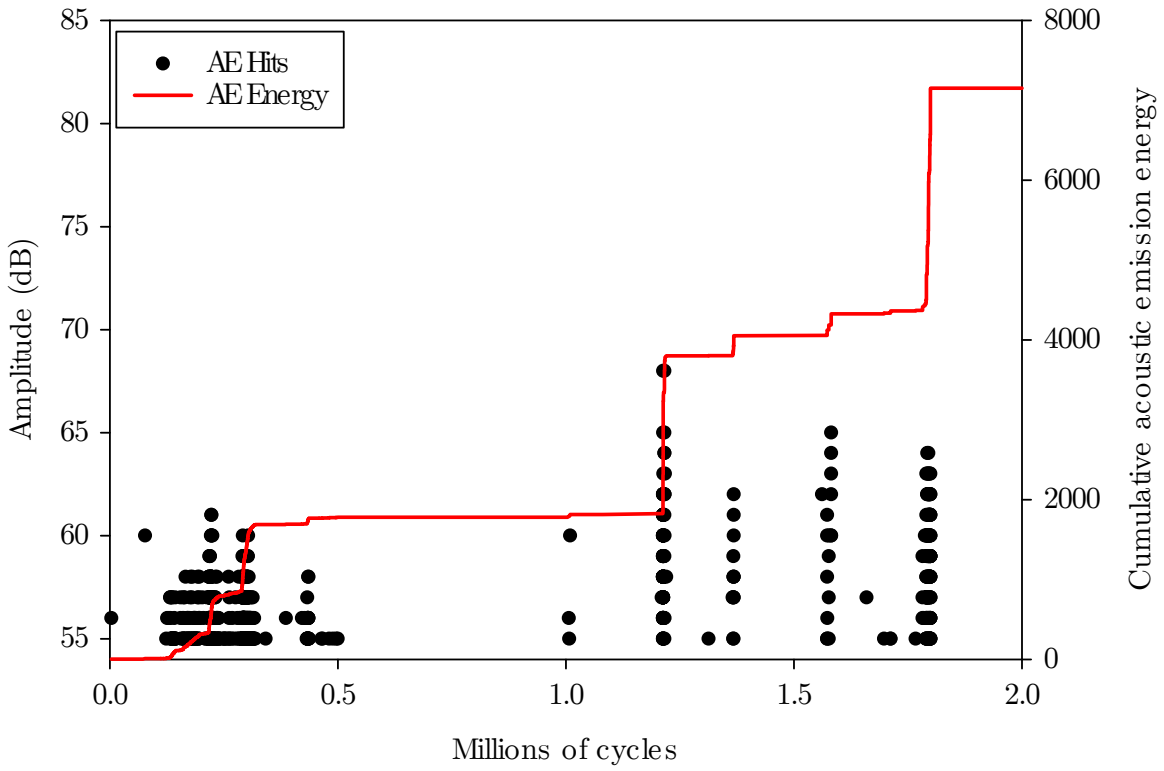

Figure 5.23: AE hits and cumulative energy of the untreated intermittent sample as a function of the number of cycles.

Due to the AE peaks being detected early in the test, SEM investigation for the intermittent test was performed at 0.4 million cycles. Several small cracks could be identified. In addition, two large cracks, parallel to each other and to the wear track edges can be seen in Figure 5.24. At this point, the cracks covered about a quarter of the entire circumference of the wheel.

After 0.7 million cycles (Figure 5.25a), these cracks are even bigger and started to branch. Other small and parallel cracks also initiated. At 1.3 million cycles, as Figure 5.25b shows, delamination can be identified. Material removal generated craters up to 300 µm in length. They are the main reason for the increase in the weight loss rate.

At the end of the test, the delamination and surface defects were visible with naked eye (Figure 5.26a). An example of a crack that would eventually delaminate and detach from the wear track edge is shown in Figure 5.26b.

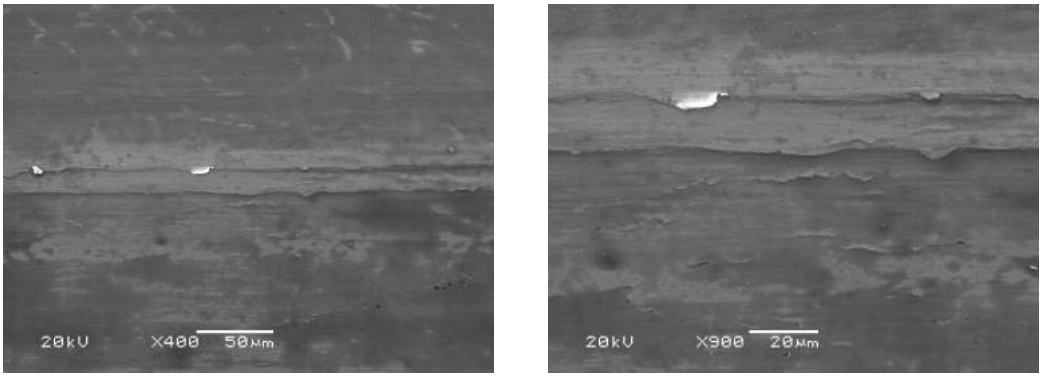

(a) (b)

Figure 5.24: SEM micrographs of the wear track of the untreated intermittent sample after 0.4 million cycles.

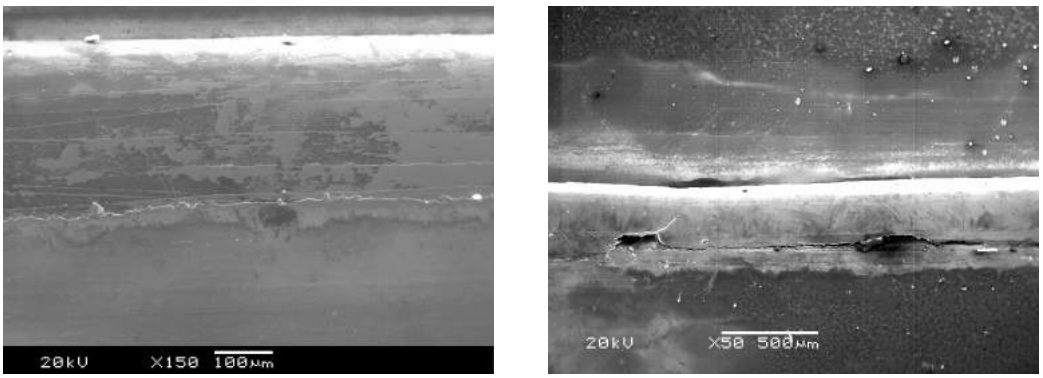

(a) (b)

Figure 5.25: SEM micrographs of the wear track of the untreated intermittent sample after 0.7 million cycles (a), and after 1.3 million cycles (b).

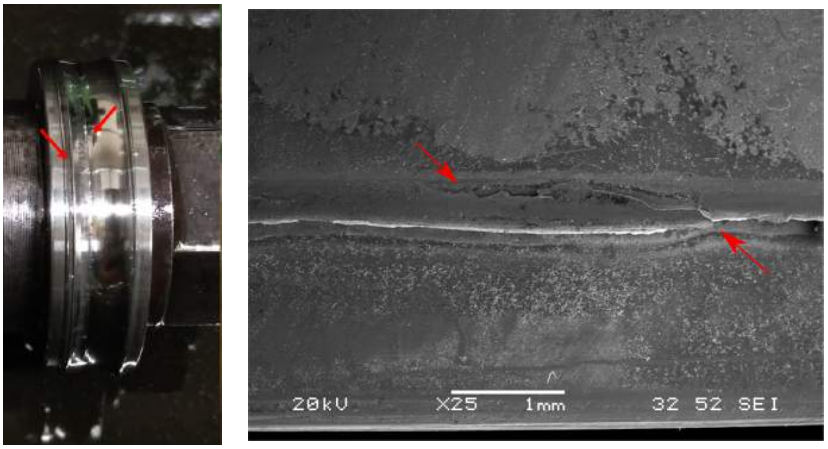

(a) (b)

Figure 5.26: Untreated intermittent sample after 2 million cycles (a). SEM micrograph after 2 million cycles.

The cross-section of the sample can be seen in Figure 5.27. Its surface is rougher than the previous samples, due to the several cracks and material removal that occurred during the wear process. Similarly to the previous samples, subsurface cracks are also present. Figure 5.27b shows the point where a piece of material delaminated.

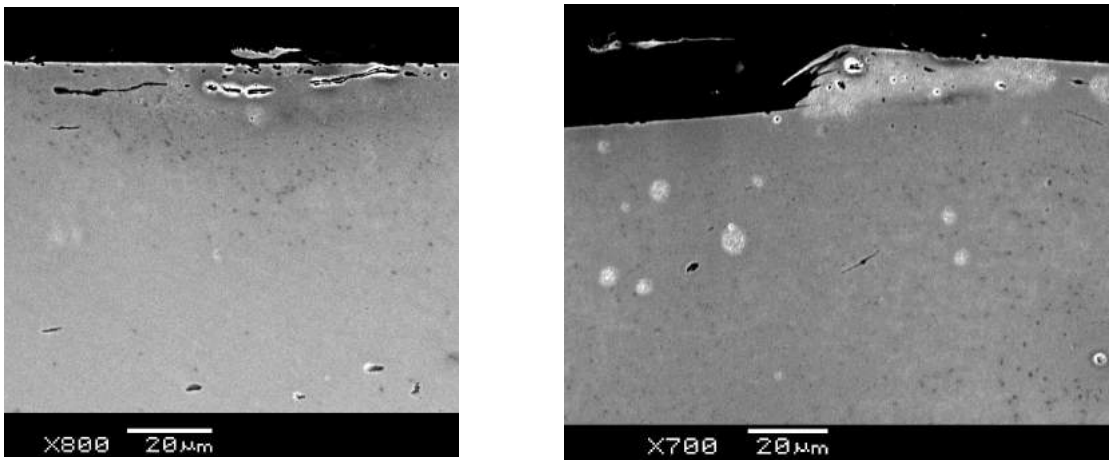

(a) (b)

Figure 5.27: SEM micrographs of the cross-section of the untreated intermittent sample.

5.2.2 EN24T DLC-treated

The weight loss of the EN24T DLC-treated sample tested under intermittent lubrication conditions is shown in Figure 5.28. Its weight loss over 0.9 million cycles is more than double that of the untreated sample. However, as pointed out in section 5.1.1, this cannot be directly compared due to the wear suffered by the WC wheel. What can be compared is the weight loss trend, which for this sample is exponentially increasing. This is different from the previous samples tested. This test was not carried out until 2 million cycles since the damage level evolution of this particular wheel sample was severe.

The AE graph is shown in Figure 5.29. The AE monitoring system did not detect any signals until 0.5 million cycles. After that, several high energy signals were detected, and the cumulative energy also has an exponential shape, matching well with the weight loss graph.

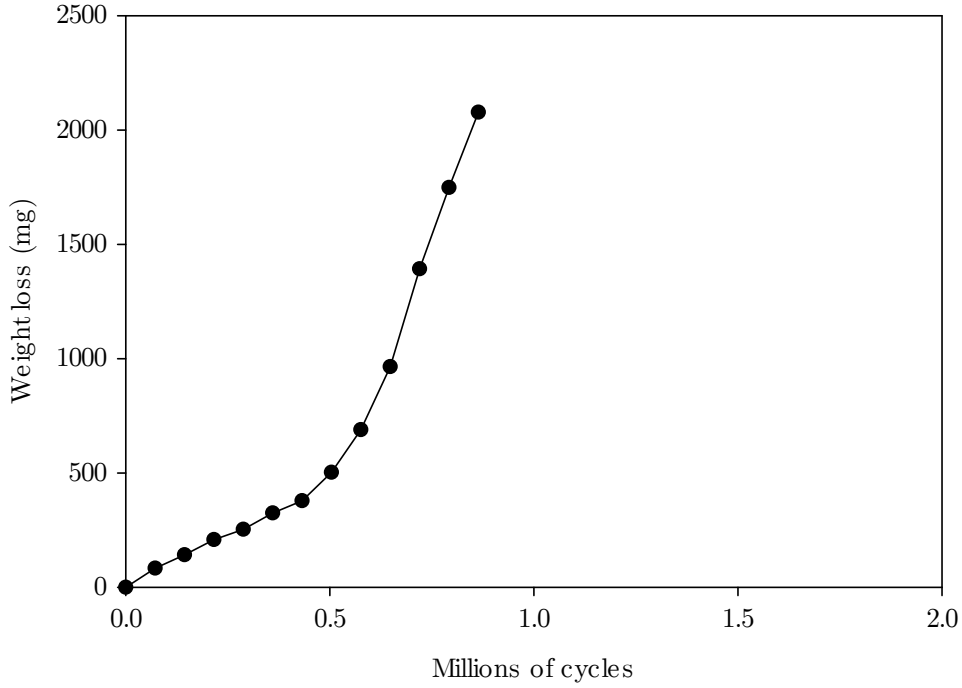

Figure 5.28: Weight loss versus number of cycles of the DLC-treated intermittent sample.

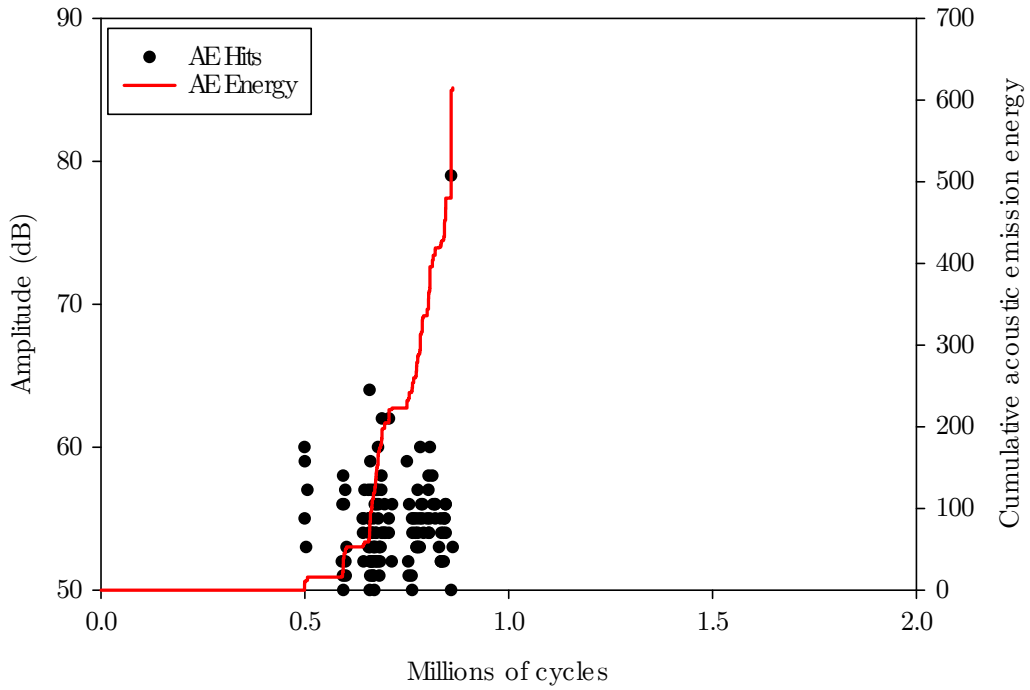

Figure 5.29: AE hits and cumulative energy of the DLC-treated intermittent sample as a function of the number of cycles.

The sample was first examined in the SEM after 0.4 million cycles. However, no defects were found. This was expected since no signals were captured by the AE monitoring system. After some signals were detected, the sample was imaged again at 0.7 million cycles as Figure 5.30 shows. It is possible to observe cracks up to 1 mm in length, which resulted in the exponential weight loss observed.

These cracks continued to grow at a fast pace, as shown in Figure 5.31. At this point, the test was interrupted and a cross-section of the sample was taken for examination. Even though this sample was tested for less than half the time of the untreated sample, it is possible to notice early stage cracking from MnS inclusions (Figure 5.32).

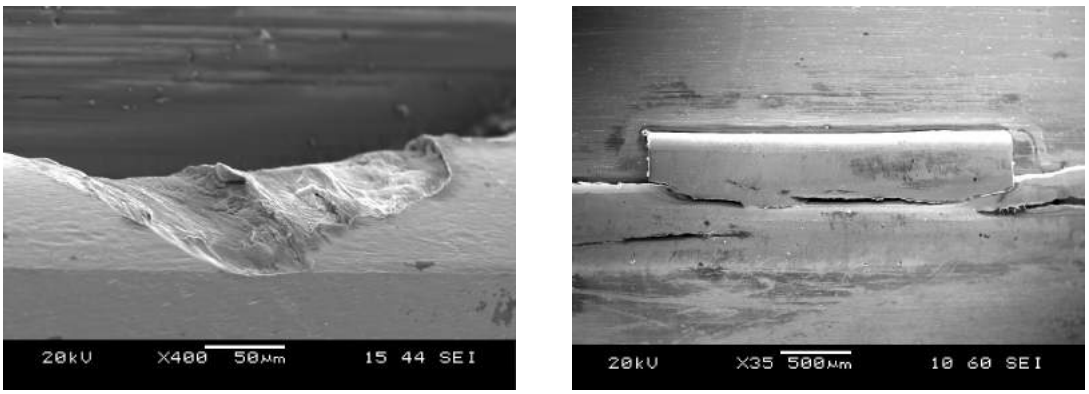

(a) (b)

Figure 5.30: SEM micrographs of the wear track of the DLC-treated intermittent sample after 0.7 million cycles.

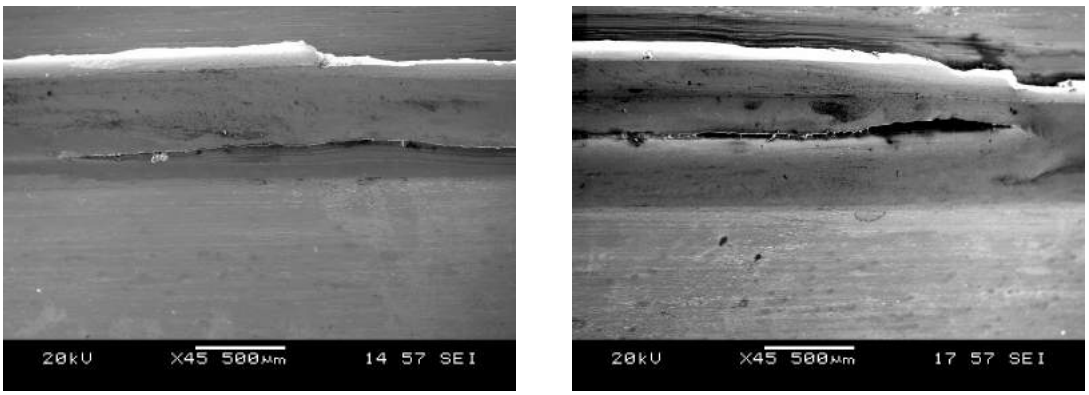

(a) (b)

Figure 5.31: SEM micrographs of the wear track of the DLC-treated intermittent sample after 0.9 million cycles.

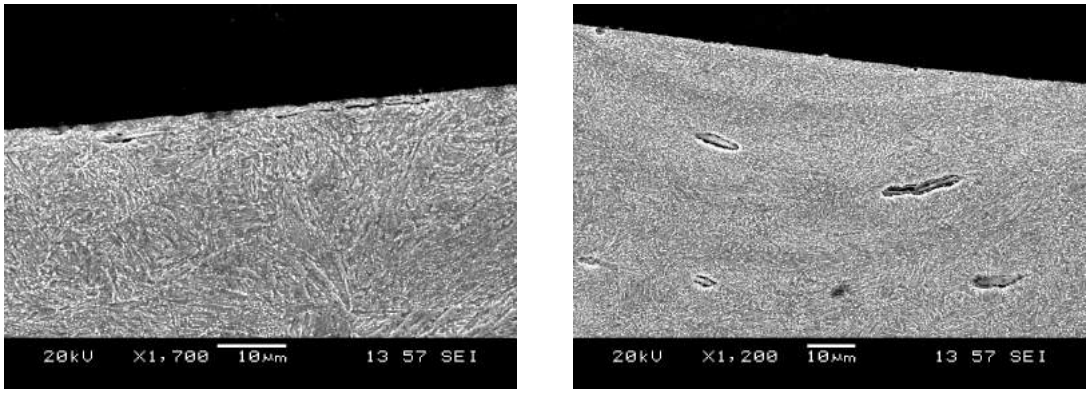

(a) (b)

Figure 5.32: SEM micrographs of the wear track of the DLC-treated intermittent sample after 0.9 million cycles. Etched with 2% nital..

The wear track edges of the sample also show an interesting feature. Due to the large stress involved in the test, the substrate, which is made of untreated and ductile steel, plastically deforms. This leads to the fracture of the DLC coating, with its debris being trapped inside the substrate. This is shown by the EDS maps on Figure 5.33.

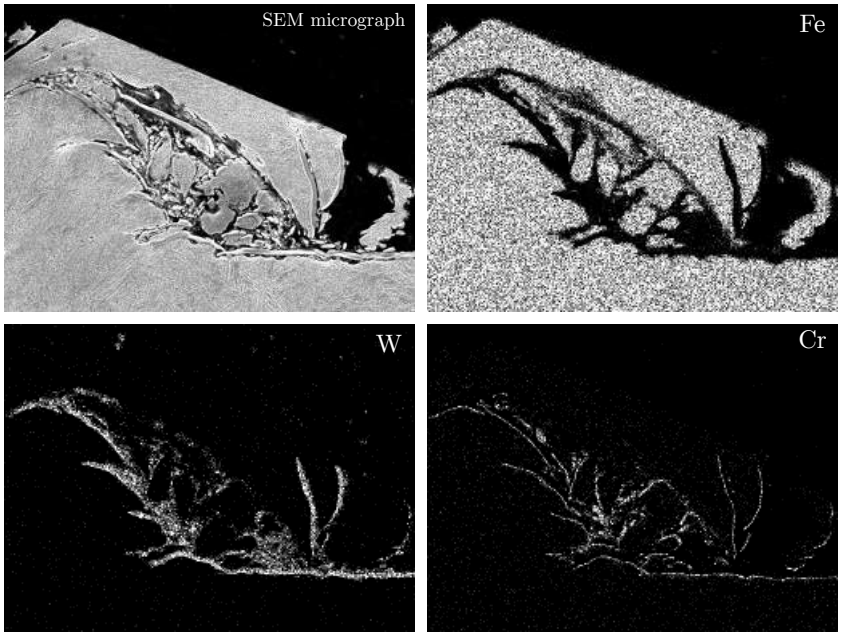

Figure 5.33: SEM micrograph of the cross-section of the DLC-treated intermittent sample (etched with 2% nital), showing the wear track edge and the EDS maps for iron, tungsten and chromium.

The combination of a ductile substrate with a DLC coating did not generate good results under high contact stresses. The difference in ductility leads to residual stresses that end

up fracturing the DLC coating and leaving the substrate exposed. This fracture, along with the cracking of the substrate, generated the AE signals detected, once again proving the reliability of this non-destructive testing technique.

5.2.3 EN40B nitrided

The plasma nitrided EN40B was tested under the same intermittent lubrication conditions. The weight loss graph is shown in Figure 5.34. After a larger wear rate at the beginning of the test, the weight loss graph follows a linear pattern.

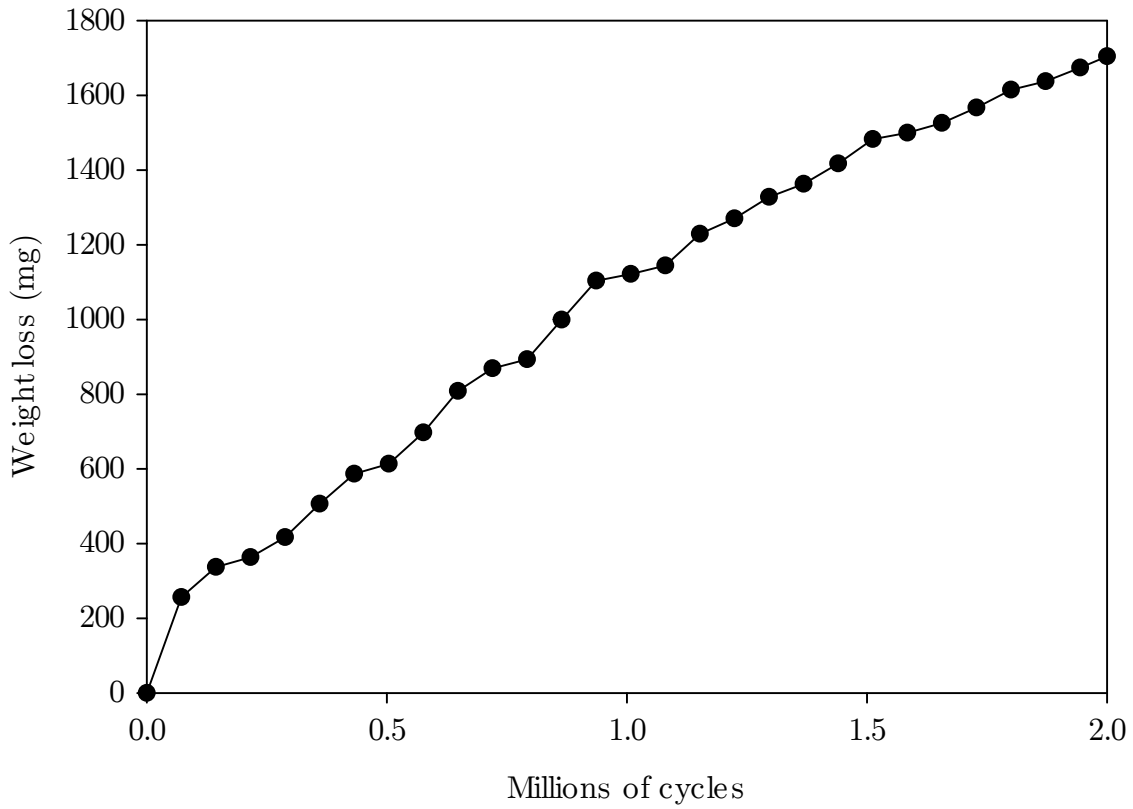

Figure 5.34: Weight loss versus number of cycles of the plasma nitrided intermittent sample.

The AE system captured several high energy signals at the very beginning of the test, which are related to the accelerated weight loss at the start of the test. This was due to the removal of the white layer, which is brittle and breaks off easily at such high contact pressures, as shown in Figure 5.36. As soon as this layer was removed, no signals were

detected up to 1 million cycles.

Signals started to be detected again in the last half of the test, and they can be associated with the cracking at the edges of the wear track, as shown in Figure 5.37. The nitrided layer is quite hard, and thus less ductile. Instead of deforming, it cracks and breaks off at the wear track edges. The centre of the wear track, however, did not have any defects, as seen in Figures 5.38 and 5.39a. A cross-section examination was also performed, and no cracks originating from the MnS inclusions were observed (Figure 5.39b).

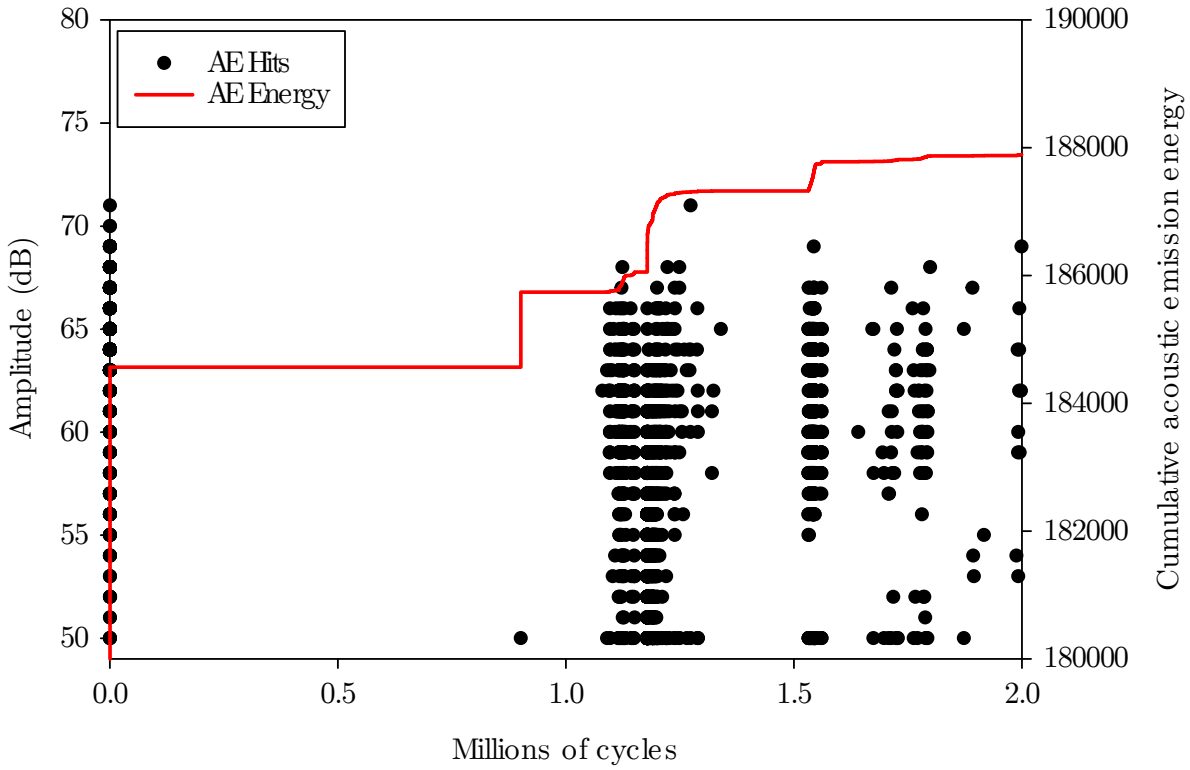

Figure 5.35: AE hits and cumulative energy of the plasma nitrided intermittent sample as a function of the number of cycles.

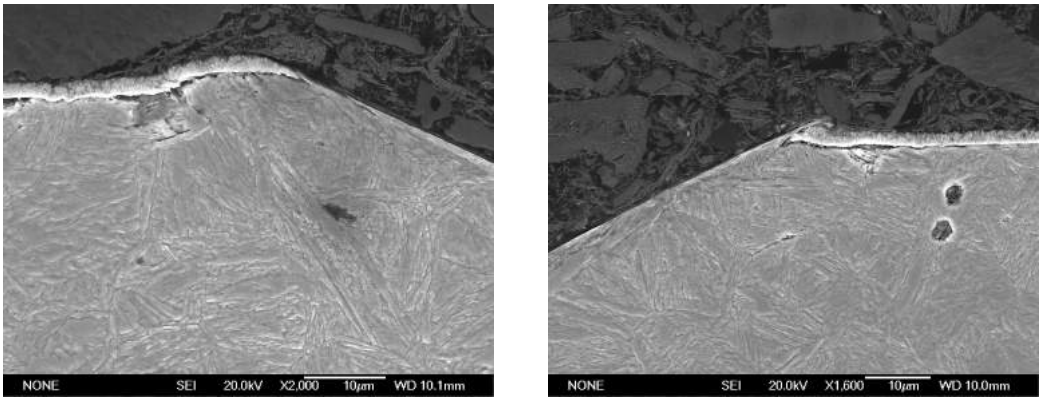

(a) (b)

Figure 5.36: SEM micrographs of the cross-section of the plasma nitrided intermittent sample after 2 million cycles, showing cracks and debonding of the white layer. Etched with 2% nital.

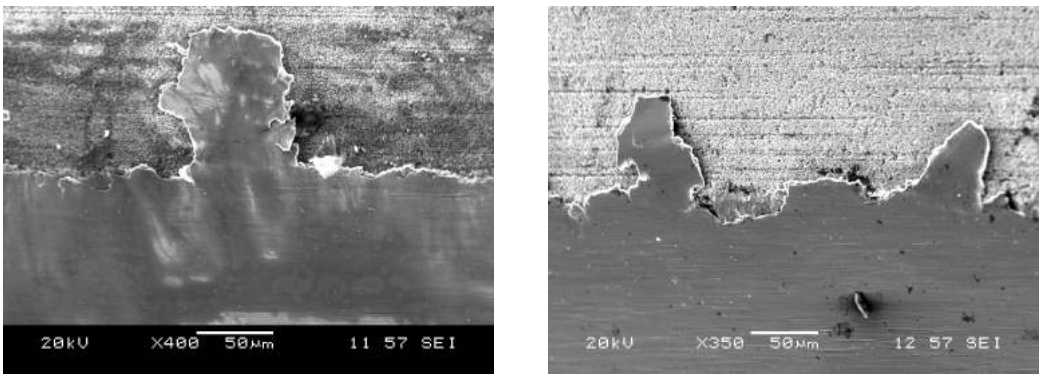

(a) (b)

Figure 5.37: SEM micrographs of the wear track edge of the plasma nitrided intermittent sample after 1.3 million cycles (a), and 2 million cycles (b).

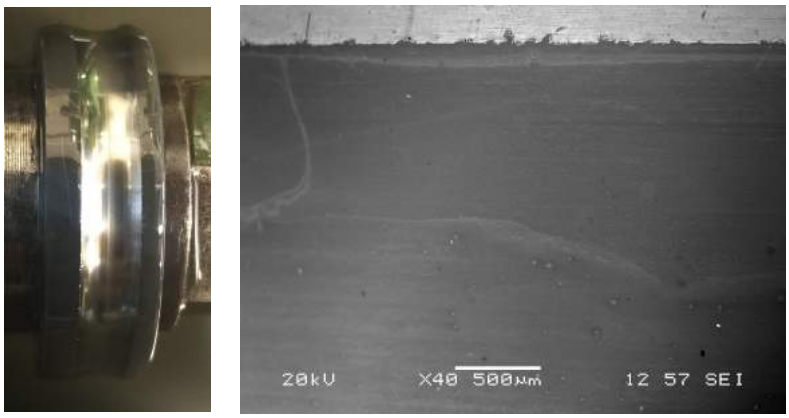

(a) (b)

Figure 5.38: Plasma nitrided intermittent sample after 2 million cycles (a). SEM micrograph after 2 million cycles (b).

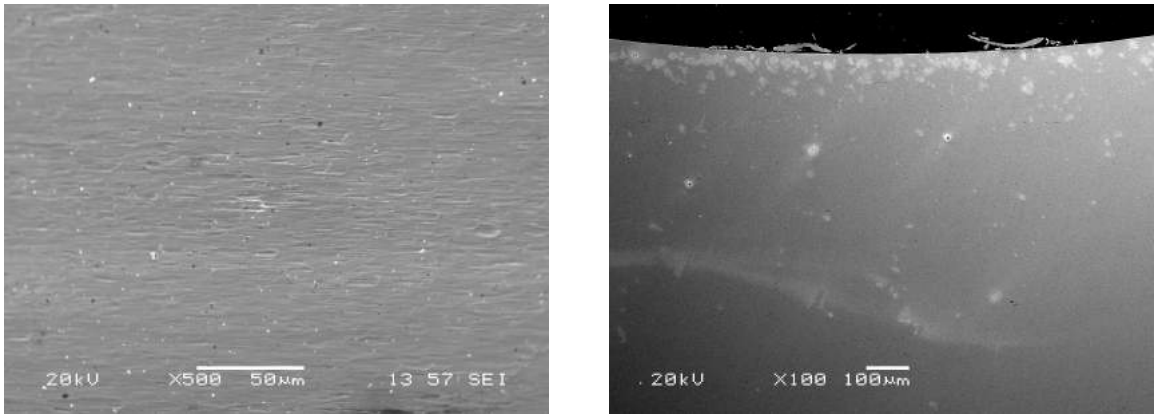

(a) (b)

Figure 5.39: SEM micrographs of the plasma nitrided sample at the wear track centre (a), cross-section (b).

A carbide-enriched layer was observed during the characterisation of the plasma nitrided samples, as shown in chapter 3. The carbides were located at the prior austenite grain boundaries and parallel to the surface. It was thought that these could reduce RCF life through initiation of cracks. However, no defects were found, as shown in Figure 5.40.

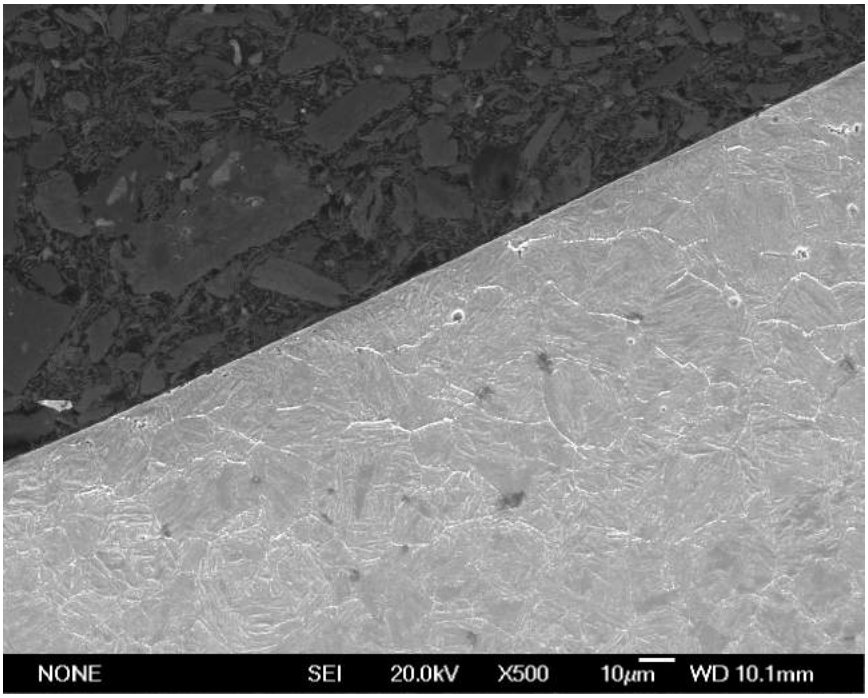

Figure 5.40: SEM micrograph showing the cross-section of the wear track at the carbide-enriched zone. Etched with 2% nital.

The plasma nitriding treatment proved to increase RCF life since no subsurface cracks

originated from MnS inclusions could be found. Defects were found at the wear track edges, but this is mainly due to the geometry used by WC wheel and the large contact stresses involved. At the wear track itself, no defects were found. Furthermore, the AE system once again proved to be a reliable monitoring method. It was able to detect the white layer removal and the cracking at the wear track edges.

5.2.4 EN40B nitrided and DLC-treated

The weight loss of the EN40B nitrided and DLC-treated tested under intermittent conditions is shown in Figure 5.41. Two different wear rates can be identified, both in a linear pattern. The first one, less severe, up to 0.5 million cycles. After this point, the wear was observed to occur at a much faster rate. Similarly to the DLC-treated sample, this test was ended before 2 million cycles, due to the severity of damage.

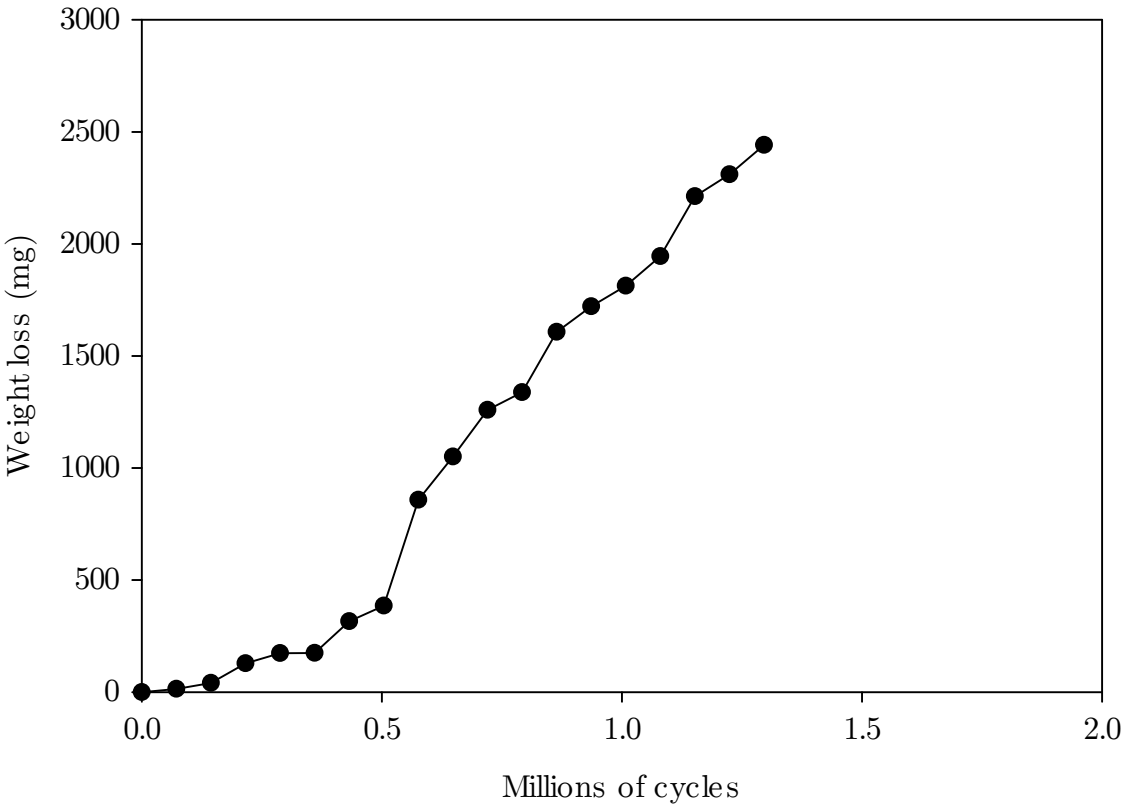

Figure 5.41: Weight loss versus number of cycles of the plasma nitrided intermittent sample.

The AE data of this sample is shown in Figure 5.42. A large number of signals were detected at the start of the test. These signals are related with the fracture of both the DLC and the white layer, as shown in Figure 5.42. After this, no signals were detected until 0.5 million cycles, which also matches the wear rate increase. These signals are related to cracking at the wear track edges, shown in Figure 5.44. This was due to the low ductility of the plasma nitrided and DLC layers. The cracking continued, with high energy signals being detected until the test was stopped at 1.3 million cycles.

Apart from the wear track edge cracks, the wear track surface appeared polished, and no defects were found at the wear track centre, as shown in Figure 5.45.

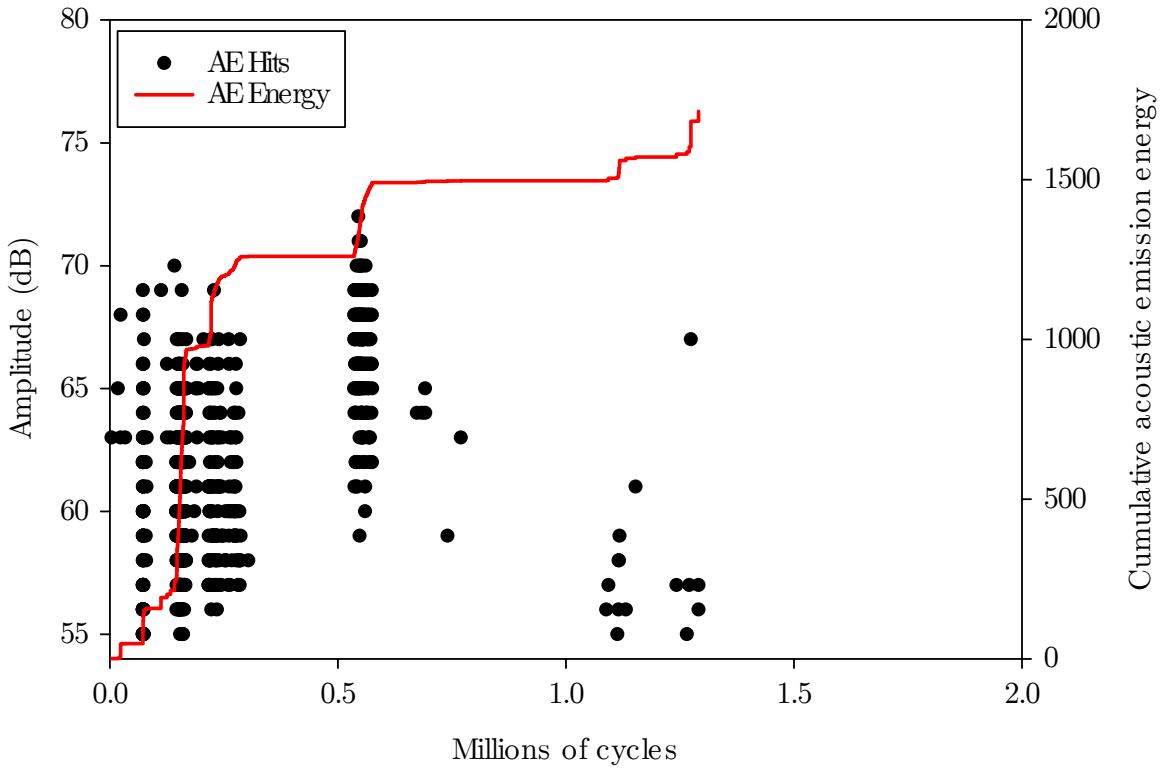

Figure 5.42: AE hits and cumulative energy of the plasma nitrided intermittent sample as a function of the number of cycles.

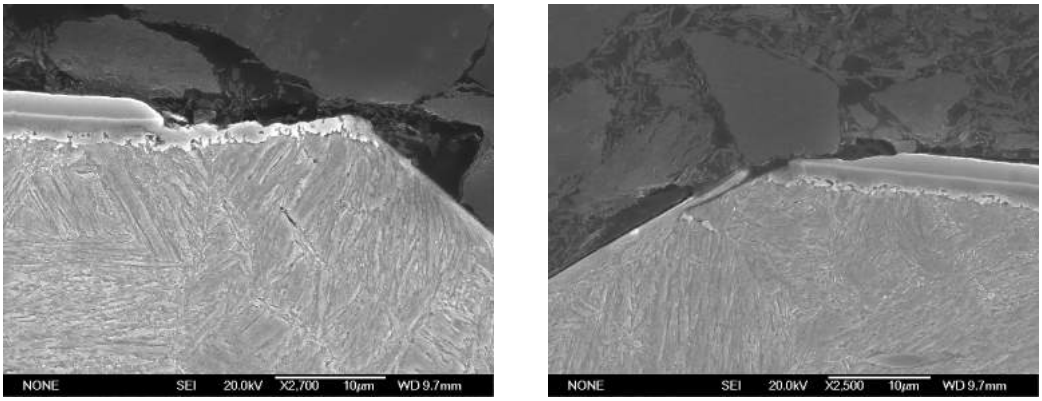

(a) (b)

Figure 5.43: SEM micrographs of the cross-section of the plasma nitrided and DLC intermittent sample after 1.3 million cycles, showing fracture of the DLC layer. Etched with 2% nital.

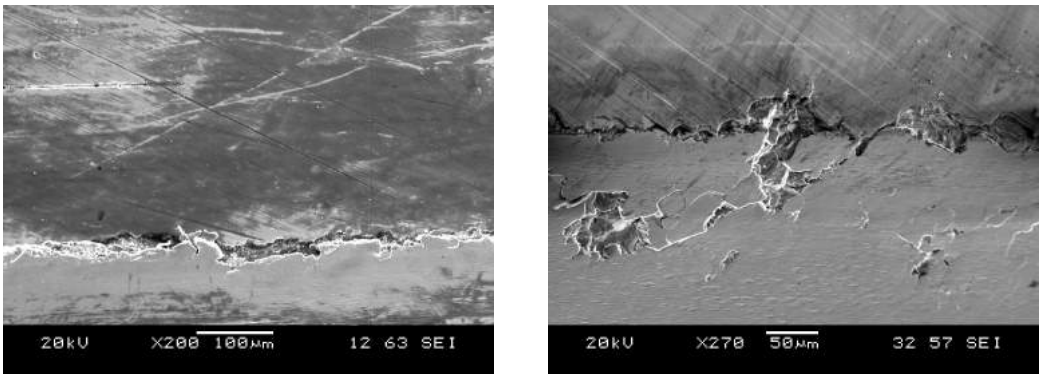

(a) (b)

Figure 5.44: SEM micrographs of the wear track edge of the plasma nitrided and DLC intermittent sample after 1.3 million cycles.

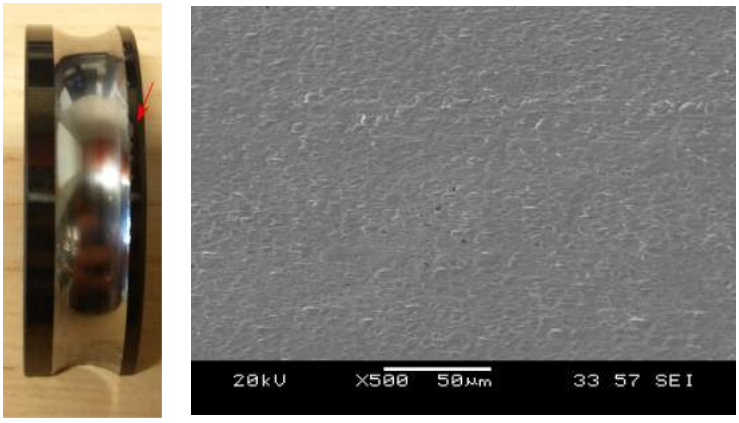

(a) (b)

Figure 5.45: Plasma nitrided and DLC intermittent sample after 1.3 million cycles (a). SEM micrograph of the wear track centre after 1.3 million cycles (b).

Finally, no subsurface cracks were found when imaging the cross-section of the sample, as Figure 5.46 shows.

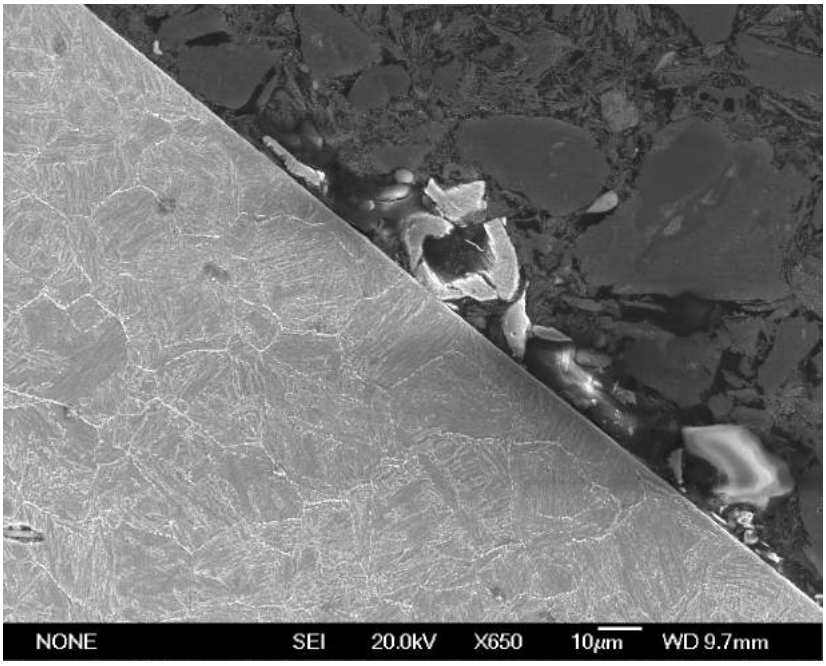

Figure 5.46: SEM micrograph of the cross-section of the plasma nitrided sample after 1.3 million cycles, etched with 2% nital.

The addition of a DLC coating to the plasma nitrided layer did not exhibit any improvement in comparison with the use of nitrided layer only. This is in line with what occured with the DLC-treated EN24T samples. The improvement in RCF lifetime is attributed to the plasma nitrided layer only. The DLC coating, being only 4 µm thick, cannot sustain the 5 GPa stress and is quickly worn away. The AE monitoring system detected the cracking of the brittle DLC coating, as well as the wear track edge cracking.

5.3 SUMMARY

Different materials and coating combinations were tested under representative lubrication conditions of interest to WTGs. Both the untreated and the DLC-treated EN24T suffered subsurface cracks, which were detectable with the AE system employed. Additionally, the difference between the substrate and the DLC coating in this sample generated an exponential wear rate.

Both the plasma nitrided, and the plasma nitrided and DLC-treated samples did not contain any defects at the wear track centre. Only wear track edge cracks were observed. Once again, the DLC coating played a role in damage initiation, due to its low ductility. No MnS initiated cracks were observed in these samples. In both cases, the AE system detected the defects successfully.

It is clear that the DLC coating increased the damage initiation and propagation of the samples. The DLC coating is brittle and thin (4 µm thickness), and thus could not sustain the 5 GPa contact stress under intermittent conditions. After breaking away from the sample surface, however, its debris played a role in increasing the damage rate on all tested samples. The plasma nitrided sample performed better than the duplex treated sample.

Finally, the AE system has been proven to be a reliable way of detecting defect initiation and propagation in RCF testing. Even though the sensor had to be coupled to the oil container, which results in reflection and absorption of part of the energy of the signal, it was still successful in detecting cracking, delamination, and subsurface cracking. This demonstrates that there is strong potential for the meaningful application of AE in WTG monitoring, as it is proven to be a reliable method for identifying and quantifying damage.

CHAPTER 6

FAILURE ANALYSIS

6.1 WIND TURBINE BEARING

A failed bearing from the high-speed shaft of a WTG was provided by a project partner for investigation. The model of the bearing is FAG NU222-E-M1-C3. It is a single row cylindrical roller bearing, with an inner diameter of 110 mm, an outer diameter of 200 mm and width of 38 mm. Firstly, a macroscopic investigation was conducted, as shown in Figure 6.1.

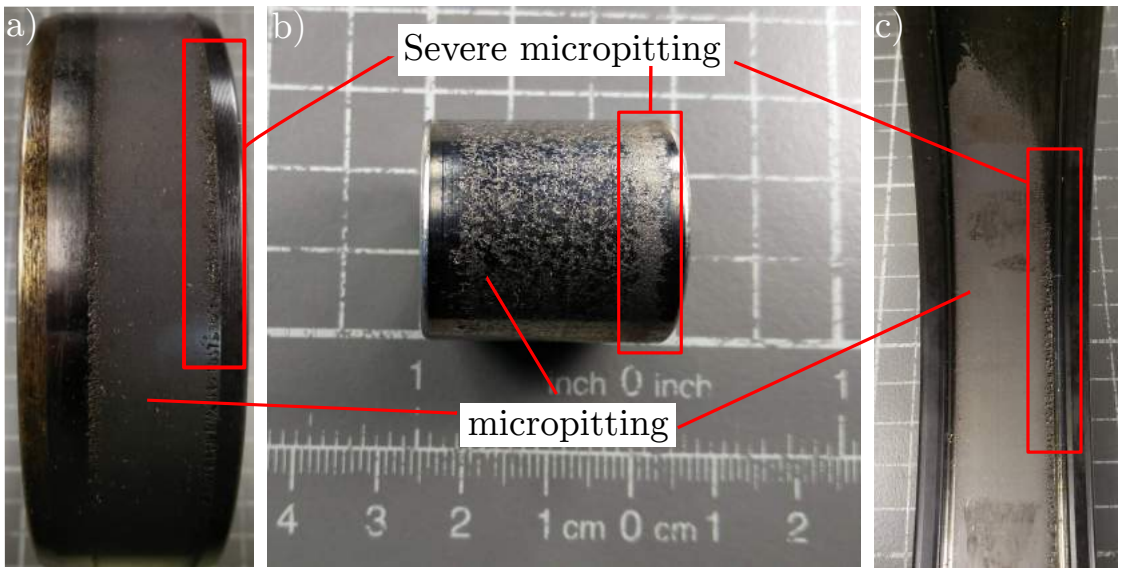

Figure 6.1: Images of the failed bearing showing the outer race (a), roller (b) and inner race (c). Each square has a side of 1 cm.

Frosting, or micropitting, can be seen in all three components. Moreover, a more severe occurrence of this type of failure can be seen at the right edges of the roller, inner race and outer race of the bearing. In fact, micropitting is more likely to occur at the ends of bearing rollers, since this region acts as a geometric stress concentrator [176]. All the rollers had a similar appearance regarding the damage type and severity.

Figure 6.2 shows SEM micrographs of the damaged roller. Figure 6.2b shows

the irregular surface of a micropit, characteristic of that initiated by ductile fatigue crack propagation. At the end of the crater, a featheredge can be seen, due to the plastic flow of the material.

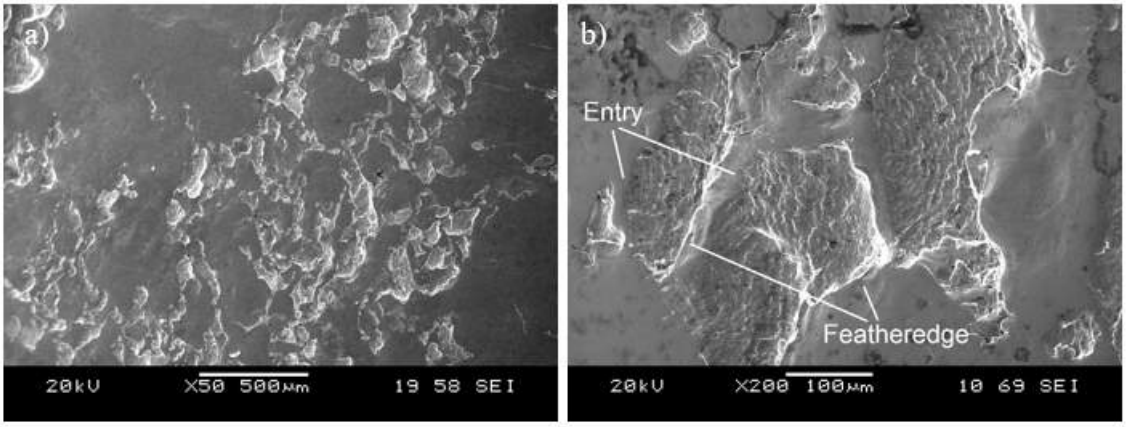

Figure 6.2: SEM micrographs of micropitting on the rollers.

The rollers were transversally cut and prepared for metallographic analysis. Figure 6.3 shows the micropit cracks, which usually begin at or near the surface and at small angles. These cracks then grow until a small piece of material is removed, creating the micropit.

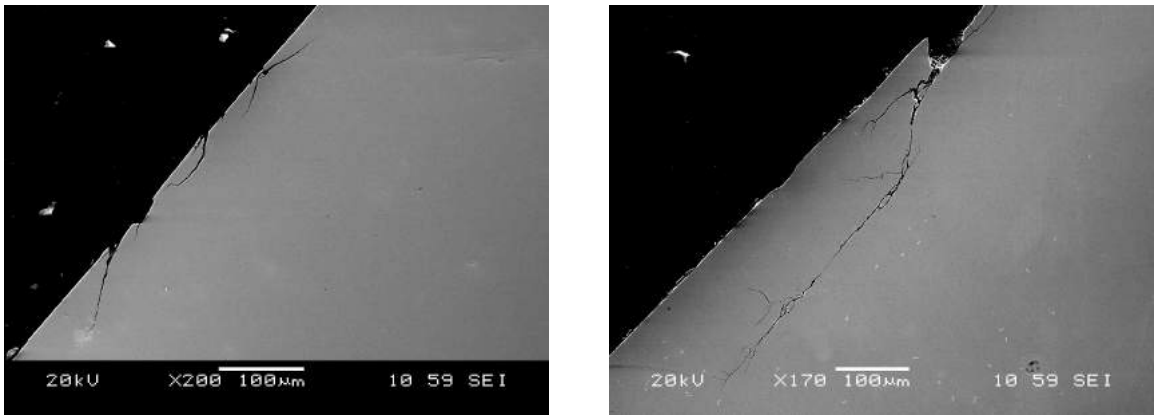

(a) (b)

Figure 6.3: SEM micrographs of micropitting cracks.

The microstructure of the rollers can be seen in Figure 6.4. It is tempered martensite with dispersed spheroidised carbides.

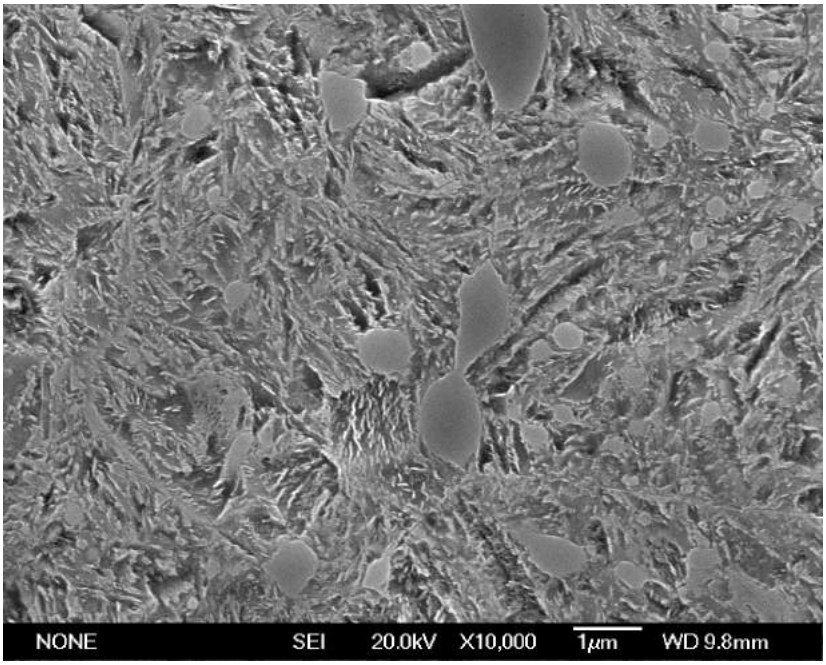

Figure 6.4: SEM micrographs of the rollers showing tempered martensite and finely dispersed carbides. Etched with 2% nital.

EDS testing (Table 6.1) was employed to reveal the composition of the roller which was found to be within the nominal alloying content set for typical bearing steel grades [177]. This particular sample was possibly made of BS534A99 steel, which is a common steel grade used in bearing manufacture. The higher amount of carbon detected is due to contamination.

Table 6.1: EDS results of the damaged roller.

Chemical element	**Wt%**
C	4.0
Cr	0.4
Si	1.5
Mn	0.4
Fe	93.8

The microhardness profile of the roller can be seen in Figure 6.5. The ISO standard 281:2007 [178] recommends a minimum hardness of at least 58 Rockwell C, which accord-

ing to the ASTM E140 Standard [179] is equal to 653 HV. The hardness of the roller is constant throughout its cross-section, with an average of 736.5 ± 15.1 HV 0.05, and therefore, meets the minimum requirements of the standard.

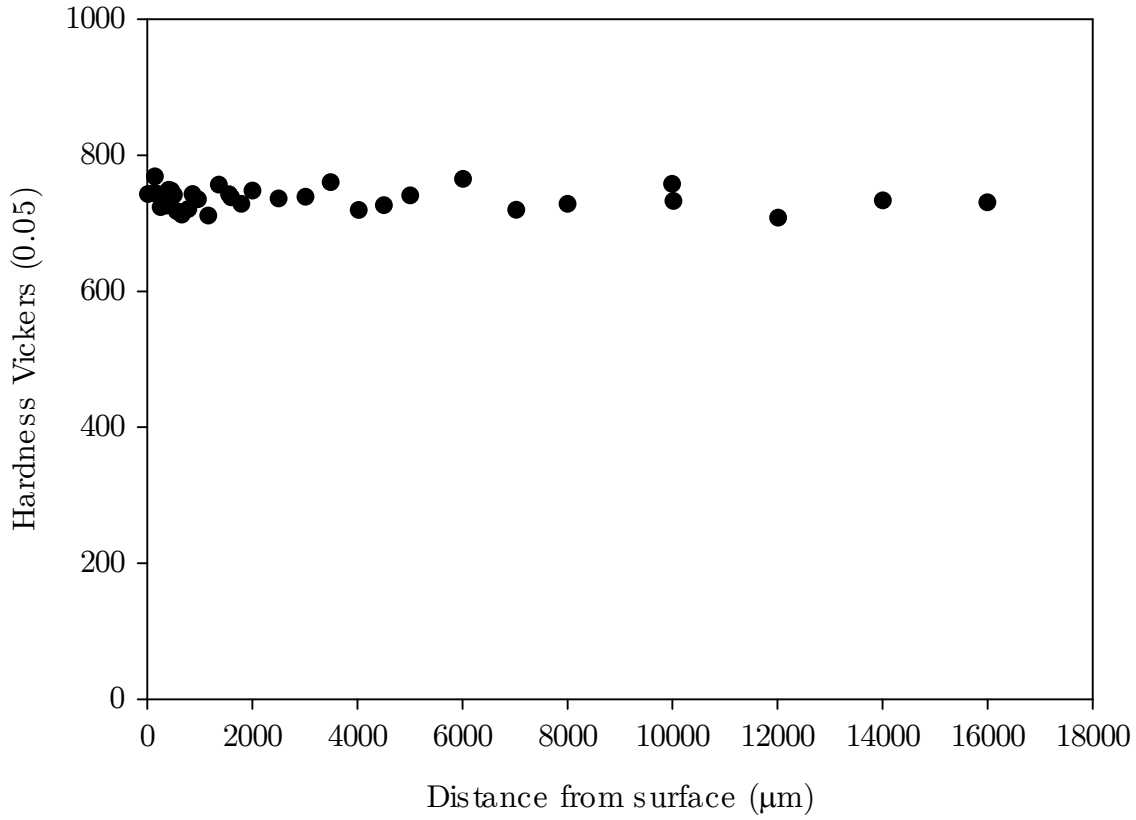

Figure 6.5: Microhardness profile of the roller.

A mixture of causes can contribute to this type of surface fatigue damage, but micropitting will generally occur due to concentrated stresses. In this case, all three components show a more severe occurrence at the right end side, which is evidence of misalignment. Whenever a bearing is end loaded, the load is no longer distributed over the full width of the bearing. This may result in localised fatigue damage and progress in the form of flaking. This will produce in turn an increase in radial clearance, finally leading to bearing failure [48].

6.2 WIND TURBINE GEAR

Gear teeth from the intermediate stage of a failed gearbox were also provided by the same project partner for investigation.

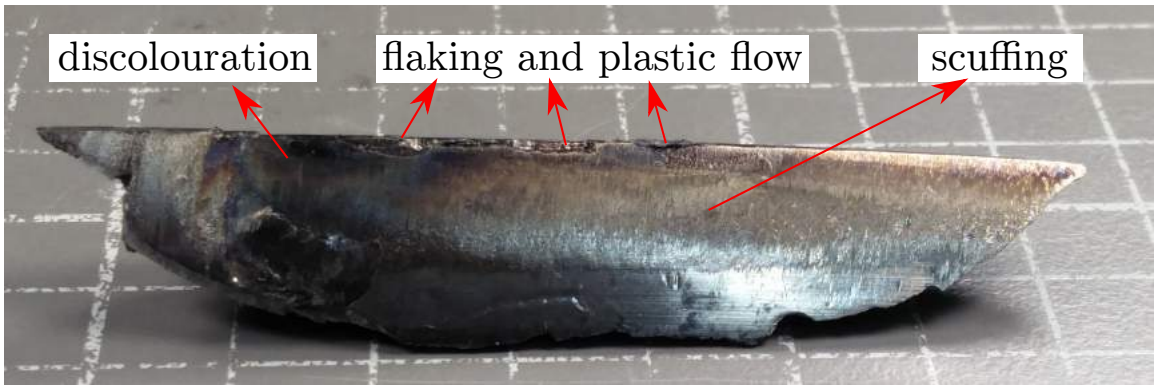

Figure 6.6: Flank of broken tooth. Each square has a side of 1 cm.

Figure 6.6 shows the flank of one tooth, where different failure mechanisms, such as scuffing, flaking, plastic flow, and discolouration can be seen. Discoloured areas are associated with overheating caused by poor or no lubrication and resulting in high frictional forces between the contact surfaces. Scuffing also occurs due to inadequate lubrication and causes local frictional heating at the surface. Flaking, in turn, occurs when cracks at the subsurface of the material propagate all the way to the surface, causing material to be removed or delaminated.

The bottom of the tooth is shown in Figure 6.7, presenting a grey and granular surface (region 1), and a bright and smooth surface (region 2). This difference in roughness and brightness suggests region 2 is the crack initiation region, whereas region 1 is the fast propagation region. The gear tooth, therefore, failed under fatigue. The surface denoted by region 1 can be seen in Figure 6.8, and shows a dimpled surface in the fractured area that is associated with ductile failure undergoing large plastic deformation. The dimples are formed due to the coalescence of microvoids [180]. Figure 6.8 demonstrates that the final mode of failure was ductile fracture.

Figure 6.7: Bottom of broken tooth. Each square has a side of 1 cm.

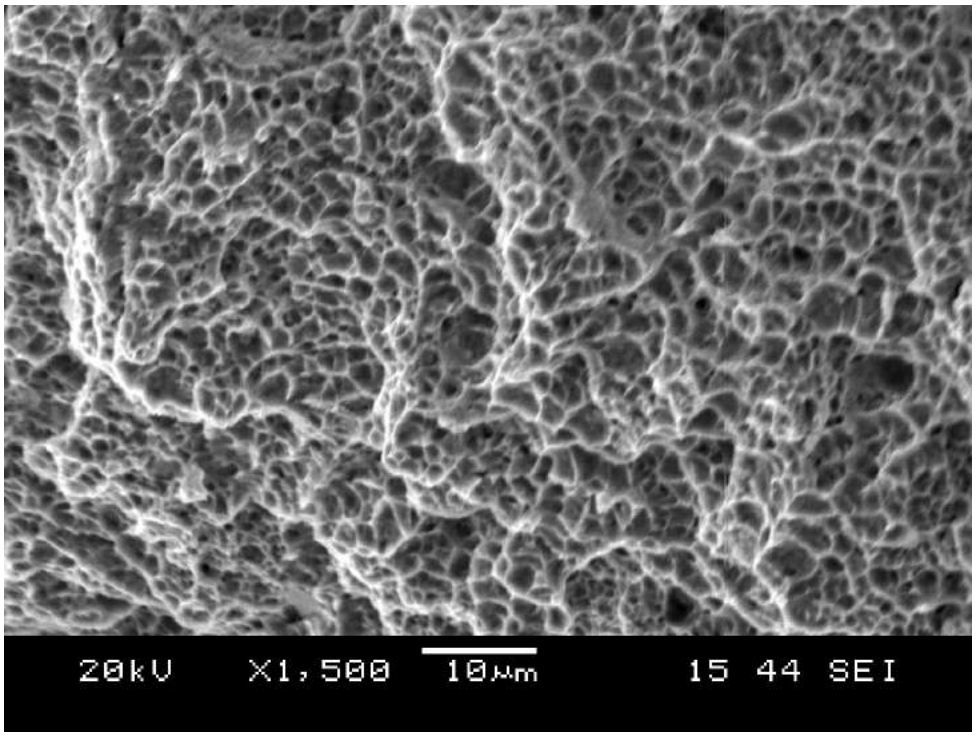

Figure 6.8: SEM micrograph of the bottom of the broken tooth, showing a dimpled surface.

Ratchet marks can also be seen at the left side of the region 1, as shown in Figure 6.9. Ratchet marks are the result of either a high stress in the component or high-stress concentrations [181].

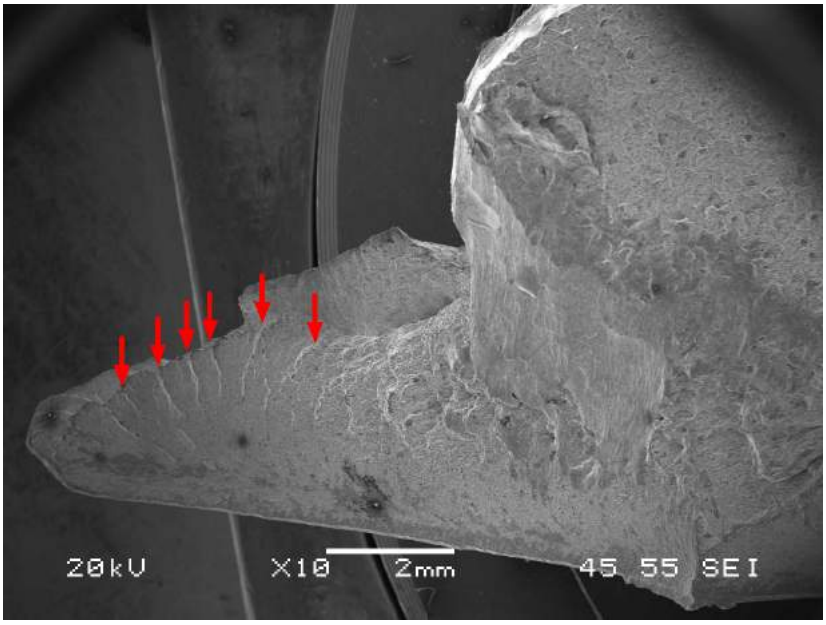

Figure 6.9: SEM micrographs of the left side of the fractured surface, showing ratchet marks.

A cross-section of the broken tooth was then cut and prepared for metallographic analysis and microhardness profile. The latter is shown in Figure 6.10. The gear is much harder at the surface than at the core. The depth of the case, defined as the distance from the surface to a point at which the hardness is 550 HV [33], is around 1.4 mm, suggesting the gear has been carburised. The recommendation of ISO 6335 [33] for carburised gears is a surface hardness between 660 to 800 HV, with no less than 40 HV difference in the outer 0.1 mm of the case. Both criteria were met by the gear tooth. The core hardness is around 500 HV, which also meets the ISO 6335 criteria.

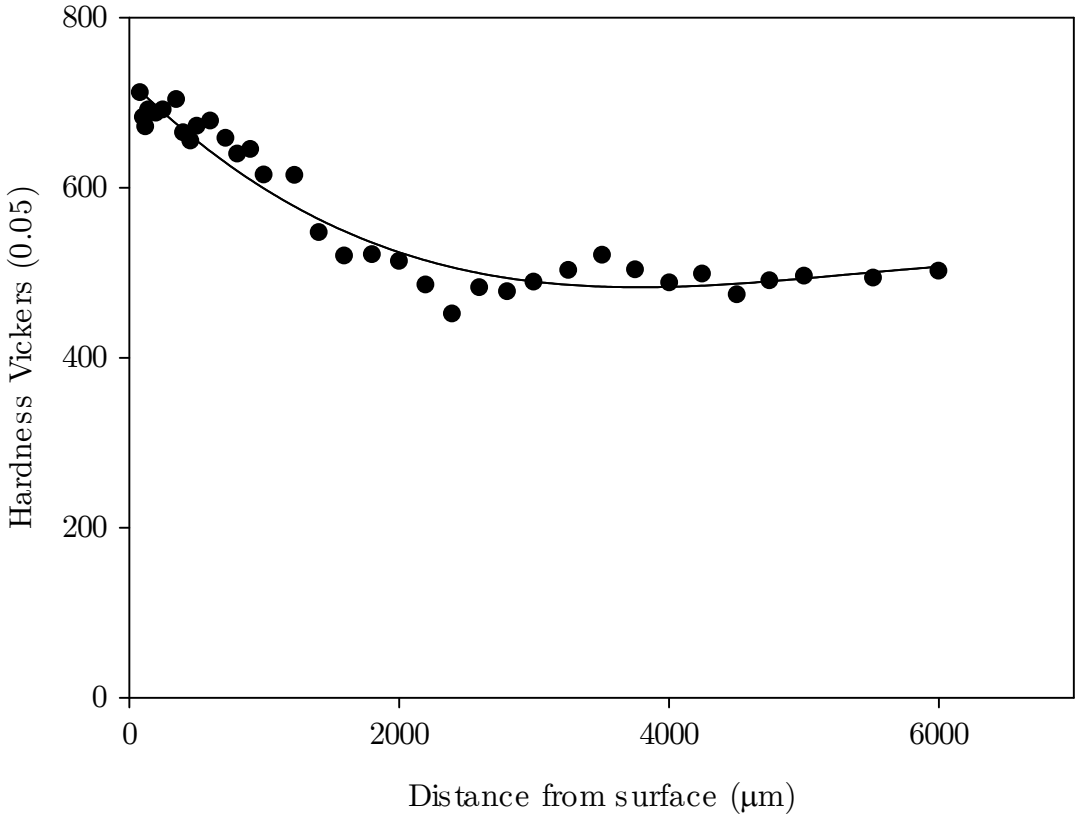

Figure 6.10: Microhardness profile of the gear tooth.

The microstructure of the gear tooth can be seen in Figure 6.11a, and it is tempered martensite. Figure 6.11b shows the carbides dispersed amongst the tempered martensite microstructure. The XRD in Figure 6.12 confirms there are no other phases present.

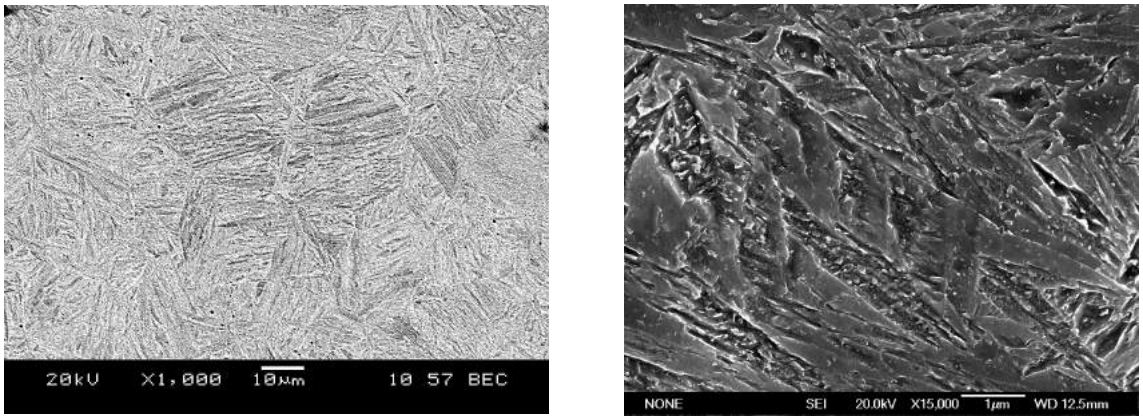

(a) (b)

Figure 6.11: SEM micrograph of the gear tooth showing the tempered martensite microstructure (a), dispersed carbides (b). Etched with 2% nital.

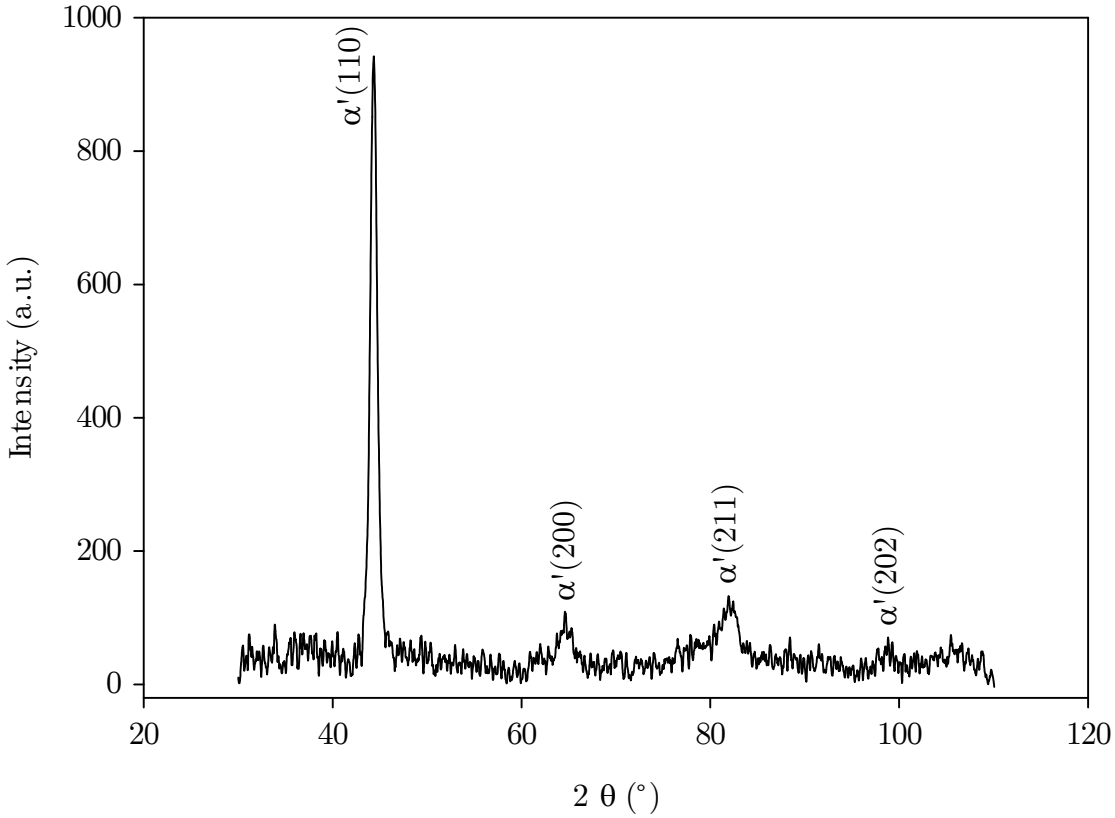

Figure 6.12: X-ray diffractogram of the gear tooth, showing martensite peaks.

Some inclusions were also found in the microstructure. They were characterised with the help of EDS and were found to be MnS as shown in Figure 6.13 and Table 6.2. The steel had Mn, Si, Cr and Ni as alloying elements.

These inclusions can act as crack initiators under high contact stress conditions [182]. Several examples of this behaviour were found near the failure area of the gear tooth. Two examples can be seen in Figure 6.14.

One of the main cracks is shown in Figure 6.15. As the dashed lines show, the crack grows to the right, and in doing so, it divides the fracture area into the areas 1 and 2 as seen in Figure 6.7. After initiating, the crack continued to grow until it reached a critical size, at which point it became unstable causing final fracture of the tooth.

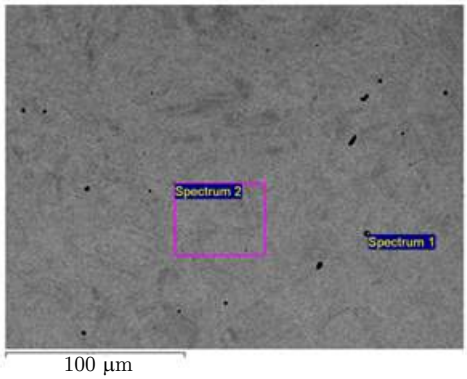

Figure 6.13: SEM micrographs of EDS locations.

Chemical element	Spectrum 1 (wt%)	Spectrum 2 (wt%)
C	3.8	1.5
Si	-	0.2
S	30.3	-
Cr	0.3	1.7
Mn	60.9	0.5
Ni	-	1.4
Fe	4.7	94.7

Table 6.2: EDS results of the locations in Figure 6.13.

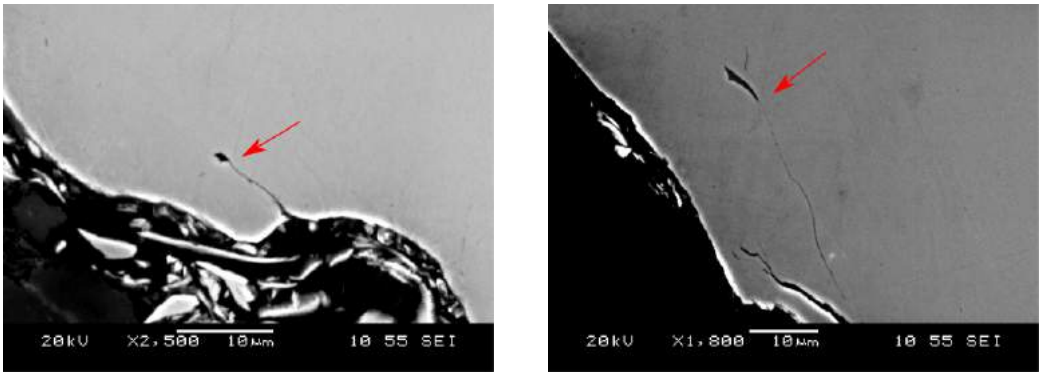

(a) (b)

Figure 6.14: SEM micrographs of MnS inclusions causing crack initiation.

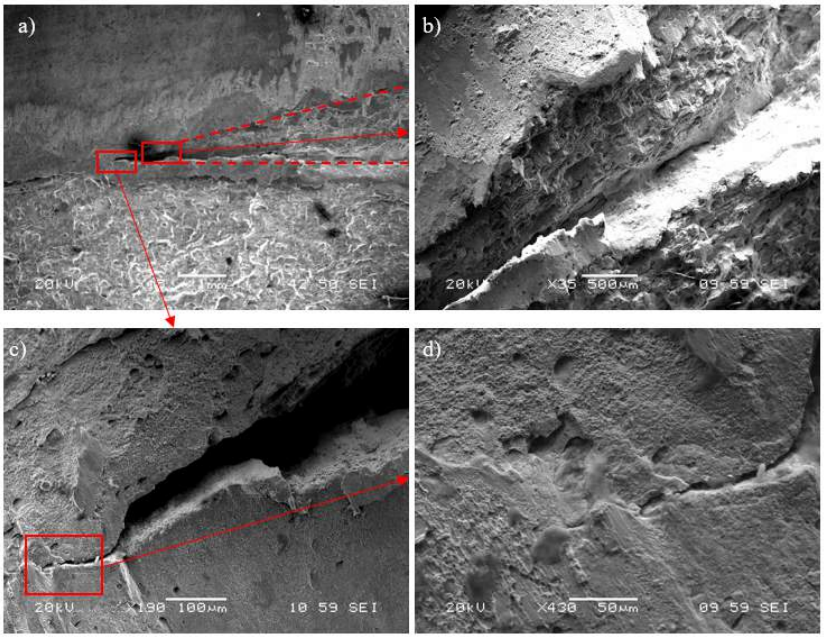

Figure 6.15: SEM micrographs of the main crack dividing the smooth and rough areas.

The evidence suggests the primary mode of failure of this gear was fatigue, which was greatly intensified due to lack of lubrication. The lack of lubricant generated scuffing and heating at the tooth surface, while also increasing the frictional forces. This increased the stresses at the gear, as confirmed by the presence of ratchet marks. These concentrated stresses accelerated the flaking damage and the growing of cracks. Additionally, the effect of possible misalignment caused by turbulence and overload could have an effect on increasing the load even more. The new damaged surface created a non-uniform loading distribution, which leads to crack growth, until it finally reached the fast propagation stage, failing by ductile fracture as evidenced by Figures 6.7 and 6.8.

6.3 WIND TURBINE GENERATOR BEARING

A wind turbine generator bearing, model BB1-7060-B SKF, was provided by a project partner for examination. It is a deep groove ball bearing, single row, with an inner diameter of 150 mm, and 65 mm width. The inner race can be seen in Figure 6.16.

Figure 6.16: Inner racing of wind turbine generator bearing.

The bearing was removed from the wind turbine due to the detection of vibration signals out of the norm by the vibration monitoring system. The vibration trends were reported

to be increasing with time indicating a fault. However, after removal, a visual examination did not reveal any surface-breaking damage.

The inner racing was cut and taken to the SEM. In Figure 6.17a one can see the majority of the surface has shallow scratches, caused by the constant movement of the balls rotating in the inner racing.

Some scratches, however, are deeper, as shown in Figure 6.17b. These scratches are parallel to the rolling direction of the balls and were continuous throughout the entirety of the sample, which might indicate that they were made by debris.

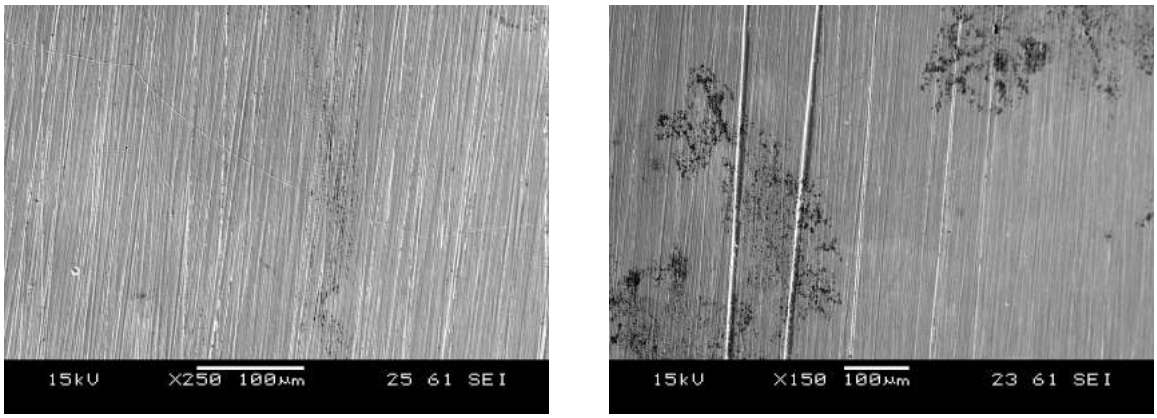

(a) (b)

Figure 6.17: Parallel scratches caused by the ball at the inner racing (a); Two deeper parallel scratches, aligned to the ball rolling direction (b).

A cross-section of the bearing was then cut and prepared for metallographic analysis. The microhardness profile (Figure 6.18) shows the hardness is constant throughout the cross-section, with an average of 690.3 ± 14.2 HV 0.3, thus meeting the requirements set in ISO 281:2007 [178].

The microstructure of the steel is formed of tempered martensite, as shown in Figure 6.19. From the micrographs and the microhardness tests, it is possible to assume that the bearing was through-hardened.

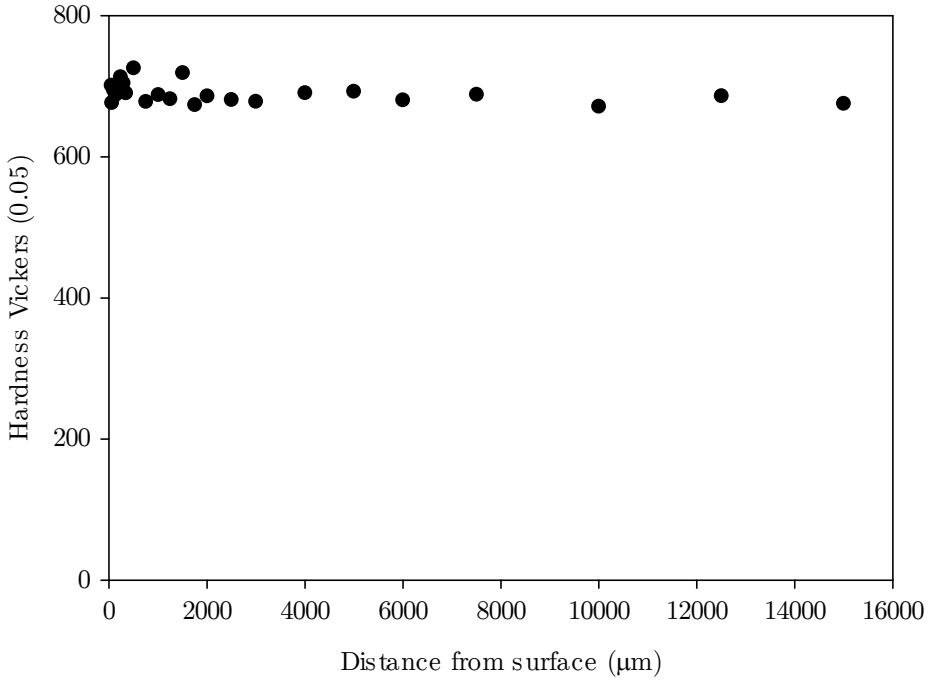

Figure 6.18: Microhardness profile of the bearing.

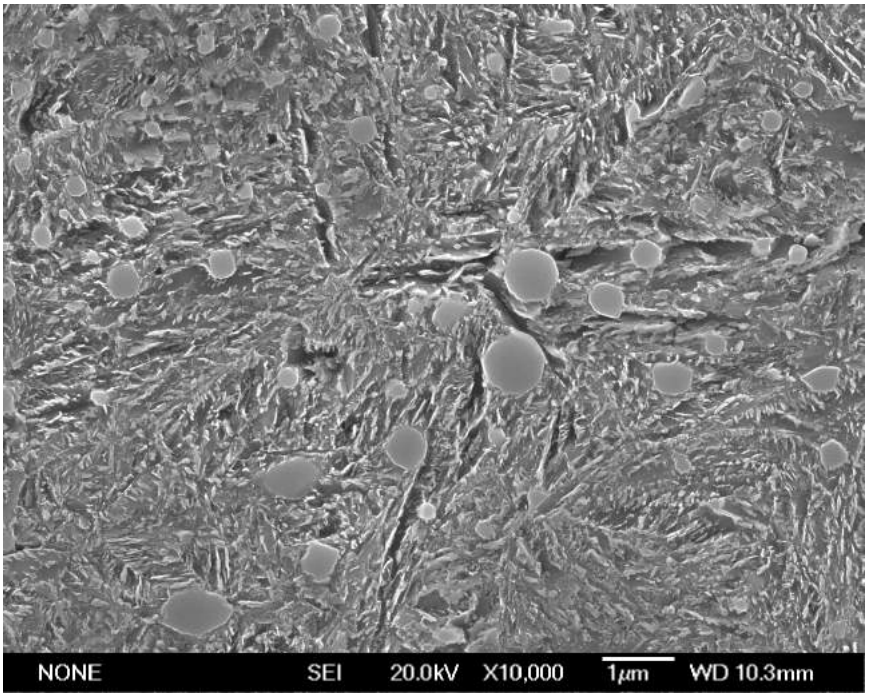

Figure 6.19: Microstructure of the inner racing, showing tempered martensite and finely dispersed carbides. Etched with 2% nital.

Finally, EDS testing was carried out in order to investigate the cleanliness of the steel

and its alloying elements. Several inclusions of different shapes were found in this steel, as presented in Figures 6.20 and 6.21, and Tables 6.3 and 6.4. The steel composition is similar to the EN31 steel, which is often used in bearing production [183].

From the EDS results, the round inclusions show a high titanium content, as well as other strong nitride forming elements, such as niobium and vanadium. The elongated inclusions, on the other hand, were found to be MnS, as shown in Figure 6.21. The steel matrix has a composition of around 2% Cr, 0.3% Si, and 0.8% Mn.

No abnormal amount of wear was found on the surface of the races of the bearing, nor the balls. The steel is relatively clean, and no microcracks were found anywhere during the inspections. Therefore, since the component is in a good health condition, the most probable cause for the out of the norm vibration signals is a misalignment. Misalignment is one of the most common causes for vibration problems in rotating machinery. A misaligned rotor can thus generate excessive vibrations [184].

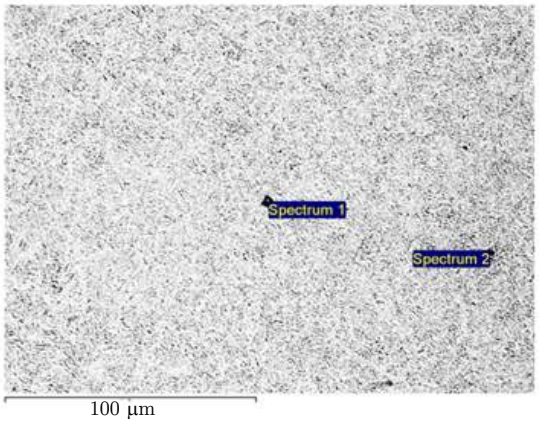

Figure 6.20: SEM micrographs of EDS locations.

Chemical element	**Spectrum 1 (wt%)**	**Spectrum 2 (wt%)**
C	2.7	2.8
Si	-	0.3
Ti	45.6	-
V	3.6	-
Cr	4.9	1.7
Mn	0.5	0.7
Nb	0.9	-
Mo	1.8	-
Fe	40.0	94.6

Table 6.3: EDS results of the locations in Figure 6.20.

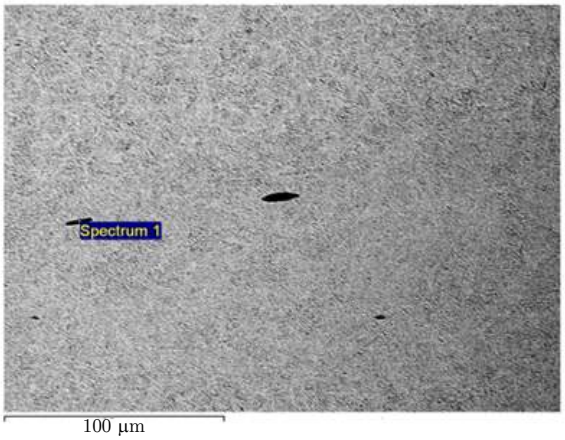

Figure 6.21: SEM micrographs of EDS location.

Chemical element	Spectrum 1 (wt%)
C	3.2
S	22.9
Cr	0.9
Mn	47.0
Fe	26.0

Table 6.4: EDS results of the elongated inclusion in Figure 6.21.

This is a case of misdiagnosis. If a spectral signal analysis was carried out, for example, the bearing tones should not have been detected. Instead, the 1X signals of the high-speed shaft that relates to the misalignment should be clearly distinguishable. Additionally, for the vibration to have been attributed to a bearing fault rather than misalignment, the defect should have been macroscopically visible.

6.4 SUMMARY

In this chapter, three wind turbine components that failed in service were provided by project partners for examination.

The first component was a bearing from the high-speed shaft, with severe micropitting. The material fulfilled the requirements set in the industrial standards. Due to the micropitting concentration on one of the sides of the bearing, misalignment is the most probable root cause. This could have been identified, for example, by employing condition monitoring systems such as vibration and AE monitoring.

The second component was a gear tooth from the intermediate stage of a WTG. The material also fulfilled the requirements set in the standards. Several defects could be identified, with lack of lubrication being the likely root cause of failure. Similarly to what was observed in the RCF experiments, this sample also contained several cracks initiating

from MnS inclusions. The final failure mode arose from fatigue. An inline oil monitoring system would have been able to detect the debris generated from scuffing. Additionally, AE would have been able to detect the subsurface cracking observed at the tooth root.

Finally, the third component received was a generator bearing, which was removed from service due to abnormal vibration signals being detected. In the end, both the material and the component itself were found to be in good condition. The most probable cause for the generation of the abnormal vibration signals is hence misalignment, which is detrimental for the component life. However, this misdiagnosis led to the unnecessary component replacement and associated downtime which could have been avoided by performing the alignment of the component.

From the failure analysis, it is clear that different condition monitoring techniques would be able to detect the defects observed. Additionally, such defects would have been detected in their early stages, avoiding catastrophic failure. Vibration analysis, oil analysis and AE monitoring can provide the wind turbine operators with meaningful information on the health of their assets and thus guide the maintenance scheduling. It is also worthy to note that training to the operators should also be provided since misdiagnosis can also lead to downtime that could be otherwise avoided with a better use and understanding of condition monitoring techniques.

CHAPTER 7

MODELLING FRAMEWORK

7.1 DEFORMATION KINEMATICS

Consider the deformation of an imaginary body from an initial configuration to the current and deformed state, as shown in Figure 7.1.

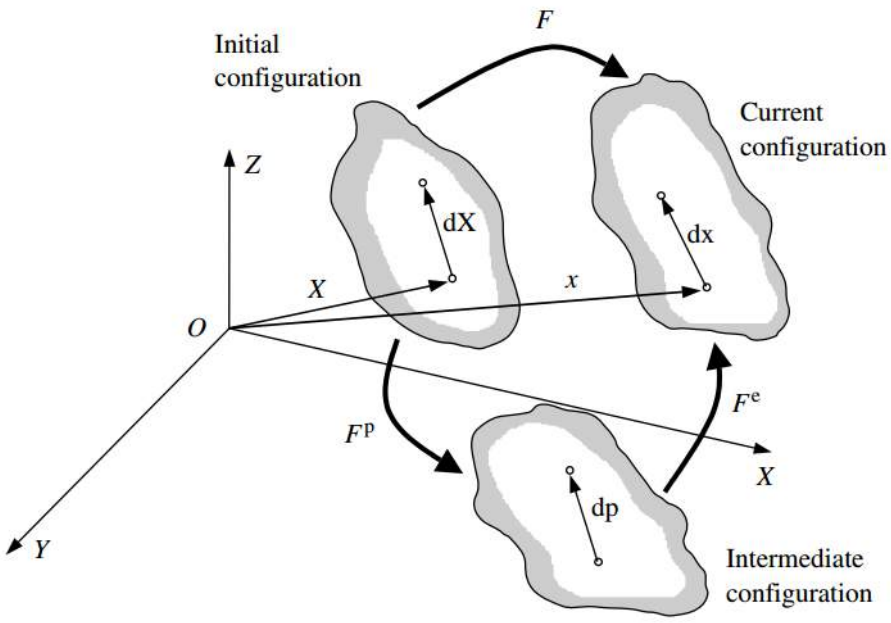

Figure 7.1: Body in initial, intermediate, and current configuration. Source: [129].

As in Figure 2.27, the body in the initial state contains a line vector d$\boldsymbol{X}$, which is transformed to d$\boldsymbol{x}$, through the deformation gradient tensor $\boldsymbol{F}$. The deformation from the initial to the current state can be decomposed into elastic and plastic deformation. The decomposition of the total deformation gradient into elastic and plastic contributions is known as:

$$\boldsymbol{F} = \boldsymbol{F}^e \boldsymbol{F}^p \tag{7.1}$$

This is the classical multiplicative decomposition of the deformation gradient by Erastus

Lee [129]. The rate at which neighbouring points are being displaced is described by the velocity gradient tensor:

$$\boldsymbol{L} = \boldsymbol{F}\dot{\boldsymbol{F}}^{-1} \tag{7.2}$$

and the insertion of equation (7.1) results in:

$$\boldsymbol{L} = \dot{\boldsymbol{F}}^{e}\boldsymbol{F}^{e-1} + \boldsymbol{F}^{e-1}\dot{\boldsymbol{F}}^{p}\boldsymbol{F}^{p-1}\boldsymbol{F}^{e} \tag{7.3}$$

The velocity gradient tensor can then be decomposed into symmetric and anti-symmetric parts, which correspond to the stretch and spin tensors, respectively. The stretch tensor describes the rate of distortion, whereas the spin tensor describes the rate of rotation of the material. These are given by:

$$\boldsymbol{D} = \mathrm{sym}(\boldsymbol{L}) = \frac{1}{2}\left(\boldsymbol{L} + \boldsymbol{L}^{T}\right) \tag{7.4}$$

$$\boldsymbol{W} = \mathrm{asym}(\boldsymbol{L}) = \frac{1}{2}\left(\boldsymbol{L} - \boldsymbol{L}^{T}\right) \tag{7.5}$$

The total stretch and spin tensors can be further decomposed into elastic and plastic contributions:

$$\boldsymbol{D} = \boldsymbol{D}^{e} + \boldsymbol{D}^{p} \tag{7.6}$$

$$\boldsymbol{W} = \boldsymbol{W}^{e} + \boldsymbol{W}^{p} \tag{7.7}$$

As the materials in this study are treated as Von Mises materials, the plastic contribution is given by:

$$\boldsymbol{D}^{p} = \frac{3}{2}\frac{\dot{\varepsilon^{p}}}{\overline{\sigma}}\boldsymbol{S} \tag{7.8}$$

Where $\dot{\varepsilon^{p}}$ is the plastic strain rate and $\boldsymbol{S}$ is the deviatoric stress tensor. The plastic strain rate will be obtained in the following section with the use of a constitutive equation.

With equations 7.6 and 7.7, the change in the local stress can now be deter-

mined. In general, the rate of change of the stress is given by the Jaumann rate of the stress tensor which is obtained from the total and plastic stretch tensors via the constitutive relation:

$$\overset{\triangledown}{\boldsymbol{\sigma}} = \boldsymbol{C}\,(\boldsymbol{D} - \boldsymbol{D}^p) \tag{7.9}$$

The Cauchy ($\dot{\boldsymbol{\sigma}}$) and Jaumman ($\overset{\triangledown}{\boldsymbol{\sigma}}$) stress rates are related through the total spins according to the relation:

$$\overset{\triangledown}{\boldsymbol{\sigma}} = \dot{\boldsymbol{\sigma}} - \boldsymbol{W}.\boldsymbol{\sigma} + \boldsymbol{\sigma}.\boldsymbol{W} \tag{7.10}$$

This last equation is used to update the local stress state.

7.2 CONSTITUTIVE MODEL

There are different ways to approach the modelling of plastic flow of a material. One of the options is to use an empirical model. Several examples of these are given in ref. [185]. For example, the power law shown on equation 7.11 has been extensively used for modelling creep [186].

$$\dot{\varepsilon} = A\ \sigma^n \tag{7.11}$$

Another option is to use a Chaboche style model [187], as was done by Bernhart et al. [188] for modelling the behaviour of a martensitic forging tool steel on high temperature low cycle fatigue. These models take into account both isotropic and kinematic hardening effects. However, extrapolation of these models is not always straight-forward and care must be taken in the parametrisation of its variables.

Yet another option is to employ a microstructure-based physical model instead. These models explicitly link the microstructure of the material to its deformation behaviour. By capturing the physical mechanism driving deformation, these models allow for better extrapolation and prediction of properties. The main challenge associated with this approach is mathematically describing the physical mechanisms in a general and easy to implement way, predicting the behaviour rather than having it hardwired into the

model. Examples of this type of model can be found in refs. [189] and [190].

In this study, a microstructure-based constitutive model based on the model developed by Basoalto and Dyson [191], which is focused on fatigue, has been used in order to determine the plastic strain rate. This model was chosen due to its ability to correlate the plastic strain to tempered martensite microstructure, as will be later discussed.

The theory behind the development of this model is that shortly after yield under monotonic loading, dislocations change in density and distribution, depending on the level of the applied equivalent stress ($\overline{\sigma}$). The creation of dislocations during the accumulation of plastic strain will lead to dislocation interactions, where dislocations of opposite sign attract and trap each other to form dipoles. Most of the dislocations dipoles are composed of edge dislocations of opposite sign since screw dislocations can easily cross slip and mutually annihilate. The network of dislocation dipoles results in bundles or walls of dislocations. In the cell walls, the dislocations are tangled and their density is high, resulting in a heterogeneous distribution of dislocations within localised hard regions. Compatibility requirements between the dislocation walls (hard regions) and channels (soft regions) will give rise to a backstress (σ^{ks}) that seeks to reduce the effective stress acting in the channels as plastic deformation progresses.

Obstacle theories of strain-rate-dependent flow demand that the flow stress is some function of this effective stress divided by an isotropic strength parameter, σ^{is} (equation 7.12). In the case where the particles are obstacles, σ^{is} will be proportional to the Orowan stress.

$$\dot{\varepsilon} \propto f\left(\frac{\overline{\sigma} - \sigma^{ks}}{\sigma^{is}}\right) \tag{7.12}$$

The isotropic strength parameter has two terms. The first one is represented by an obstacle strength term, σ^{p}. This is associated with the lath spacing of tempered martensite. The laths act as barriers for the dislocations, and they have to be overcome for the strain

to increase. The second contribution is from the dislocation interactions. Dislocations on associated slip planes begin to intersect one another, and the resultant network will progressively also form additional barriers.

The model equations used are given by the following set of constitutive equations:

$$\dot{\varepsilon^p} = C^1 \ \rho \ sinh \left(\frac{\overline{\sigma} - \sigma^{ks}}{\sigma^{is}(1-\psi)} \right) \tag{7.13}$$

$$\dot{\sigma}^{ks} = h^s \left(1 - \frac{\sigma^{ks}}{H^* \ \overline{\sigma}} \right) \dot{\varepsilon^p} \tag{7.14}$$

$$\dot{\rho} = C^2 \ \sqrt{\rho} \left(1 - \sqrt{\frac{\rho}{\rho^{ss}}} \right) \dot{\varepsilon^p} \tag{7.15}$$

$$\dot{\psi} = \left(\frac{k^D}{(1-\psi)} \right) \dot{\varepsilon^p} \tag{7.16}$$

$$\rho^{ss} = \left[C^3 \left(\frac{\overline{\sigma} - \sigma^{ks}}{1-\psi} \right) \right]^2 \tag{7.17}$$

$$\sigma^{is} = \sqrt{(\sigma^p)^2 + C^4 \ \rho} \tag{7.18}$$

$$\sigma^p = \frac{MkT\sigma^{or}}{Gb_v^3} \tag{7.19}$$

$$C^1 = \dot{\varepsilon}_0'' \ exp \left(\frac{-Q_{j/v}}{RT} \right) \tag{7.20}$$

$$C^2 = \frac{M}{b_v \beta} \tag{7.21}$$

$$C^3 = \frac{2\pi}{b_v \beta G M} \tag{7.22}$$

$$C^4 = \left(\frac{kT}{b_v^2} \right)^2 \tag{7.23}$$

The model parameters (Table 7.1) were found by fitting the equations to the tensile data.

Table 7.1: Model parameters and descriptions.

Parameter	**Description**	**Value**	**Unit**
$\dot{\varepsilon^p}$	Plastic strain rate	Variable	s^{-1}
ρ	Mobile dislocation density	Variable	m^{-2}

Table 7.1: Model parameters and descriptions.

Parameter	**Description**	**Value**	**Unit**
$\overline{\sigma}$	Applied equivalent stress	Variable	MPa
σ^{ks}	Substructural substructural kinematic stress	Variable	MPa
σ^{is}	Isotropic strength parameter	Variable	MPa
ψ	Damage parameter	Variable	-
h^s	Effective modulus of the hard phase	10000	MPa
H^*	Maximum possible stress that can be redistributed	0.36	-
$\dot{\rho}$	Rate of change of dislocation density	Variable	m^{-2} s^{-1}
ρ^{ss}	Steady state mobile dislocation density	Variable	m^{-2}
$\dot{\psi}$	Rate of change of damage	Variable	-
k_D	Model parameter	2.675	- s^{-1}
σ_p	Obstacle strength parameter	Variable	MPa
M	Taylor factor	3.1	-
k	Boltzmann constant	1.38×10^{-23}	m^2 kg s^{-2} K^{-1}
T_p	Temperature	293.15	K
σ^{or}	Orowan stress	1000	MPa
G	Shear modulus	60150	MPa
b_v	Burger's vector	2.4×10^{-10}	m
$\dot{\varepsilon}_0^{''}$	Model parameter	1.5×10^{14}	$m^2 s^{-1}$
$Q_{j/v}$	Diffusion activation energy	3×10^5	J mol^{-1}
R	Gas constant	8.314	J mol^{-1} K^{-1}
β	Constant reflecting statistical nature of the process	250	-
$C1, C2, C3, C4$	Constants	-	-

In the above equations, the kinematic stress is grouped in the numerator of the hyperbolic sine, whereas the isotropic stress goes into the denominator. The justification is that kinematic stresses arise from field interactions between dislocations and/or dislocation/particles and alter the effective stress. The isotropic strength parameter, however, measures the strength of the obstacles impeding dislocation motion and is not to be confused with the applied stress.

Currently, the exact evolution relation for σ^{ks} is unknown. However, a stress transfer evolution relationship that takes into account the stress transfer between the hard carbides and the matrix can be set as a starting point. With this approach, two parameters are used: the effective modulus of the hard phase, h^s, and the maximum possible stress that can be redistributed, H^*. A disadvantage of this approach is that h^s is a constant, and therefore it does not reflect the gradual build-up of hard regions. Instead, it assumes that they were already present and do not change.

The dislocation multiplication kinetics described by $\dot{\rho}$ were derived from a continuum description of plastic flow based on a dislocation generation-trapping model, where the rate of change of the mobile dislocation density, ρ, is given by the generation rate subtracted of the rate of trapping [192–194]. The trapping term is associated with the formation of dislocation dipoles, whereas the generation term arises from a dislocation multiplication mechanism. The details can be found in ref. [191].

Similarly, the evolution of the damage ($\dot{\psi}$) is also unknown. Nevertheless, a Kachanov-Rabotnov approach is used. A parabolic evolution is thought to describe well the evolution of damage - as more damage is initiated, the easier it is for more damage to initiate - and thus the lifetime reduces exponentially.

In order to simulate the stress/strain behaviour, the above equations must be supplemented with an additional equation that governs the applied load evolution, as well as the initial boundary conditions. In this work, it will be assumed that the spins can be ignored, and thus, from equation 7.10, the Jaumann rate becomes the Cauchy rate. Therefore, the stress evolution is given by the following equation:

$$\dot{\boldsymbol{\sigma}} = \boldsymbol{C} \ (\boldsymbol{D} - \boldsymbol{D^p}) \tag{7.24}$$

The equations listed above can be solved either explicitly or implicitly. Implicit integration algorithms, while harder to implement, ensure that the answers are unconditionally stable. Additionally, they are less dependant on the time step size than the explicit integration

scheme. In order to guarantee a stable solution, the implicit integration technique was chosen and implemented in this work.

7.2.1 Implicit integration

A Newton-Ralphson implicit algorithm was used solve the system of non-linear equations.

An $\boldsymbol{X}$ vector is then created, and its components are formed by the four state variables and the six stress components, as is shown in equation 7.25:

$$\boldsymbol{X} = \begin{bmatrix} \varepsilon^p \\ \sigma^{ks} \\ \rho \\ \psi \\ \sigma_1 \\ \cdots \\ \sigma_6 \end{bmatrix} = X_i \tag{7.25}$$

The rate of change of the $\boldsymbol{X}$ vector, $\dot{\boldsymbol{X}}$, is then defined by equation 7.26:

$$\dot{\boldsymbol{X}} = \begin{bmatrix} \dot{\varepsilon}^p \\ \dot{\sigma}^{ks} \\ \dot{\rho} \\ \dot{\psi} \\ \dot{\sigma}_1 \\ \cdots \\ \dot{\sigma}_6 \end{bmatrix} = \boldsymbol{f}(\boldsymbol{X}, t) \tag{7.26}$$

In an implicit method, a solution is found by solving an equation involving both the current state of the system and the later one, in this case:

$$\boldsymbol{X}_{(t+\triangle t)} = \boldsymbol{X}_t + \dot{\boldsymbol{X}}_{(t+\triangle t)} \ \triangle t \tag{7.27}$$

Where t is time. Let $\boldsymbol{X}_{(t+\triangle t)}$ be $\boldsymbol{X}^n$, $\boldsymbol{X}_t$ be $\boldsymbol{X}^0$, and $\dot{\boldsymbol{X}}_{(t+\triangle t)}$ be $\dot{\boldsymbol{X}}^n$. The new equation is:

$$\boldsymbol{X}^n = \boldsymbol{X}^0 + \dot{\boldsymbol{X}}^n \triangle t \tag{7.28}$$

It is now possible to construct the function $\boldsymbol{G}$:

$$\boldsymbol{G}(\boldsymbol{X}^n) = \boldsymbol{X}^n - \boldsymbol{X}^0 - \dot{\boldsymbol{X}}^n \triangle t \tag{7.29}$$

The idea is to find a value for $\boldsymbol{X} = \boldsymbol{X}^*$ such that $\boldsymbol{G}(\boldsymbol{X}^*) = 0$.

The Newton-Raphson method is an iterative method for finding successively better approximations to the roots of a function, and is given by equation 7.30:

$$\boldsymbol{X}^{n+1} = \boldsymbol{X}^n - \boldsymbol{J}^{-1}(\boldsymbol{X}^n) \cdot \boldsymbol{G}(\boldsymbol{X}^n) \tag{7.30}$$

For the first iteration, $n = 0$ and $\boldsymbol{X}^0$ is given by the boundary conditions shown in equation 7.31, with all values being null with the exception of ρ:

$$\boldsymbol{X}^0 = \begin{bmatrix} \varepsilon^p \\ \sigma^{ks} \\ \rho \\ \psi \\ \sigma_1 \\ \dots \\ \sigma_6 \end{bmatrix} = \begin{bmatrix} 0.0 \\ 0.0 \\ 10^{10} \\ 0.0 \\ 0.0 \\ \dots \\ 0.0 \end{bmatrix} \tag{7.31}$$

And $\boldsymbol{J}$ is the Jacobian, defined in the equation 7.32:

$$\boldsymbol{J}(\boldsymbol{X}^n) = \frac{\partial \boldsymbol{G}}{\partial \boldsymbol{X}} = \boldsymbol{I} - \frac{\partial \dot{\boldsymbol{X}}}{\partial \boldsymbol{X}} \tag{7.32}$$

Where $\boldsymbol{I}$ is the identity matrix and $\frac{\partial \dot{\boldsymbol{X}}}{\partial \boldsymbol{X}}$ is given by:

$$\frac{\partial \dot{\boldsymbol{X}}}{\partial \boldsymbol{X}} = \begin{bmatrix}
\frac{\partial \dot{\varepsilon^p}}{\partial \varepsilon^p} & \frac{\partial \dot{\varepsilon^p}}{\partial \sigma^{ks}} & \frac{\partial \dot{\varepsilon^p}}{\partial \rho} & \frac{\partial \dot{\varepsilon^p}}{\partial \psi} & \frac{\partial \dot{\varepsilon^p}}{\partial \sigma_1} & \frac{\partial \dot{\varepsilon^p}}{\partial \sigma_2} & \frac{\partial \dot{\varepsilon^p}}{\partial \sigma_3} & \frac{\partial \dot{\varepsilon^p}}{\partial \sigma_4} & \frac{\partial \dot{\varepsilon^p}}{\partial \sigma_5} & \frac{\partial \dot{\varepsilon^p}}{\partial \sigma_6} \\
\frac{\partial \dot{\sigma}^{ks}}{\partial \varepsilon^p} & \frac{\partial \dot{\sigma}^{ks}}{\partial \sigma^{ks}} & \frac{\partial \dot{\sigma}^{ks}}{\partial \rho} & \frac{\partial \dot{\sigma}^{ks}}{\partial \psi} & \frac{\partial \dot{\sigma}^{ks}}{\partial \sigma_1} & \frac{\partial \dot{\sigma}^{ks}}{\partial \sigma_2} & \frac{\partial \dot{\sigma}^{ks}}{\partial \sigma_3} & \frac{\partial \dot{\sigma}^{ks}}{\partial \sigma_4} & \frac{\partial \dot{\sigma}^{ks}}{\partial \sigma_5} & \frac{\partial \dot{\sigma}^{ks}}{\partial \sigma_6} \\
\frac{\partial \dot{\rho}}{\partial \varepsilon^p} & \frac{\partial \dot{\rho}}{\partial \sigma^{ks}} & \frac{\partial \dot{\rho}}{\partial \rho} & \frac{\partial \dot{\rho}}{\partial \psi} & \frac{\partial \dot{\rho}}{\partial \sigma_1} & \frac{\partial \dot{\rho}}{\partial \sigma_2} & \frac{\partial \dot{\rho}}{\partial \sigma_3} & \frac{\partial \dot{\rho}}{\partial \sigma_4} & \frac{\partial \dot{\rho}}{\partial \sigma_5} & \frac{\partial \dot{\rho}}{\partial \sigma_6} \\
\frac{\partial \dot{\psi}}{\partial \varepsilon^p} & \frac{\partial \dot{\psi}}{\partial \sigma^{ks}} & \frac{\partial \dot{\psi}}{\partial \rho} & \frac{\partial \dot{\psi}}{\partial \psi} & \frac{\partial \dot{\psi}}{\partial \sigma_1} & \frac{\partial \dot{\psi}}{\partial \sigma_2} & \frac{\partial \dot{\psi}}{\partial \sigma_3} & \frac{\partial \dot{\psi}}{\partial \sigma_4} & \frac{\partial \dot{\psi}}{\partial \sigma_5} & \frac{\partial \dot{\psi}}{\partial \sigma_6} \\
\frac{\partial \dot{\sigma}_1}{\partial \varepsilon^p} & \frac{\partial \dot{\sigma}_1}{\partial \sigma^{ks}} & \frac{\partial \dot{\sigma}_1}{\partial \rho} & \frac{\partial \dot{\sigma}_1}{\partial \psi} & \frac{\partial \dot{\sigma}_1}{\partial \sigma_1} & \frac{\partial \dot{\sigma}_1}{\partial \sigma_2} & \frac{\partial \dot{\sigma}_1}{\partial \sigma_3} & \frac{\partial \dot{\sigma}_1}{\partial \sigma_4} & \frac{\partial \dot{\sigma}_1}{\partial \sigma_5} & \frac{\partial \dot{\sigma}_1}{\partial \sigma_6} \\
\frac{\partial \dot{\sigma}_2}{\partial \varepsilon^p} & \frac{\partial \dot{\sigma}_2}{\partial \sigma^{ks}} & \frac{\partial \dot{\sigma}_2}{\partial \rho} & \frac{\partial \dot{\sigma}_2}{\partial \psi} & \frac{\partial \dot{\sigma}_2}{\partial \sigma_1} & \frac{\partial \dot{\sigma}_2}{\partial \sigma_2} & \frac{\partial \dot{\sigma}_2}{\partial \sigma_3} & \frac{\partial \dot{\sigma}_2}{\partial \sigma_4} & \frac{\partial \dot{\sigma}_2}{\partial \sigma_5} & \frac{\partial \dot{\sigma}_2}{\partial \sigma_6} \\
\frac{\partial \dot{\sigma}_3}{\partial \varepsilon^p} & \frac{\partial \dot{\sigma}_3}{\partial \sigma^{ks}} & \frac{\partial \dot{\sigma}_3}{\partial \rho} & \frac{\partial \dot{\sigma}_3}{\partial \psi} & \frac{\partial \dot{\sigma}_3}{\partial \sigma_1} & \frac{\partial \dot{\sigma}_3}{\partial \sigma_2} & \frac{\partial \dot{\sigma}_3}{\partial \sigma_3} & \frac{\partial \dot{\sigma}_3}{\partial \sigma_4} & \frac{\partial \dot{\sigma}_3}{\partial \sigma_5} & \frac{\partial \dot{\sigma}_3}{\partial \sigma_6} \\
\frac{\partial \dot{\sigma}_4}{\partial \varepsilon^p} & \frac{\partial \dot{\sigma}_4}{\partial \sigma^{ks}} & \frac{\partial \dot{\sigma}_4}{\partial \rho} & \frac{\partial \dot{\sigma}_4}{\partial \psi} & \frac{\partial \dot{\sigma}_4}{\partial \sigma_1} & \frac{\partial \dot{\sigma}_4}{\partial \sigma_2} & \frac{\partial \dot{\sigma}_4}{\partial \sigma_3} & \frac{\partial \dot{\sigma}_4}{\partial \sigma_4} & \frac{\partial \dot{\sigma}_4}{\partial \sigma_5} & \frac{\partial \dot{\sigma}_4}{\partial \sigma_6} \\
\frac{\partial \dot{\sigma}_5}{\partial \varepsilon^p} & \frac{\partial \dot{\sigma}_5}{\partial \sigma^{ks}} & \frac{\partial \dot{\sigma}_5}{\partial \rho} & \frac{\partial \dot{\sigma}_5}{\partial \psi} & \frac{\partial \dot{\sigma}_5}{\partial \sigma_1} & \frac{\partial \dot{\sigma}_5}{\partial \sigma_2} & \frac{\partial \dot{\sigma}_5}{\partial \sigma_3} & \frac{\partial \dot{\sigma}_5}{\partial \sigma_4} & \frac{\partial \dot{\sigma}_5}{\partial \sigma_5} & \frac{\partial \dot{\sigma}_5}{\partial \sigma_6} \\
\frac{\partial \dot{\sigma}_6}{\partial \varepsilon^p} & \frac{\partial \dot{\sigma}_6}{\partial \sigma^{ks}} & \frac{\partial \dot{\sigma}_6}{\partial \rho} & \frac{\partial \dot{\sigma}_6}{\partial \psi} & \frac{\partial \dot{\sigma}_6}{\partial \sigma_1} & \frac{\partial \dot{\sigma}_6}{\partial \sigma_2} & \frac{\partial \dot{\sigma}_6}{\partial \sigma_3} & \frac{\partial \dot{\sigma}_6}{\partial \sigma_4} & \frac{\partial \dot{\sigma}_6}{\partial \sigma_5} & \frac{\partial \dot{\sigma}_6}{\partial \sigma_6}
\end{bmatrix} \tag{7.33}$$

Therefore, in order to calculate the Jacobian and run the Newton-Raphson algorithm, the components of the $\frac{\partial \dot{\boldsymbol{X}}}{\partial \boldsymbol{X}}$ tensor need to be solved.

The partial derivatives will be solved line by line. The first component is (1,1), given by:

$$\frac{\partial \dot{\varepsilon^p}}{\partial \varepsilon^p} = \frac{\partial}{\partial \varepsilon^p}\left[C_1\ \rho\ sinh\left(\frac{\overline{\sigma} - \sigma^{ks}}{\sigma^{is}(1-\psi)}\right)\right] = 0 \tag{7.34}$$

Since $\dot{\varepsilon^p}$ does not depend on ε^p. The next component is the (1,2), given by:

$$\frac{\partial \dot{\varepsilon^p}}{\partial \sigma^{ks}} = \frac{\partial}{\partial \sigma^{ks}} \left[C_1 \ \rho \ \sinh \left(\frac{\overline{\sigma} - \sigma^{ks}}{\sigma^{is}(1-\psi)} \right) \right] \tag{7.35}$$

$$= C_1 \ \rho \ \frac{\partial}{\partial \sigma^{ks}} \left[\sinh \left(\frac{\overline{\sigma} - \sigma^{ks}}{\sigma^{is}(1-\psi)} \right) \right] \tag{7.36}$$

$$= C_1 \ \rho \ \cosh \left(\frac{\overline{\sigma} - \sigma^{ks}}{\sigma^{is}(1-\psi)} \right) \ \frac{\partial}{\partial \sigma^{ks}} \left(\frac{\overline{\sigma} - \sigma^{ks}}{\sigma^{is}(1-\psi)} \right) \tag{7.37}$$

$$= C_1 \ \rho \ \cosh \left(\frac{\overline{\sigma} - \sigma^{ks}}{\sigma^{is}} \right) \ \frac{\partial}{\partial \sigma^{ks}} \left(\frac{-\sigma^{ks}}{\sigma^{is}(1-\psi)} \right) \tag{7.38}$$

$$= -\frac{C_1 \ \rho}{\sigma^{is}(1-\psi)} \cosh \left(\frac{\overline{\sigma} - \sigma^{ks}}{\sigma^{is}(1-\psi)} \right) \tag{7.39}$$

For the sake of convenience, we can write:

$$\frac{\partial \dot{\varepsilon^p}}{\partial \sigma^{ks}} = -\frac{C_1 \ \rho}{\sigma^{is}(1-\psi)} \cosh \left(\sigma^{total} \right) \tag{7.40}$$

By considering:

$$\sigma^{total} = \frac{\overline{\sigma} - \sigma^{ks}}{\sigma^{is}(1-\psi)} \tag{7.41}$$

The next component is (1,3):

$$\frac{\partial \dot{\varepsilon^p}}{\partial \rho} = \frac{\partial}{\partial \rho} \left[C_1 \ \rho \ sinh \left(\frac{\overline{\sigma} - \sigma^{ks}}{\sigma^{is}(1-\psi)} \right) \right] \tag{7.42}$$

$$= C_1 \ \frac{\partial}{\partial \rho} \left[\rho \ sinh \left(\frac{\overline{\sigma} - \sigma^{ks}}{\sigma^{is}(1-\psi)} \right) \right] \tag{7.43}$$

Solving it with the use of the chain rule:

$$\frac{\partial \dot{\varepsilon^p}}{\partial \rho} = C_1 \left[\rho \frac{\partial}{\partial \rho} \left(\sinh \left(\frac{\overline{\sigma} - \sigma^{ks}}{\sigma^{is}(1-\psi)} \right) \right) + \sinh \left(\frac{\overline{\sigma} - \sigma^{ks}}{\sigma^{is}(1-\psi)} \right) \right] \tag{7.44}$$

$$= C_1 \rho \cosh \left(\frac{\overline{\sigma} - \sigma^{ks}}{\sigma^{is}(1-\psi)} \right) \frac{\partial}{\partial \rho} \left(\frac{\overline{\sigma} - \sigma^{ks}}{\sigma^{is}(1-\psi)} \right) + C_1 \sinh \left(\frac{\overline{\sigma} - \sigma^{ks}}{\sigma^{is}(1-\psi)} \right) \tag{7.45}$$

$$= C_1 \rho \cosh \left(\sigma^{total} \right) \left(\frac{\overline{\sigma} - \sigma^{ks}}{(1-\psi)} \right) \frac{\partial}{\partial \rho} \left(\frac{1}{\sigma^{is}} \right) + \frac{\dot{\varepsilon^p}}{\rho} \tag{7.46}$$

$$= C_1 \rho \cosh \left(\sigma^{total} \right) \left(\frac{\overline{\sigma} - \sigma^{ks}}{(1-\psi)} \right) \frac{-1}{(\sigma^{is})^2} \frac{\partial \sigma^{is}}{\partial \rho} + \frac{\dot{\varepsilon^p}}{\rho} \tag{7.47}$$

Rearranging the terms, we get:

$$\frac{\partial \dot{\varepsilon^p}}{\partial \rho} = \frac{\dot{\varepsilon^p}}{\rho} - C_1 \rho \cosh \left(\sigma^{total} \right) \frac{\sigma^{total}}{\sigma^{is}} \frac{\partial \sigma^{is}}{\partial \rho} \tag{7.48}$$

Therefore, in order to evaluate the fourth component of the first line, the partial derivative of σ^{is} with respect to ρ needs to be calculated:

$$\frac{\partial \sigma^{is}}{\partial \rho} = \frac{\partial}{\partial \rho} \left(\sqrt{(\sigma^p)^2 + C_4 \rho} \right) \tag{7.49}$$

$$= \frac{1}{2 \sqrt{(\sigma^p)^2 + C_4 \rho}} \frac{\partial}{\partial \rho} \left((\sigma^p)^2 + C_4 \rho \right) \tag{7.50}$$

$$= \frac{C_4}{2 \sigma^{is}} \tag{7.51}$$

And thus, finally, the third component of the first line is:

$$\frac{\partial \dot{\varepsilon^p}}{\partial \rho} = \frac{\dot{\varepsilon^p}}{\rho} - \frac{C_1 C_4 \rho \sigma^{total}}{2 (\sigma^{is})^2} \cosh \left(\sigma^{total} \right) \tag{7.52}$$

The fourth component is given by:

$$\frac{\partial \dot{\varepsilon^p}}{\partial \psi} = \frac{\partial}{\partial \psi}\left[C_1\ \rho\ sinh\left(\frac{\overline{\sigma}-\sigma^{ks}}{\sigma^{is}(1-\psi)}\right)\right] \tag{7.53}$$

$$= C_1\ \rho\ \frac{\partial}{\partial \psi}\left[\ sinh\left(\frac{\overline{\sigma}-\sigma^{ks}}{\sigma^{is}(1-\psi)}\right)\right] \tag{7.54}$$

$$= C_1\ \rho\ \ cosh\left(\frac{\overline{\sigma}-\sigma^{ks}}{\sigma^{is}(1-\psi)}\right)\frac{\partial}{\partial \psi}\left(\frac{\overline{\sigma}-\sigma^{ks}}{\sigma^{is}(1-\psi)}\right) \tag{7.55}$$

$$= C_1\ \rho\ \ cosh\left(\sigma^{total}\right)\left(\frac{\overline{\sigma}-\sigma^{ks}}{\sigma^{is}}\right)\frac{\partial}{\partial \psi}\frac{1}{(1-\psi)} \tag{7.56}$$

$$= C_1\ \rho\ \ cosh\left(\sigma^{total}\right)\left(\frac{\overline{\sigma}-\sigma^{ks}}{\sigma^{is}}\right)\frac{-1}{(1-\psi)^2}(-1) \tag{7.57}$$

$$= \frac{C_1\ \rho\ \sigma^{total}}{(1-\psi)}\ \ cosh\left(\sigma^{total}\right) \tag{7.58}$$

The components (1,5) to (1,10) can be calculated together if we consider the σ_i vector:

$$\frac{\partial \dot{\varepsilon^p}}{\partial \sigma_i} = \frac{\partial}{\partial \sigma_i}\left[C_1\ \rho\ sinh\left(\frac{\overline{\sigma}-\sigma^{ks}}{\sigma^{is}(1-\psi)}\right)\right] \tag{7.59}$$

$$= C_1\ \rho\ \frac{\partial}{\partial \sigma_i}\left[\ sinh\left(\frac{\overline{\sigma}-\sigma^{ks}}{\sigma^{is}(1-\psi)}\right)\right] \tag{7.60}$$

$$= C_1\ \rho \cosh\left(\frac{\overline{\sigma}-\sigma^{ks}}{\sigma^{is}(1-\psi)}\right)\frac{\partial}{\partial \sigma_i}\left(\frac{\overline{\sigma}-\sigma^{ks}}{\sigma^{is}(1-\psi)}\right) \tag{7.61}$$

$$= C_1\ \rho \cosh\left(\sigma^{total}\right)\frac{\partial}{\partial \sigma_i}\left(\frac{\overline{\sigma}}{\sigma^{is}(1-\psi)}\right) \tag{7.62}$$

$$= \frac{C_1\ \rho}{\sigma^{is}(1-\psi)} \cosh\left(\sigma^{total}\right)\frac{\partial \overline{\sigma}}{\partial \sigma_i} \tag{7.63}$$

The partial derivative of the Von Mises stress with respect to the stress tensor can be written as:

$$\frac{\partial \overline{\sigma}}{\partial \sigma_i} = \frac{\partial \overline{\sigma}}{\partial S_j} \cdot \frac{\partial S_j}{\partial \sigma_i} \tag{7.64}$$

where S_j is the deviatoric stress vector. The equations for the deviatoric stress and the Von Mises stress are:

$$\overline{\sigma}^2 = \frac{3}{2} S_j \cdot S_j \tag{7.65}$$

$$S_j = \sigma_j - \frac{1}{3} tr(\sigma)\delta_j \tag{7.66}$$

And thus the partial derivatives on equation 7.64 can be written as:

$$2\overline{\sigma}\frac{\partial \overline{\sigma}}{\partial S_j} = \frac{3}{2}\left(S_j \frac{\partial S_j}{\partial S_j} + \frac{\partial S_j}{\partial S_j} S_j\right) \tag{7.67}$$

$$2\overline{\sigma}\frac{\partial \overline{\sigma}}{\partial S_j} = \frac{3}{2}\left(2\ S_j\right) \tag{7.68}$$

$$\frac{\partial \overline{\sigma}}{\partial S_j} = \frac{3}{2\ \overline{\sigma}}\ S_j \tag{7.69}$$

and

$$\frac{\partial S_j}{\partial \sigma_i} = \frac{\partial}{\partial \sigma_i}\left(\sigma_j - \frac{1}{3}\sigma_{kk}\delta_j\right) \tag{7.70}$$

$$= \delta_{ij} - \frac{1}{3}\delta_{ik}\delta_{jk} \tag{7.71}$$

$$= \delta_{ij} - \frac{1}{3}\delta_{ij} \tag{7.72}$$

$$= \frac{2}{3}\delta_{ij} \tag{7.73}$$

Therefore, the last item needed to complete the components (1,5) to (1,10) is:

$$\frac{\partial \overline{\sigma}}{\partial \sigma_i} = \frac{\delta_{ij}\ S_j}{\overline{\sigma}} \tag{7.74}$$

And this completes the first line of the $\frac{\partial \dot{\boldsymbol{X}}}{\partial \boldsymbol{X}}$ matrix. The second line of the $\frac{\partial \dot{\boldsymbol{X}}}{\partial \boldsymbol{X}}$ matrix will now be calculated. The first component, (2,1), is given by:

$$\frac{\partial \dot{\sigma}^{ks}}{\partial \varepsilon^p} = \frac{\partial}{\partial \varepsilon^p}\left[h^s\left(1 - \frac{\sigma^{ks}}{H^*\ \overline{\sigma}}\right)\dot{\varepsilon^p}\right] = 0 \tag{7.75}$$

Since $\dot{\sigma}^{ks}$ does not depend on ε^p. The term (2,2) is then:

$$\frac{\partial \dot{\sigma}^{ks}}{\partial \sigma^{ks}} = \frac{\partial}{\partial \sigma^{ks}}\left[h^s\left(1 - \frac{\sigma^{ks}}{H^*\overline{\sigma}}\right)\dot{\varepsilon^p}\right] \tag{7.76}$$

$$= h^s\frac{\partial \dot{\varepsilon^p}}{\partial \sigma^{ks}} - \frac{h^s}{H^*\ \overline{\sigma}}\ \frac{\partial}{\partial \sigma^{ks}}\left(\sigma^{ks}\dot{\varepsilon^p}\right) \tag{7.77}$$

$$= h^s\frac{\partial \dot{\varepsilon^p}}{\partial \sigma^{ks}} - \frac{h^s}{H^*\ \overline{\sigma}}\left(\sigma^{ks}\frac{\partial \dot{\varepsilon^p}}{\partial \sigma^{ks}} + \dot{\varepsilon^p}\right) \tag{7.78}$$

$$= h^s\left(1 - \frac{\sigma^{ks}}{H^*\ \overline{\sigma}}\right)\frac{\partial \dot{\varepsilon^p}}{\partial \sigma^{ks}} - \frac{h^s\dot{\varepsilon^p}}{H^*\ \overline{\sigma}} \tag{7.79}$$

$$= \frac{\dot{\sigma}^{ks}}{\dot{\varepsilon^p}}\frac{\partial \dot{\varepsilon^p}}{\partial \sigma^{ks}} - \frac{h^s\dot{\varepsilon^p}}{H^*\ \overline{\sigma}} \tag{7.80}$$

And the component (2,3):

$$\frac{\partial \dot{\sigma}^{ks}}{\partial \rho} = \frac{\partial}{\partial \rho}\left[h^s\left(1 - \frac{\sigma^{ks}}{H^*\ \overline{\sigma}}\right)\dot{\varepsilon^p}\right] \tag{7.81}$$

$$= h^s\left(1 - \frac{\sigma^{ks}}{H^*\ \overline{\sigma}}\right)\frac{\partial \dot{\varepsilon^p}}{\partial \rho} \tag{7.82}$$

$$= \frac{\dot{\sigma}^{ks}}{\dot{\varepsilon^p}}\frac{\partial \dot{\varepsilon^p}}{\partial \rho} \tag{7.83}$$

The component (2,4) is given by:

$$\frac{\partial \dot{\sigma}^{ks}}{\partial \psi} = \frac{\partial}{\partial \psi}\left[h^s\left(1 - \frac{\sigma^{ks}}{H^*\ \overline{\sigma}}\right)\dot{\varepsilon^p}\right] \tag{7.84}$$

$$= h^s\left(1 - \frac{\sigma^{ks}}{H^*\ \overline{\sigma}}\right)\frac{\partial \dot{\varepsilon^p}}{\partial \psi} \tag{7.85}$$

$$= \frac{\dot{\sigma}^{ks}}{\dot{\varepsilon^p}}\frac{\partial \dot{\varepsilon^p}}{\partial \psi} \tag{7.86}$$

The components (2,5) to (2,10) can be calculated together:

$$\frac{\partial \dot{\sigma}^{ks}}{\partial \sigma_i} = \frac{\partial}{\partial \sigma_i}\left[h^s\left(1 - \frac{\sigma^{ks}}{H^*\,\overline{\sigma}}\right)\dot{\varepsilon^p}\right] \tag{7.87}$$

$$= h^s \frac{\partial \dot{\varepsilon^p}}{\partial \sigma_i} - \frac{h^s \sigma^{ks}}{H^*}\frac{\partial}{\partial \sigma_i}\left(\frac{\dot{\varepsilon^p}}{\overline{\sigma}}\right) \tag{7.88}$$

The first partial derivative is already known (equation 7.63), and the second one can be calculated with the chain rule:

$$\frac{\partial}{\partial \sigma_i}\left(\frac{\dot{\varepsilon^p}}{\overline{\sigma}}\right) = \dot{\varepsilon^p}\left(\frac{-1}{(\overline{\sigma})^2}\right)\frac{\partial \overline{\sigma}}{\partial \sigma_i} + \frac{1}{\overline{\sigma}}\frac{\partial \dot{\varepsilon^p}}{\partial \sigma_i} \tag{7.89}$$

$$= \frac{1}{\overline{\sigma}}\frac{\partial \dot{\varepsilon^p}}{\partial \sigma_i} - \frac{\dot{\varepsilon^p}}{(\overline{\sigma})^2}\frac{\partial \overline{\sigma}}{\partial \sigma_i} \tag{7.90}$$

Substituting equation 7.90 into equation 7.88 we get:

$$\frac{\partial \dot{\sigma}^{ks}}{\partial \sigma_i} = h^s \frac{\partial \dot{\varepsilon^p}}{\partial \sigma_i} - \frac{h^s \sigma^{ks}}{H^*}\left(\frac{1}{\overline{\sigma}}\frac{\partial \dot{\varepsilon^p}}{\partial \sigma_i} - \frac{\dot{\varepsilon^p}}{(\overline{\sigma})^2}\frac{\partial \overline{\sigma}}{\partial \sigma_i}\right) \tag{7.91}$$

$$= h^s \frac{\partial \dot{\varepsilon^p}}{\partial \sigma_i} - \frac{h^s \sigma^{ks}}{H^* \overline{\sigma}}\frac{\partial \dot{\varepsilon^p}}{\partial \sigma_i} + \frac{h^s \sigma^{ks} \dot{\varepsilon^p}}{H^* \overline{(\sigma)}^2}\frac{\partial \overline{\sigma}}{\partial \sigma_i} \tag{7.92}$$

$$= \frac{\dot{\sigma}^{ks}}{\dot{\varepsilon^p}}\frac{\partial \dot{\varepsilon^p}}{\partial \sigma_i} + \frac{h^s \sigma^{ks} \dot{\varepsilon^p}}{H^* \overline{(\sigma)}^2}\frac{\partial \overline{\sigma}}{\partial \sigma_i} \tag{7.93}$$

Moving to the third line of the $\frac{\partial \dot{\boldsymbol{X}}}{\partial \boldsymbol{X}}$ matrix, the first component is given by:

$$\frac{\partial \dot{\rho}}{\partial \varepsilon^p} = \frac{\partial}{\partial \varepsilon^p}\left[C_2\,\sqrt{\rho}\left(1 - \sqrt{\frac{\rho}{\rho^{ss}}}\right)\dot{\varepsilon^p}\right] = 0 \tag{7.94}$$

Since $\dot{\rho}$ does not depend on ε^p. The next term, (3,2), is given by:

$$\frac{\partial \dot{\rho}}{\partial \sigma^{ks}} = \frac{\partial}{\partial \sigma^{ks}} \left[C_2 \sqrt{\rho} \left(1 - \sqrt{\frac{\rho}{\rho^{ss}}} \right) \dot{\varepsilon}^p \right] \tag{7.95}$$

$$= C_2 \sqrt{\rho} \frac{\partial \dot{\varepsilon}^p}{\partial \sigma^{ks}} - C_2 \rho \frac{\partial}{\partial \sigma^{ks}} \left(\frac{\dot{\varepsilon}^p}{\sqrt{\rho^{ss}}} \right) \tag{7.96}$$

$$= C_2 \sqrt{\rho} \frac{\partial \dot{\varepsilon}^p}{\partial \sigma^{ks}} - C_2 \rho \left[\dot{\varepsilon}^p \frac{-1}{2} \frac{1}{(\rho^{ss})^{3/2}} \frac{\partial \rho^{ss}}{\partial \sigma^{ks}} + \frac{1}{\sqrt{\rho^{ss}}} \frac{\partial \dot{\varepsilon}^p}{\partial \sigma^{ks}} \right] \tag{7.97}$$

$$= C_2 \sqrt{\rho} \frac{\partial \dot{\varepsilon}^p}{\partial \sigma^{ks}} - C_2 \rho \left[- \frac{\dot{\varepsilon}^p}{2 \ (\rho^{ss})^{3/2}} \frac{\partial \rho^{ss}}{\partial \sigma^{ks}} + \frac{1}{\sqrt{\rho^{ss}}} \frac{\partial \dot{\varepsilon}^p}{\partial \sigma^{ks}} \right] \tag{7.98}$$

$$= C_2 \sqrt{\rho} \frac{\partial \dot{\varepsilon}^p}{\partial \sigma^{ks}} \left(1 - \sqrt{\frac{\rho}{\rho^{ss}}} \right) + \frac{C_2 \rho \ \dot{\varepsilon}^p}{2 \ (\rho^{ss})^{3/2}} \frac{\partial \rho^{ss}}{\partial \sigma^{ks}} \tag{7.99}$$

$$= \frac{\partial \dot{\varepsilon}^p}{\partial \sigma^{ks}} \ \frac{\dot{\rho}}{\dot{\varepsilon}^p} + \frac{C_2 \rho \ \dot{\varepsilon}^p}{2 \ (\rho^{ss})^{3/2}} \frac{\partial \rho^{ss}}{\partial \sigma^{ks}} \tag{7.100}$$

And thus the partial derivative of ρ^{ss} with respect to σ^{ks} needs to be calculated:

$$\frac{\partial \rho^{ss}}{\partial \sigma^{ks}} = \frac{\partial}{\partial \sigma^{ks}} \left[C_3 \left(\frac{\overline{\sigma} - \sigma^{ks}}{1 - \psi} \right) \right]^2 \tag{7.101}$$

$$= 2 \ \left[C_3 \left(\frac{\overline{\sigma} - \sigma^{ks}}{1 - \psi} \right) \right] \ \frac{\partial}{\partial \sigma^{ks}} \left[C_3 \left(\frac{\overline{\sigma} - \sigma^{ks}}{1 - \psi} \right) \right] \tag{7.102}$$

$$= 2 \ \sqrt{\rho^{ss}} \ \frac{C_3}{(1 - \psi)} \frac{\partial}{\partial \sigma^{ks}} \left(\overline{\sigma} - \sigma^{ks} \right) \tag{7.103}$$

$$= 2 \ \sqrt{\rho^{ss}} \ \frac{C_3}{(1 - \psi)} (-1) \tag{7.104}$$

$$= - \frac{2 C_3 \sqrt{\rho^{ss}}}{(1 - \psi)} \tag{7.105}$$

Substituting equation 7.105 into equation 7.100 we get:

$$\frac{\partial \dot{\rho}}{\partial \sigma^{ks}} = \frac{\partial \dot{\varepsilon}^p}{\partial \sigma^{ks}} \ \frac{\dot{\rho}}{\dot{\varepsilon}^p} + \frac{C_2 \rho \ \dot{\varepsilon}^p}{2 \ (\rho^{ss})^{3/2}} \left(- \frac{2 C_3 \sqrt{\rho^{ss}}}{(1 - \psi)} \right) \tag{7.106}$$

$$= \frac{\partial \dot{\varepsilon}^p}{\partial \sigma^{ks}} \ \frac{\dot{\rho}}{\dot{\varepsilon}^p} - \frac{C_2 C_3 \rho \ \dot{\varepsilon}^p}{\rho^{ss} (1 - \psi)} \tag{7.107}$$

The term (3,3) is given by:

$$\frac{\partial \dot{\rho}}{\partial \rho} = \frac{\partial}{\partial \rho}\left[C_2\sqrt{\rho}\left(1-\sqrt{\frac{\rho}{\rho^{ss}}}\right)\dot{\varepsilon^p}\right] \tag{7.108}$$

$$= C_2\left[\frac{\partial}{\partial \rho}\left(\sqrt{\rho}\ \dot{\varepsilon^p}\right) - \frac{1}{\sqrt{\rho^{ss}}}\ \frac{\partial}{\partial \rho}\left(\rho\ \dot{\varepsilon^p}\right)\right] \tag{7.109}$$

$$= C_2\left[\left(\sqrt{\rho}\frac{\partial \dot{\varepsilon^p}}{\partial \rho} + \frac{\dot{\varepsilon^p}}{2\ \sqrt{\rho}}\right) - \frac{1}{\sqrt{\rho^{ss}}}\ \left(\rho\frac{\partial \dot{\varepsilon^p}}{\partial \rho} + \dot{\varepsilon^p}\right)\right] \tag{7.110}$$

Rearranging the terms, we get:

$$\frac{\partial \dot{\rho}}{\partial \rho} = C_2\sqrt{\rho}\ \frac{\partial \dot{\varepsilon^p}}{\partial \rho}\left(1-\sqrt{\frac{\rho}{\rho^{ss}}}\right) + C_2\ \dot{\varepsilon^p}\left(\frac{1}{2\ \sqrt{\rho}} - \frac{1}{\sqrt{\rho^{ss}}}\right) \tag{7.111}$$

$$= \frac{\partial \dot{\varepsilon^p}}{\partial \rho}\frac{\dot{\rho}}{\dot{\varepsilon^p}} + C_2\dot{\varepsilon^p}\left(\frac{1}{2\ \sqrt{\rho}} - \frac{1}{\sqrt{\rho^{ss}}}\right) \tag{7.112}$$

The component (3,4) is given by:

$$\frac{\partial \dot{\rho}}{\partial \psi} = \frac{\partial}{\partial \psi}\left[C_2\ \sqrt{\rho}\left(1-\sqrt{\frac{\rho}{\rho^{ss}}}\right)\dot{\varepsilon^p}\right] \tag{7.113}$$

$$= C_2\sqrt{\rho}\ \frac{\partial \dot{\varepsilon^p}}{\partial \psi} - C_2\rho\frac{\partial}{\partial \psi}\left(\frac{\dot{\varepsilon^p}}{\sqrt{\rho^{ss}}}\right) \tag{7.114}$$

$$= C_2\sqrt{\rho}\ \frac{\partial \dot{\varepsilon^p}}{\partial \psi} - C_2\rho\left[\dot{\varepsilon^p}\frac{-1}{2}\frac{1}{(\rho^{ss})^{3/2}}\frac{\partial \rho^{ss}}{\partial \psi} + \frac{1}{\sqrt{\rho^{ss}}}\frac{\partial \dot{\varepsilon^p}}{\partial \psi}\right] \tag{7.115}$$

$$= C_2\sqrt{\rho}\frac{\partial \dot{\varepsilon^p}}{\partial \psi} - C_2\rho\left[-\frac{\dot{\varepsilon^p}}{2\ (\rho^{ss})^{3/2}}\frac{\partial \rho^{ss}}{\partial \psi} + \frac{1}{\sqrt{\rho^{ss}}}\frac{\partial \dot{\varepsilon^p}}{\partial \psi}\right] \tag{7.116}$$

$$= C_2\sqrt{\rho}\frac{\partial \dot{\varepsilon^p}}{\partial \psi}\left(1-\sqrt{\frac{\rho}{\rho^{ss}}}\right) + \frac{C_2\rho\ \dot{\varepsilon^p}}{2\ (\rho^{ss})^{3/2}}\frac{\partial \rho^{ss}}{\partial \psi} \tag{7.117}$$

$$= \frac{\partial \dot{\varepsilon^p}}{\partial \psi}\ \frac{\dot{\rho}}{\dot{\varepsilon^p}} + \frac{C_2\rho\ \dot{\varepsilon^p}}{2\ (\rho^{ss})^{3/2}}\frac{\partial \rho^{ss}}{\partial \psi} \tag{7.118}$$

The partial derivative of ρ^{ss} with respect to ψ needs to be calculated:

$$\frac{\partial \rho^{ss}}{\partial \psi} = \frac{\partial}{\partial \psi}\left[C_3\left(\frac{\overline{\sigma}-\sigma^{ks}}{1-\psi}\right)\right]^2 \tag{7.119}$$

$$= 2\ \left[C_3\left(\frac{\overline{\sigma}-\sigma^{ks}}{1-\psi}\right)\right]\ \frac{\partial}{\partial \psi}\left[C_3\left(\frac{\overline{\sigma}-\sigma^{ks}}{1-\psi}\right)\right] \tag{7.120}$$

$$= 2\ (\rho^{ss})^{1/2}\ [C_3\ (\overline{\sigma}-\sigma^{ks})]\frac{\partial}{\partial \psi}\left[\left(\frac{1}{1-\psi}\right)\right] \tag{7.121}$$

$$= 2\ (\rho^{ss})^{1/2}\ [C_3\ (\overline{\sigma}-\sigma^{ks})]\frac{-1}{(1-\psi)^2}(-1) \tag{7.122}$$

$$= \frac{2C_3(\overline{\sigma}-\sigma^{ks})(\rho^{ss})^{1/2}}{(1-\psi)^2} \tag{7.123}$$

Substituting equation 7.123 into equation 7.118 we get:

$$\frac{\partial \dot{\rho}}{\partial \psi} = \frac{\partial \dot{\varepsilon}^p}{\partial \psi}\ \frac{\dot{\rho}}{\dot{\varepsilon}^p} + \frac{C_2\rho\ \dot{\varepsilon}^p}{2\ (\rho^{ss})^{3/2}}\frac{\partial \rho^{ss}}{\partial \psi}\left(\frac{2C_3(\overline{\sigma}-\sigma^{ks})(\rho^{ss})^{1/2}}{(1-\psi)^2}\right) \tag{7.124}$$

$$= \frac{\partial \dot{\varepsilon}^p}{\partial \psi}\ \frac{\dot{\rho}}{\dot{\varepsilon}^p} + \frac{C_2\ C_3\rho\ \dot{\varepsilon}^p(\overline{\sigma}-\sigma^{ks})}{\rho^{ss}(1-\psi)^2} \tag{7.125}$$

The terms (3,5) to (3,10) can be calculated together:

$$\frac{\partial \dot{\rho}}{\partial \sigma_i} = \frac{\partial}{\partial \sigma_i}\left[C_2\ \sqrt{\rho}\left(1-\sqrt{\frac{\rho}{\rho^{ss}}}\right)\dot{\varepsilon^p}\right] \tag{7.126}$$

$$= C_2\sqrt{\rho}\ \frac{\partial \dot{\varepsilon}^p}{\partial \sigma_i} - C_2\rho\frac{\partial}{\partial \sigma_i}\left(\frac{\dot{\varepsilon^p}}{\sqrt{\rho^{ss}}}\right) \tag{7.127}$$

$$= C_2\sqrt{\rho}\ \frac{\partial \dot{\varepsilon}^p}{\partial \sigma_i} - C_2\rho\left[\dot{\varepsilon}^p\frac{-1}{2}\frac{1}{(\rho^{ss})^{3/2}}\frac{\partial \rho^{ss}}{\partial \sigma_i} + \frac{1}{\sqrt{\rho^{ss}}}\frac{\partial \dot{\varepsilon}^p}{\partial \sigma_i}\right] \tag{7.128}$$

$$= C_2\sqrt{\rho}\frac{\partial \dot{\varepsilon}^p}{\partial \sigma_i} - C_2\rho\left[-\frac{\dot{\varepsilon}^p}{2\ (\rho^{ss})^{3/2}}\frac{\partial \rho^{ss}}{\partial \sigma_i} + \frac{1}{\sqrt{\rho^{ss}}}\frac{\partial \dot{\varepsilon}^p}{\partial \sigma_i}\right] \tag{7.129}$$

$$= C_2\sqrt{\rho}\frac{\partial \dot{\varepsilon}^p}{\partial \sigma_i}\left(1-\sqrt{\frac{\rho}{\rho^{ss}}}\right) + \frac{C_2\rho\ \dot{\varepsilon}^p}{2\ (\rho^{ss})^{3/2}}\frac{\partial \rho^{ss}}{\partial \sigma_i} \tag{7.130}$$

$$= \frac{\partial \dot{\varepsilon}^p}{\partial \sigma_i}\ \frac{\dot{\rho}}{\dot{\varepsilon}^p} + \frac{C_2\rho\ \dot{\varepsilon}^p}{2\ (\rho^{ss})^{3/2}}\frac{\partial \rho^{ss}}{\partial \sigma_i} \tag{7.131}$$

The partial derivative of ρ^{ss} with respect to σ_i needs to be calculated:

$$\frac{\partial \rho^{ss}}{\partial \sigma_i} = \frac{\partial}{\partial \sigma_i}\left[C_3\left(\frac{\overline{\sigma}-\sigma^{ks}}{1-\psi}\right)\right]^2 \tag{7.132}$$

$$= 2\ \left[C_3\left(\frac{\overline{\sigma}-\sigma^{ks}}{1-\psi}\right)\right]\ \frac{\partial}{\partial \sigma_i}\left[C_3\left(\frac{\overline{\sigma}-\sigma^{ks}}{1-\psi}\right)\right] \tag{7.133}$$

$$= 2\ \sqrt{\rho^{ss}}\ \frac{C_3}{(1-\psi)}\frac{\partial}{\partial \sigma_i}\left(\overline{\sigma}-\sigma^{ks}\right) \tag{7.134}$$

$$= 2\ \sqrt{\rho^{ss}}\ \frac{C_3}{(1-\psi)}\frac{\partial \overline{\sigma}}{\partial \sigma_i} \tag{7.135}$$

$$= \frac{2C_3\sqrt{\rho^{ss}}}{(1-\psi)}\frac{\partial \overline{\sigma}}{\partial \sigma_i} \tag{7.136}$$

Substituting equation 7.136 into equation 7.131 we get:

$$\frac{\partial \dot{\rho}}{\partial \sigma_i} = \frac{\partial \dot{\varepsilon}^p}{\partial \sigma_i}\ \frac{\dot{\rho}}{\dot{\varepsilon}^p} + \frac{C_2\rho\ \dot{\varepsilon}^p}{2\ (\rho^{ss})^{3/2}}\left(\frac{2C_3\sqrt{\rho^{ss}}}{(1-\psi)}\frac{\partial \overline{\sigma}}{\partial \sigma_i}\right) \tag{7.137}$$

$$= \frac{\partial \dot{\varepsilon}^p}{\partial \sigma_i}\ \frac{\dot{\rho}}{\dot{\varepsilon}^p} + \frac{C_2\ C_3\rho\ \dot{\varepsilon}^p}{\rho^{ss}(1-\psi)}\frac{\partial \overline{\sigma}}{\partial \sigma_i} \tag{7.138}$$

The fourth line of the $\frac{\partial \dot{\boldsymbol{X}}}{\partial \boldsymbol{X}}$ matrix will now be calculated. The first component is given by:

$$\frac{\partial \dot{\psi}}{\partial \varepsilon^p} = \frac{\partial}{\partial \varepsilon^p}\left[\left(\frac{k^D}{(1-\psi)}\right)\dot{\varepsilon^p}\right] = 0 \tag{7.139}$$

Since $\dot{\psi}$ does not depend on ε^p. The next term, (4,2), is given by:

$$\frac{\partial \dot{\psi}}{\partial \sigma^{ks}} = \frac{\partial}{\partial \sigma^{ks}}\left[\left(\frac{k^D}{(1-\psi)}\right)\dot{\varepsilon^p}\right] \tag{7.140}$$

$$= \left(\frac{k^D}{(1-\psi)}\right)\frac{\partial \dot{\varepsilon^p}}{\partial \sigma^{ks}} \tag{7.141}$$

Similarly, (4,3) is given by:

$$\frac{\partial \dot{\psi}}{\partial \rho} = \frac{\partial}{\partial \rho}\left[\left(\frac{k^D}{(1-\psi)}\right)\dot{\varepsilon^p}\right] \tag{7.142}$$

$$= \left(\frac{k^D}{(1-\psi)}\right)\frac{\partial \dot{\varepsilon^p}}{\partial \rho} \tag{7.143}$$

And (4,4) can be calculated as:

$$\frac{\partial \dot{\psi}}{\partial \psi} = \frac{\partial}{\partial \psi}\left[\left(\frac{k^D}{(1-\psi)}\right)\dot{\varepsilon^p}\right] \tag{7.144}$$

$$= k^D \frac{\partial}{\partial \psi}\left[\frac{\dot{\varepsilon^p}}{(1-\psi)}\right] \tag{7.145}$$

$$= k^D \left[\dot{\varepsilon^p}\frac{-1}{(1-\psi)^2}(-1) + \frac{1}{(1-\psi)}\frac{\partial \dot{\varepsilon^p}}{\partial \psi}\right] \tag{7.146}$$

$$= \frac{k^D}{(1-\psi)}\frac{\partial \dot{\varepsilon^p}}{\partial \psi} + \frac{k^D \dot{\varepsilon^p}}{(1-\psi)^2} \tag{7.147}$$

$$= \frac{\dot{\psi}}{\dot{\varepsilon^p}}\frac{\partial \dot{\varepsilon^p}}{\partial \psi} + \frac{\dot{\psi}}{(1-\psi)} \tag{7.148}$$

The terms (4,5) to (4,10) can be calculated together:

$$\frac{\partial \dot{\psi}}{\partial \sigma_i} = \frac{\partial}{\partial \sigma_i}\left[\left(\frac{k^D}{(1-\psi)}\right)\dot{\varepsilon^p}\right] \tag{7.149}$$

$$= \left(\frac{k^D}{(1-\psi)}\right)\frac{\partial \dot{\varepsilon^p}}{\partial \sigma_i} \tag{7.150}$$

The first four lines of the $\frac{\partial \dot{\boldsymbol{X}}}{\partial \boldsymbol{X}}$ matrix are already known. The next step is to calculate the partial column (5,1) to (10,1), which is given by:

$$\frac{\partial \dot{\sigma}_i}{\partial \varepsilon^p} = \frac{\partial}{\partial \varepsilon^p}\left[C_{ij}(D_j - D_j^p)\right] \tag{7.151}$$

$$= -C_{ij}\frac{\partial D_j^p}{\partial \varepsilon^p} \tag{7.152}$$

The vector D_j^p is given by:

$$D_j^p = \frac{3}{2}\frac{\dot{\varepsilon}^p}{\overline{\sigma}} S_j \tag{7.153}$$

thus:

$$\frac{\partial \dot{\sigma}_i}{\partial \varepsilon^p} = -C_{ij}\frac{\partial D_j^p}{\partial \varepsilon^p} = 0 \tag{7.154}$$

Since D_j^p does not depend on ε^p. The next partial column to be calculated is from (5,2) to (10,2), which is given by:

$$\frac{\partial \dot{\sigma}_i}{\partial \sigma^{ks}} = \frac{\partial}{\partial \sigma^{ks}}\left[C_{ij}(D_j - D_j^p)\right] \tag{7.155}$$

$$= -C_{ij}\frac{\partial D_j^p}{\partial \sigma^{ks}} \tag{7.156}$$

$$= -C_{ij}\frac{\partial}{\partial \sigma^{ks}}\left(\frac{3}{2}\frac{\dot{\varepsilon}^p}{\overline{\sigma}} S_j\right) \tag{7.157}$$

$$= -\frac{3}{2}\frac{}{\overline{\sigma}} C_{ij} S_j \frac{\partial \dot{\varepsilon}^p}{\partial \sigma^{ks}} \tag{7.158}$$

The third partial column is (5,3) to (10,3), given by:

$$\frac{\partial \dot{\sigma}_i}{\partial \rho} = \frac{\partial}{\partial \rho}\left[C_{ij}(D_j - D_j^p)\right] \tag{7.159}$$

$$= -C_{ij}\frac{\partial D_j^p}{\partial \rho} \tag{7.160}$$

$$= -C_{ij}\frac{\partial}{\partial \rho}\left(\frac{3}{2}\frac{\dot{\varepsilon}^p}{\overline{\sigma}} S_j\right) \tag{7.161}$$

$$= -\frac{3}{2}\frac{}{\overline{\sigma}} C_{ij} S_j \frac{\partial \dot{\varepsilon}^p}{\partial \rho} \tag{7.162}$$

The last partial column to be calculated is (5,4) to (10,4):

$$\frac{\partial \dot{\sigma}_i}{\partial \psi} = \frac{\partial}{\partial \psi}\left[C_{ij}(D_j - D_j^p)\right] \tag{7.163}$$

$$= -C_{ij}\frac{\partial D_j^p}{\partial \psi} \tag{7.164}$$

$$= -C_{ij}\frac{\partial}{\partial \psi}\left(\frac{3}{2}\frac{\dot{\varepsilon}^p}{\overline{\sigma}}S_j\right) \tag{7.165}$$

$$= -\frac{3}{2}\frac{}{\overline{\sigma}}C_{ij}S_j\frac{\partial \dot{\varepsilon}^p}{\partial \psi} \tag{7.166}$$

Finally, the last step to finalise the $\frac{\partial \dot{\boldsymbol{X}}}{\partial \boldsymbol{X}}$ matrix is to calculate the square matrix formed by components (5,5) to (10,10), and given by:

$$\frac{\partial \dot{\sigma}_l}{\partial \sigma_l} = \frac{\partial}{\partial \sigma_l}\left[C_{ij}(D_j - D_j^p)\right] \tag{7.167}$$

$$= -C_{ij}\frac{\partial D_j^p}{\partial \sigma_l} \tag{7.168}$$

$$= -C_{ij}\frac{\partial}{\partial \sigma_l}\left(\frac{3}{2}\frac{\dot{\varepsilon}^p}{\overline{\sigma}}S_j\right) \tag{7.169}$$

$$= -\frac{3}{2}C_{ij}\frac{\partial}{\partial \sigma_l}\left(\frac{\dot{\varepsilon}^p}{\overline{\sigma}}\ S_j\right) \tag{7.170}$$

$$= -\frac{3}{2}C_{ij}\left[S_j\frac{\partial}{\partial \sigma_l}\left(\frac{\dot{\varepsilon}^p}{\overline{\sigma}}\right) + \frac{\dot{\varepsilon}^p}{\overline{\sigma}}\frac{\partial S_j}{\partial \sigma_l}\right] \tag{7.171}$$

Both partial derivatives above were already calculated and are given by equations 7.73 and 7.90 and are substituted in the equations below.

$$\frac{\partial \dot{\sigma}_i}{\partial \sigma_l} = -\frac{3}{2}C_{ij}\left[S_j\left(\frac{1}{\overline{\sigma}}\frac{\partial \dot{\varepsilon^p}}{\partial \sigma_l} - \frac{\dot{\varepsilon^p}}{(\overline{\sigma})^2}\ \frac{\partial \overline{\sigma}}{\partial \sigma_l}\right) + \frac{\dot{\varepsilon}^p}{\overline{\sigma}}\left(\frac{2}{3}\delta_{jl}\right)\right] \tag{7.172}$$

$$= -\frac{3}{2\ \overline{\sigma}}\ C_{ij}\left[S_j\left(\frac{\partial \dot{\varepsilon^p}}{\partial \sigma_l} - \frac{\dot{\varepsilon^p}}{\overline{\sigma}}\frac{\partial \overline{\sigma}}{\partial \sigma_l}\right) + \frac{2}{3}\delta_{jl}\ \dot{\varepsilon^p}\right] \tag{7.173}$$

Now that the Jacobian is known, equation 7.30 can be finally solved. The next step is to check for convergence. The convergence is given by the absolute value of the difference between the new and previous answers obtained by the Newton-Ralphson algorithm. If

this value is lower than an established tolerance, as shown in the equation 7.174, the values have converged.

$$|X_i^{n+1} - X_i^n| \leq \text{tolerance} \tag{7.174}$$

If the values have not converged, X_i^n is updated to X_i^{n+1} and the process is repeated. If the new values have converged, the solution has been achieved. This ensures a stable solution, differently from explicit integration methods.

A flowchart showing the algorithm process is shown in Figure 7.2.

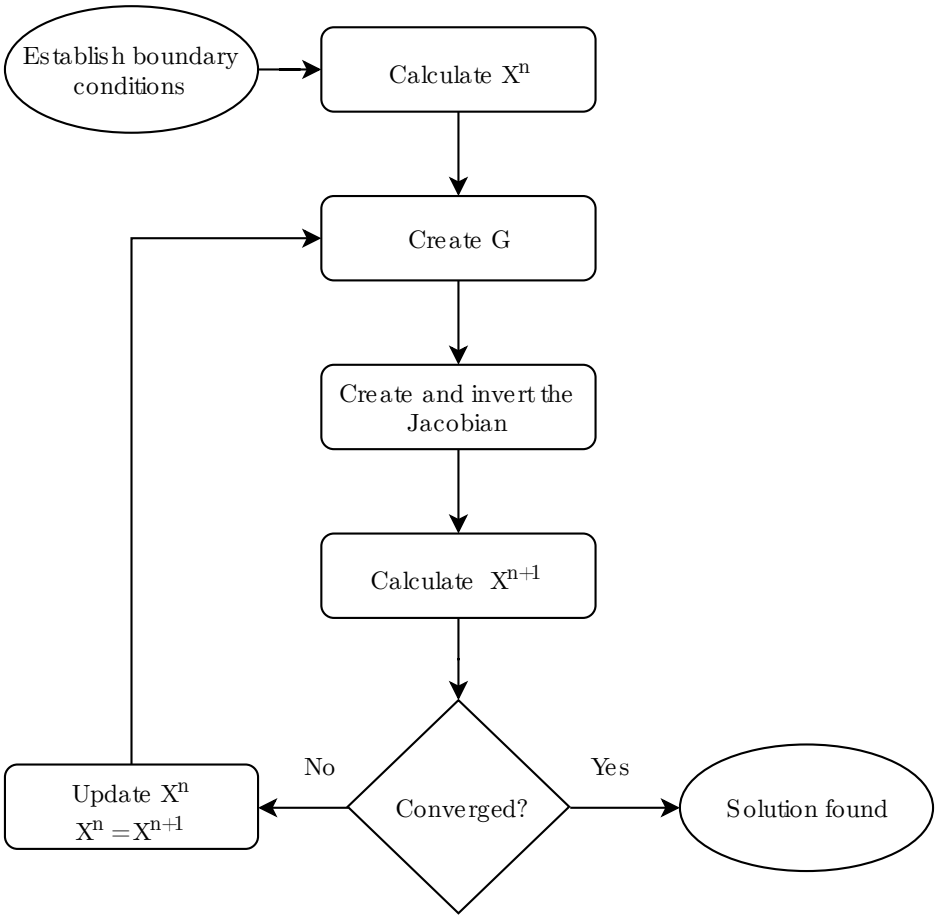

Figure 7.2: Flowchart of the implicit integration algorithm.

The implicit integration algorithm was then coded in FORTRAN 77 and coupled to the commercial finite element code "ABAQUS" under a user-defined material subroutine.

7.2.2 Parameter calibration

In order to validate the model, the user-defined material subroutine was used in a finite element simulation and then compared with the uniaxial tensile tests shown in chapter 4.

To replicate the uniaxial tensile test, a cube with a side of 1000 mm was modelled. As boundary conditions, one of the faces on the XY plane had its vertices constrained in the Z direction, one of the faces on the YZ plane had its vertices constrained in the X direction and one of the faces on the XZ direction had its vertices constrained on the Y direction. A displacement was then introduced on the Y direction. The boundary conditions described can be seen in Figure 7.3. The strain rate applied was the same as in the tensile test, 10^{-3} s^{-1}.

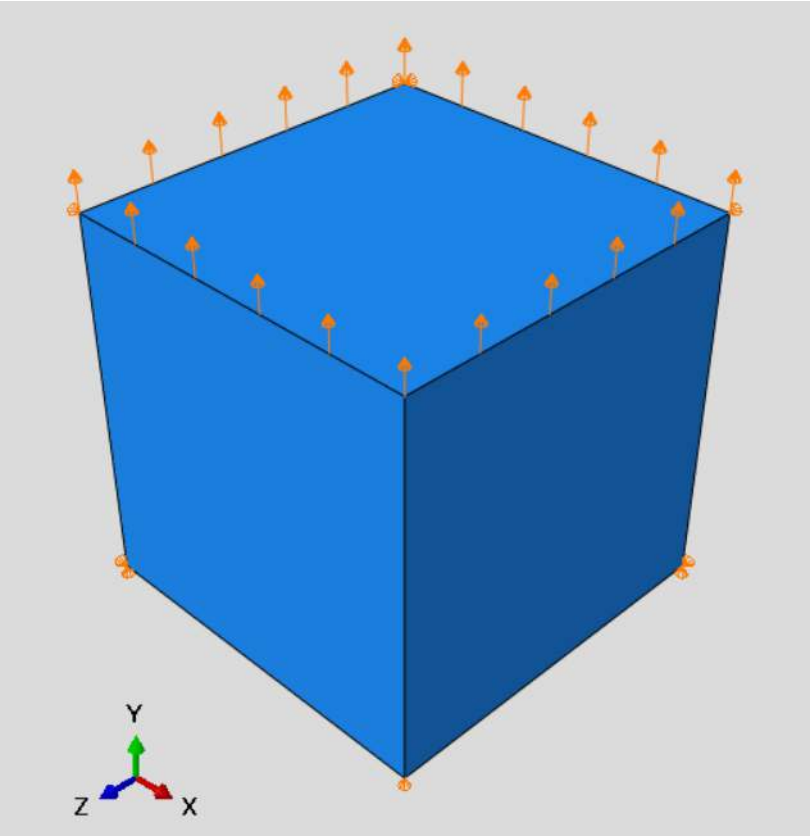

Figure 7.3: Boundary conditions applied on the uniaxial tensile testing.

The results of the model were then compared to the results of the EN24T steel as shown in Figure 7.4. A good agreement was obtained. The material in the model was deemed

as failed when the damage variable reached a value of 0.5. Such value makes the failure strain of the simulation to match that of experiment. The results were not corrected for necking, as they should not change significantly.

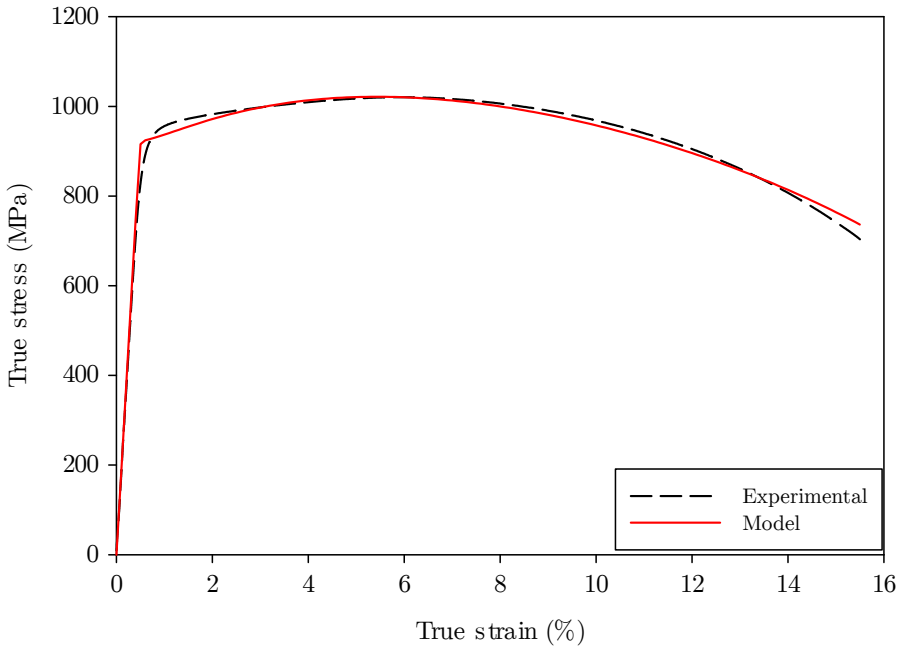

Figure 7.4: Comparison between the true stress-strain curves of the EN24T steel and the model.

The evolution of the four state variables can be seen in Figure 7.5. A common point for all of them is that the evolution only starts at around 1% strain. This happens since the backstress, dislocation density and damage depend on the plastic strain, which only kicks off when the material yields. The plastic strain follows a linear trend, while the damage variable has a parabolic relationship, as expected.

The backstress peaks at 11% strain and then starts to slightly decrease. The dislocation density reaches a steady state at 6% strain.

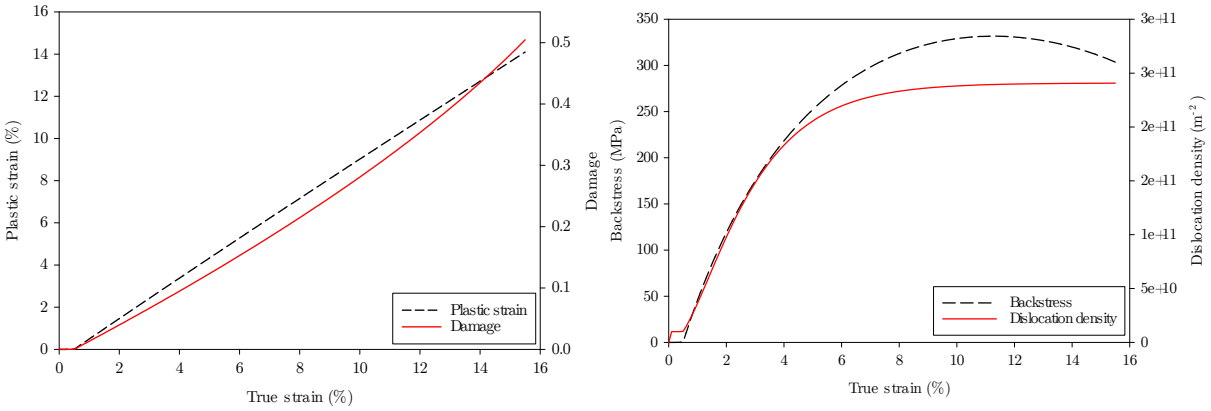

(a) (b)

Figure 7.5: Evolution of the state variables: plastic strain and damage (a), and backstress and dislocation density (b).

Since the model will be used in a rolling contact fatigue simulation, it is important to understand how the state variables evolve under fatigue. The same model was used in a strain-controlled cyclic test for three different alternating strains, for 5,000 cycles. The alternating strain shape can be seen in Figure 7.6. The strain rate was kept the same as in the tensile testing, and the R-ratio was equal to zero.

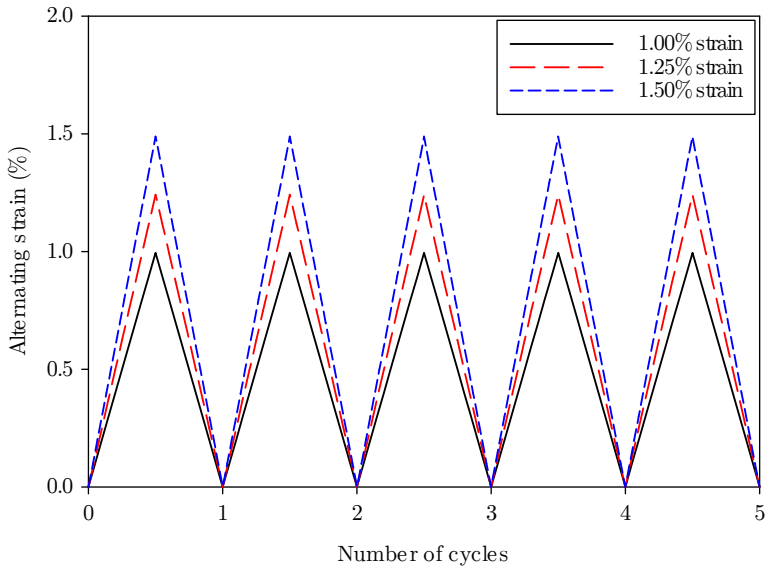

Figure 7.6: Alternating strain profile versus number of cycles of the strain-controlled cyclic simulations.

Figures 7.7 and 7.8 show the state variable evolution of three different maximum strains. All state variables, in all three simulations, achieve a steady state quickly. Additionally, the higher the strain, the faster this steady state is achieved. As expected, the higher the strain, the higher the values of all state variables, since they are all dependant on the plastic strain.

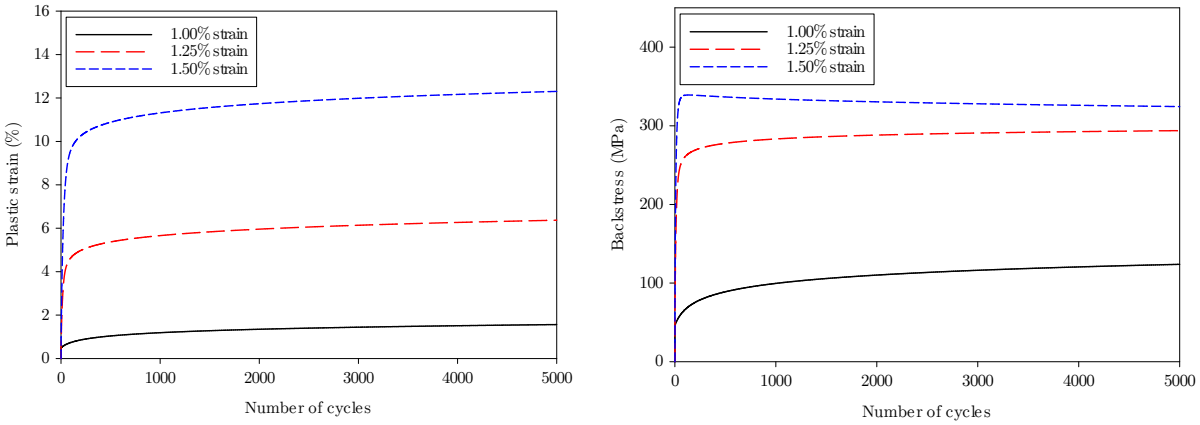

(a) (b)

Figure 7.7: Evolution of the state variables: plastic strain (a), and backstress (b), in a cyclic strain-controlled simulation with R-ratio = 0.

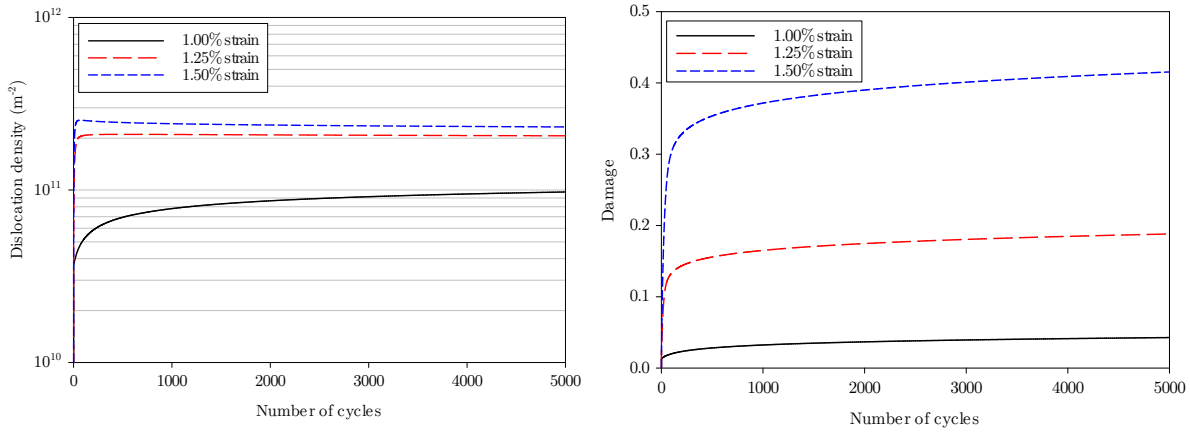

(a) (b)

Figure 7.8: Evolution of the state variables: dislocation density (a), and damage (b), in a cyclic strain-controlled simulation with R-ratio = 0.

The model was also tested under negative R-ratios and it was found to capture the

Bauschinger effect. These conditions, however, are not experienced by wind turbine gearbox components.

7.3 FINITE ELEMENT IMPLEMENTATION

The equations presented in the previous sections will be solved with the use of the commercial finite element code "ABAQUS". The goal of this section is to summarise the information needed to recreate the simulations carried out as a part of this study. The finite element implementation will be described in detail in the following subsections.

ABAQUS is divided into several modules, and this section follows the order of each module the user needs to create to perform the analysis.

7.3.1 Units in ABAQUS

Before starting, the user needs to define which unit system will be used by ABAQUS. Since the software does not possess an integrated unit system, the inserted values must be defined in compatible units. Unit names are not to be included when inserting data. Table 7.2 shows consistent sets of units. The SI (mm) set of units was used in this work [195].

Table 7.2: Consistent sets of units for use in ABAQUS. Source: [195].

Quantity	**SI**	**SI (mm)**	**US Unit (ft)**	**US Unit (inch)**
Length	m	mm	ft	in
Force	N	N	lbf	lbf
Mass	kg	tonne	slug	lbf s^2/in
Time	s	s	s	s
Stress	Pa	MPa	lbf/ft^2	psi
Energy	J	mJ	ft lbf	in lbf
Density	kg/m^3	tonne/mm^3	slug/ft^3	lbf s^2/in^4

7.3.2 Part module: spur gear design

ABAQUS allows the user to either draw a part or import it from a different CAD software packages. In this study, the gears were drawn in ABAQUS with the use of a python script adapted from the work of Tharmakulasingam [196].

Tharmakulasingam [196] used 2D gears with a design based on the diametric pitch relationship (US units), whereas the adapted model generates 3D gears based on the module relationship (SI units). The adapted code (appendix A) allows the user to draw any pair of spur gears by inserting the value of the module, number of teeth, and the face width. An example of a gear generated with the python script is shown in Figure 7.9.

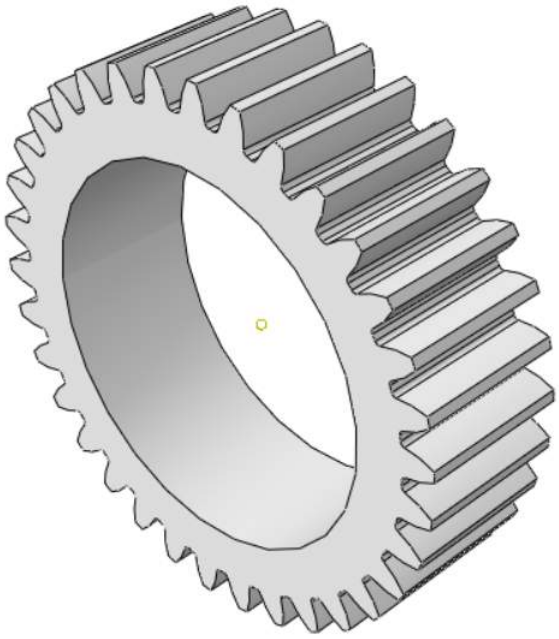

Figure 7.9: Gear generated with the python script.

After generation, each gear had three teeth partitioned, as shown in Figure 7.10. This allows the use of different material properties and finite element meshes on the partitioned teeth, making the model more time-efficient.

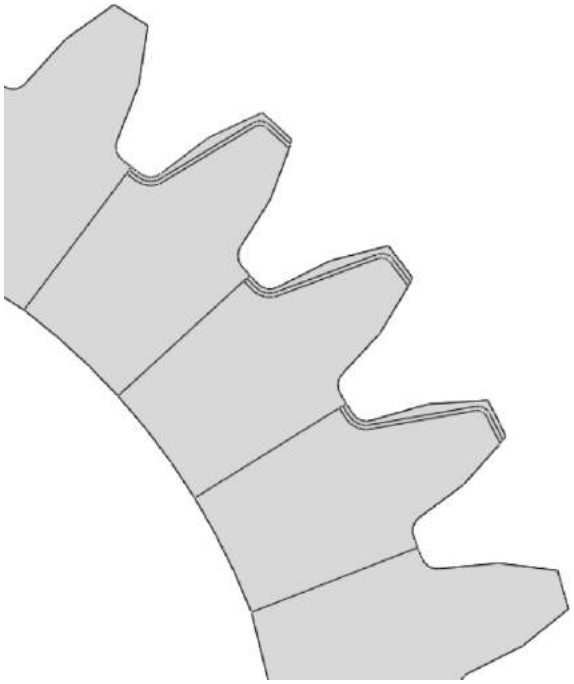

Figure 7.10: Partitions created on three gear teeth, front view.

The parameters for the construction of the gear pair can be found in Table 7.3. In this simulation, both gears have the same size, and therefore, the velocity ratio is equal to 1.

Table 7.3: Gear pair specification.

Gear parameter	**Value**	**Unit**
Module	2	mm
Number of teeth of the pinion	34	-
Number of teeth of the gear	34	-
Pitch radius of the pinion	68	mm
Pitch radius of the gear	68	mm
Face width	20	mm
Pressure angle	20	°
Addendum	2	mm
Dedendum	2.5	mm
Tooth height	4.5	mm
Root fillet radius	0.6	mm
Clearance	0.5	mm
Tip relief	0.25	mm

The pinion is always the smaller gear on a gear pair. As this gear pair employs two gears

of equal size, the "pinion" will refer to the gear where the torque is applied, whereas the "gear" will be the gear to which angular velocity will be applied.

7.3.3 Property module

In the property module, the user needs to define a material and its properties. The steel of choice for this project was the EN24T steel, which was characterised for this work. Its properties are shown in Table 7.4. A perfectly elastic material behaviour was considered in the first stages of this simulation. Later on, a user-defined material was employed for the three partitioned teeth of each gear, while the remaining of the gear was still considered perfectly elastic. The details of the user-defined material were specified in section 7.2.

Table 7.4: Material properties used in the finite element model.

Material property	**Value**
Young's modulus (GPa)	187
Poisson's ratio	0.30

The next step was to create a section and assign it to the part so that the software can recognise the material properties on the component. A solid and homogeneous section was created and assigned to both gears.

7.3.4 Assembly module

After the generation of the spur gear pair, the gears were brought into contact by translating one of them by their centre distance. The centre distance (c_d) between both gears can be found from equation 7.175, where d_p is the pitch diameter of the pinion and d_g is the pitch diameter of the gear. For this gear pair, the centre distance is 68 mm.

$$cd = \frac{(d_p + d_g)}{2} \tag{7.175}$$

One gear was then rotated with respect to its shaft axis so one of the teeth would slightly overlap the other in order to establish contact. This overclosure will be corrected in the interaction module. The final position of the gears can be seen in Figure 7.11.

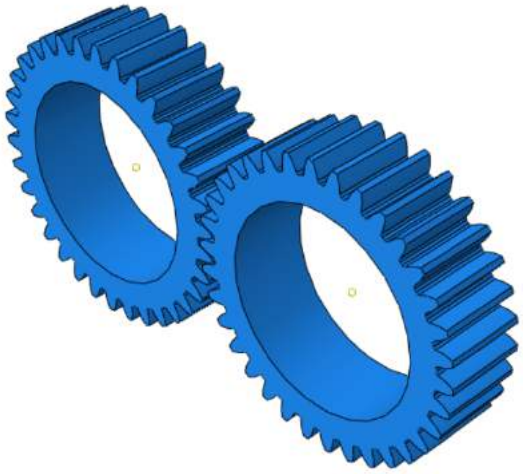

Figure 7.11: Final design of spur gear pair, isometric view.

7.3.5 Step module

After finalising the assembly module setup, the step module must be defined. This simulation was divided into three steps. For each step, different field and history outputs can be requested. As gears of the high-speed shaft are usually the most damaged by wear [197], their velocity of usually 1500 rpm (or 157.08 rad/s) was assigned to the gears. This means that one whole turn of this gear pair would occur every 0.04 rad/s (frequency of 25 Hz).

The first step was created in order to establish contact between the gear pair. In this step, the torque was applied with the default amplitude (ramped), while the angular velocity was applied instantly. Applying the torque as a ramped function instead of instantaneously aids convergence. The type of the step chosen was "static, general", with a time period of 1.25 ms. This is the time required for the first 2 teeth of each gear to engage. No data from this step was required since the goal of this step is to establish contact and to bring the torque to a constant value. Therefore, in order to save computational resources, the field and history outputs for this request were set to "last increment only".

The second step is from where the data will actually be extracted from. In this step, the gears are already in contact, and the angular velocity and torque have a

constant value. The time period set for this step was 3.75 ms, which is the time for the third, fourth and fifth teeth for each gear to engage from start to end. The field and history output of this step were requested at every 0.1 ms.

The goal of the third step is to rotate the gear in order to bring it to the same position as in the start of the test, making it repeatable. Therefore, the time period set was 35 ms, which summed with the time for the first and second step, finishes the rotation in 40 ms. The field and history outputs were again set to "last increment only".

7.3.6 Interaction module

The interaction module is where the contact surfaces, contact interactions, and model constraints can be defined. This is a crucial step since the results will depend on the choices made in this module.

- **Defining surfaces**

Regardless of the method used, surfaces in contact must be created by selecting regions of the part. For this gear model, the contact surfaces are the flanks of the teeth. Since there are 34 teeth in each gear, 34 contact pairs need to be established. Figure 7.12 shows one of these pairs.

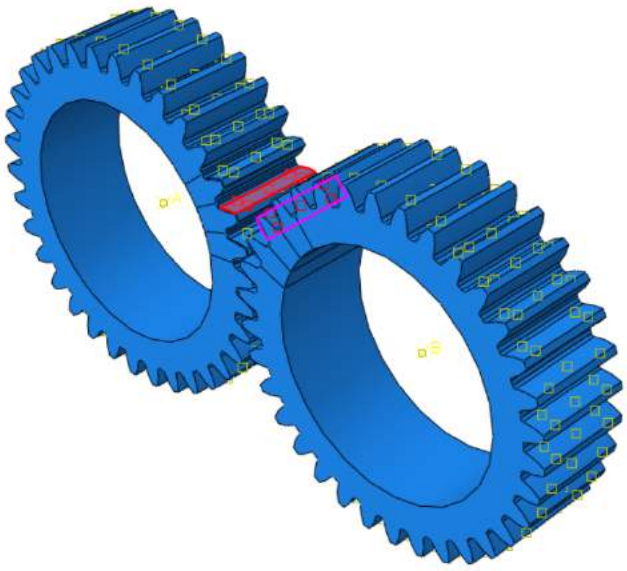

Figure 7.12: Contact surfaces of a tooth pair highlighted in red and purple, isometric view.

- **Interaction property**

Before creating the interaction itself, an interaction property must be created. The interaction property allows the user to include the normal and tangential components of the contact. In this case, a contact interaction was chosen since the objective is to define a contact. Then, a frictionless tangential behaviour and a "hard contact" normal behaviour was chosen. At the first stage of the simulation, the model was set as frictionless in order to maintain coherency with the theoretical equations for the contact stress, which neglect friction.

- **Interaction**

After defining the surfaces and the interaction property, the user can then proceed to create the interaction itself. A surface-to-surface contact was created, and finite sliding was selected. A master and a slave surface must be defined in this module. The ABAQUS manual [195] advises that the master surface must always be the hardest and most finely meshed surface. Since both gears are made from the same material and have the same mesh density, the surface of the pinion was randomly chosen as the master surface. On the "slave adjustment" option, a tolerance for adjustment zone must be defined as zero. This is what allows the software to correct the overclosure created at the assembly step and makes it able to transpose any penetrating nodes to the surface of the part, as shown in Figure 7.13. The dotted line is the initial scenario while the full line is the result after ABAQUS transposes the penetrating nodes.

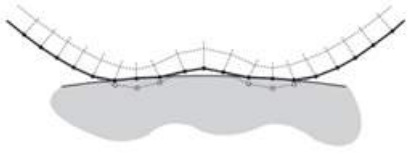

Figure 7.13: ABAQUS correction of overclosure surfaces. Source: [195].

- **Constraints**

Since shafts were not modelled in this simulation, coupling constraints were used to simulate them. Coupling constraints allow the user to define which degrees of freedom should be coupled. In this simulation, reference points were created on the exact centre of each gear. All degrees of freedom of the reference point were then constrained with the inner surface of the gear. This allows the application of the boundary conditions to the reference point, meaning that if an angular velocity is applied to it, the whole gear will rotate at the same given speed. Figure 7.14 shows the coupling constraints applied to the gear pair.

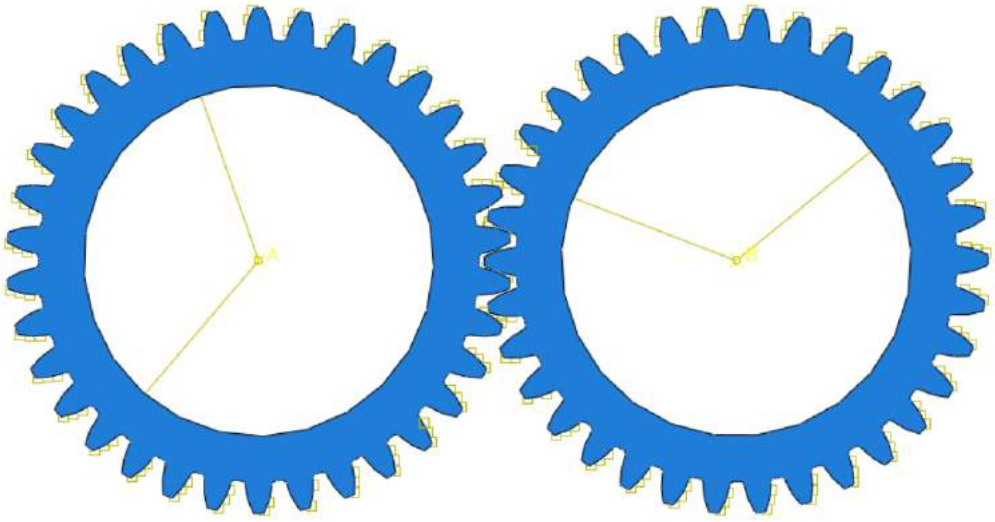

Figure 7.14: Coupling constraints applied to the gear pair, front view.

7.3.7 Load module (boundary conditions)

The load module is where the loads and boundary conditions are defined. The coordinate system in ABAQUS is given by the directions 1, 2, and 3, which are the x, y, and z-direction, respectively. First, two equal boundary conditions were created and applied to the reference point on the pinion and gear, restraining both gears from moving in all directions except the UR3 (rotational direction in the z-axis). Then, an angular velocity of 157.08 rad/s was applied instantaneously to the gear and a torque of 5 N $\cdot$ m was applied to the pinion with a ramped amplitude. All the boundary conditions were generated at the first step and transmitted to the following steps. Table 7.5 summarises the boundary

conditions applied.

Table 7.5: Summary of the boundary conditions applied to the gear pair.

Boundary condition	**Pinion**	**Gear**
U1	0	0
U2	0	0
U3	0	0
UR1	0	0
UR2	0	0
UR3	Free	Free
Torque (N · m)	5 - 200	0
Angular velocity (rad/s)	0	157.08

7.3.8 Mesh module

In this module, both gears were divided into finite elements (meshed). ABAQUS provides an extensive element library, and each element is best suited for a particular application. The choice of the element and mesh density impacts the results of the simulation. Figure 7.15 illustrates the different element families in ABAQUS. Since the gears are made from solid materials, the continuum elements family was chosen.

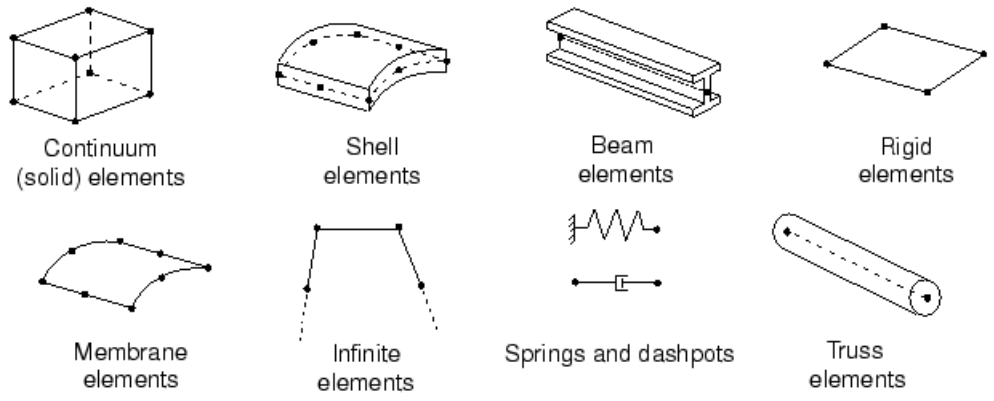

Figure 7.15: Element families in ABAQUS. Source: [195].

ABAQUS offers both quadratic and linear continuum elements, with full and reduced integration. A C3D20R element, for example, is continuum, 3D, has 20 nodes and uses reduced integration. A C3D8, on the other hand, is a continuum 3D brick of 8 nodes and uses full integration. According to the ABAQUS manual [195], quadratic elements do

not perform well in contact simulations, leaving the choice restricted to linear elements. The C3D8 element was chosen due to its full integration, which leads to more accurate calculations. Beyond the element choice, the mesh density must also be defined. In order to do so, a mesh convergence analysis was performed.

7.3.9 Mesh convergence analysis

Since the three previously partitioned teeth are the main area of interest, this was where the mesh refinement took place. The remaining of the gear was seeded with a coarse mesh, and the refinement was done by edge seeding only the partitioned teeth. This is a common practice in finite element analysis (FEA) since it can save on computational resources without impacting the results. Figure 7.16 shows one of the meshed gears.

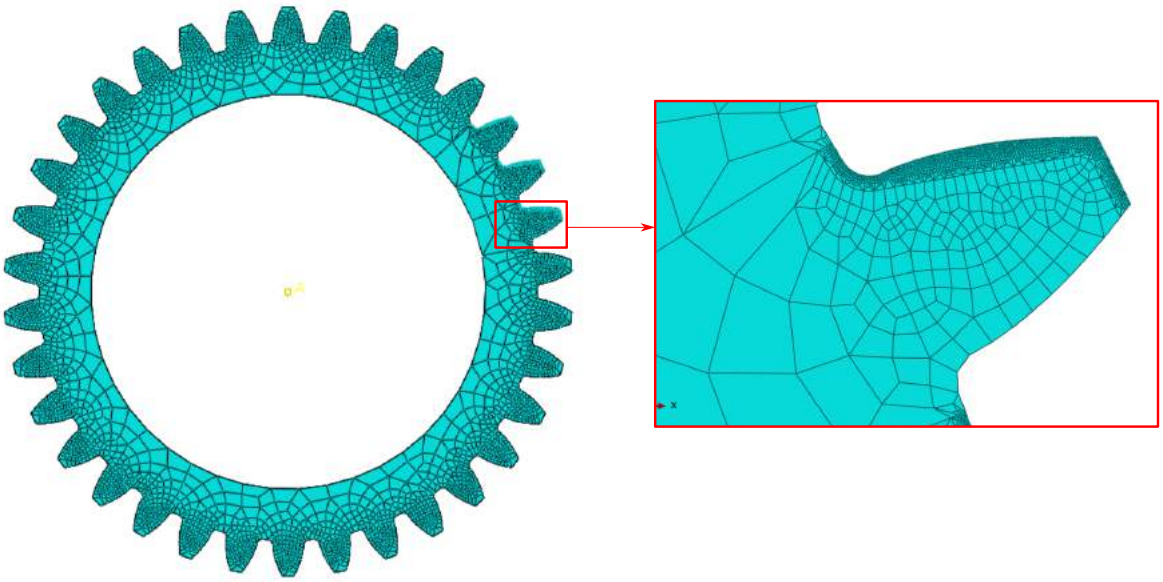

Figure 7.16: Mesh generated on one of the gears, showing the coarse mesh on the majority of the gear (left) and fine mesh on one of the partitioned teeth (right).

The mesh convergence analysis results for the maximum Von Mises stress, maximum contact stress, maximum bending stress and maximum shear stress for the entire model can be seen in Figure 7.17.

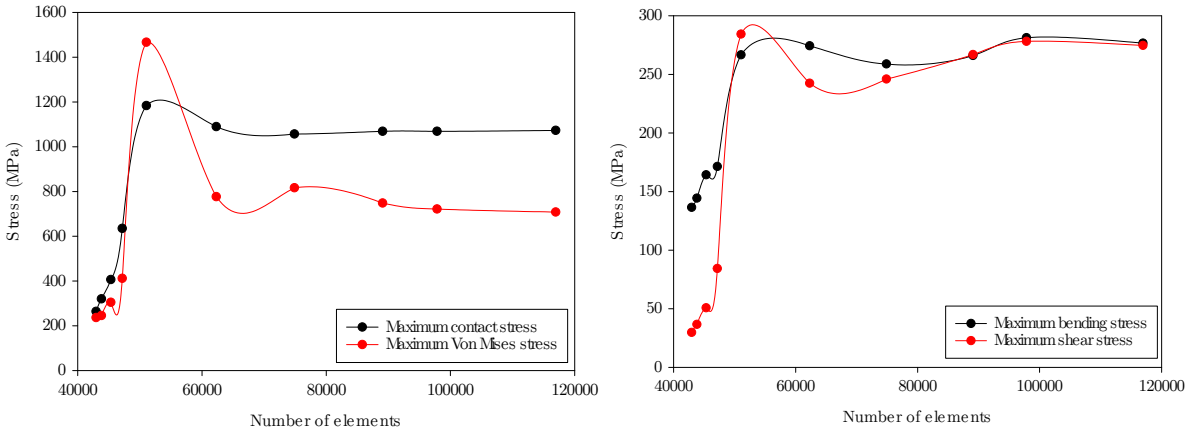

(a) (b)

Figure 7.17: Mesh convergence analysis results showing: the maximum Von Mises and contact stress (a), and the maximum bending and shear stress (b).

The local number of elements was gradually increased until a variation of less than 2% on all four stresses was achieved. This occurred at around 120,000 elements, and the final mesh was the one previously shown in Figure 7.16. An ABAQUS input file for the model can be seen in Appendix B. A comparison with the theoretical data on the contact and bending stress of gears is performed on the next section.

7.4 AGMA CONTACT STRESS EQUATION

The American Gear Manufacturers Association (AGMA) developed two fundamental stress equations [198], for both bending stress and contact stress (also called pitting resistance equation). The AGMA fundamental equation for bending stress is given by equation 7.176, while the AGMA fundamental equation for contact stress is given by equation 7.177 [61]. These equations will be used to compare and validate the data obtained from the finite element model.

$$\sigma_b = \frac{W_t K_o K_v K_s K_H K_B}{F_w m_t Y_J} \tag{7.176}$$

$$\sigma_c = Z_E \sqrt{\frac{W_t K_o K_v K_s K_H Z_R}{d_p F_w Z_I}} \tag{7.177}$$

A description of each parameter is given in Table 7.6. A more detailed explanation of each parameter is given on the following subsections.

Table 7.6: Parameters and descriptions of the AGMA stress equations.

Parameter	**Description**	**Unit**
σ_b	Bending stress	MPa
W_t	Tangential transmitted load	N
K_o	Overload factor	-
K_v	Dynamic factor	-
K_s	Size factor	-
K_H	Load distribution factor	-
K_B	Rim-thickness factor	-
F_w	Face width	mm
m_t	Transverse metric module	mm
Y_j	Geometry factor for bending strength	-
σ_c	Contact stress	MPa
Z_E	Elastic coefficient	$\text{MPa}^{1/2}$
Z_R	Surface condition factor	-
d_p	Pitch diameter of the pinion	mm
Z_I	Geometry factor for pitting resistance	-

- **Tangential load** (W_t)

The tangential transmitted load is obtained from the torque, as shown in equation 7.178.

$$W_T = \frac{2T_q}{d_g} \tag{7.178}$$

Where T is the torque applied to the gear and d_g is the pitch diameter of the gear to which the torque was applied.

- **Overload factor** (K_o)

The overload factor takes into account externally applied loads that exceed the tangential load [198]. This factor can only be established after a reasonable field experience in a particular application [61, 198]. In this specific simulation, the only load applied is

derived from the torque, which experiences no variation whatsoever throughout the entire simulation. Due to this, the overload factor was set to 1.

- **Dynamic factor** (K_v)

Whenever a gear couple is moving at high speeds, dynamic effects will be present [61]. The dynamic factor takes into account tooth loads that are produced due to the non-conjugate mating of the gear teeth [198]. The dynamic factor is given by equation 7.179:

$$K_v = \left(\frac{A_v + \sqrt{200V}}{A_v} \right) \tag{7.179}$$

where V is the pitch line velocity, in this case 5.34 m/s, and A_v and B_v are given by equations 7.180 and 7.181:

$$A_v = 50 + 56(1 - B_v) \tag{7.180}$$

$$B_v = 0.25(12 - Q_v)^{(2/3)} \tag{7.181}$$

Q_v is the AGMA transmission accuracy level, which goes from 3 to 12, the latter being the highest precision quality [61]. A value of 11 was assumed, and the calculated dynamic factor was 1.08.

- **Dynamic factor** (K_v)

The size factor takes into consideration the variation of material properties regarding size. Since standard size factors have not yet been established [198], the size factor can be assumed as 1.

- **Load distribution factor** (K_H)

The role of the load distribution factor is to reflect the variation of the load across the line of contact. The nonuniformity of the load can be caused by manufacturing variation

of gears, assembly variations of installed gears, deflections due to applied loads and distortions due to thermal and centrifugal effects [198]. The load distribution factor is given by equation 7.182.

$$K_H = 1 + C_{mc}(C_{pf}C_{pm} + C_{ma}C_e) \tag{7.182}$$

Where C_{mc} is the lead correction factor, C_{pf} is the pinion proportion factor, C_{pm} is the pinion proportion modifier, C_{ma} is the mesh alignment factor, and C_e is the mesh alignment correction factor. A detailed explanation on how to calculate each factor can be found in refs. [61, 198]. For this simulation, all factors have the value of unity, except for the C_{pf}, that has a value of 0.05, and the C_{ma}, that has a value of 0.04. Therefore, the calculated value of K_H is 1.09.

- **Rim-thickness factor** (K_b)

If the rim-thickness is not big enough to accommodate the tooth root, bending failure may happen at the rim instead of the fillet. If that is the case, it is recommended that the rim-thickness factor is applied, in order to correct the bending stress calculation. The backup ratio (m_B) is equal to the rim thickness (t_R) divided by the tooth height (h_t), as shown in equation 7.183. If the backup ratio is equal or greater than 1.2, as it happens in this simulation, then a rim-thickness factor of 1 must be used. For all other cases, the equation 7.184 must be used [61].

$$m_B = \frac{t_R}{h_t} \tag{7.183}$$

$$K_B = 1.6 \ln\left(\frac{2.242}{m_B}\right) \qquad if \quad m_B < 1.2 \tag{7.184}$$

- **Transverse metric module** (m_t)

The transverse metric module (m_t) is the ratio of the module (m) to the cosine of the

pressure angle (θ) in radians, as shown in equation 7.185.

$$m_t = \frac{m}{cos\ \theta} \tag{7.185}$$

- **Geometry factor for bending strength** (Y_j)

The AGMA bending equation uses an adapted Lewis form factor given by Y, a fatigue stress concentration factor given by K_f, and a tooth load sharing ratio given by m_N [61]. The geometry factor formula of bending strength of spur gears is shown in equation 7.186.

$$Y_j = \frac{Y}{K_f} \tag{7.186}$$

The geometry factor for this simulation was obtained from Figure 14-6 in ref. [61], and the value for both gears in this simulation is 0.39.

- **Elastic coefficient** (Z_E)

AGMA defines an elastic coefficient (Z_E) as shown in equation 7.187 [198].

$$Z_E = \sqrt{\frac{1}{\pi \left(\frac{1-\nu_p^2}{E_p} + \frac{1-\nu_g^2}{E_g} \right)}} \tag{7.187}$$

Where ν_p and ν_g are the Poisson's ratio for the pinion and the gear, respectively, and the E_p and E_g are the elastic moduli for the pinion and the gear, respectively. In this simulation, both the gear and the pinion are made from the same material, with a Young's modulus of 187 GPa and a Poisson's ratio of 0.30. The result for Z_E is then 180.85 $\sqrt{\text{MPa}}$.

- **Surface condition factor** (Z_R)

The surface condition factor is supposed to take into account the residual stress, plastic effects and surface finish. However, a standard surface condition factor for gears is still undefined [61], and therefore, a value of 1 was used.

- **Geometry factor for pitting resistance** (Z_I)

The Z_I factor for external spur gears is defined by equation 7.188 [61]:

$$Z_I = \frac{m_s \cos\ \theta\ \sin\ \theta}{2\ (m_s + 1)} \tag{7.188}$$

where θ is the pressure angle in radians, and m_s is the speed ratio defined by equation 7.189.

$$m_s = \frac{N_g}{N_p} \tag{7.189}$$

Where N_g and N_p are the number of teeth of the gear and the pinion, respectively. The calculated Z_I for this gear pair is 0.08.

7.5 AGMA AND FEA COMPARISON

By using the equations 7.176 and 7.177, and the summarised data from Table 7.7, it is possible to calculate the AGMA bending and contact stresses for different torque values.

Table 7.7: Summarised variable data for the evaluation of equations 7.176 and 7.177.

Variable	**Value**	**Unit**
K_o	1	-
K_v	1.08	-
K_s	1	-
K_b	1	-
F	20	mm
m_t	2.13	mm
Y_j	0.39	-
Z_E	180.85	$\sqrt{\text{MPa}}$
K_H	1.09	-
Z_R	1	-
d_p	68	mm
Z_I	0.08	-

A comparison between results obtained from ABAQUS and the AGMA equations is now possible, and the results are shown Figure 7.18. A good agreement can be seen, especially for the contact stresses.

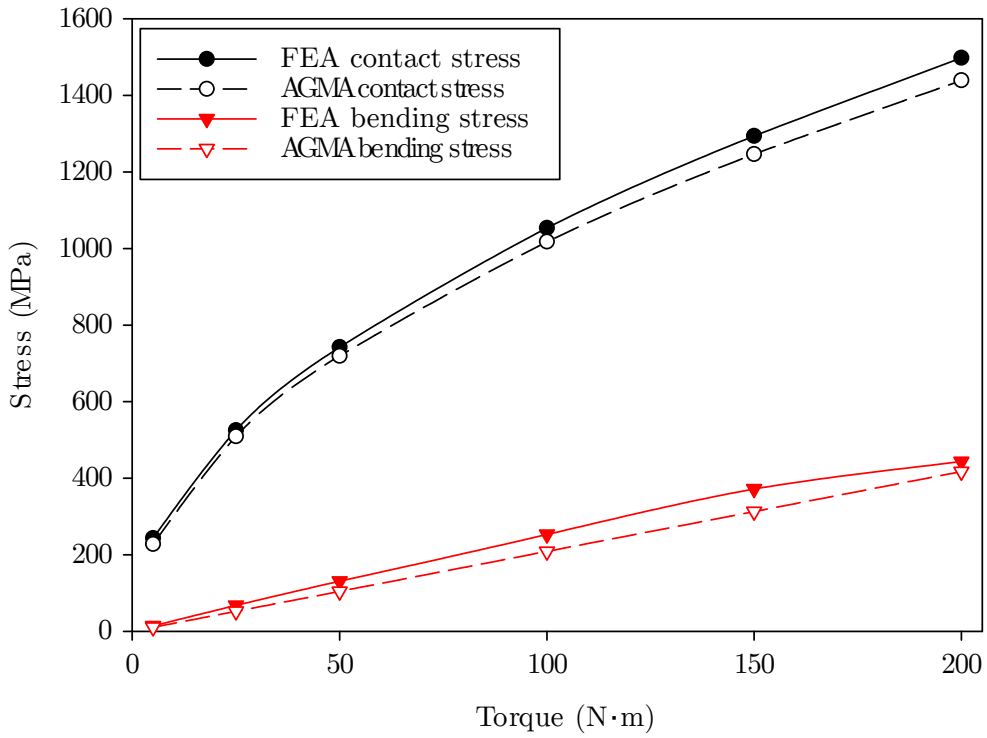

Figure 7.18: Comparison between FEA results and AGMA calculations of contact and bending stresses.

7.6 SUMMARY

This section presented the methodology for the creation and validation of a finite element model coupled with a user-defined material from a constitutive model. A gear pair was developed in ABAQUS and a mesh convergence analysis was performed. After convergence was achieved, the bending and contact stresses results were compared with theoretical equations, where a good agreement was found.

In order to be able to model damage and estimate the remaining useful lifetime of the gear pair, a constitutive model containing four state variables was coded and coupled with the finite element model. This constitutive model was solved implicitly by using the Newton-Ralphson algorithm.

The results for the constitutive model were validated against tensile tests performed on the EN24T steel, detailed in section 4.2, and a good agreement was found. Additionally, the model was tested in cyclic strain-controlled simulations. A steady state was quickly achieved for all tested scenarios.

The next chapter will present the results of the finite element model coupled to the constitutive model.

CHAPTER 8

NUMERICAL RESULTS

8.1 CONTOUR PLOTS

ABAQUS can be used to calculate stress concentrations, such as the location of the highest Von Mises stress, and display this information in the form of contour plots. Figure 8.1 shows the contour plot of the gear pair from section 7.3, with an applied torque of 200 $N \cdot m$ and a coefficient of friction of 0.05. The highest stresses are concentrated below the contact area between the two gears. A stress concentration at gear fillets, caused by the bending stress, can also be seen.

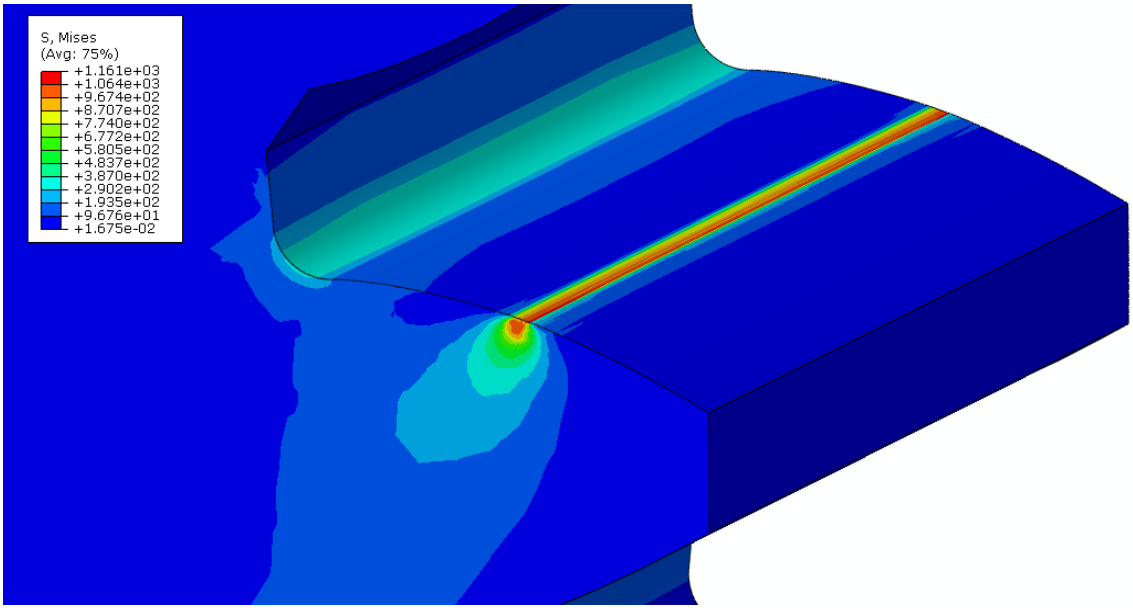

Figure 8.1: Von Mises (MPa) contour plot of gear pair, isometric view.

Figure 8.2 shows the contact stress at the flank of the tooth, with the highest stresses located along its contact line. Figure 8.3 shows the shear stress distribution at the contact point. The warmer colours show the distribution of the tensile stresses, where colder colours are related to compressive stresses. The distribution of the tensile stresses are important since these will be the driving force behind subsurface crack initiation and

propagation.

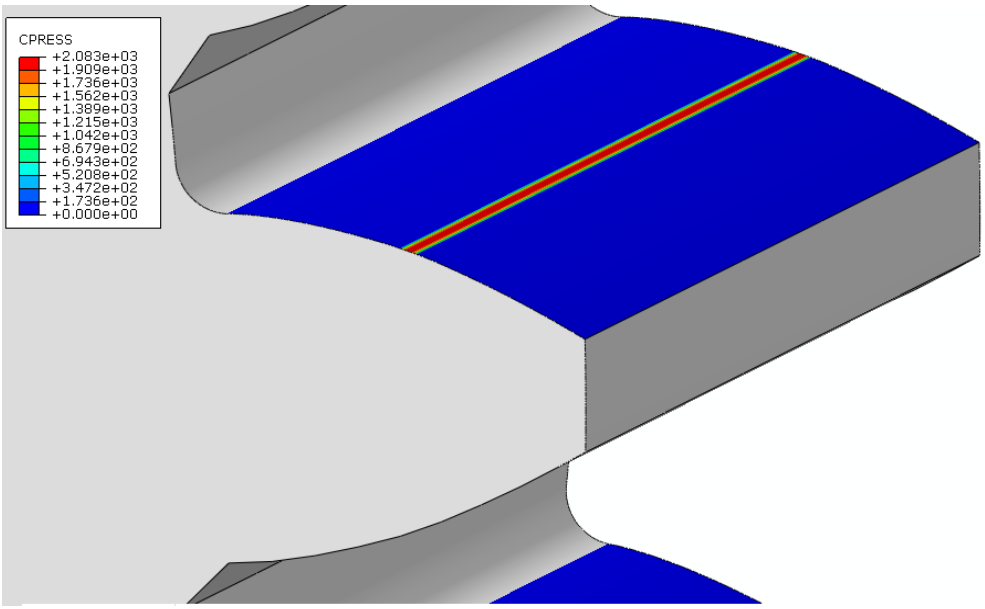

Figure 8.2: Contact stress (MPa) contour plot of gear pair, isometric view.

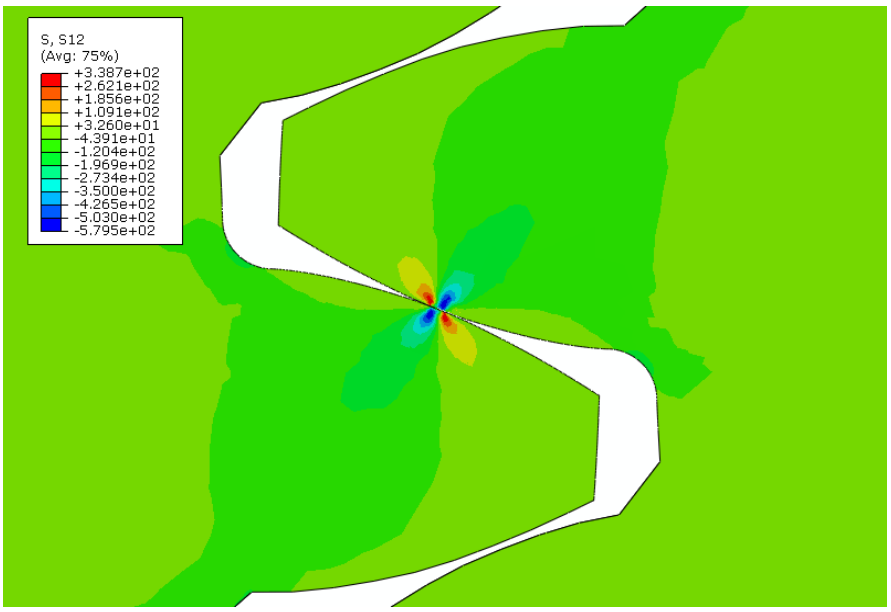

Figure 8.3: Shear stress (MPa) contour plot of gear pair, front view.

8.2 INFLUENCE OF SERVICE CONDITIONS

The model created and validated in chapter 7 has been used in the investigation of several service conditions, such as overloading, poor lubrication and misalignments. These situations are common on WTGs due to the highly varying loads that these components

experience, especially due to wind gusts and turbulence.

8.2.1 Overloading

The finite element model was tested for three different torque values, 100, 150, and 200 $N \cdot m$. The gear pair was perfectly aligned and a coefficient of friction of 0.05 was used. The simulations were run for a number of 10 cycles each, yielding a processing time of 25 days in total. They were run using BlueBEAR, the high-performance computing service provided by the University of Birmingham.

Figure 8.4 shows the equivalent stress and damage contours for three different torque values. These results were obtained in the last cycle of the simulation. As expected, a higher torque value leads to a higher contact stress. Additionally, the bending stresses are higher on the simulation with 200 $N \cdot m$. Consequently, the damage is higher on this simulation, being barely noticeable on the 150 $N \cdot m$ simulation and insignificant on the 100 $N \cdot m$ simulation.

It is worthy to note that the direction and location of the damage match the location of the tensile stresses seen in Figure 8.3. As the location of the tensile stresses are always changing as the gears turn, the damage and dislocation density move with it, creating the shape that resembles that of a micropit or subsurface cracks, which were observed in the RCF tests.

The finite element with the highest value for the damage variable was then selected for data extraction. Stress and state variables values during the entire simulation were obtained. Figure 8.4 shows the stress values of these elements. There are 10 stress peaks for each simulation, which correspond to the moment when the selected element was in contact with the other gear. It is also noticeable that after the first contact, the stress values of the 200 and 150 $N \cdot m$ simulations do not return to zero. This is due to the residual stress that was generated upon contact. For the 100 $N \cdot m$ simulation, this residual stress is barely noticeable.

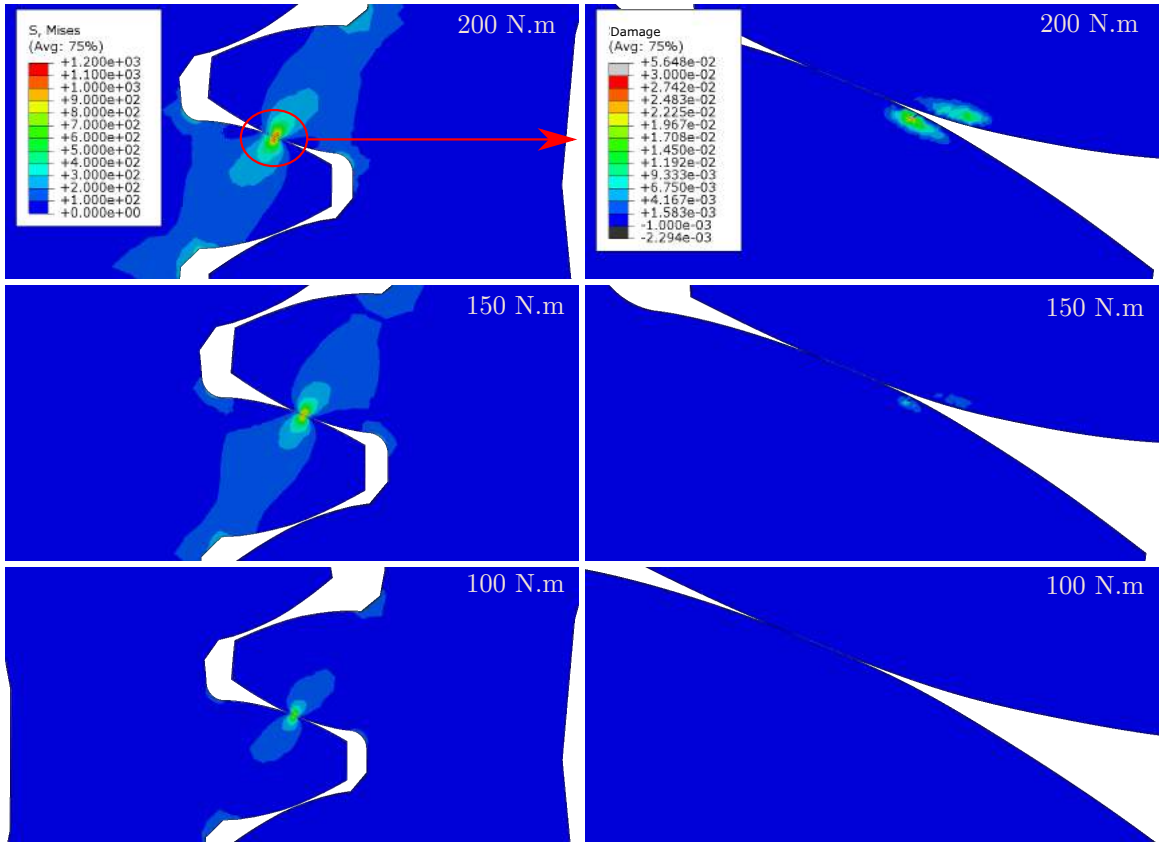

Figure 8.4: Von Mises (MPa) and damage contour plots after 10 turns, for three different torque values.

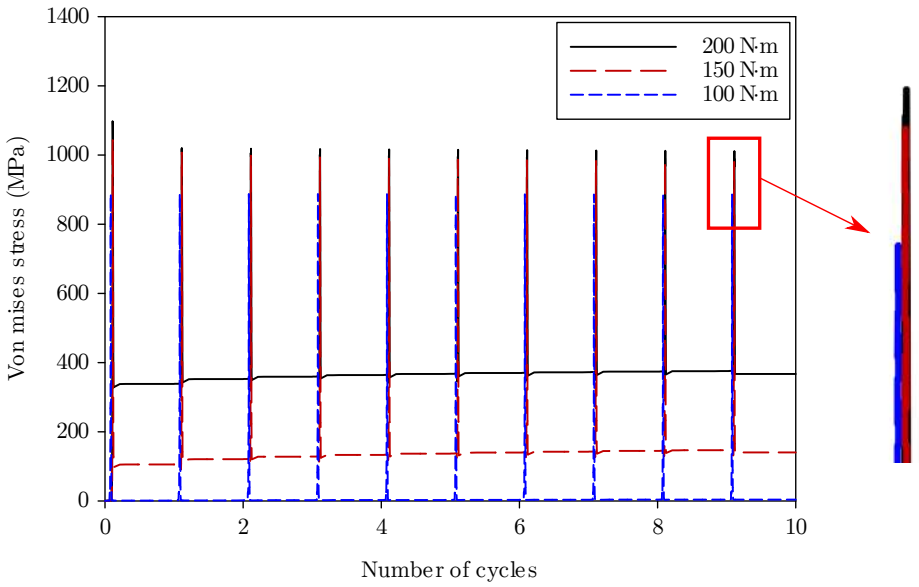

Figure 8.5: Stress values of finite element with the maximum accumulated damage in each simulation.

Figures 8.6 and 8.7 show the state variable evolution of all three simulations. They all present a step-like behaviour, due to the way that the stress is applied to these elements, as previously shown. On every cycle, stress is transferred in between the gears. Plastic strain and damage are accumulated. This behaviour becomes more noticeable at higher torque values. Moreover, similarly to the strain-controlled cyclic simulation performed on chapter 7, the state variables are evolving towards a steady state behaviour. Almost no difference is observed in the 100 N · m simulation, since the stress values obtained are not high enough to cause plastic deformation and kick off the plastic strain variable.

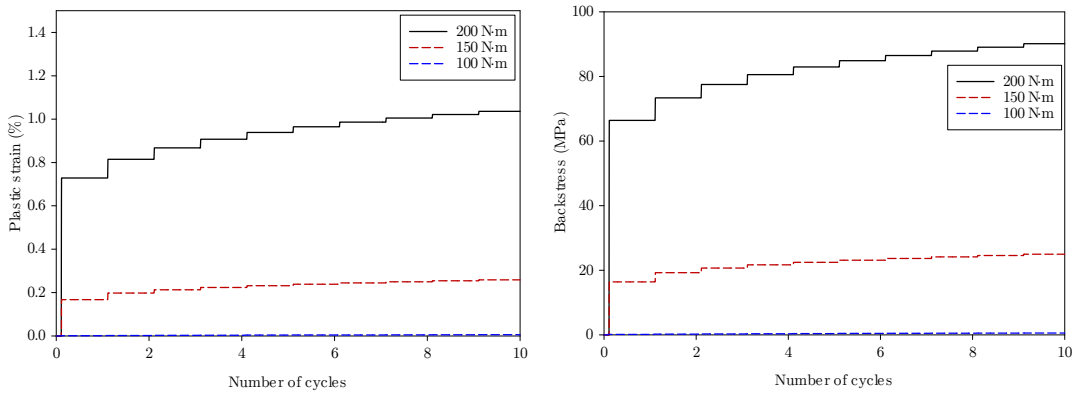

(a) (b)

Figure 8.6: Evolution of the state variables: plastic strain (a), and backstress (b), after 10 cycles.

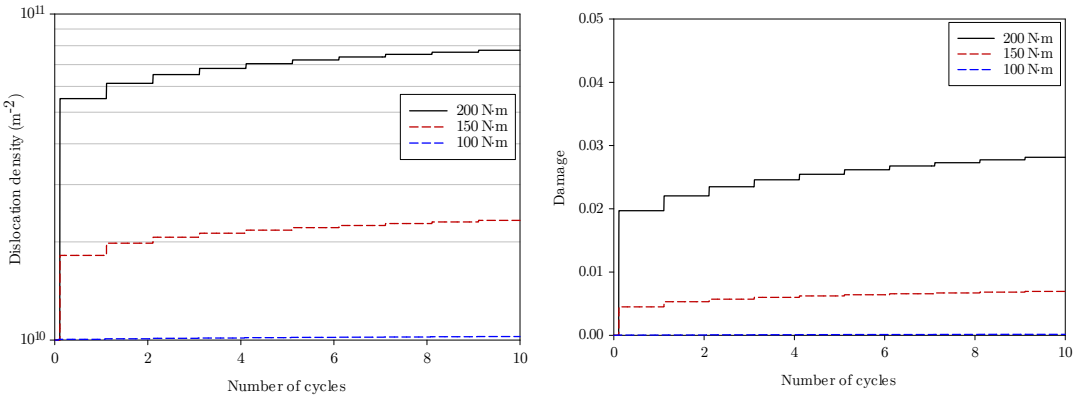

(a) (b)

Figure 8.7: Evolution of the state variables: dislocation density (a), and damage (b), after 10 cycles.

8.2.2 Lubrication

Due to overloading or instant misalignment events, the oil lubricating the gears may be squeezed away, leading to an alternation between dry and lubricated periods. Rebbechi et al. [199] found the coefficient of friction of lubricated gears is usually in the range of 0.04 and 0.06. The coefficient of friction for dry steel on steel contact, on the other hand, is around 0.75 [200]. In this section, two simulations were run, namely "lubricated" and "dry" simulations. Their coefficients of friction are 0.05 and 0.75, respectively. A torque of 10 $\mathrm{N} \cdot \mathrm{m}$ was applied in each case, during 5 cycles.

Figure 8.8 shows the Von Mises stress contour plots for both simulations. With the increase of the coefficient of friction, the location of the highest stress moves from the subsurface towards the contact surface, as demonstrated by Hamilton in ref. [201]. The highest values for the Von Mises, contact, and shear stresses are shown in Figure 8.9.

With a higher coefficient of friction, the friction forces increase, thus increasing the contact stress as well. The increase in the Von Mises stress and contact stress are 58% and 14%, respectively. The shear stress has the highest increase, at 146%. Such high values for the Von Mises and shear stresses might generate plastic deformation, micropitting, and scuffing.

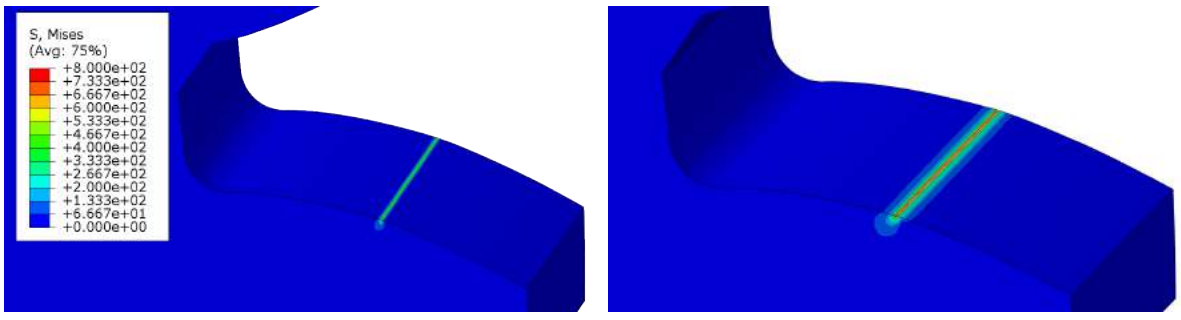

(a) (b)

Figure 8.8: Von Mises (MPa) contour plot of the highest stress obtained during the lubricated (a), and dry (b) simulations.

Similarly as in the previous subsection, the finite element with the highest accumulated damage was chosen for data extraction. Due to the lower torque applied

(10 N · m, in comparison to the 200 N · m applied in the overloading simulations), the damage values are expected to be small. A comparison between the lubricated and dry simulations is shown in Figure 8.10. The damage variable is 10 orders of magnitude higher in the dry simulation. This shows the oscillation between dry and lubricated regimes can be quite detrimental and severely reduce WTG life.

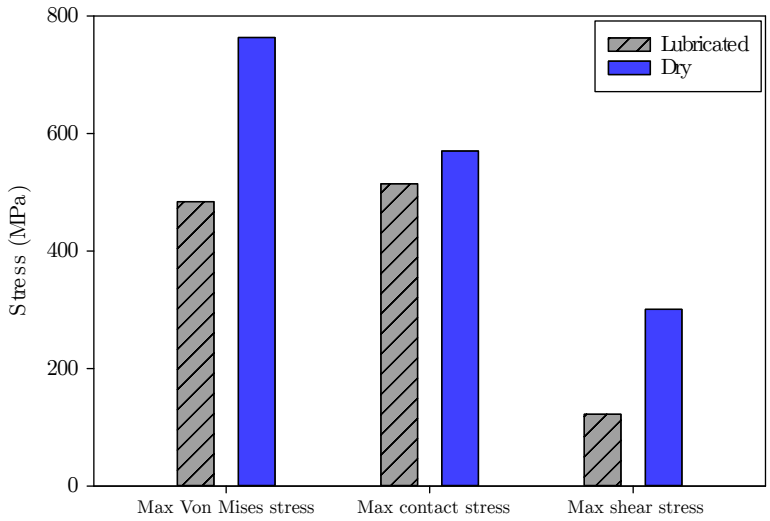

Figure 8.9: Maximum values of the Von Mises, contact, and shear stresses during the lubricated and dry simulations.

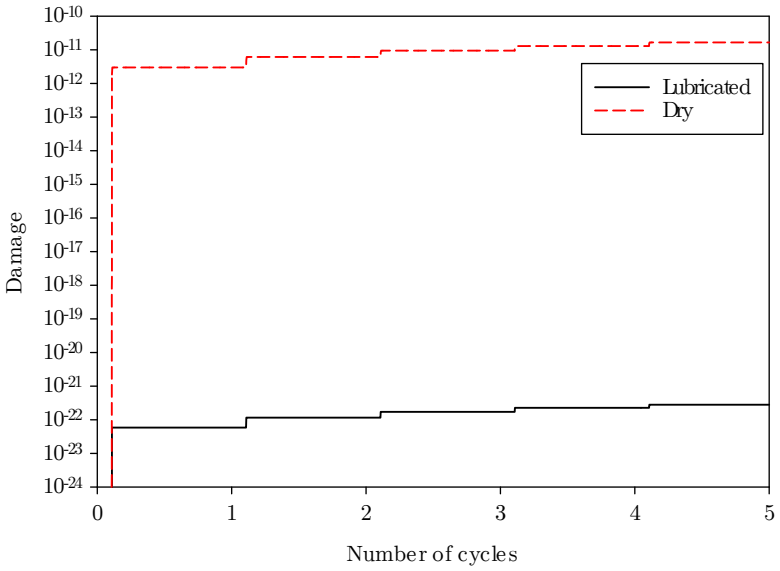

Figure 8.10: Evolution of the damage variable of the lubricated and dry simulations.

8.2.3 Parallel misalignment

Different types of misalignment can occur in a gearbox. One of these is the parallel misalignment, where one of the gears is offset as shown in Figure 8.11.

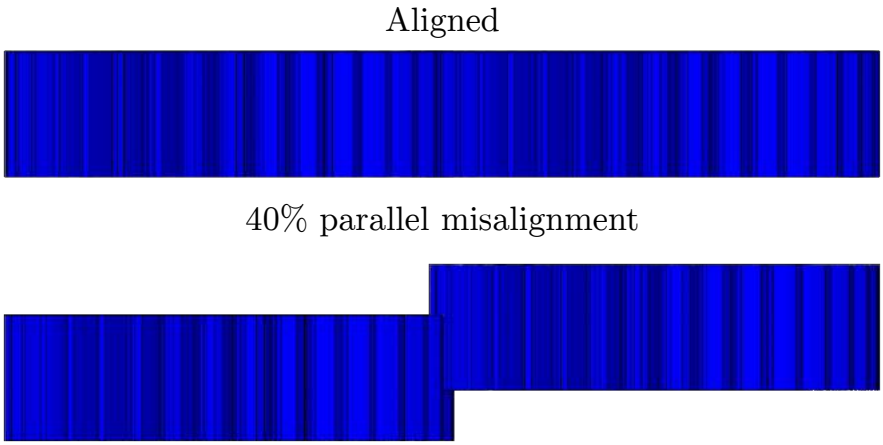

Figure 8.11: Comparison between a perfectly aligned gear pair and a pair with 8 mm parallel misalignment, top view.

The parallel misalignment was generated by translating one of the gears along its z-axis by 8 mm. This is a quite severe condition, where only 60% of the contact surface of the gears would actually be in contact since the face width of the gears is 20 mm. A torque of 10 $\mathrm{N} \cdot \mathrm{m}$ and a coefficient of friction of 0.05 were used.

The equivalent stress contour plot of the gear with parallel misalignment is shown in Figure 8.12. The stress distribution is not uniform along the tooth width. The highest stress concentrations occur at the edges of both gears. A comparison between stress states of an aligned and parallel misaligned gear is shown in Figure 8.13.

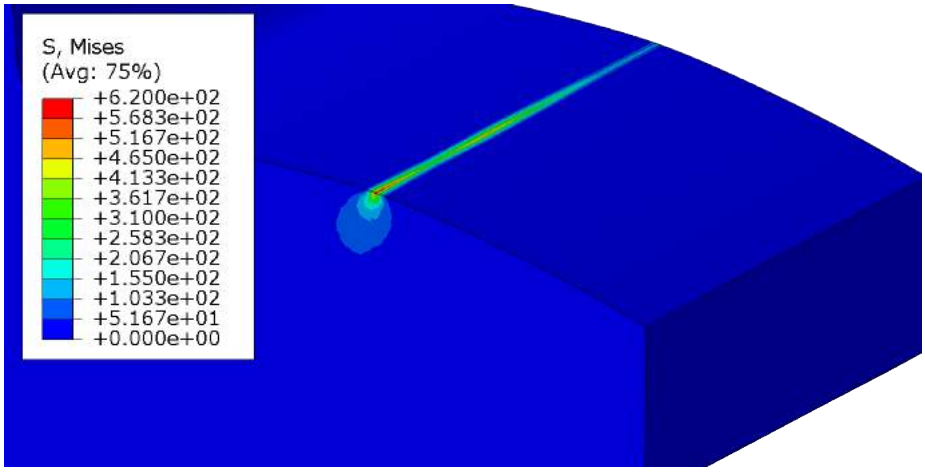

Figure 8.12: Von Mises (MPa) stress contour plot of the gear with 40% parallel misalignment.

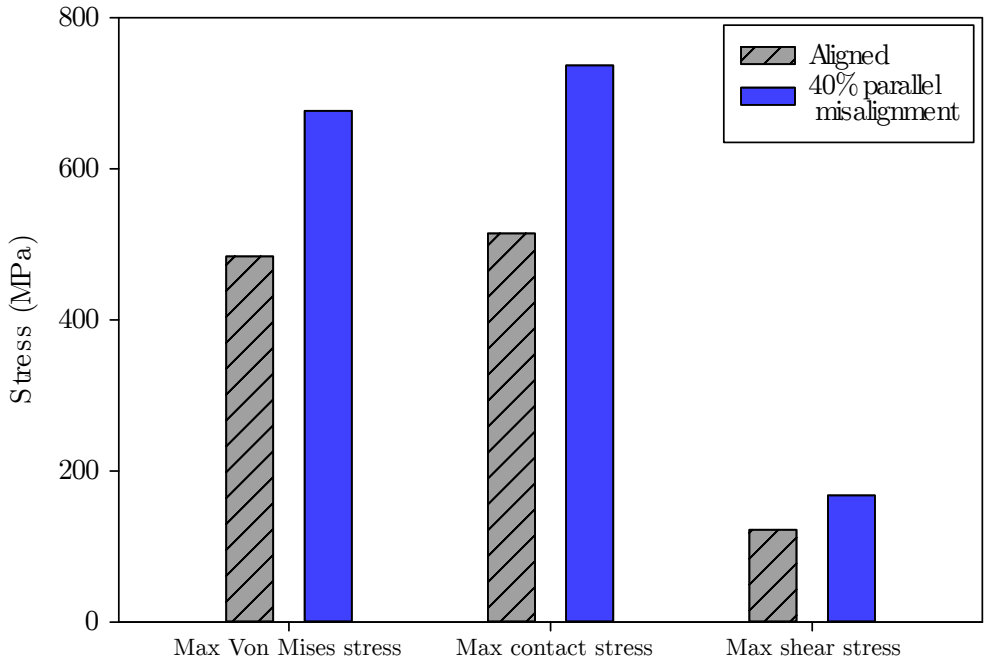

Figure 8.13: Maximum values of the Von Mises, contact, and shear stresses during the aligned and parallel misaligned simulation.

The equivalent stress, contact stress and shear stress increased by 40%, 43%, and 37%, respectively. When compared to the dry simulation, the equivalent stress and shear stress increase are lower, whereas the contact stress increase is four times higher. The contact stress increase occurs mostly due to the reduced area of contact.

Once again, the finite element with the highest accumulated damage was chosen for data extraction. The results for the damage variable over 5 cycles are shown in Figure 8.14. There is an increase of 5 orders of magnitude for the misaligned simulation, showing that this type of misalignment is not as detrimental as poor lubrication.

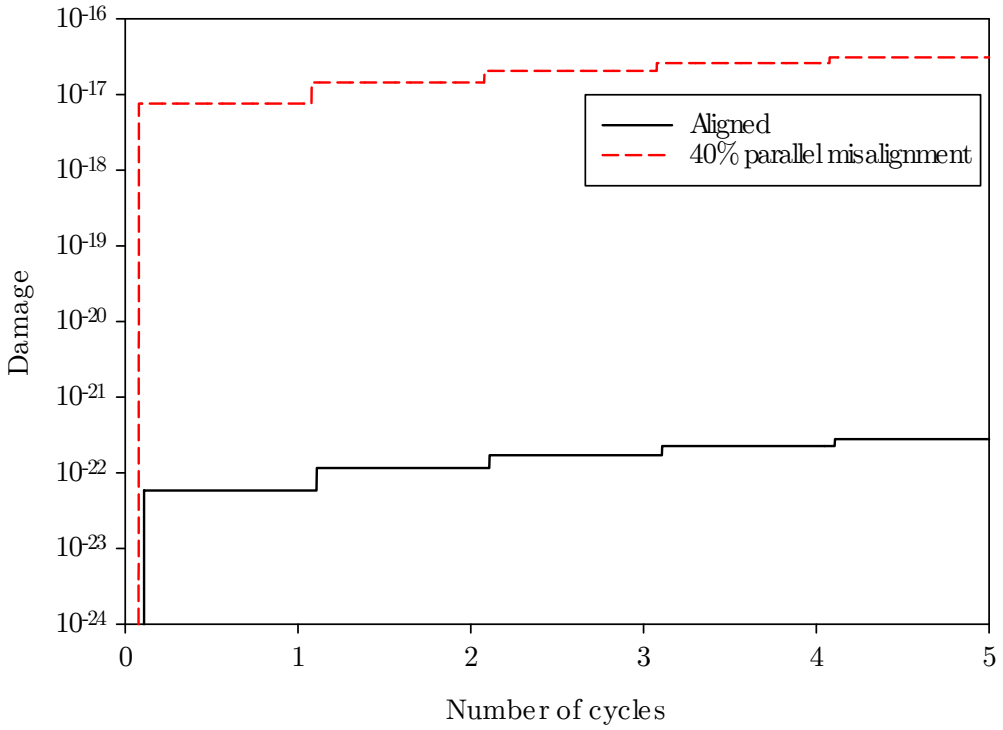

Figure 8.14: Evolution of the damage variable of the aligned and radial misaligned simulation.

8.2.4 Radial misalignment

In order to produce the radial misalignment (Figure 8.15), the assembly module was changed and one of the gears was translated along the x-axis by 1.80 mm. The tooth height for this gear pair is 4.50 mm, and thus the radial misalignment is 40%. A torque of 10 N · m was applied and the friction coefficient was set to 0.05.

The Von Mises contour plot of the 40% radially misaligned gear is shown in Figure 8.16. The highest stresses are localised at the tooth tip. Even though there is a tip relief of 250 µm, the pitch lines of the gears are not in contact as they should be. The involute profile of the gears is manufactured so that the velocity of the gears is constant,

avoiding accelerations and decelerations. The misalignment causes the involute profiles of the gears to engage earlier than they should, generating stress concentrations which could lead to surface damage such as scuffing.

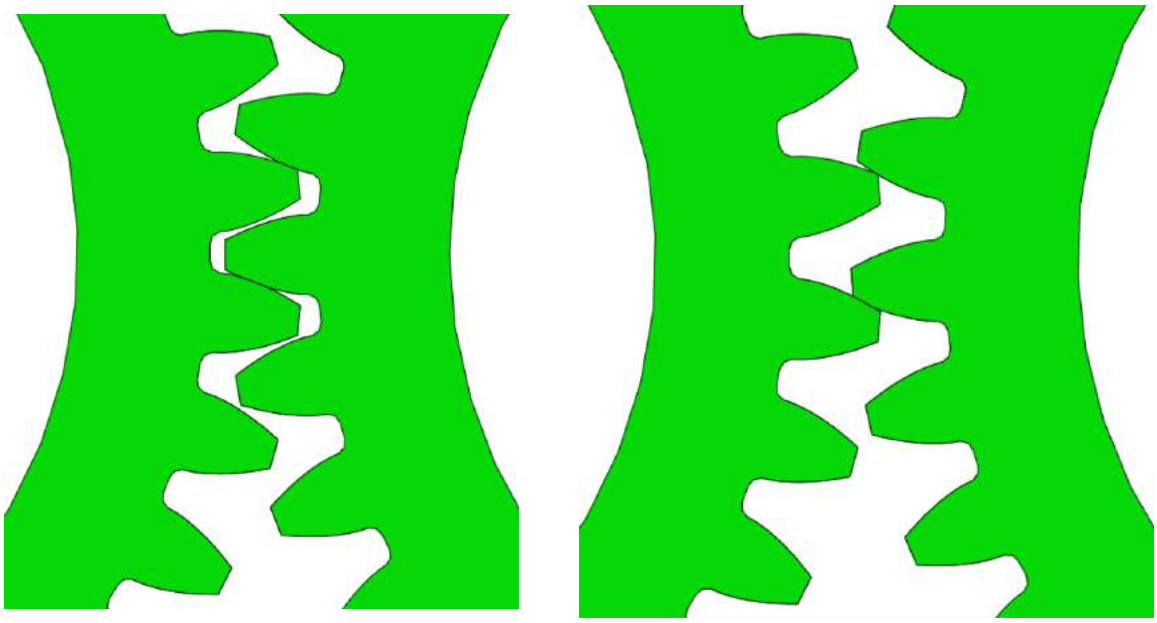

(a) (b)

Figure 8.15: Gear pair in perfect alignment (a); gear pair in radial misalignment (b).

Figure 8.17 shows the shear stress experiences almost no change when compared to a perfectly aligned gear. However, the Von Mises stress and the contact stress increase by 212% and 178%, respectively.

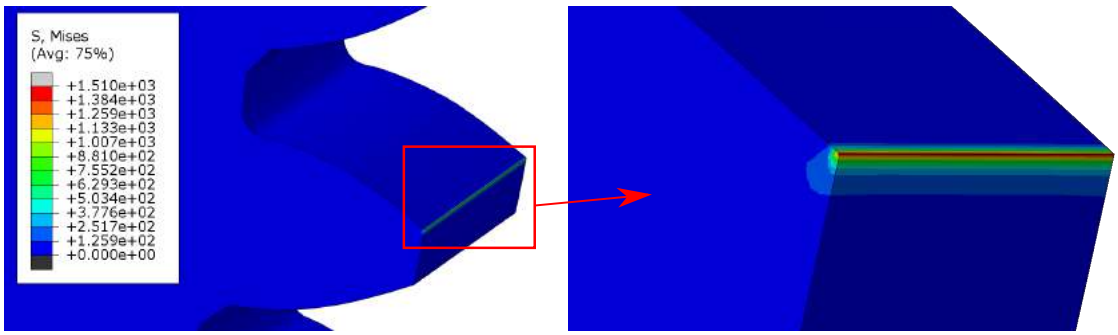

Figure 8.16: Von Mises (MPa) stress contour plot of the 40% radial misalignment simulation.

The evolution of the damage variable is shown in Figure 8.18. The difference between an aligned gear and a gear with 40% misaligned is 17 orders of magnitude. Even though 40%

is a high value, so was the 40% parallel misalignment, which did not generate such fast damage evolution in comparison. The radial alignment is extremely important in order to preserve the involute profile and facilitate the engagement of gears.

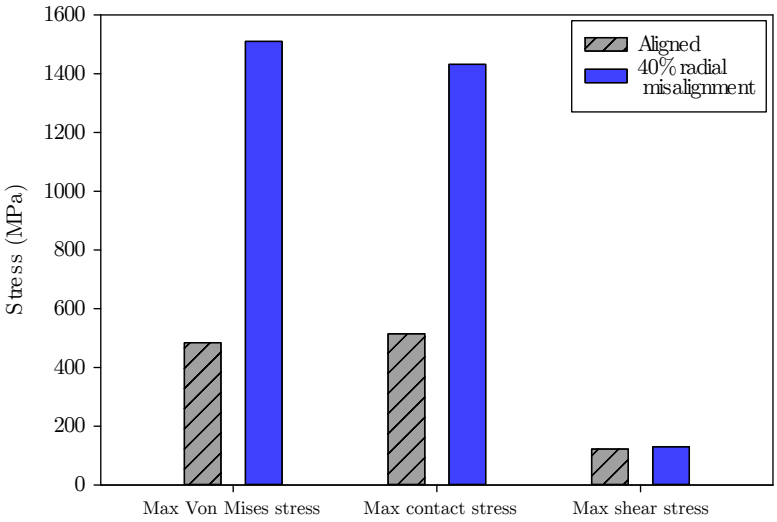

Figure 8.17: Maximum values of the Von Mises, contact, and shear stresses during the aligned and radial misaligned simulation.

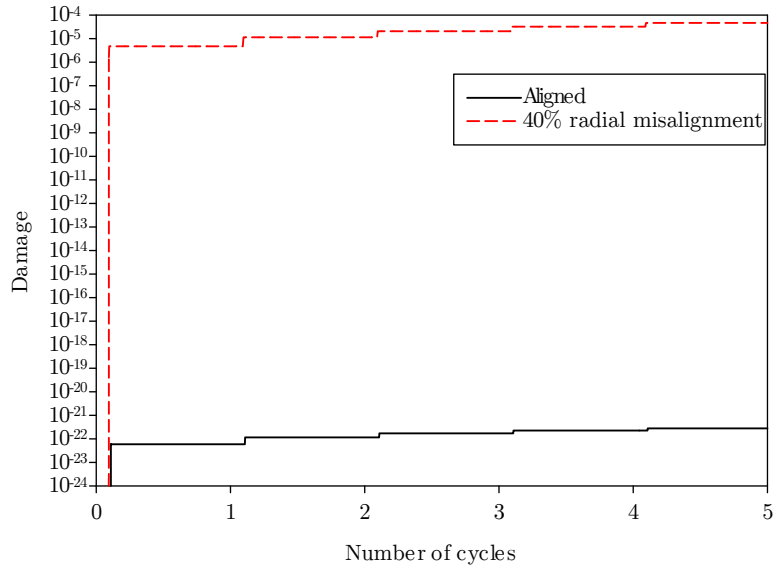

Figure 8.18: Evolution of the damage variable of the aligned and radial misaligned simulation.

8.2.5 Angular misalignment

The angular misalignment was the last service condition tested. In order to generate the angular alignment, one of the gears was rotated along its y-axis by 0.5° (Figure 8.19). The torque and coefficient of friction were 10 N · m and 0.05, respectively.

The Von Mises contour plot can be seen in Figure 8.20. The shape and location of the stress concentrations are similar to that of the parallel misalignment case. However, the stress values are more than double. The angular misalignment creates a stress concentration that might be an initiation site for damage and is likely to lead to fracture.

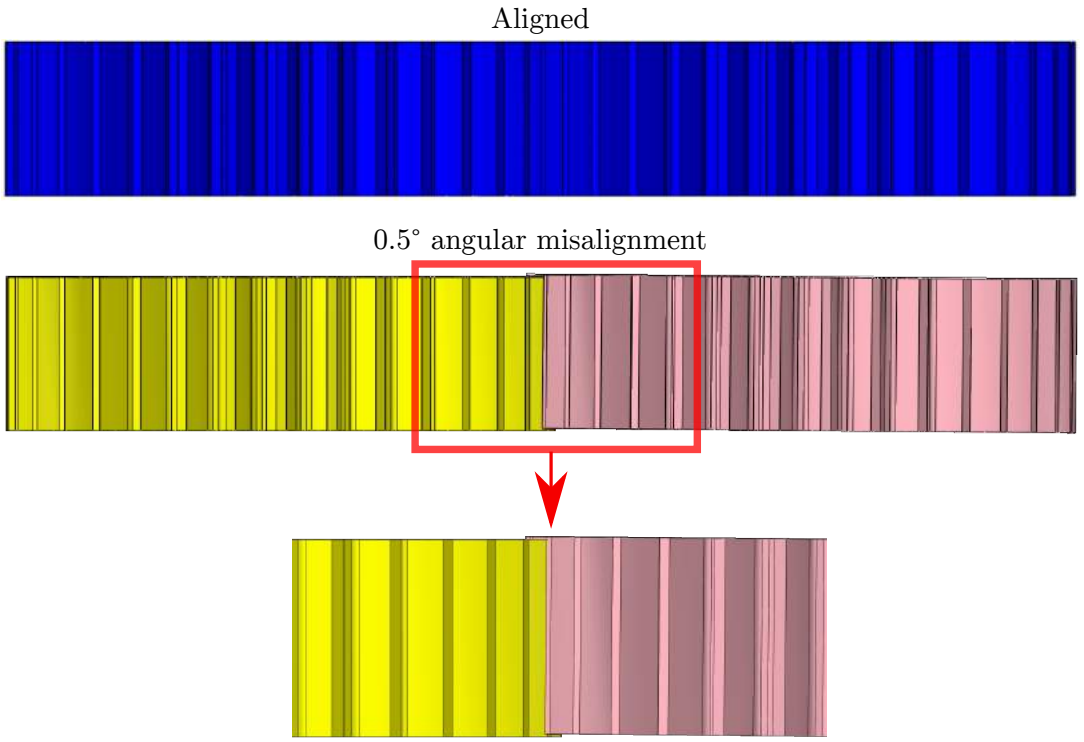

Figure 8.19: Comparison between a perfectly aligned gear pair and a pair with 0.5° angular misalignment, top view.

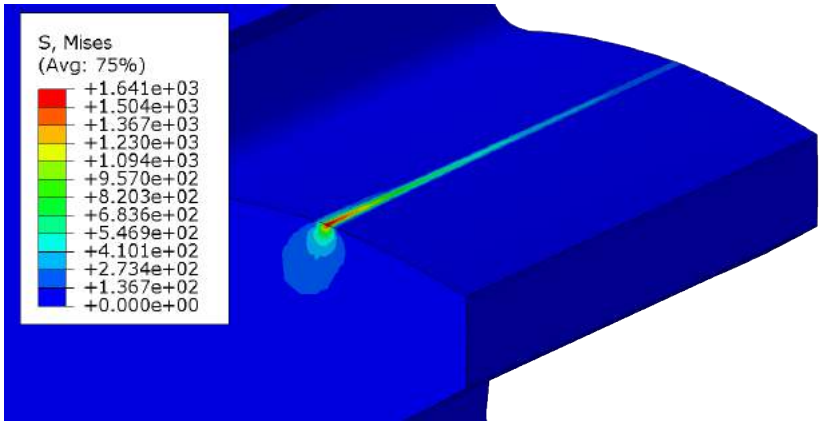

Figure 8.20: Von Mises (MPa) stress contour plot of 0.5° angular misalignment. Colours were changed for better visualisation.

An angular misalignment of 0.5° is much more likely to happen than a 40% parallel or radial misalignment. And even such small misalignment has a strong effect on the stresses, as shown in Figure 8.21. The equivalent stress, contact stress, and shear stress increase by 239%, 136%, and 290%, respectively. Similarly to the radial misalignment, the involute profile of the gears is out of synchronization, which leads to poor meshing and stress concentrations.

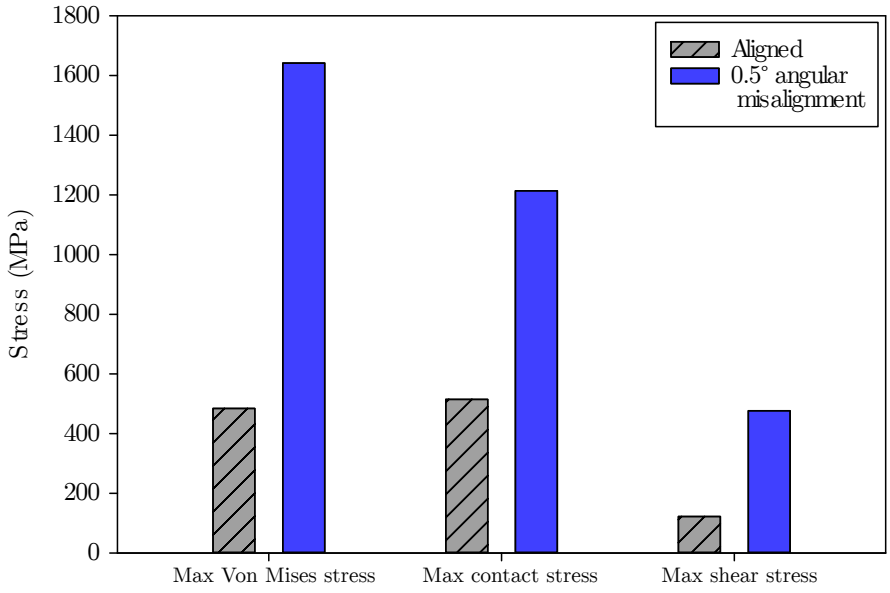

Figure 8.21: Maximum values of the Von Mises, contact, and shear stresses during the aligned and angular misaligned simulation.

This type of misalignment is the most detrimental to gear life, as shown by Figure 8.22. The damage variable has an increase of over 18 orders of magnitude, with only 0.5° of misalignment. It is also noteworthy that the torque values of this simulations are only 10 N · m. Under normal service conditions, this torque would be higher, and even an instantaneous misalignment, caused by a wind gust, could severely increase damage and reduce the remaining useful lifetime of the component.

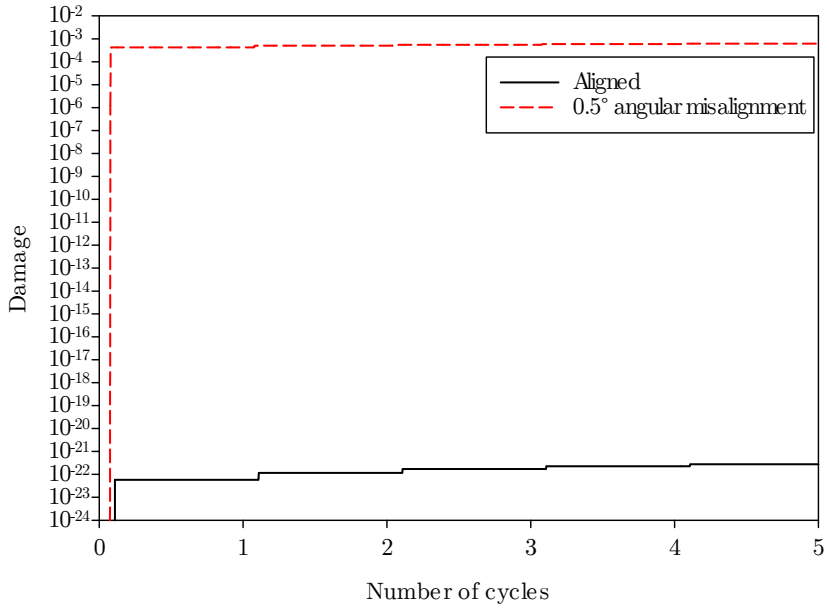

Figure 8.22: Evolution of the damage variable of the aligned and angular misaligned simulation.

8.3 LIFETIME ESTIMATION

Most WTG maintenance carried out nowadays is corrective or preventive. There is a great effort from the industry in moving towards a more condition-based approach, with the use of vibration analysis, oil monitoring and acoustic emission monitoring, for example.

Due to the highly varying loads to which they are subjected to, being able to predict the damage state of the WTG component is an extremely difficult and complex task. In this section, the data obtained from the service conditions simulations will be used in order to compare and estimate the lifetime of the gear pair used in this study.

Due to the high computational cost, it is impractical to run the previous simu-

lations for more than a dozen of cycles. However, it is clear from the previous results that all state variables enter a steady state condition with only a few number of cycles. This means that at every new cycle, the increment on each state variable can be considered as constant.

Therefore, the incremental damage accumulated from the tenth cycle was employed in a Miner's rule [202] approach, which assumes a linear damage accumulation. This allows the estimation of the lifetime of the component, and the creation of a stress-cycles (S-N) curve, as shown in Figure 8.23.

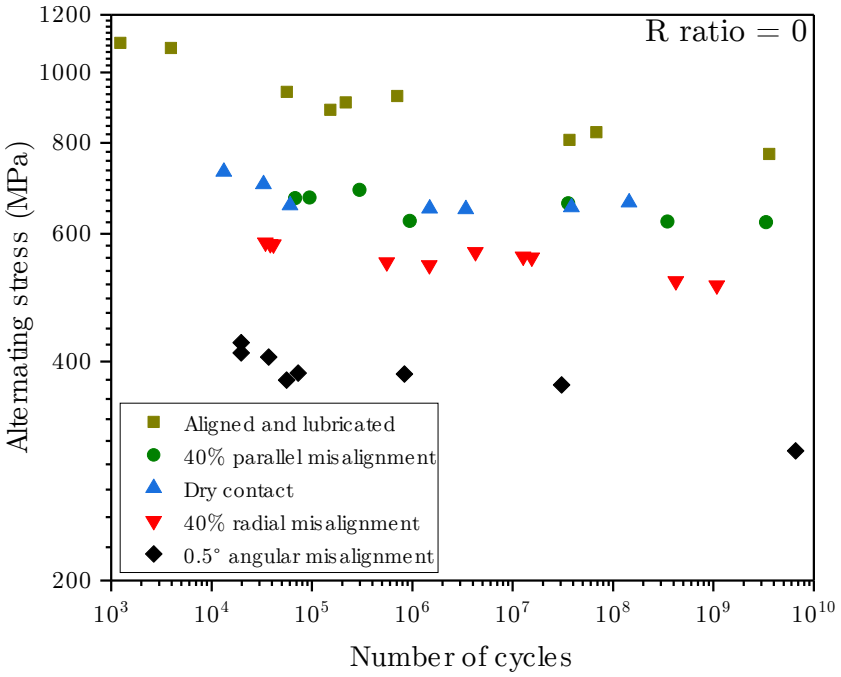

Figure 8.23: Stress-cycles curve of different service conditions.

From the S-N curve, it becomes clear once again that the angular misalignment is the most detrimental between the tested service conditions, followed by the radial misalignment. The dry contact simulation and the parallel misalignment simulation achieved similar results. The fully lubricated and aligned simulation results are also shown, as a comparison between the other service conditions.

But more than only a comparison of different service conditions, the graph in Figure 8.23 is an example on how operators can use this model in order to estimate the remaining useful lifetime. For example, if a misalignment event was detected by the

vibration monitoring system, the number of cycles of this event can be calculated. With this information, an estimation of the percentage of the useful lifetime that was lost in the event can be made!

For example, 500 cycles of dry contact at 650 MPa would result in a loss of 0.003% of the total useful lifetime. On the other hand, 500 cycles at 400 MPa with an angular misalignment of only 0.5° reduces the total lifetime by 2.5%! Considering the high speed stage gear rotating at 1500 rpm, it would take minutes for a brand new gear to completely fail. It is noteworthy, however, that this is a conservative estimation, since it is likely that damage will progress at a faster rate at the late stages, diminishing the lifetime even more.

This graph shows the importance of monitoring the WTG service conditions, since even instant misalignment events produced by wind gusts can greatly increase the accumulated damage within the material, and thus reduce the remaining useful lifetime considerably.

8.4 SUMMARY

Different service conditions were tested with the use of the finite element model coupled to the constitutive model. The results for the equivalent stress, contact stress and shear stresses were analysed, and a summary of the results can be seen in Figure 8.24.

The angular misalignment generated the highest equivalent and shear stresses concentration, whereas the radial misalignment was responsible for the highest contact stress observed. Following that, the evolution of the damage state variable was also recorded and is shown in Figure 8.25 for all service conditions.

As previously shown, the angular misalignment is the most detrimental service condition of all the compared cases. The damage evolution occurs quickly and then evolves to a more steady state condition.

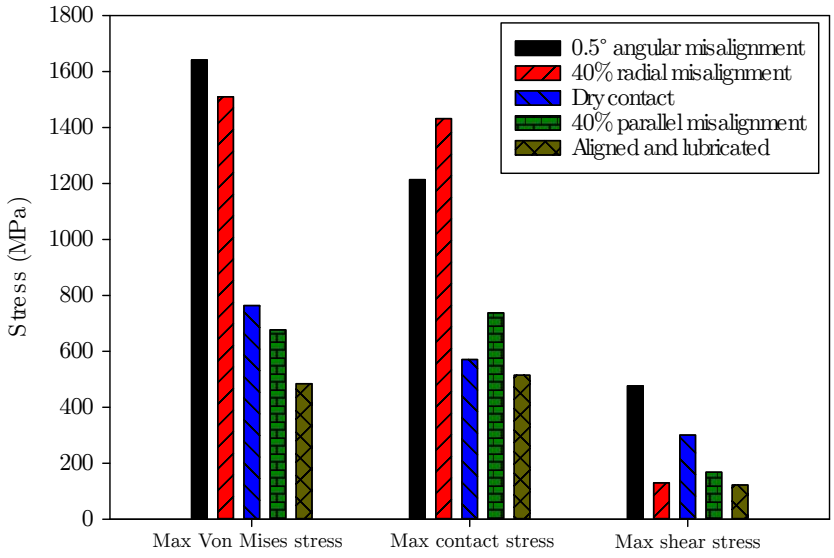

Figure 8.24: Maximum values of the Von Mises, contact, and shear stresses for all service condition simulations with a torque of 10 N · m.

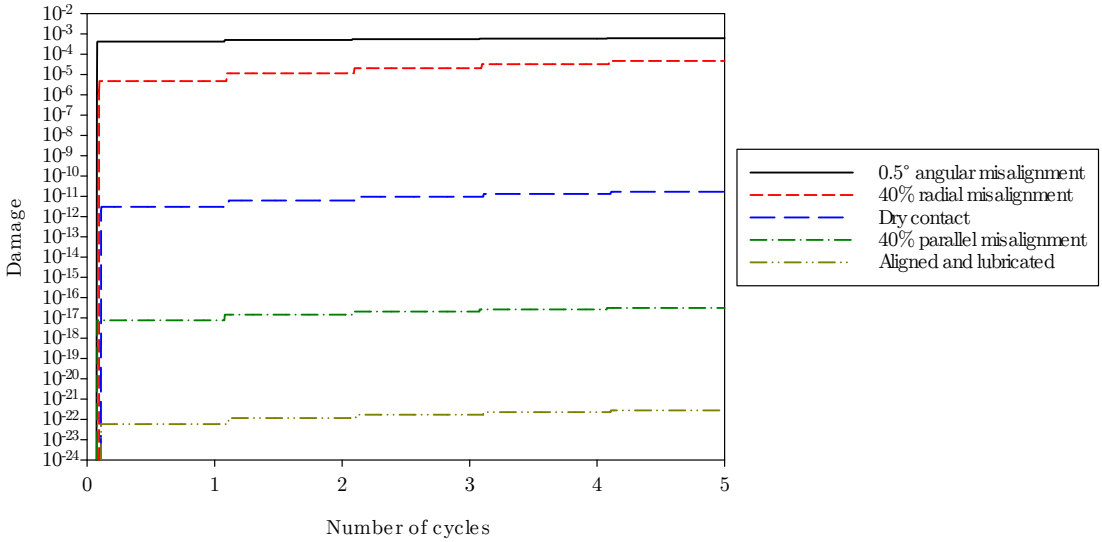

Figure 8.25: Evolution of the damage variable of all service condition simulations with a torque of 10 N · m.

Finally, an S-N curve was obtained for all service conditions. This allows wind farm operators to actually quantify damage based on the service conditions experienced by the components, and establish a preventive maintenance approach. Coupled with the use of monitoring techniques, such as acoustic emission, the model has great potential to predict damage levels and help manage maintenance planning effectively.

CHAPTER 9

CONCLUSIONS AND FUTURE WORK

9.1 CONCLUSIONS

Referring to the aims and objectives of this work, the first goal of this study was to carry out failure analysis of wind turbine gearbox components provided by wind farm operators, in order to better understand their root cause and failure mechanisms. By analysing the failed components, it was observed that:

- MnS inclusions were found to be the initiation site for subsurface cracks.
- Poor lubrication is detrimental to gear life. It can lead to scuffing, overheating and alter the stress states leading to fatigue failure.
- Misalignment in gears and bearings can also alter the stress distributions, generating defects such as micropitting. On the other hand, a misdiagnosis, as the one observed on the generator bearing, can lead to downtime and lost production.

The second goal of this work was to better understand material damage initiation and propagation under rolling contact fatigue conditions similar to those experienced by wind turbine gearboxes and evaluate the influence of different surface engineering methods. The following conclusions could be drawn:

- MnS inclusions were found to initiate subsurface cracks, similarly to what was observed in the samples analysed from the field.
- The "dry-lubricated" and intermittent tested samples were damaged far earlier and quicker than the fully lubricated sample. All samples presented subsurface cracks, however, only the "dry-lubricated" and intermittent samples had cracks at the wear track. This reiterates the importance of a good lubrication regime in order to prolong rolling contact fatigue lifetime of rotating components.

- The plasma nitrided material was more resistant to rolling contact fatigue and did not show any subsurface cracks. No cracks at the wear track centre were observed either.

- The samples with the diamond-like carbon coating showed severe cracking and delamination. This is attributed to the high contact stress (5 GPa) used during the rolling contact fatigue tests, as well as the coating being thin and hard. The diamond-like carbon coating did not improve rolling contact fatigue life of the tested samples. Overall, single treated samples performed better than duplex samples.

The third goal of this work was to monitor rolling contact fatigue and mechanical tests via advanced acoustic emission monitoring, in order to evaluate and quantify damage initiation and propagation. It was found that:

- Acoustic emission monitoring proved to be a reliable technique in detecting small defects during fatigue crack growth.

- Acoustic emission monitoring was especially useful when detecting defects originating from rolling contact fatigue, such as subsurface cracking, and delamination, as well as the propagation of these defects.

Finally, the last objective of this work was to develop a reliable and accurate finite element model coupled with a micromechanical damage evolution law that simulates failure in WTG components. The following conclusions were drawn:

- A constitutive model was developed and calibrated to the EN24T steel. The model was then coupled to a finite element model of a spur gear pair, which presented good correlation to the American Gear Manufacturing Association equations.

- The damage evolution depends on the loading and contact conditions. Several service conditions, such as overloading, poor lubrication and misalignments were tested. It was found that the angular misalignment was the most detrimental service condition, followed by radial misalignment, dry contact, and parallel misalignment.

- Stress-cycles curves based on the simulations and on the constitutive model were created. They show the model can be used to successfully estimate the remaining useful lifetime of a wind turbine gearbox component. This is a great step towards the implementation of a true predictive maintenance approach.

Based on these conclusions, some recommendations can be made in order to improve the reliability and useful lifetime of wind turbine gearboxes. For example, the use of acoustic emission monitoring proved to have great potential in rolling contact fatigue applications. This technique can be employed in wind turbine gearbox in order to monitor incipient damage, as well as damage propagation.

MnS inclusions were also found to act as crack initiators. Therefore, the material used in the manufacture of wind turbine gearbox components should be as clean as possible.

Poor lubrication and misalignments were proven to be detrimental to rolling contact fatigue life. Condition monitoring techniques, such as oil analysis and vibration analysis should be employed in order to monitor the oil quality and component alignment.

Finally, these condition monitoring techniques should be complemented with the use of physical models, such as the one developed in this work. Such models can be employed in damage quantification, providing the operator with more information regarding the remaining useful lifetime of the component. Condition monitoring and physical models are the means to changing the maintenance style from a preventive to a true predictive approach.

9.2 FUTURE WORK

During this study, several cracks were detected to initiate and propagate along MnS inclusions, both in the rolling contact fatigue laboratory tests, as well as from samples retrieved from the field. The execution of rolling contact fatigue tests with similar steel grades, except for the MnS inclusion content, in order to quantify the effect of the inclusions on the rolling contact fatigue life is therefore suggested.

Additionally, it would be interesting to employ the model used in this study with several random MnS inclusion distributions and analyse the model behaviour with different variables such as inclusion size, distribution, and orientation. Such model, however, would need an extraordinary amount of computational power, and thus is suggested as a future work, when processors and software are expected to continue improving.

It is also suggested the construction of a full wind turbine gearbox model, or the construction of different gear designs, such as helical gears. Again, this project was hindered by computational power, but it is expected that in the future a full model will be able to provide even more insight in increasing wind turbine gearbox reliability.

The performance of longer rolling contact fatigue tests with more samples is also suggested. This study suggests that the duplex coatings tested have lower rolling contact fatigue performance when compared to the single coated samples. However, it is recognised that a bigger sample size is required, and could not be achieved due to the time constraints of this study. Additionally, the testing of different coating systems could also show potential in increasing rolling contact fatigue.

Finally, the model generated in this study can drive forward the development of a true digital twin for the wind turbine gearbox. A digital twin is a prognostics and health management tool that virtually mirrors the monitored component and simulates its operation [203]. A digital twin can use data from several sensors, such as temperature, vibration, acoustic emission, power output, wind speed and direction, among others. This significant amount of data collected makes digital twins great tools for real time monitoring of key performance indicators [204]. However, due to the computational cost of storing and processing this data, physical models are usually oversimplified to a point where the prognostics are commonly incorrect. The employment of the model developed in this work coupled with data from these sensors is suggested.

REFERENCES

[1] O. Pechak, G. Mavrotas, and D. Diakoulaki, "Role and contribution of the clean development mechanism to the development of wind energy", *Renewable and Sustainable Energy Reviews*, vol. 15, no. 7, pp. 3380–3387, 2011.

[2] The European Parliament, "Directive 2009/28/EC of the European Parliament and of the Council of 23 April 2009 on the promotion of the use of energy from renewable sources and amending and subsequently repealing Directives 2001/77/EC and 2003/30/EC", *Official Journal of the European Union*, vol. 5, p. 2009, 2009.

[3] Global Energy Wind Council, "Global wind energy statistics report", 2017.

[4] MHI Vestas, *MHI Vestas Launches the First 10 MW Wind Turbine in History*, `http://www.mhivestasoffshore.com/mhi-vestas-launches-the-first-10-mw-wind-turbine-in-history/`, Web Page, 2018. (visited on 11/11/2018).

[5] GE Renewable Energy, *An industry first*, `https://www.ge.com/renewableenergy/wind-energy/turbines/haliade-x-offshore-turbine`, Web Page, 2018. (visited on 11/11/2018).

[6] E. Di Lorenzo, G. Kosova, U. Musella, S. Manzato, B. Peeters, *et al.*, "Structural health monitoring challenges on the 10-MW offshore wind turbine model", *Journal of Physics: Conference Series*, vol. 628, no. 1, p. 12 081, 2015.

[7] T. Bruce, E. Rounding, H. Long, and R. Dwyer-Joyce, "Characterisation of white etching crack damage in wind turbine gearbox bearings", *Wear*, vol. 338-339, pp. 164–167, 2015.

[8] Z. Shahan, "History of wind turbines", *Renewable Energy World*, 2014.

[9] J. M. P. Perez, F. P. G. Marquez, A. Tobias, and M. Papaelias, "Wind turbine reliability analysis", *Renewable and Sustainable Energy Reviews*, vol. 23, pp. 463–472, 2013.

[10] D. Spera, *Wind turbine technology: fundamental concepts of wind turbine engineering*, 2nd ed. New York, 2009.

[11] UKA Group, *How does a wind generator work?*, `https://www.uka-gruppe.de/en/citizens-and-communities/operating-principle-of-a-wind-turbine/`, Web Page, 2019. (visited on 02/02/2019).

[12] F. Marquez, A. Tobias, J. Perez, and M. Papaelias, "Condition monitoring of wind turbines: Techniques and methods", *Renewable Energy*, vol. 46, pp. 169–178, 2012.

[13] W. Steel, *Siemens looks toward next-generation 10-20 MW wind turbines*, `https://cleantechnica.com/2015/09/15/siemens-looks-toward-next-generation-10-20-mw-wind-turbines/`, Web Page, 2015. (visited on 08/08/2018).

[14] J. Hall, C. Mecklenborg, D. Chen, and S. Pratap, "Wind energy conversion with a variable-ratio gearbox: Design and analysis", *Renewable Energy*, vol. 36, pp. 1075–80, 2011.

[15] Global Energy Wind Council, "Global wind energy statistics report", 2016.

[16] W. Musial, S. Butterfield, and B. McNiff, "Improving wind turbine gearbox reliability: Preprint", National Renewable Energy Lab (NREL), Golden, CO (United States), Tech. Rep., 2007.

[17] H. Polinder, F. Van der Pijl, D. Vilder, and P. Tavner, "Comparison of direct-drive and geared generator concepts for wind turbines", *IEEE Transactions on Energy Conversion*, vol. 21, no. 3, pp. 725–733, 2006.

[18] P. Tavner, G. Van Bussel, and F. Spinato, "Machine and converter reliabilities in wind turbines", 2006.

[19] J. Helsen, F. Vanhollebeke, F. De Coninck, D. Vandepitte, and W. Desmet, "Insights in wind turbine drive train dynamics gathered by validating advanced models on a newly developed 13.2 MW dynamically controlled test-rig", *Mechatronics*, vol. 21, pp. 737–752, 2011.

[20] A. Greco, S. Sheng, J. Keller, and A. Erdemir, "Material wear and fatigue in wind turbine systems", *Wear*, vol. 302, pp. 1583–1591, 2013.

[21] S. Schmidt and A. Vath, "Comparison of existing medium-speed drive train concepts with a differential gearbox approach", *European Wind Energy Association, Copenhagen*, 2012.

[22] Olympus, *Inspections of wind turbine gearboxes*, `https://www.olympus-ims.com/en/applications/rvi-wind-turbine/`, Web Page, 2019. (visited on 02/02/2019).

[23] J. Coultate, D. Edwards, Z. Zhang, C. Halse, A. R. Crowther, *et al.*, "An investigation into the effect of lateral and axial aerodynamic loads on wind turbine gearbox reliability", in *European Wind Energy Conference and Exhibition (EWEC), Marseille*, 2009.

[24] S. Struggl, V. Berbyuk, and H. Johansson, "Review on wind turbines with focus on drive train system dynamics", *Wind Energy*, vol. 18, pp. 567–590, 2015.

[25] Y. Feng, Y. Qiu, and C. Crabtree, "Monitoring wind turbine gearboxes", *Wind Energy*, vol. 16, pp. 728–740, 2013.

[26] M. Kotzalas and G. Doll, "Tribological advancements for reliable wind turbine performance", *Philosophical Transactions of the Royal Society a-Mathematical Physical and Engineering Sciences*, vol. 368, pp. 4829–4850, 2010.

[27] G. Livingstone, J. Ameye, and D. Wooton, "Optimizing a wind turbine oil condition monitoring program", *Journal of ASTM International*, vol. 8, no. 10, pp. 1–11, 2011.

[28] A. Hamilton and F. Quail, "Detailed state of the art review for the different online/inline oil analysis techniques in context of wind turbine gearboxes", *Journal of Tribology*, vol. 133, no. 44001, pp. 1–18, 2011.

[29] G. Lindell and D. Herring, "Heat treating heavy-duty gears", *Gear Solutions*, 2007.

[30] A. Greco, K. Mistry, V. Sista, O. Eryilmaz, and A. Erdemir, "Friction and wear behaviour of boron based surface treatment and nano-particle lubricant additives for wind turbine gearbox applications", *Wear*, vol. 271, no. 9, pp. 1754–1760, 2011.

[31] P. Dearnley, *Wear resistant surfaces in engineering: a guide to their production, properties and selection*, ser. Surface Engineering. London, 1986.

[32] ANSI/AGMA/AWEA 6006-A03, *Standard for design and specification of gearboxes for wind turbines*, Standard, 2004.

[33] ISO 6336-5, *Calculation of load capacity of spur and helical gears - Part 5: Strength and quality of materials*, Standard, 2003.

[34] IEC 61400-4, *Wind turbines - Part 4: Design requirements for wind turbine gearboxes*, Standard, 2012.

[35] D. McVittie, "ISO 6336-5 strength and quality of materials", *Gear Technology (USA)*, vol. 16, no. 1, pp. 20–23, 1999.

[36] M. LaPlante, "Carburizing wind turbine gears", *Gear Solutions Magazine*, vol. 5, pp. 32–37, 2009.

[37] R. Errichelo, "Application requirements for wind turbine gearboxes", *NREL*, 1994.

[38] M. Nie and L. Wang, "Review of condition monitoring and fault diagnosis technologies for wind turbine gearbox", *Procedia CIRP*, vol. 11, pp. 287–290, 2013.

[39] R. Ahmed, "Rolling contact fatigue", *ASM handbook*, vol. 11, pp. 941–956, 2002.

[40] F. Sadeghi, B. Jalalahmadi, T. S. Slack, N. Raje, and N. K. Arakere, "A review of rolling contact fatigue", *Journal of tribology*, vol. 131, no. 4, p. 041 403, 2009.

[41] N. K. Arakere, "Gigacycle rolling contact fatigue of bearing steels: A review", *International Journal of Fatigue*, vol. 93, pp. 238–249, 2016.

[42] J. W. Ringsberg, "Life prediction of rolling contact fatigue crack initiation", *International Journal of fatigue*, vol. 23, no. 7, pp. 575–586, 2001.

[43] S. Way, "Pitting due to rolling contact", *ASME J. Applied Mechanics*, vol. 2, A49, 1935.

[44] J. Hoo, *Rolling contact fatigue testing of bearing steels: a symposium*, 771. ASTM International, 1982.

[45] W. Tyfour, J. Beynon, and A. Kapoor, "Deterioration of rolling contact fatigue life of pearlitic rail steel due to dry-wet rolling-sliding line contact", *Wear*, vol. 197, no. 1-2, pp. 255–265, 1996.

[46] D. Fletcher and J. Beynon, "The effect of intermittent lubrication on the fatigue life of pearlitic rail steel in rolling-sliding contact", *Proceedings of the Institution of Mechanical Engineers, Part F: Journal of Rail and Rapid Transit*, vol. 214, no. 3, pp. 145–158, 2000.

[47] M. Faccoli, C. Petrogalli, M. Lancini, A. Ghidini, and A. Mazzu, "Rolling contact fatigue and wear behavior of high-performance railway wheel steels under various rolling-sliding contact conditions", *Journal of Materials Engineering and Performance*, vol. 26, no. 7, pp. 3271–3284, 2017.

[48] S. Sheng, *Wind Turbine Micropitting Workshop: A Recap*. National Renewable Energy Laboratory, 2010.

[49] A. Milburn, "Wind turbine gearbox wear and failure modes and detection methods", in *NREL Wind Turbine Condition Monitoring Workshop*, 2011.

[50] R. Errichelo, "Another perspective: False brinelling and fretting corrosion", *Tribology & Lubrication Technology*, no. 60, pp. 34–36, 2004.

[51] K. Stadler, *How black oxide coated bearings can make an impact on cutting O&M costs for wind turbines*, `http://evolution.skf.com/us/how-black-oxide-coated-bearings-can-make-an-impact-on-cutting-om-costs-for-wind-turbines/`, Web Page, 2013. (visited on 08/08/2018).

[52] H. Al-Tameemi, H. Long, and R. Dwyer-Joyce, "Initiation of sub-surface micro-cracks and white etching areas from debonding at non-metallic inclusions in wind turbine gearbox bearing", *Wear*, vol. 406, pp. 22–32, 2018.

[53] P. Fernandes, "Tooth bending fatigue failures in gears", *Engineering Failure Analysis*, vol. 3, no. 3, pp. 219–225, 1996.

[54] R. Errichello, "How to analyze gear failures", *Journal of Failure Analysis and Prevention*, vol. 2, no. 6, pp. 8–16, 2002.

[55] R. Errichello and J. Muller, "Oil cleanliness in wind turbine gearboxes", *Machinery Lubrication*, vol. 2, no. 4, pp. 34–40, 2002.

[56] W. Needelman, M. Barris, and G. LaVallee, "Contamination control for wind turbine gearboxes", *Power Engineering*, vol. 113, no. 11, p. 112, 2009.

[57] T. Verbruggen, "Wind turbine operation & maintenance based on condition monitoring", *WT-O. Final report. ECN-C-03-047*, 2003.

[58] T. Burton, D. Sharpe, N. Jenkins, and E. Bossanyi, *Wind energy handbook*. John Wiley & Sons Ltd, 2001.

[59] P. Tavner, R. Gindele, S. Faulstich, M. Whittle, D. Greenwood, *et al.*, "Study of effects of weather & location on wind turbine failure rates", in *Proceedings of the European wind energy conference EWEC*.

[60] D. Dudley, *Handbook of practical gear design*. CRC Press, 1994.

[61] R. Budynas and J. Nisbett, *Shigley's mechanical engineering design*, 9th edition. McGraw-Hill, 2011.

[62] P. Childs, *Mechanical design engineering handbook*. Butterworth-Heinemann, 2013.

[63] J. Coy, D. Townsend, and E. Zaretsky, "Gearing", National Aeronautics and Space Administration, Lewis research center, Report, 1985.

[64] P. J. O'Keefe, *Spur gear tooth geometry and the involute curve*, http://www.engineeringexpert.net/Engineering-Expert-Witness-Blog/spur-gear-tooth-geometry-and-the-involute-curve, Web Page, 2014. (visited on 08/08/2018).

[65] D. Pirro and A. Wessol, *Lubrication fundamentals*. CRC Press, 2001.

[66] A. Szeri, *Fluid film lubrication*. Cambridge University Press, 2010.

[67] R. Budny, "Good lubrication practices can reduce gearbox failures", *North American Wind Power*, 2013.

[68] B. Bhushan, *Introduction to tribology*. John Wiley & Sons, 2013.

[69] W. Bartz, *Lubrication of gearing: lubricants and their properties, design of gears, practical gear lubrication, failure analysis*. Wiley, 1993.

[70] E. Terrell, *Webinar: Modeling tribological contacts in wind turbine gearboxes*, http://sentientscience.com/videos/webinar-archives/modeling-tribological-contacts-calculate-time-system-failure-wind-turbine-gearboxes/, Web Page, 2015. (visited on 08/08/2018).

[71] R. Errichello, S. Sheng, J. Keller, and A. Greco, "Wind turbine tribology seminar-a recap", National Renewable Energy Laboratory (NREL), Golden, CO., Tech. Rep., 2012.

[72] B. Rao, *Handbook of condition monitoring*. Elsevier Science Ltd, 1996.

[73] R. Gao, R. Yan, S. Sheng, and L. Zhang, "Sensor placement and signal processing for bearing condition monitoring", in *Condition-based monitoring and control for intelligent manufacturing*, L. Wang and R. X. Gao, Eds. Springer-Verlag, 2006, pp. 167–191.

[74] E. Becker and P. Poste, "Keeping the blades turning: Condition monitoring of wind turbine gears", *Refocus*, vol. 7, no. 2, 26:32, 2006.

[75] W. Yang and P. Tavner, "Cost-effective condition monitoring for wind turbines", *IEEE Transactions on Industrial Electronics*, vol. 57, no. 1, pp. 263–271, 2010.

[76] P. Tamilselvan, P. Wang, S. Sheng, and J. Twomey, "A two-stage diagnosis framework for wind turbine gearbox condition monitoring", *IJPHM Special Issue on Wind Turbine PHM*, pp. 21–31, 2013.

[77] S. Hajiabady, S. Kerkyras, S. Hillmansen, P. Tricoli, and M. Papaelias, "Efficient diagnostic condition monitoring for industrial wind turbines", 2014.

[78] S. Sheng and P. Veers, "Wind turbine drivetrain condition monitoring - An overview", NREL, Golden, CO., Tech. Rep., 2011.

[79] Z. Hameed, A. S.H., and Y. Cho, "Practical aspects of a condition monitoring system for a wind turbine with emphasis on its design, system architecture, testing and installation", *Renewable Energy*, no. 35, pp. 879–894, 2010.

[80] Y. Wang and D. Infield, "Supervisory control and data acquisition data-based non-linear state estimation technique for wind turbine gearbox condition monitoring", *IET Renewable Power Generation*, vol. 7, no. 4, pp. 350–358, 2013.

[81] A. Zaher, S. McArthur, D. Infield, and Y. Patel, "Online wind turbine fault detection through automated SCADA data analysis", *Wind Energy*, vol. 12, no. 6, pp. 574–593, 2009.

[82] J. P. Salameh, S. Cauet, E. Etien, A. Sakout, and L. Rambault, "Gearbox condition monitoring in wind turbines: A review", *Mechanical Systems and Signal Processing*, vol. 111, pp. 251–264, 2018.

[83] A. Davies, *Handbook of condition monitoring: techniques and methodology*. Chapman & Hall, 1998.

[84] R. Barron, *Engineering condition monitoring*. Longman, 1996.

[85] P. McFadden, "Examination of a technique for the early detection of failure in gears by signal processing of the time domain average of the meshing vibration", *Mechanical systems and signal processing*, vol. 1, no. 2, pp. 173–183, 1987.

[86] D. Coronado and C. Kupferschmidt, "Assessment and validation of oil sensor systems for on-line oil condition monitoring of wind turbine gearboxes", *Procedia Technology*, vol. 15, pp. 748–755, 2014.

[87] B. Lu, Y. Li, X. Wu, and Z. Yang, "A review of recent advances in wind turbine condition monitoring and fault diagnosis", *Power Electronics and Machines in Wind Applications*, pp. 1–7, 2009.

[88] S. Sheng, "Monitoring of wind turbine gearbox condition through oil and wear debris analysis: A full-scale testing perspective", *Tribology Transactions*, vol. 59, no. 1, pp. 149–162, 2016.

[89] P. Tchakoua, R. Wamkeue, M. Ouhrouche, F. Slaoui-Hasnaoui, T. Tameghe, *et al.*, "Wind turbine condition monitoring: State-of-the-art review, new trends, and future challenges", *Energies*, vol. 7, no. 4, pp. 2595–2630, 2014.

[90] D. Mba and B. Rao, "Development of acoustic emission technology for condition monitoring and diagnosis of rotating machines; bearings, pumps, gearboxes, engines and rotating structures", *The Shock and Vibration Digest*, vol. 38, no. 1, pp. 3–16, 2006.

[91] V. Baranov, E. Kudryavtsev, G. Sarychev, and V. Schavelin, *Acoustic emission in friction*. Elsevier, 2011, vol. 53.

[92] D. Gu, Y. An, and B. Choi, "Detection of faults in gearboxes using acoustic emission signal", *Journal of mechanical science and technology*, vol. 25, no. 5, pp. 1279–1286, 2011.

[93] J. Miettinen and P. Pataniitty, "Acoustic emission in monitoring extremely slowly rotating rolling bearing", *Proceedings of COMADEM 99*, pp. 289–297, 1999.

[94] C. Hellier, *Handbook of nondestructive evaluation*. McGraw-Hill, 2013.

[95] C. U. Grosse and M. Ohtsu, *Acoustic emission testing*. Springer Science & Business Media, 2008.

[96] S. Rosner, A. Klein, R. Wimmer, and B. Karlsson, "Extraction of features from ultrasound acoustic emissions: A tool to assess the hydraulic vulnerability of norway spruce trunkwood?", *New Phytologist*, vol. 171, no. 1, pp. 105–116, 2006.

[97] C. Grosse, *Acoustic emission (AE) felicity effect*, `http://www.ndt.net/ndtaz/content.php?id=471`, Web Page, 2002. (visited on 08/08/2018).

[98] C. Grosse and M. Ohtsu, *Acoustic emission testing*. Springer Science & Business Media, 2008.

[99] T. Toutountzakis and D. Mba, "Observations of acoustic emission activity during gear defect diagnosis", *NDT & E International*, vol. 36, no. 7, pp. 471–477, 2003.

[100] H. Sentoku, "AE in tooth surface failure process of spur gears", *Journal of acoustic emission*, vol. 16, no. 1-4, pp. 19–24, 1998.

[101] A. Al-Ghamd and D. Mba, "A comparative experimental study on the use of acoustic emission and vibration analysis for bearing defect identification and estimation of defect size", *Mechanical systems and signal processing*, vol. 20, no. 7, p. 1537, 2006.

[102] M. Elforjani and D. Mba, "Accelerated natural fault diagnosis in slow speed bearings with acoustic emission", *Engineering Fracture Mechanics*, vol. 77, no. 1, pp. 112–127, 2010.

[103] K. Strafford and C. Subramanian, "Surface engineering: An enabling technology for manufacturing industry", *Journal of Materials processing technology*, vol. 53, no. 1, pp. 393–403, 1995.

[104] B. Leonard, F. Sadeghi, R. Evans, G. Doll, and P. Shiller, "Fretting of WC/a-C:H and Cr2N coatings under grease-lubricated and unlubricated conditions", *Tribology Transactions*, vol. 53, no. 1, pp. 145–153, 2009.

[105] M. Boniardi, F. D'Errico, and C. Tagliabue, "Influence of carburizing and nitriding on failure of gears - A case study", *Engineering Failure Analysis*, vol. 13, no. 3, pp. 312–339, 2006.

[106] C. Stickels, *Gas carburizing*, ser. ASM Handbook. 1991, vol. 4, pp. 312–324.

[107] M. Zlatanovic, N. Popovic, and M. Mitric, "Plasma processing in carbon containing atmosphere for possible treatment of wind turbine components", *Thin Solid Films*, vol. 516, no. 2, pp. 228–232, 2007.

[108] O. Karabelchtchikova, "Fundamentals of mass transfer in gas carburizing (doctoral dissertation)", *Worcester Polytechnic Institute*, 2007.

[109] E. Mittemeijer, "Fundamentals of nitriding and nitrocarburizing", in *ASM handbook - Steel Heat Treating Fundamentals and Processes*. ASM International, 2013, vol. 4A, pp. 619–646.

[110] J. O'Brien and D. Goodman, "Plasma (ion) nitriding of steels", in *ASM Handbook*. ASM International, 1991, vol. 4, pp. 944–954.

[111] G. Totten, *Steel heat treatment: metallurgy and technologies*. CRC Press, 2006.

[112] M. Hudis, "Study of ion nitriding", *Journal of Applied Physics*, vol. 44, no. 4, pp. 1489–1496, 1973.

[113] C. Li, J. Georges, and X. Li, "Active screen plasma nitriding of austenitic stainless steel", *Surface Engineering*, vol. 18, no. 6, pp. 453–457, 2002.

[114] C. Li, T. Bell, and H. Dong, "A study of active screen plasma nitriding", *Surface Engineering*, vol. 18, no. 3, pp. 174–181, 2002.

[115] C. Zhao, C. Li, H. Dong, and T. Bell, "Study on the active screen plasma nitriding and its nitriding mechanism", *Surface and Coatings Technology*, vol. 201, no. 6, pp. 2320–2325, 2006.

[116] S. C. Gallo and H. Dong, "On the fundamental mechanisms of active screen plasma nitriding", *Vacuum*, vol. 84, no. 2, pp. 321–325, 2009.

[117] C. Li, "Active screen plasma nitriding – an overview", *Surface Engineering*, vol. 26, no. 1-2, pp. 135–141, 2010.

[118] T. Bell, H. Dong, and Y. Sun, "Realising the potential of duplex surface engineering", *Tribology International*, vol. 31, no. 1, pp. 127–137, 1998.

[119] J. Batista, C. Godoy, and A. Matthews, "Impact testing of duplex and non-duplex (Ti, Al)N and Cr-N PVD coatings", *Surface and Coatings Technology*, vol. 163, pp. 353–361, 2003.

[120] H. Dong and T. Bell, "Designer surfaces for titanium components", *Anti-corrosion methods and materials*, vol. 46, no. 3, pp. 181–188, 1999.

[121] H. Tian and N. Saka, "Finite element analysis of an elasticplastic two-layer half space: Sliding contact", *Wear*, vol. 148, pp. 261–285, 1991.

[122] R. Martins, R. Amaro, and J. Seabra, "Influence of low friction coatings on the scuffing load capacity and efficiency of gears", *Tribology International*, vol. 41, no. 4, pp. 234–243, 2008.

[123] D. Teer, "New solid lubricant coatings", *Wear*, vol. 251, no. 1, pp. 1068–1074, 2001.

[124] R. D. Evans, C. H. Hager, and R. D. Logsdon, "Friction and wear performance of candidate surface treatments for wind turbine gearbox bearings in high slip contacts", in *ASME/STLE 2009 International Joint Tribology Conference*, American Society of Mechanical Engineers, 2009, pp. 491–493.

[125] R. Amaro, R. Martins, J. Seabra, N. Renevier, and D. Teer, "Molybdenum disulphide/titanium low friction coating for gears application.", *Tribology International*, vol. 38, no. 4, pp. 423–434, 2005.

[126] W. F. Hosford, *Solid mechanics*. Cambridge University Press, 2012.

[127] G. T. Mase, R. E. Smelser, and G. E. Mase, *Continuum mechanics for engineers*. CRC press, 2009.

[128] R. Richards Jr, *Principles of solid mechanics*. CRC Press, 2000.

[129] F. Dunne and N. Petrinic, *Introduction to computational plasticity*. Oxford University Press on Demand, 2005.

[130] S. Nair, *Introduction to continuum mechanics*. Cambridge University Press, 2009.

[131] K. K. Chawla and M. Meyers, *Mechanical behavior of materials*. Prentice Hall, 1999.

[132] P. Lagace, *Yield (and failure) criteria*, `http://web.mit.edu/16.unified/www/SPRING/materials/Lectures/M5.3-Unified09.pdf`, Web Page, 2008. (visited on 08/08/2018).

[133] L. Kachanov, *Introduction to continuum damage mechanics*. Martinus Nijhoff Publishers, 1986, vol. 10.

[134] S. Murakami, "Progress of continuum damage mechanics", *JSME international journal*, vol. 30, no. 263, pp. 701–710, 1987.

[135] D. Francois, A. Pineau, and A. Zaoui, *Mechanical behavior of materials, volume II: Fracture mechanics and damage*, 2013.

[136] L. M. Kachanov, "Time of the rupture process under creep conditions", *Nank SSR Otd Tech Nauk*, vol. 8, pp. 26–31, 1958.

[137] Y. N. Rabotnov, "Creep problems in structural members", 1969.

[138] J. Lemaitre, *A course on damage mechanics*. Springer Science & Business Media, 2012.

[139] F. A. McClintock, "A criterion for ductile fracture by the growth of holes", ASME, 1968.

[140] J. R. Rice and D. M. Tracey, "On the ductile enlargement of voids in triaxial stress fields", *Journal of the Mechanics and Physics of Solids*, vol. 17, no. 3, pp. 201–217, 1969.

[141] B. Marino, F. Mudry, and A. Pineau, "Experimental study of cavity growth in ductile rupture", *Engineering Fracture Mechanics*, vol. 22, no. 6, pp. 989–996, 1985.

[142] A. L. Gurson, "Continuum theory of ductile rupture by void nucleation and growth: Part I - yield criteria and flow rules for porous ductile media", *Journal of engineering materials and technology*, vol. 99, no. 1, pp. 2–15, 1977.

[143] J. Besson, "Continuum models of ductile fracture: A review", *International Journal of Damage Mechanics*, vol. 19, no. 1, pp. 3–52, 2010.

[144] V. Tvergaard and A. Needleman, "Analysis of the cup-cone fracture in a round tensile bar", *Acta metallurgica*, vol. 32, no. 1, pp. 157–169, 1984.

[145] C. Chu and A. Needleman, "Void nucleation effects in biaxially stretched sheets", *Journal of Engineering Materials and Technology (Transactions of the ASME)*, vol. 102, no. 3, pp. 249–256, 1980.

[146] A. S. Pandkar, N. Arakere, and G. Subhash, "Microstructure-sensitive accumulation of plastic strain due to ratcheting in bearing steels subject to rolling contact fatigue", *International Journal of Fatigue*, vol. 63, pp. 191–202, 2014.

[147] T. Osman and P. Velex, "A model for the simulation of the interactions between dynamic tooth loads and contact fatigue in spur gears", *Tribology International*, vol. 46, no. 1, pp. 84–96, 2012.

[148] M. Franulovic, R. Basan, R. Kunc, and I. Prebil, "Numerical modeling of life prediction of gears", *Procedia Engineering*, vol. 10, pp. 562–567, 2011.

[149] J. A. Brandao, J. H. Seabra, and J. Castro, "Surface initiated tooth flank damage: Part I: Numerical model", *Wear*, vol. 268, no. 1, pp. 1–12, 2010.

[150] J. A. Brandao, J. H. Seabra, and J. Castro, "Surface initiated tooth flank damage. Part II: Prediction of micropitting initiation and mass loss", *Wear*, vol. 268, no. 1, pp. 13–22, 2010.

[151] B. Yazici, T. Kraft, and H. Riedel, "Finite element modelling of PM surface densification process", *Powder Metallurgy*, vol. 51, no. 3, pp. 211–216, 2008.

[152] C. J. Li and S. Choi, "Spur gear root fatigue crack prognosis via crack diagnosis and fracture mechanics", in *Proceedings of the 56th Meeting of the Society of Mechanical Failures Prevention Technology*, 2002, pp. 311–320.

[153] C. J. Li and H. Lee, "Gear fatigue crack prognosis using embedded model, gear dynamic model and fracture mechanics", *Mechanical systems and signal processing*, vol. 19, no. 4, pp. 836–846, 2005.

[154] S. Glodez, M. Sraml, and J. Kramberger, "A computational model for determination of service life of gears", *International Journal of Fatigue*, vol. 24, no. 10, pp. 1013–1020, 2002.

[155] I. Dinwoodie, D. McMillan, M. Revie, I. Lazakis, and Y. Dalgic, "Development of a combined operational and strategic decision support model for offshore wind", *Energy Procedia*, vol. 35, pp. 157–166, 2013.

[156] S. Lampman, "Introduction to surface hardening of steels", *ASM International, ASM Handbook*, vol. 4, pp. 259–267, 1991.

[157] West Yorkshire Steel, *EN24T alloy steel*, `https://www.westyorkssteel.com/alloy-steel/engineering-steel/en24t/`, Web Page, 2018. (visited on 08/08/2018).

[158] West Yorkshire Steel, *EN40B nitriding steel*, `https://www.westyorkssteel.com/alloy-steel/nitriding-steel/en40b/`, Web Page, 2018. (visited on 08/08/2018).

[159] M. Dvorakova, A. Rek, and F. Mika, "How to prevent hydrocarbon contamination in SEM", 2008.

[160] P. Kuisma-Kursula, "Accuracy, precision and detection limits of SEM-WDS, SEM-EDS and PIXE in the multielemental analysis of medieval glass", *X-ray Spectrometry*, vol. 29, no. 1, pp. 111–118, 2000.

[161] G. Vander Voort, *Microstructure of nitrided steels*, https://vacaero.com/information-resources/metallography-with-george-vander-voort/1138-microstructure-of-nitrided-steels.html, Web Page, 2011. (visited on 08/08/2018).

[162] S. Mridha and D. Jack, "Characterization of nitrided 3% chromium steel", *Metal Science*, vol. 16, no. 8, pp. 398–404, 1982, ISSN: 0306-3453.

[163] L. Barrallier, V. Traskine, and S. Botchenkov, "Morphology of intergranular cementite arrays in nitrided chromium-alloyed steels", *Materials Science and Engineering: A*, vol. 393, no. 1, pp. 247–253, 2005, ISSN: 0921-5093.

[164] W. C. Oliver and G. M. Pharr, "An improved technique for determining hardness and elastic modulus using load and displacement sensing indentation experiments", *Journal of materials research*, vol. 7, no. 06, pp. 1564–1583, 1992.

[165] K. Al Mahmud, M. A. Kalam, H. H. Masjuki, H. Mobarak, and N. Zulkifli, "An updated overview of diamond-like carbon coating in tribology", *Critical reviews in solid state and materials sciences*, vol. 40, no. 2, pp. 90–118, 2015.

[166] ISO 12108:2002, "Metallic materials – fatigue testing – fatigue crack growth method", *British Standards Institution*,

[167] K.-H. Schwalbe and D. Hellmann, "Application of the electrical potential method to crack length measurements using Johnson's formula", *Journal of Testing and Evaluation*, vol. 9, no. 3, pp. 218–220, 1981.

[168] P. C. Paris and F. Erdogan, "A critical analysis of crack propagation laws", ASME, 1963.

[169] A. F. Bower, *Applied mechanics of solids*. CRC press, 2009.

[170] J. Musuva and J. Radon, "The effect of stress ratio and frequency on fatigue crack growth", *Fatigue & Fracture of Engineering Materials & Structures*, vol. 1, no. 4, pp. 457–470, 1979.

[171] ASTM E8, "Standard test method for tension testing of metallic materials", 2011.

[172] C. Gorla, F. Rosa, E. Conrado, and H. Albertini, "Bending and contact fatigue strength of innovative steels for large gears", *Proceedings of the Institution of Mechanical Engineers, Part C: Journal of Mechanical Engineering Science*, vol. 228, no. 14, pp. 2469–2482, 2014.

[173] J. Zhou, "Investigation of surface engineering and monitoring for reliable wind turbine gearboxes (doctoral dissertation)", *University of Birmingham*, 2017.

[174] X. Ai and S. C. Lee, "Effect of slide-to-roll ratio on interior stresses around a dent in EHL contacts", *Tribology Transactions*, vol. 39, no. 4, pp. 881–889, 1996.

[175] R. Dwyer-Joyce, "Tribological design data part 3: Contact mechanics", *University of Sheffield*, 1997.

[176] R. Errichello, "Morphology of micropitting", *The Journal of Gear Technology*, vol. 6, pp. 74–81, 2012.

[177] M. J. Neale and D. F. Wilcock, *Tribology handbook*, 1975.

[178] ISO 281:2007, *Rolling bearings - dynamic load ratings and rating life*, Standard, 2007.

[179] ASTM E140, "Standard hardness conversion tables for metals relationship among brinell hardness", *Vickers Hardness, Rockwell Hardness, Superficial Hardness, Knoop Hardness, Scleroscope Hardness, and Leeb Hardness, ASTM international E140-12b*, vol. 1,

[180] M. Kuna, "Classification of fracture processes", pp. 13–20, 2013.

[181] N. W. Sachs, "Understanding the surface features of fatigue fractures: How they describe the failure cause and the failure history", *Journal of Failure Analysis and Prevention*, vol. 5, no. 2, pp. 11–15, 2005.

[182] T. Bruce, H. Long, T. Slatter, and R. Dwyer Joyce, "Formation of white etching cracks at manganese sulfide (MnS) inclusions in bearing steel due to hammering impact loading", *Wind Energy*, 2016, ISSN: 1099-1824.

[183] B. Harichandra, P. Mrudula, M. Mahantayya, and S. Prakash, "Evaluation of mechanical properties of EN31 steel heat treated using biodegradable oils", *International Journal of Applied Engineering Research*, vol. 10, no. 50, p. 2015, 2015.

[184] M. Nakhaeinejad and S. Ganeriwala, "Observations on dynamic responses of misalignments", *Technologial Notes. SpectraQuest Inc*, 2009.

[185] A. K. Gupta, V. Anirudh, and S. K. Singh, "Constitutive models to predict flow stress in austenitic stainless steel 316 at elevated temperatures", *Materials & Design*, vol. 43, pp. 410–418, 2013.

[186] H. McQueen and N. Ryan, "Constitutive analysis in hot working", *Materials Science and Engineering: A*, vol. 322, no. 1-2, pp. 43–63, 2002.

[187] J. Chaboche, K. D. Van, and G. Cordier, "Modelization of the strain memory effect on the cyclic hardening of 316 stainless steel", 1979.

[188] G. Bernhart, G. Moulinier, O. Brucelle, and D. Delagnes, "High temperature low cycle fatigue behaviour of a martensitic forging tool steel", *International Journal of fatigue*, vol. 21, no. 2, pp. 179–186, 1999.

[189] H. Semba, B. Dyson, and M. McLean, "Microstructure-based creep modelling of a 9% cr martensitic steel", *Materials at High Temperatures*, vol. 25, no. 3, pp. 131–137, 2008.

[190] Y. Kadoya, N. Nishimura, B. Dyson, and M. McLean, "Origins of tertiary creep in high chromium steels", in *7 th International Conference on Creep and Fracture of Engineering Materials and Structures*, 1997, pp. 343–352.

[191] H. Basoalto and B. Dyson, "Predicting stress relaxation & LCF using a microstructure-based constitutive model", IC Consultants Ltd London, Report, 2003.

[192] U. Kocks, A. Argon, and M. Ashby, *Progress in materials science (edited by B. Chalmers, JW Christian and TB Massalski), vol. 19*, 1975.

[193] J. Friedel, "Dislocations pergamon", *New York*, vol. 1964274, 1964.

[194] H. Mecking and K. Lucke, "A new aspect of the theory of flow stress of metals", *Scripta Metallurgica*, vol. 4, no. 6, pp. 427–432, 1970.

[195] Dassault Systemes Simulia Corp, *ABAQUS analysis user's manual*. RI, USA, 2007.

[196] R. Tharmakulasingam, "Transmission error in spur gears: Static and dynamic finite-element modeling and design optimization", Thesis, 2009.

[197] G. J. Sroka and R. Benson, "Refurbishing wind turbine gears", 2011.

[198] ANSI/AGMA 2001-D04, *Fundamental rating factors and calculation methods for involute spur and helical gear teeth*, Standard, 2004.

[199] B. Rebbechi, F. B. Oswald, and D. P. Townsend, "Measurement of gear tooth dynamic friction", 1996.

[200] I. S. Grigoriev, E. Z. Meilikhov, and A. A. Radzig, *Handbook of physical quantities*. CRC Press Boca Raton, 1997, vol. 324.

[201] G. Hamilton, "Explicit equations for the stresses beneath a sliding spherical contact", *Proceedings of the Institution of Mechanical Engineers, Part C: Journal of Mechanical Engineering Science*, vol. 197, no. 1, pp. 53–59, 1983.

[202] M. Miner, "Cumulative damage in fatigue", *Journal of Applied Mechanics 12*, 1945.

[203] F. Tao, M. Zhang, Y. Liu, and A. Nee, "Digital twin driven prognostics and health management for complex equipment", *CIRP Annals*, 2018.

[204] V. Ogewell, *Digital Twins: Beware of Naive Faith in Simplicity*, `https://www.engineering.com/PLMERP/ArticleID/16272/Digital-Twins-Beware-of-Naive-Faith-in-Simplicity.aspx`, Web Page, 2018. (visited on 11/11/2018).

APPENDIX A: PYTHON SCRIPT FOR GEAR PAIR GENERATION

```
from math import *
from abaqus import *
from abaqusConstants import *
session.Viewport(name='Viewport: 1', origin=(0.0, 0.0), width
    =194.23828125, height=193)
session.viewports['Viewport: 1'].makeCurrent()
session.viewports['Viewport: 1'].maximize()
from caeModules import *
from driverUtils import executeOnCaeStartup
executeOnCaeStartup()
Mdb()
#: A new model database has been created.
#: The model "Model-1" has been created.
session.viewports['Viewport: 1'].setValues(displayedObject=None)

m1 = 2
m2 = m1 # Module
N1 = 34 # Number of teeth
N2 = 34
facewidth = 20 # Facewidth
theta = 20 # Pressure angle
ratio = N1/N2
Npoints = 10
tip_relief = 0.25
rootfact = 0.3
theta = radians(theta)
p1 = m1*N1 # Pitch circle diameter
p2 = m2*N2
cd = (p1+p2)/2 # Xenter distance
d = (p1*(1+ratio))/(2*ratio)
cn1 = [0.,0.,0.]
cn2 = [0.,cn1[1]+cd,cn1[2]]
rr1 = rootfact*m1 # Root radius
rr2 = rootfact*m2
w1 = 2.*pi/N1
w2 = 2.*pi/N2
rb1 = p1/2.*cos(theta) # Radius of base circle
rb2 = p2/2.*cos(theta)
rp1 = p1/2. # Radius of pitch circle
rp2 = p2/2.
rs1 = 25 # Shaft radius
rs2 = 25
rded1 = (p1 - 2.5*m1)/2. # Dedendum radius
rded2 = (p2 - 2.5*m2)/2.
radd1 = (p1 + 2.*m1)/2.  # Addendum radius
radd2 = (p2 + 2.*m2)/2.
rbvec1 = [0., rb1,0.]
rbvec2 = [0., -rb2,0.]
```

```
ve1=[0.,1.,0.]
ve2=[0.,-1.,0.]
rsvec1 = [rs1,0.]
rsvec2 = [rs2,0.]
betaded1=0
betaded2=0
betaadd1=sqrt((pow(radd1,2)/pow(rb1,2))-1)
betaadd2=sqrt((pow(radd2,2)/pow(rb2,2))-1)
betap1 = sqrt((pow(rp1,2)/pow(rb1,2))-1)
betap2 = sqrt((pow(rp2,2)/pow(rb2,2))-1)
betar1 = acos(rb1/(rded1+rr1))
betar2 = acos(rb2/(rded2+rr2))
si1 = ((pi/2)- betar1)
si2 = ((pi/2)- betar2)
raddmod1=rb1*sqrt(1.+pow((betaadd1-tip_relief/rb1),2))
raddmod2=rb2*sqrt(1.+pow((betaadd2-tip_relief/rb2),2))
rfil1 = sqrt((pow(rb1,2)+ pow((rb1*betar1),2)))
rfil2 = sqrt((pow(rb2,2)+ pow((rb2*betar2),2)))
IdMat = [0.,1.,0.,0.,1.]

s = mdb.models['Model-1'].ConstrainedSketch(name='__profile__',
    sheetSize=200.0)
g, v, d, c = s.geometry, s.vertices, s.dimensions, s.constraints
s.setPrimaryObject(option=STANDALONE)
pointA=[(0.,0.)]*(N1+1)
pointB=[(0.,0.)]*(N1+1)
Inv = [0.]*(2*(Npoints+1)+1)
Inve = [0.]*(2*(Npoints+1)+1)
InvMir = [0.]*(2*(Npoints+1)+1)
midpointA = [(0.,0.,0.)]*(N1+1)
midpointB = [(0.,0.,0.)]*(N1+1)
midpointC = [(0.,0.,0.)]*(N1+1)
auxpoint1 = [(0.,0.,0.)]*(N1+1)
auxadd1 = [(0.,0.,0.)]*(N1+1)
arcded1 = [(0.,0.,0.)]*(N1+1)
rfilcen1 = [(0.,0.)]*(N1+1)
rfilend1 = [(0.,0.)]*(N1+1)
rfilcenmir1 = [(0.,0.)]*(N1+1)
rfilendmir1 = [(0.,0.)]*(N1+1)
arcadd1 = [(0.,0.,0.)]*(N1+1)
toppointA = [(0.,0.,0.)]*(N1+1)
StartPoints=[(0.,0.,0.)]*(N1+1)
CenPoints=[(0.,0.,0.)]*(N1+1)
EndPoints=[(0.,0.,0.)]*(N1+1)
StartPointsMir1=[(0.,0.,0.)]*(N1+1)
CenPointsMir1=[(0.,0.,0.)]*(N1+1)
EndPointsMir1=[(0.,0.,0.)]*(N1+1)
gammamir1=(pi/(2.*N1))+(betap1 - (atan(betap1)))
for q in range (1, N1+1):
  b = [0.,0.,0.]
  bmir = [0.,0.,0.]
  rot=(q-1)*w1-(gammamir1+(pi/N1))
  gamma1 = rot + gammamir1
  rb1vec1 = [0.,cos(rot)*rbvec1[1]-sin(rot)*rbvec1[2],sin(rot)*rbvec1
    [1]+cos(rot)*rbvec1[2]]
```

```
rve1= [0.,cos(-si1)*(rb1vec1[1]/rb1)-sin(-si1)*(rb1vec1[2]/rb1),sin(-
 si1)*(rb1vec1[1]/rb1)+cos(-si1)*(rb1vec1[2]/rb1)]
rfiladd1 = [0., rr1*rve1[1], rr1*rve1[2]]
rfilbase1 = [0.,cos(si1)*(-rfiladd1[1])-sin(si1)*(-rfiladd1[2]),sin(
 si1)*(-rfiladd1[1])+cos(si1)*(-rfiladd1[2])]
rotaux=pi/N1
mirr=[0.,cos(gamma1)*ve1[1]-sin(gamma1)*ve1[2],sin(gamma1)*ve1[1]+cos(
 gamma1)*ve1[2]]
auxpoint1[q]=[0.,rfil1*(cos(rotaux)*mirr[1]-sin(rotaux)*mirr[2]),rfil1
 *(sin(rotaux)*mirr[1]+cos(rotaux)*mirr[2])]
MirrMatvec=[0.,0.,0.,0.,0.]
for k in range (1,3):
  for j in range (1,3):
    MirrMatvec[2*(j-1)+k]=2*mirr[k]*mirr[j]-IdMat[2*(j-1)+k]
arcded1[q]=(cn1[1]+auxpoint1[q][1],cn1[2]+auxpoint1[q][2],0.)
InvPoints= [(0.,0.)]*((Npoints+1))
startPoints= [(0.,0.)]*((1))
cenPoints= [(0.,0.)]*((1))
endPoints= [(0.,0.)]*((1))
startPointsMir1= [(0.,0.)]*((1))
cenPointsMir1= [(0.,0.)]*((1))
endPointsMir1= [(0.,0.)]*((1))
for i in range (1, Npoints+2):
  b = [0.,0.,0.]
  beta=betaded1+((i-1)*(betaadd1-betaded1))/Npoints
  if(beta>betap1): addmod=(beta-betap1)/(betaadd1-betap1)*tip_relief
  else:addmod=0.
  fact=addmod/sqrt(rbvec1[1]*rbvec1[1]+rbvec1[2]*rbvec1[2])
  vaux = [0.,(cos(rot)*rbvec1[2]+sin(rot)*rbvec1[1])*beta*(1.-fact),(
 sin(rot)*rbvec1[2]-cos(rot)*rbvec1[1])*beta*(1.-fact)]
  bmir = [0.,0.,0.]
  InvMirPoints= [(0.,0.)]*((Npoints+1))
  Rott = [0.,cos(beta),sin(beta),-sin(beta),cos(beta)]
  for k in range (1,3):
    for j in range (1,3):
      b[k]=b[k]+Rott[2*(j-1)+k]*(rb1vec1[j]+vaux[j])
    Inv[2*(i-1)+k]=cn1[k]+b[k]
  for k in range (1,3):
    for j in range (1,3):
      bmir[k]=bmir[k]+MirrMatvec[2*(j-1)+k]*b[j]
    InvMir[2*(i-1)+k]=cn1[k]+bmir[k]
for i in range (1, Npoints +2):
  InvPoints[i-1]=(Inv[2*i-1],Inv[2*i])
  InvMirPoints[i-1]=(InvMir[2*i-1],InvMir[2*i])
rfiladdmir1=[0.,0.,0.]
rfilbasemir1=[0.,0.,0.]
for k in range (1,3):
  for j in range (1,3):
    rfiladdmir1[k]=rfiladdmir1[k]+MirrMatvec[2*(j-1)+k]*rfiladd1[j]
    rfilbasemir1[k]=rfilbasemir1[k]+MirrMatvec[2*(j-1)+k]*rfilbase1[j]
rfilcen1[q] = (rfiladd1[1] + Inv[1],rfiladd1[2] + Inv[2])
rfilend1[q] = (rfilcen1[q][0]+ rfilbase1[1],rfilcen1[q][1]+ rfilbase1
 [2])
rfilcenmir1[q] = (rfiladdmir1[1] + InvMir[1],rfiladdmir1[2] + InvMir
 [2])
```

```
149   rfilendmir1[q] = (rfilcenmir1[q][0]+ rfilbasemir1[1],rfilcenmir1[q
       ][1]+rfilbasemir1[2])
      startPoints=InvPoints[0]
151   cenPoints=(rfilcen1[q])
      endPoints=(rfilend1[q])
153   startPointsMir1=InvMirPoints[0]
      cenPointsMir1=(rfilcenmir1[q])
155   endPointsMir1=(rfilendmir1[q])
      invfsp=tuple(InvPoints)
157   invfspe=tuple(arcded1)
      StartPoints=tuple(startPoints)
159   CenPoints=tuple(cenPoints)
      EndPoints=tuple(endPoints)
161   StartPointsMir1=tuple(startPointsMir1)
      CenPointsMir1=tuple(cenPointsMir1)
163   EndPointsMir1=tuple(endPointsMir1)
      mirfsp=tuple(InvMirPoints)
165   midpointA[q]= (invfsp[2][0],invfsp[2][1],0.)
      midpointB[q]= (mirfsp[2][0],mirfsp[2][1],0.)
167   midpointC[q]= (invfspe[q][0],invfspe[q][1],0.)
      raddmod1=sqrt((pow((invfsp[-1][0]-cn1[1]),2.))+(pow((invfsp[-1][1]-cn1
       [2]),2.)))
169   auxadd1[q]=[0.,raddmod1*(cos(gamma1)*ve1[1]-sin(gamma1)*ve1[2]),
       raddmod1*(sin(gamma1)*ve1[1]+cos(gamma1)*ve1[2])]
      arcadd1[q]=(cn1[1]+auxadd1[q][1],cn1[2]+auxadd1[q][2],0.)
171   mirfspe=tuple(arcadd1)
      toppointA[q]= (mirfspe[q][0],mirfspe[q][1],0.)
173   s.Spline(points=(invfsp))
      s.Spline(points=(mirfsp))
175   s.ArcByCenterEnds(center=(cn1[1], cn1[2]), point1=(invfsp[-1]), point2
       =(mirfsp[-1]),direction=COUNTERCLOCKWISE)
      s.ArcByCenterEnds(center=CenPoints, point1=StartPoints, point2=
       EndPoints,direction=COUNTERCLOCKWISE)
177   s.ArcByCenterEnds(center=CenPointsMir1, point1=StartPointsMir1,point2=
       EndPointsMir1,direction=CLOCKWISE)
      pointA[q] = EndPoints
179   pointB[q] = EndPointsMir1

181 for x in range(1,N1):
      s.ArcByCenterEnds(center=(cn1[1], cn1[2]), point1=(pointB[x]),point2=(
       pointA[x+1]),direction=COUNTERCLOCKWISE)
183 s.ArcByCenterEnds(center=(cn1[1], cn1[2]), point1=(pointB[N1]), point2=(
       pointA[1]),direction=COUNTERCLOCKWISE)
    s.CircleByCenterPerimeter(center=(cn1[1], cn1[2]), point1=(cn1[1], cn1
       [2]+rs1))
185
    p = mdb.models['Model-1'].Part(name='Part-1', dimensionality=THREE_D,
       type=DEFORMABLE_BODY)
187 p = mdb.models['Model-1'].parts['Part-1']
    p.BaseSolidExtrude(depth=facewidth, sketch=s)
189 s.unsetPrimaryObject()
    p = mdb.models['Model-1'].parts['Part-1']
191 session.viewports['Viewport: 1'].setValues(displayedObject=p)
    del mdb.models['Model-1'].sketches['__profile__']
193
```

```
s1 = mdb.models['Model-1'].ConstrainedSketch(name='__profile__',
    sheetSize=200.0)
g, v, d, c = s1.geometry, s1.vertices, s1.dimensions, s1.constraints
s1.setPrimaryObject(option=STANDALONE)
pointA2=[(0.,0.)]*(N2+1)
pointB2=[(0.,0.)]*(N2+1)
Inv2 = [0.]*(2*(Npoints+1)+1)
Inve2 = [0.]*(2*(Npoints+1)+1)
InvMir2 = [0.]*(2*(Npoints+1)+1)
midpointD = [(0.,0.,0.)]*(N2+1)
midpointE = [(0.,0.,0.)]*(N2+1)
midpointF = [(0.,0.,0.)]*(N2+1)
auxpoint2 = [(0.,0.,0.)]*(N2+1)
auxadd2 = [(0.,0.,0.)]*(N2+1)
arcded2 = [(0.,0.,0.)]*(N2+1)
rfilcen2 = [(0.,0.,0.)]*(N2+1)
rfilend2 = [(0.,0.,0.)]*(N2+1)
rfilcenmir2 = [(0.,0.)]*(N2+1)
rfilendmir2 = [(0.,0.)]*(N2+1)
arcadd2 = [(0.,0.,0.)]*(N2+1)
toppointB = [(0.,0.,0.)]*(N2+1)
StartPoints2=[(0.,0.,0.)]*(N2+1)
CenPoints2=[(0.,0.,0.)]*(N2+1)
EndPoints2=[(0.,0.,0.)]*(N2+1)
StartPointsMir2=[(0.,0.,0.)]*(N2+1)
CenPointsMir2=[(0.,0.,0.)]*(N2+1)
EndPointsMir2=[(0.,0.,0.)]*(N2+1)
gammamir2=((pi/(2.*N2))+(betap2 - (atan(betap2))))
for q in range (1, (N2)+1):
  b2 = [0.,0.,0.]
  bmir2 = [0.,0.,0.]
  rot2=(q-1)*w2-(gammamir2)
  gamma2 = rot2 + gammamir2
  rb2vec2 = [0.,cos(rot2)*rbvec2[1]-sin(rot2)*rbvec2[2],sin(rot2)*rbvec2
   [1]+cos(rot2)*rbvec2[2]]
  rve2= [0.,cos(-si2)*(rb2vec2[1]/rb2)-sin(-si2)*(rb2vec2[2]/rb2),sin(-
   si2)*(rb2vec2[1]/rb2)+cos(-si2)*(rb2vec2[2]/rb2)]
  rfiladd2 = [0., rr2*rve2[1], rr2*rve2[2]]
  rfilbase2 = [0.,cos(si2)*-rfiladd2[1]-sin(si2)*-rfiladd2[2],sin(si2)*-
   rfiladd2[1]+cos(si2)*-rfiladd2[2]]
  rotaux2=pi/N2
  mirr2=[0.,cos(gamma2)*ve2[1]- sin(gamma2)*ve2[2],sin(gamma2)*ve2[1]+
   cos(gamma2)*ve2[2]]
  auxpoint2[q]=[0.,rfil2*(cos(rotaux2)*mirr2[1]-sin(rotaux2)*mirr2[2]),
   rfil2*(sin(rotaux2)*mirr2[1]+cos(rotaux2)*mirr2[2])]
  MirrMatvec2=[0.,0.,0.,0.,0.]
  for k in range (1,3):
    for j in range (1,3):
      MirrMatvec2[2*(j-1)+k]=2*mirr2[k]*mirr2[j]-IdMat[2*(j-1)+k]
  arcded2[q]=(cn2[1]+auxpoint2[q][1],cn2[2]+auxpoint2[q][2],0.)
  InvPoints2= [(0.,0.)]*((Npoints+1))
  startPoints2= [(0.,0.)]*((1))
  cenPoints2= [(0.,0.)]*((1))
  endPoints2= [(0.,0.)]*((1))
  startPointsMir2= [(0.,0.)]*((1))
  cenPointsMir2= [(0.,0.)]*((1))
```

```
  endPointsMir2= [(0.,0.)]*((1))
245 for i in range (1, Npoints+2):
    b2 = [0.,0.,0.]
247   beta2=betaded2+((i-1)*(betaadd2-betaded2))/Npoints
    if(beta2>betap2): addmod2=(beta2-betap2)/(betaadd2-betap2)*
   tip_relief
249   else:addmod2=0.
    fact2=addmod2/sqrt(rbvec2[1]*rbvec2[1]+rbvec2[2]*rbvec2[2])
251   vaux2 = [0.,(cos(rot2)*rbvec2[2]+sin(rot2)*rbvec2[1])*beta2*(1.-
   fact2),(sin(rot2)*rbvec2[2]-cos(rot2)*rbvec2[1])*beta2*(1.-fact2)]
    bmir2 = [0.,0.,0.]
253   InvMirPoints2= [(0.,0.)]*((Npoints+1))
    Rott = [0.,cos(beta2),sin(beta2),-sin(beta2),cos(beta2)]
255   for k in range (1,3):
      for j in range (1,3):
257     b2[k]=b2[k]+Rott[2*(j-1)+k]*(rb2vec2[j]+vaux2[j])
      Inv2[2*(i-1)+k]=cn2[k]+b2[k]
259   for k in range (1,3):
      for j in range (1,3):
261     bmir2[k]=bmir2[k]+MirrMatvec2[2*(j-1)+k]*b2[j]
      InvMir2[2*(i-1)+k]=cn2[k]+bmir2[k]
263 for i in range (1, Npoints +2):
    InvPoints2[i-1]=(Inv2[2*i-1],Inv2[2*i])
265   InvMirPoints2[i-1]=(InvMir2[2*i-1],InvMir2[2*i])
  rfiladdmir2=[0.,0.,0.]
267 rfilbasemir2=[0.,0.,0.]
  for k in range (1,3):
269   for j in range (1,3):
      rfiladdmir2[k]=rfiladdmir2[k]+MirrMatvec2[2*(j-1)+k]*rfiladd2[j]
271     rfilbasemir2[k]=rfilbasemir2[k]+MirrMatvec2[2*(j-1)+k]*rfilbase2[j
   ]
  rfilcen2[q] = (rfiladd2[1] + Inv2[1],rfiladd2[2] + Inv2[2]) # Defining
    the centre points (rFc) for the root fillet
273 rfilend2[q] = (rfilcen2[q][0]+ rfilbase2[1],rfilcen2[q][1]+ rfilbase2
   [2]) # Defining the end points (rF2) for the root fillet
  rfilcenmir2[q] = (rfiladdmir2[1] + InvMir2[1],rfiladdmir2[2] + InvMir2
   [2]) # Defining the centre points (rFc) for the root fillet
275 rfilendmir2[q] = (rfilcenmir2[q][0]+ rfilbasemir2[1],rfilcenmir2[q
   ][1]+rfilbasemir2[2]) # Defining the end points (rF2) for the root
   fillet
  startPoints2=InvPoints2[0]
277 cenPoints2=(rfilcen2[q])
  endPoints2=(rfilend2[q])
279 startPointsMir2=InvMirPoints2[0]
  cenPointsMir2=(rfilcenmir2[q])
281 endPointsMir2=(rfilendmir2[q])
  invfsp2=tuple(InvPoints2)
283 invfspe2=tuple(arcded2)
  StartPoints2=tuple(startPoints2)
285 CenPoints2=tuple(cenPoints2)
  EndPoints2=tuple(endPoints2)
287 StartPointsMir2=tuple(startPointsMir2)
  CenPointsMir2=tuple(cenPointsMir2)
289 EndPointsMir2=tuple(endPointsMir2)
  mirfsp2=tuple(InvMirPoints2)
291 midpointD[q]= (invfsp2[2][0],invfsp2[2][1],0.)
```

```
    midpointE[q]= (mirfsp2[2][0],mirfsp2[2][1],0.)
293 midpointF[q]= (invfspe2[q][0],invfspe2[q][1],0.)
    raddmod2=sqrt((pow((invfsp2[-1][0]-cn2[1]),2.))+(pow((invfsp2[-1][1]-
     cn2[2]),2.)))
295 auxadd2[q]=[0.,raddmod2*(cos(gamma2)*ve2[1]-sin(gamma2)*ve2[2]),
     raddmod2*(sin(gamma2)*ve2[1]+cos(gamma2)*ve2[2])]
    arcadd2[q]=(cn2[1]+auxadd2[q][1],cn2[2]+auxadd2[q][2],0.)
297 mirfspe2=tuple(arcadd2)
    toppointB[q]= (mirfspe2[q][0],mirfspe2[q][1],0.)
299 s1.Spline(points=(invfsp2))
    s1.Spline(points=(mirfsp2))
301 s1.ArcByCenterEnds(center=(cn2[1], cn2[2]), point1=(invfsp2[-1]),
     point2=(mirfsp2[-1]),direction=COUNTERCLOCKWISE)
    s1.ArcByCenterEnds(center=CenPoints2, point1=StartPoints2, point2=
     EndPoints2,direction=COUNTERCLOCKWISE)
303 s1.ArcByCenterEnds(center=CenPointsMir2, point1=StartPointsMir2,point2
     =EndPointsMir2,direction=CLOCKWISE)
    pointA2[q] = EndPoints2
305 pointB2[q] = EndPointsMir2

307 for x in range(1,N2):
    s1.ArcByCenterEnds(center=(cn2[1], cn2[2]), point1=(pointB2[x]),point2
     =(pointA2[x+1]),direction=COUNTERCLOCKWISE)
309 s1.ArcByCenterEnds(center=(cn2[1], cn2[2]), point1=(pointB2[N2]),point2
     =(pointA2[1]),direction=COUNTERCLOCKWISE)
  s1.CircleByCenterPerimeter(center=(cn2[1], cn2[2]), point1=(cn2[1], cn2
     [2]+rs2))
311 p = mdb.models['Model-1'].Part(name='Part-2', dimensionality=THREE_D,
     type=DEFORMABLE_BODY)
  p = mdb.models['Model-1'].parts['Part-2']
313 p.BaseSolidExtrude(depth=facewidth, sketch=s1)
  s1.unsetPrimaryObject()
315 p = mdb.models['Model-1'].parts['Part-2']
  session.viewports['Viewport: 1'].setValues(displayedObject=p)
317 del mdb.models['Model-1'].sketches['__profile__']
```

Appendix_A.py

APPENDIX B: ABAQUS INPUT FILE

```
*Heading
Meshing gear pair of 34 teeth each, with 31 teeth behaving as a fully
elastic material and 3 teeth as a plastic material following an umat
subroutine. Torque set to 150Nm, coefficient of friction of 0.05.
Perfect alignment. Gears set to perform 10 rotations.
Node listing was omitted due to file size.
** Job name: T150k_ParDam Model name: Model-1
** Generated by: Abaqus/CAE 6.13-1
*Preprint, echo=NO, model=NO, history=NO, contact=NO
**
** PARTS
**
*Part, name=A_Gear
*End Part
**
*Part, name=B_Gear
*End Part
**
**
** ASSEMBLY
**
*Assembly, name=Assembly
**
*Instance, name=A_Gear-1, part=A_Gear
*Node
  [OMITTED]
*Element, type=C3D8
  [OMITTED]
*Node
  [OMITTED]
*Nset, nset=A_Gear-1-RefPt_, internal
  [OMITTED]
*Nset, nset=A_whole, generate
  [OMITTED]
*Elset, elset=A_whole, generate
  [OMITTED]
*Nset, nset=A_Elastic
  [OMITTED]
*Elset, elset=A_Elastic, generate
  [OMITTED]
*Nset, nset=A_UMAT
  [OMITTED]
*Elset, elset=A_UMAT, generate
  [OMITTED]
*Nset, nset=A_Inner
  [OMITTED]
*Elset, elset=A_Inner
  [OMITTED]
** Section: UMAT
*Solid Section, elset=A_UMAT, material=UMAT
,
** Section: Steel_Elastic
```

```
53 *Solid Section, elset=A_Elastic, material=Steel_Elastic
,
55 *End Instance
**
57 *Instance, name=B_Gear-1, part=B_Gear
   [OMITTED]
59 *Node
   [OMITTED]
61 *Element, type=C3D8
   [OMITTED]
63 *Node
   [OMITTED]
65 *Nset, nset=B_Gear-1-RefPt_, internal
   [OMITTED]
67 *Nset, nset=B_Elastic
   [OMITTED]
69 *Elset, elset=B_Elastic, generate
   [OMITTED]
71 *Nset, nset=B_UMAT
   [OMITTED]
73 *Elset, elset=B_UMAT
   [OMITTED]
75 *Nset, nset=Seeds-Medium, instance=A_Gear-1
   [OMITTED]
77 *Nset, nset=Seeds-Medium, instance=B_Gear-1
   [OMITTED]
79 *Elset, elset=Seeds-Medium, instance=A_Gear-1
   [OMITTED]
81 *Elset, elset=Seeds-Medium, instance=B_Gear-1
   [OMITTED]
83 *Nset, nset=Seeds-Other-teeth, instance=A_Gear-1
   [OMITTED]
85 *Nset, nset=Seeds-Other-teeth, instance=B_Gear-1
   [OMITTED]
87 *Elset, elset=Seeds-Other-teeth, instance=A_Gear-1
   [OMITTED]
89 *Elset, elset=Seeds-Other-teeth, instance=B_Gear-1
   [OMITTED]
91 *Nset, nset=Seeds-Pillars, instance=A_Gear-1
   [OMITTED]
93 *Nset, nset=Seeds-Pillars, instance=B_Gear-1
   [OMITTED]
95 *Elset, elset=Seeds-Pillars, instance=A_Gear-1
   [OMITTED]
97 *Elset, elset=Seeds-Pillars, instance=B_Gear-1
   [OMITTED]
99 *Nset, nset=Seeds_Fine, instance=A_Gear-1
   [OMITTED]
101 *Nset, nset=Seeds_Fine, instance=B_Gear-1
   [OMITTED]
103 *Elset, elset=Seeds_Fine, instance=A_Gear-1
   [OMITTED]
105 *Elset, elset=Seeds_Fine, instance=B_Gear-1
   [OMITTED]
107 *Nset, nset=_PickedSet98, internal, instance=B_Gear-1
   [OMITTED]
```

```
*Elset, elset=_A_inner_S5, internal, instance=A_Gear-1
  [OMITTED]
*Elset, elset=_A_inner_S3, internal, instance=A_Gear-1
  [OMITTED]
*Elset, elset=_A_inner_S4, internal, instance=A_Gear-1
  [OMITTED]
*Elset, elset=_A_inner_S6, internal, instance=A_Gear-1
  [OMITTED]
*Surface, type=ELEMENT, name=A_inner
_A_inner_S5, S5
_A_inner_S3, S3
_A_inner_S4, S4
_A_inner_S6, S6
*Elset, elset=_B_inner_S5, internal, instance=B_Gear-1
  [OMITTED]
*Elset, elset=_B_inner_S3, internal, instance=B_Gear-1
  [OMITTED]
*Elset, elset=_B_inner_S6, internal, instance=B_Gear-1
  [OMITTED]
*Elset, elset=_B_inner_S4, internal, instance=B_Gear-1
  [OMITTED]
*Surface, type=ELEMENT, name=B_inner
_B_inner_S5, S5
_B_inner_S3, S3
_B_inner_S6, S6
_B_inner_S4, S4
*Elset, elset=__PickedSurf29_S3, internal, instance=A_Gear-1, generate
  [OMITTED]
*Elset, elset=__PickedSurf29_S5, internal, instance=A_Gear-1
  [OMITTED]
*Elset, elset=__PickedSurf29_S4, internal, instance=A_Gear-1
  [OMITTED]
*Surface, type=ELEMENT, name=_PickedSurf29, internal
__PickedSurf29_S3, S3
__PickedSurf29_S5, S5
__PickedSurf29_S4, S4
*Elset, elset=__PickedSurf30_S5, internal, instance=B_Gear-1
  [OMITTED]
*Elset, elset=__PickedSurf30_S3, internal, instance=B_Gear-1
  [OMITTED]
*Elset, elset=__PickedSurf30_S6, internal, instance=B_Gear-1, generate
  [OMITTED]
*Elset, elset=__PickedSurf30_S4, internal, instance=B_Gear-1
  [OMITTED]
*Surface, type=ELEMENT, name=_PickedSurf30, internal
__PickedSurf30_S5, S5
__PickedSurf30_S3, S3
__PickedSurf30_S6, S6
__PickedSurf30_S4, S4
*Elset, elset=__PickedSurf31_S5, internal, instance=A_Gear-1
  [OMITTED]
*Elset, elset=__PickedSurf31_S3, internal, instance=A_Gear-1
  [OMITTED]
*Elset, elset=__PickedSurf31_S4, internal, instance=A_Gear-1
  [OMITTED]
*Surface, type=ELEMENT, name=_PickedSurf31, internal
```

```
__PickedSurf31_S5, S5
__PickedSurf31_S3, S3
__PickedSurf31_S4, S4
*Elset, elset=__PickedSurf32_S3, internal, instance=B_Gear-1
  [OMITTED]
*Elset, elset=__PickedSurf32_S4, internal, instance=B_Gear-1
  [OMITTED]
*Elset, elset=__PickedSurf32_S6, internal, instance=B_Gear-1, generate
  [OMITTED]
*Elset, elset=__PickedSurf32_S5, internal, instance=B_Gear-1, generate
  [OMITTED]
*Surface, type=ELEMENT, name=_PickedSurf32, internal
__PickedSurf32_S3, S3
__PickedSurf32_S4, S4
__PickedSurf32_S6, S6
__PickedSurf32_S5, S5
*Elset, elset=__PickedSurf33_S6, internal, instance=A_Gear-1
  [OMITTED]
*Elset, elset=__PickedSurf33_S5, internal, instance=A_Gear-1
  [OMITTED]
*Elset, elset=__PickedSurf33_S3, internal, instance=A_Gear-1
  [OMITTED]
*Elset, elset=__PickedSurf33_S4, internal, instance=A_Gear-1
  [OMITTED]
*Surface, type=ELEMENT, name=_PickedSurf33, internal
__PickedSurf33_S6, S6
__PickedSurf33_S5, S5
__PickedSurf33_S4, S4
__PickedSurf33_S3, S3
*Elset, elset=__PickedSurf34_S5, internal, instance=B_Gear-1
  [OMITTED]
*Elset, elset=__PickedSurf34_S6, internal, instance=B_Gear-1
  [OMITTED]
*Elset, elset=__PickedSurf34_S3, internal, instance=B_Gear-1
  [OMITTED]
*Elset, elset=__PickedSurf34_S4, internal, instance=B_Gear-1
  [OMITTED]
*Surface, type=ELEMENT, name=_PickedSurf34, internal
__PickedSurf34_S5, S5
__PickedSurf34_S6, S6
__PickedSurf34_S4, S4
__PickedSurf34_S3, S3
*Elset, elset=__PickedSurf35_S4, internal, instance=A_Gear-1
  [OMITTED]
*Elset, elset=__PickedSurf35_S5, internal, instance=A_Gear-1
  [OMITTED]
*Elset, elset=__PickedSurf35_S3, internal, instance=A_Gear-1
  [OMITTED]
*Elset, elset=__PickedSurf35_S6, internal, instance=A_Gear-1
  [OMITTED]
*Surface, type=ELEMENT, name=_PickedSurf35, internal
__PickedSurf35_S4, S4
__PickedSurf35_S5, S5
__PickedSurf35_S6, S6
__PickedSurf35_S3, S3
*Elset, elset=__PickedSurf36_S4, internal, instance=B_Gear-1
```

```
  [OMITTED]
*Elset, elset=__PickedSurf36_S3, internal, instance=B_Gear-1
  [OMITTED]
*Elset, elset=__PickedSurf36_S6, internal, instance=B_Gear-1
  [OMITTED]
*Elset, elset=__PickedSurf36_S5, internal, instance=B_Gear-1
  [OMITTED]
*Surface, type=ELEMENT, name=_PickedSurf36, internal
__PickedSurf36_S4, S4
__PickedSurf36_S3, S3
__PickedSurf36_S6, S6
__PickedSurf36_S5, S5
*Elset, elset=__PickedSurf37_S6, internal, instance=A_Gear-1
  [OMITTED]
*Elset, elset=__PickedSurf37_S3, internal, instance=A_Gear-1
  [OMITTED]
*Elset, elset=__PickedSurf37_S5, internal, instance=A_Gear-1
  [OMITTED]
*Elset, elset=__PickedSurf37_S4, internal, instance=A_Gear-1
  [OMITTED]
*Surface, type=ELEMENT, name=_PickedSurf37, internal
__PickedSurf37_S6, S6
__PickedSurf37_S3, S3
__PickedSurf37_S4, S4
__PickedSurf37_S5, S5
*Elset, elset=__PickedSurf38_S3, internal, instance=B_Gear-1
  [OMITTED]
*Elset, elset=__PickedSurf38_S5, internal, instance=B_Gear-1
  [OMITTED]
*Elset, elset=__PickedSurf38_S4, internal, instance=B_Gear-1
  [OMITTED]
*Elset, elset=__PickedSurf38_S6, internal, instance=B_Gear-1
  [OMITTED]
*Surface, type=ELEMENT, name=_PickedSurf38, internal
__PickedSurf38_S3, S3
__PickedSurf38_S5, S5
__PickedSurf38_S4, S4
__PickedSurf38_S6, S6
*Elset, elset=__PickedSurf40_S5, internal, instance=A_Gear-1
  [OMITTED]
*Elset, elset=__PickedSurf40_S3, internal, instance=A_Gear-1
  [OMITTED]
*Elset, elset=__PickedSurf40_S6, internal, instance=A_Gear-1, generate
  [OMITTED]
*Elset, elset=__PickedSurf40_S4, internal, instance=A_Gear-1
  [OMITTED]
*Surface, type=ELEMENT, name=_PickedSurf40, internal
__PickedSurf40_S5, S5
__PickedSurf40_S3, S3
__PickedSurf40_S6, S6
__PickedSurf40_S4, S4
*Elset, elset=__PickedSurf41_S5, internal, instance=B_Gear-1
  [OMITTED]
*Elset, elset=__PickedSurf41_S3, internal, instance=B_Gear-1
  [OMITTED]
*Elset, elset=__PickedSurf41_S4, internal, instance=B_Gear-1
```

```
277   [OMITTED]
*Surface, type=ELEMENT, name=_PickedSurf41, internal
279 __PickedSurf41_S5, S5
__PickedSurf41_S3, S3
281 __PickedSurf41_S4, S4
*Elset, elset=__PickedSurf42_S5, internal, instance=A_Gear-1
283   [OMITTED]
*Elset, elset=__PickedSurf42_S4, internal, instance=A_Gear-1
285   [OMITTED]
*Surface, type=ELEMENT, name=_PickedSurf42, internal
287 __PickedSurf42_S5, S5
__PickedSurf42_S4, S4
289 *Elset, elset=__PickedSurf43_S5, internal, instance=B_Gear-1
    [OMITTED]
291 *Elset, elset=__PickedSurf43_S4, internal, instance=B_Gear-1
    [OMITTED]
293 *Elset, elset=__PickedSurf43_S6, internal, instance=B_Gear-1, generate
    [OMITTED]
295 *Surface, type=ELEMENT, name=_PickedSurf43, internal
__PickedSurf43_S5, S5
297 __PickedSurf43_S4, S4
__PickedSurf43_S6, S6
299 *Elset, elset=__PickedSurf44_S5, internal, instance=A_Gear-1
    [OMITTED]
301 *Elset, elset=__PickedSurf44_S4, internal, instance=A_Gear-1
    [OMITTED]
303 *Elset, elset=__PickedSurf44_S3, internal, instance=A_Gear-1
    [OMITTED]
305 *Surface, type=ELEMENT, name=_PickedSurf44, internal
__PickedSurf44_S5, S5
307 __PickedSurf44_S4, S4
__PickedSurf44_S3, S3
309 *Elset, elset=__PickedSurf45_S5, internal, instance=B_Gear-1
    [OMITTED]
311 *Elset, elset=__PickedSurf45_S3, internal, instance=B_Gear-1
    [OMITTED]
313 *Elset, elset=__PickedSurf45_S6, internal, instance=B_Gear-1, generate
    [OMITTED]
315 *Elset, elset=__PickedSurf45_S4, internal, instance=B_Gear-1
    [OMITTED]
317 *Surface, type=ELEMENT, name=_PickedSurf45, internal
__PickedSurf45_S5, S5
319 __PickedSurf45_S3, S3
__PickedSurf45_S6, S6
321 __PickedSurf45_S4, S4
*Elset, elset=__PickedSurf46_S5, internal, instance=A_Gear-1
323   [OMITTED]
*Elset, elset=__PickedSurf46_S3, internal, instance=A_Gear-1
325   [OMITTED]
*Elset, elset=__PickedSurf46_S4, internal, instance=A_Gear-1
327   [OMITTED]
*Surface, type=ELEMENT, name=_PickedSurf46, internal
329 __PickedSurf46_S5, S5
__PickedSurf46_S3, S3
331 __PickedSurf46_S4, S4
*Elset, elset=__PickedSurf47_S5, internal, instance=B_Gear-1
```

```
333   [OMITTED]
*Elset, elset=__PickedSurf47_S4, internal, instance=B_Gear-1
335   [OMITTED]
*Elset, elset=__PickedSurf47_S6, internal, instance=B_Gear-1, generate
337   [OMITTED]
*Surface, type=ELEMENT, name=_PickedSurf47, internal
339 __PickedSurf47_S5, S5
__PickedSurf47_S4, S4
341 __PickedSurf47_S6, S6
*Elset, elset=__PickedSurf48_S5, internal, instance=A_Gear-1
343   [OMITTED]
*Elset, elset=__PickedSurf48_S4, internal, instance=A_Gear-1
345   [OMITTED]
*Elset, elset=__PickedSurf48_S6, internal, instance=A_Gear-1, generate
347   [OMITTED]
*Elset, elset=__PickedSurf48_S3, internal, instance=A_Gear-1, generate
349   [OMITTED]
*Surface, type=ELEMENT, name=_PickedSurf48, internal
351 __PickedSurf48_S5, S5
__PickedSurf48_S4, S4
353 __PickedSurf48_S6, S6
__PickedSurf48_S3, S3
355 *Elset, elset=__PickedSurf49_S5, internal, instance=B_Gear-1
    [OMITTED]
357 *Elset, elset=__PickedSurf49_S3, internal, instance=B_Gear-1
    [OMITTED]
359 *Elset, elset=__PickedSurf49_S4, internal, instance=B_Gear-1
    [OMITTED]
361 *Surface, type=ELEMENT, name=_PickedSurf49, internal
__PickedSurf49_S5, S5
363 __PickedSurf49_S3, S3
__PickedSurf49_S4, S4
365 *Elset, elset=__PickedSurf50_S5, internal, instance=A_Gear-1, generate
    [OMITTED]
367 *Elset, elset=__PickedSurf50_S6, internal, instance=A_Gear-1
    [OMITTED]
369 *Elset, elset=__PickedSurf50_S3, internal, instance=A_Gear-1
    [OMITTED]
371 *Elset, elset=__PickedSurf50_S4, internal, instance=A_Gear-1
    [OMITTED]
373 *Surface, type=ELEMENT, name=_PickedSurf50, internal
__PickedSurf50_S5, S5
375 __PickedSurf50_S6, S6
__PickedSurf50_S4, S4
377 __PickedSurf50_S3, S3
*Elset, elset=__PickedSurf51_S5, internal, instance=B_Gear-1
379   [OMITTED]
*Elset, elset=__PickedSurf51_S4, internal, instance=B_Gear-1
381   [OMITTED]
*Elset, elset=__PickedSurf51_S3, internal, instance=B_Gear-1, generate
383   [OMITTED]
*Surface, type=ELEMENT, name=_PickedSurf51, internal
385 __PickedSurf51_S5, S5
__PickedSurf51_S4, S4
387 __PickedSurf51_S3, S3
*Elset, elset=__PickedSurf52_S3, internal, instance=A_Gear-1
```

```
  [OMITTED]
*Elset, elset=__PickedSurf52_S4, internal, instance=A_Gear-1
  [OMITTED]
*Elset, elset=__PickedSurf52_S5, internal, instance=A_Gear-1
  [OMITTED]
*Surface, type=ELEMENT, name=_PickedSurf52, internal
__PickedSurf52_S3, S3
__PickedSurf52_S4, S4
__PickedSurf52_S5, S5
*Elset, elset=__PickedSurf53_S5, internal, instance=B_Gear-1
  [OMITTED]
*Elset, elset=__PickedSurf53_S3, internal, instance=B_Gear-1
  [OMITTED]
*Elset, elset=__PickedSurf53_S4, internal, instance=B_Gear-1
  [OMITTED]
*Surface, type=ELEMENT, name=_PickedSurf53, internal
__PickedSurf53_S5, S5
__PickedSurf53_S3, S3
__PickedSurf53_S4, S4
*Elset, elset=__PickedSurf54_S3, internal, instance=A_Gear-1
  [OMITTED]
*Elset, elset=__PickedSurf54_S5, internal, instance=A_Gear-1
  [OMITTED]
*Elset, elset=__PickedSurf54_S4, internal, instance=A_Gear-1
  [OMITTED]
*Elset, elset=__PickedSurf54_S6, internal, instance=A_Gear-1, generate
  [OMITTED]
*Surface, type=ELEMENT, name=_PickedSurf54, internal
__PickedSurf54_S3, S3
__PickedSurf54_S5, S5
__PickedSurf54_S4, S4
__PickedSurf54_S6, S6
*Elset, elset=__PickedSurf55_S5, internal, instance=B_Gear-1
  [OMITTED]
*Elset, elset=__PickedSurf55_S6, internal, instance=B_Gear-1
  [OMITTED]
*Elset, elset=__PickedSurf55_S3, internal, instance=B_Gear-1, generate
  [OMITTED]
*Elset, elset=__PickedSurf55_S4, internal, instance=B_Gear-1
  [OMITTED]
*Surface, type=ELEMENT, name=_PickedSurf55, internal
__PickedSurf55_S5, S5
__PickedSurf55_S6, S6
__PickedSurf55_S4, S4
__PickedSurf55_S3, S3
*Elset, elset=__PickedSurf56_S3, internal, instance=A_Gear-1
  [OMITTED]
*Elset, elset=__PickedSurf56_S4, internal, instance=A_Gear-1
  [OMITTED]
*Elset, elset=__PickedSurf56_S6, internal, instance=A_Gear-1, generate
  [OMITTED]
*Elset, elset=__PickedSurf56_S5, internal, instance=A_Gear-1, generate
  [OMITTED]
*Surface, type=ELEMENT, name=_PickedSurf56, internal
__PickedSurf56_S3, S3
__PickedSurf56_S4, S4
```

```
__PickedSurf56_S6, S6
__PickedSurf56_S5, S5
*Elset, elset=__PickedSurf57_S3, internal, instance=B_Gear-1
  [OMITTED]
*Elset, elset=__PickedSurf57_S5, internal, instance=B_Gear-1, generate
  [OMITTED]
*Elset, elset=__PickedSurf57_S6, internal, instance=B_Gear-1, generate
  [OMITTED]
*Elset, elset=__PickedSurf57_S4, internal, instance=B_Gear-1
  [OMITTED]
*Surface, type=ELEMENT, name=_PickedSurf57, internal
__PickedSurf57_S3, S3
__PickedSurf57_S5, S5
__PickedSurf57_S6, S6
__PickedSurf57_S4, S4
*Elset, elset=__PickedSurf58_S5, internal, instance=A_Gear-1
  [OMITTED]
*Elset, elset=__PickedSurf58_S4, internal, instance=A_Gear-1
  [OMITTED]
*Elset, elset=__PickedSurf58_S6, internal, instance=A_Gear-1, generate
  [OMITTED]
*Surface, type=ELEMENT, name=_PickedSurf58, internal
__PickedSurf58_S5, S5
__PickedSurf58_S4, S4
__PickedSurf58_S6, S6
*Elset, elset=__PickedSurf59_S5, internal, instance=B_Gear-1
  [OMITTED]
*Elset, elset=__PickedSurf59_S4, internal, instance=B_Gear-1
  [OMITTED]
*Elset, elset=__PickedSurf59_S6, internal, instance=B_Gear-1, generate
  [OMITTED]
*Surface, type=ELEMENT, name=_PickedSurf59, internal
__PickedSurf59_S5, S5
__PickedSurf59_S4, S4
__PickedSurf59_S6, S6
*Elset, elset=__PickedSurf60_S5, internal, instance=A_Gear-1
  [OMITTED]
*Elset, elset=__PickedSurf60_S3, internal, instance=A_Gear-1
  [OMITTED]
*Elset, elset=__PickedSurf60_S4, internal, instance=A_Gear-1
  [OMITTED]
*Surface, type=ELEMENT, name=_PickedSurf60, internal
__PickedSurf60_S5, S5
__PickedSurf60_S3, S3
__PickedSurf60_S4, S4
*Elset, elset=__PickedSurf61_S5, internal, instance=B_Gear-1
  [OMITTED]
*Elset, elset=__PickedSurf61_S3, internal, instance=B_Gear-1, generate
  [OMITTED]
*Elset, elset=__PickedSurf61_S4, internal, instance=B_Gear-1
  [OMITTED]
*Elset, elset=__PickedSurf61_S6, internal, instance=B_Gear-1, generate
  [OMITTED]
*Surface, type=ELEMENT, name=_PickedSurf61, internal
__PickedSurf61_S5, S5
__PickedSurf61_S3, S3
```

```
501 __PickedSurf61_S4, S4
    __PickedSurf61_S6, S6
503 *Elset, elset=__PickedSurf62_S5, internal, instance=A_Gear-1
      [OMITTED]
505 *Elset, elset=__PickedSurf62_S4, internal, instance=A_Gear-1
      [OMITTED]1
507 *Elset, elset=__PickedSurf62_S3, internal, instance=A_Gear-1, generate
      [OMITTED]
509 *Surface, type=ELEMENT, name=_PickedSurf62, internal
    __PickedSurf62_S5, S5
511 __PickedSurf62_S4, S4
    __PickedSurf62_S3, S3
513 *Elset, elset=__PickedSurf63_S5, internal, instance=B_Gear-1
      [OMITTED]
515 *Elset, elset=__PickedSurf63_S4, internal, instance=B_Gear-1
      [OMITTED]
517 *Elset, elset=__PickedSurf63_S3, internal, instance=B_Gear-1, generate
      [OMITTED]
519 *Surface, type=ELEMENT, name=_PickedSurf63, internal
    __PickedSurf63_S5, S5
521 __PickedSurf63_S4, S4
    __PickedSurf63_S3, S3
523 *Elset, elset=__PickedSurf64_S5, internal, instance=A_Gear-1
      [OMITTED]
525 *Elset, elset=__PickedSurf64_S4, internal, instance=A_Gear-1
      [OMITTED]
527 *Elset, elset=__PickedSurf64_S3, internal, instance=A_Gear-1, generate
      [OMITTED]
529 *Surface, type=ELEMENT, name=_PickedSurf64, internal
    __PickedSurf64_S5, S5
531 __PickedSurf64_S4, S4
    __PickedSurf64_S3, S3
533 *Elset, elset=__PickedSurf65_S5, internal, instance=B_Gear-1
      [OMITTED]
535 *Elset, elset=__PickedSurf65_S6, internal, instance=B_Gear-1, generate
      [OMITTED]
537 *Elset, elset=__PickedSurf65_S3, internal, instance=B_Gear-1, generate
      [OMITTED]
539 *Elset, elset=__PickedSurf65_S4, internal, instance=B_Gear-1
      [OMITTED]
541 *Surface, type=ELEMENT, name=_PickedSurf65, internal
    __PickedSurf65_S5, S5
543 __PickedSurf65_S6, S6
    __PickedSurf65_S4, S4
545 __PickedSurf65_S3, S3
    *Elset, elset=__PickedSurf66_S5, internal, instance=A_Gear-1
547   [OMITTED]
    *Elset, elset=__PickedSurf66_S4, internal, instance=A_Gear-1
549   [OMITTED]
    *Elset, elset=__PickedSurf66_S6, internal, instance=A_Gear-1, generate
551   [OMITTED]
    *Surface, type=ELEMENT, name=_PickedSurf66, internal
553 __PickedSurf66_S5, S5
    __PickedSurf66_S4, S4
555 __PickedSurf66_S6, S6
    *Elset, elset=__PickedSurf67_S3, internal, instance=B_Gear-1
```

```
557   [OMITTED]
*Elset, elset=__PickedSurf67_S4, internal, instance=B_Gear-1
559   [OMITTED]
*Elset, elset=__PickedSurf67_S5, internal, instance=B_Gear-1, generate
561   [OMITTED]
*Surface, type=ELEMENT, name=_PickedSurf67, internal
563 __PickedSurf67_S3, S3
__PickedSurf67_S4, S4
565 __PickedSurf67_S5, S5
*Elset, elset=__PickedSurf68_S5, internal, instance=A_Gear-1
567   [OMITTED]
*Elset, elset=__PickedSurf68_S3, internal, instance=A_Gear-1
569   [OMITTED]
*Elset, elset=__PickedSurf68_S4, internal, instance=A_Gear-1
571   [OMITTED]
*Elset, elset=__PickedSurf68_S6, internal, instance=A_Gear-1, generate
573   [OMITTED]
*Surface, type=ELEMENT, name=_PickedSurf68, internal
575 __PickedSurf68_S5, S5
__PickedSurf68_S3, S3
577 __PickedSurf68_S4, S4
__PickedSurf68_S6, S6
579 *Elset, elset=__PickedSurf69_S5, internal, instance=B_Gear-1
    [OMITTED]
581 *Elset, elset=__PickedSurf69_S3, internal, instance=B_Gear-1, generate
    [OMITTED]
583 *Elset, elset=__PickedSurf69_S4, internal, instance=B_Gear-1
    [OMITTED]
585 *Surface, type=ELEMENT, name=_PickedSurf69, internal
__PickedSurf69_S5, S5
587 __PickedSurf69_S3, S3
__PickedSurf69_S4, S4
589 *Elset, elset=__PickedSurf70_S5, internal, instance=A_Gear-1
    [OMITTED]
591 *Elset, elset=__PickedSurf70_S3, internal, instance=A_Gear-1
    [OMITTED]
593 *Elset, elset=__PickedSurf70_S6, internal, instance=A_Gear-1, generate
    [OMITTED]
595 *Elset, elset=__PickedSurf70_S4, internal, instance=A_Gear-1
    [OMITTED]
597 *Surface, type=ELEMENT, name=_PickedSurf70, internal
__PickedSurf70_S5, S5
599 __PickedSurf70_S3, S3
__PickedSurf70_S6, S6
601 __PickedSurf70_S4, S4
*Elset, elset=__PickedSurf71_S3, internal, instance=B_Gear-1, generate
603   [OMITTED]
*Elset, elset=__PickedSurf71_S5, internal, instance=B_Gear-1
605   [OMITTED]
*Elset, elset=__PickedSurf71_S4, internal, instance=B_Gear-1
607   [OMITTED]
*Surface, type=ELEMENT, name=_PickedSurf71, internal
609 __PickedSurf71_S3, S3
__PickedSurf71_S5, S5
611 __PickedSurf71_S4, S4
*Elset, elset=__PickedSurf72_S5, internal, instance=A_Gear-1
```

```
  [OMITTED]
*Elset, elset=__PickedSurf72_S4, internal, instance=A_Gear-1
  [OMITTED]
*Elset, elset=__PickedSurf72_S3, internal, instance=A_Gear-1
  [OMITTED]
*Surface, type=ELEMENT, name=_PickedSurf72, internal
__PickedSurf72_S5, S5
__PickedSurf72_S4, S4
__PickedSurf72_S3, S3
*Elset, elset=__PickedSurf73_S5, internal, instance=B_Gear-1
  [OMITTED]
*Elset, elset=__PickedSurf73_S3, internal, instance=B_Gear-1, generate
  [OMITTED]
*Elset, elset=__PickedSurf73_S4, internal, instance=B_Gear-1
  [OMITTED]
*Elset, elset=__PickedSurf73_S6, internal, instance=B_Gear-1, generate
  [OMITTED]
*Surface, type=ELEMENT, name=_PickedSurf73, internal
__PickedSurf73_S5, S5
__PickedSurf73_S3, S3
__PickedSurf73_S4, S4
__PickedSurf73_S6, S6
*Elset, elset=__PickedSurf74_S5, internal, instance=A_Gear-1
  [OMITTED]
*Elset, elset=__PickedSurf74_S4, internal, instance=A_Gear-1
  [OMITTED]
*Surface, type=ELEMENT, name=_PickedSurf74, internal
__PickedSurf74_S5, S5
__PickedSurf74_S4, S4
*Elset, elset=__PickedSurf75_S5, internal, instance=B_Gear-1
  [OMITTED]
*Elset, elset=__PickedSurf75_S3, internal, instance=B_Gear-1
  [OMITTED]
*Elset, elset=__PickedSurf75_S4, internal, instance=B_Gear-1
  [OMITTED]
*Elset, elset=__PickedSurf75_S6, internal, instance=B_Gear-1, generate
  [OMITTED]
*Surface, type=ELEMENT, name=_PickedSurf75, internal
__PickedSurf75_S5, S5
__PickedSurf75_S3, S3
__PickedSurf75_S4, S4
__PickedSurf75_S6, S6
*Elset, elset=__PickedSurf76_S3, internal, instance=A_Gear-1
  [OMITTED]
*Elset, elset=__PickedSurf76_S6, internal, instance=A_Gear-1
  [OMITTED]
*Elset, elset=__PickedSurf76_S4, internal, instance=A_Gear-1
  [OMITTED]
*Surface, type=ELEMENT, name=_PickedSurf76, internal
__PickedSurf76_S3, S3
__PickedSurf76_S6, S6
__PickedSurf76_S4, S4
*Elset, elset=__PickedSurf77_S5, internal, instance=B_Gear-1
  [OMITTED]
*Elset, elset=__PickedSurf77_S3, internal, instance=B_Gear-1
  [OMITTED]
```

```
669 *Elset, elset=__PickedSurf77_S6, internal, instance=B_Gear-1, generate
      [OMITTED]
671 *Elset, elset=__PickedSurf77_S4, internal, instance=B_Gear-1
      [OMITTED]
673 *Surface, type=ELEMENT, name=_PickedSurf77, internal
    __PickedSurf77_S5, S5
675 __PickedSurf77_S3, S3
    __PickedSurf77_S6, S6
677 __PickedSurf77_S4, S4
    *Elset, elset=__PickedSurf78_S3, internal, instance=A_Gear-1
679   [OMITTED]
    *Elset, elset=__PickedSurf78_S5, internal, instance=A_Gear-1, generate
681   [OMITTED]
    *Elset, elset=__PickedSurf78_S6, internal, instance=A_Gear-1, generate
683   [OMITTED]
    *Elset, elset=__PickedSurf78_S4, internal, instance=A_Gear-1
685   [OMITTED]
    *Surface, type=ELEMENT, name=_PickedSurf78, internal
687 __PickedSurf78_S3, S3
    __PickedSurf78_S5, S5
689 __PickedSurf78_S6, S6
    __PickedSurf78_S4, S4
691 *Elset, elset=__PickedSurf79_S5, internal, instance=B_Gear-1
      [OMITTED]
693 *Elset, elset=__PickedSurf79_S4, internal, instance=B_Gear-1
      [OMITTED]
695 *Surface, type=ELEMENT, name=_PickedSurf79, internal
    __PickedSurf79_S5, S5
697 __PickedSurf79_S4, S4
    *Elset, elset=__PickedSurf80_S5, internal, instance=A_Gear-1
699   [OMITTED]
    *Elset, elset=__PickedSurf80_S3, internal, instance=A_Gear-1
701   [OMITTED]
    *Elset, elset=__PickedSurf80_S4, internal, instance=A_Gear-1
703   [OMITTED]
    *Surface, type=ELEMENT, name=_PickedSurf80, internal
705 __PickedSurf80_S5, S5
    __PickedSurf80_S3, S3
707 __PickedSurf80_S4, S4
    *Elset, elset=__PickedSurf81_S5, internal, instance=B_Gear-1
709   [OMITTED]
    *Elset, elset=__PickedSurf81_S4, internal, instance=B_Gear-1
711   [OMITTED]
    *Elset, elset=__PickedSurf81_S6, internal, instance=B_Gear-1, generate
713   [OMITTED]
    *Surface, type=ELEMENT, name=_PickedSurf81, internal
715 __PickedSurf81_S5, S5
    __PickedSurf81_S4, S4
717 __PickedSurf81_S6, S6
    *Elset, elset=__PickedSurf82_S3, internal, instance=A_Gear-1
719   [OMITTED]
    *Elset, elset=__PickedSurf82_S6, internal, instance=A_Gear-1
721   [OMITTED]
    *Elset, elset=__PickedSurf82_S4, internal, instance=A_Gear-1
723   [OMITTED]
    *Surface, type=ELEMENT, name=_PickedSurf82, internal
```

```
__PickedSurf82_S3, S3
__PickedSurf82_S6, S6
__PickedSurf82_S4, S4
*Elset, elset=__PickedSurf83_S5, internal, instance=B_Gear-1
  [OMITTED]
*Elset, elset=__PickedSurf83_S3, internal, instance=B_Gear-1
  [OMITTED]
*Elset, elset=__PickedSurf83_S4, internal, instance=B_Gear-1
  [OMITTED]
*Surface, type=ELEMENT, name=_PickedSurf83, internal
__PickedSurf83_S5, S5
__PickedSurf83_S3, S3
__PickedSurf83_S4, S4
*Elset, elset=__PickedSurf84_S5, internal, instance=A_Gear-1
  [OMITTED]
*Elset, elset=__PickedSurf84_S4, internal, instance=A_Gear-1
  [OMITTED]
*Elset, elset=__PickedSurf84_S6, internal, instance=A_Gear-1, generate
  [OMITTED]
*Surface, type=ELEMENT, name=_PickedSurf84, internal
__PickedSurf84_S5, S5
__PickedSurf84_S4, S4
__PickedSurf84_S6, S6
*Elset, elset=__PickedSurf85_S3, internal, instance=B_Gear-1
  [OMITTED]
*Elset, elset=__PickedSurf85_S4, internal, instance=B_Gear-1
  [OMITTED]
*Elset, elset=__PickedSurf85_S5, internal, instance=B_Gear-1, generate
  [OMITTED]
*Surface, type=ELEMENT, name=_PickedSurf85, internal
__PickedSurf85_S3, S3
__PickedSurf85_S4, S4
__PickedSurf85_S5, S5
*Elset, elset=__PickedSurf86_S3, internal, instance=A_Gear-1
  [OMITTED]
*Elset, elset=__PickedSurf86_S4, internal, instance=A_Gear-1
  [OMITTED]
*Elset, elset=__PickedSurf86_S6, internal, instance=A_Gear-1, generate
  [OMITTED]
*Surface, type=ELEMENT, name=_PickedSurf86, internal
__PickedSurf86_S3, S3
__PickedSurf86_S4, S4
__PickedSurf86_S6, S6
*Elset, elset=__PickedSurf87_S5, internal, instance=B_Gear-1
  [OMITTED]
*Elset, elset=__PickedSurf87_S3, internal, instance=B_Gear-1
  [OMITTED]
*Elset, elset=__PickedSurf87_S6, internal, instance=B_Gear-1, generate
  [OMITTED]
*Elset, elset=__PickedSurf87_S4, internal, instance=B_Gear-1
  [OMITTED]
*Surface, type=ELEMENT, name=_PickedSurf87, internal
__PickedSurf87_S5, S5
__PickedSurf87_S3, S3
__PickedSurf87_S6, S6
__PickedSurf87_S4, S4
```

```
781 *Elset, elset=__PickedSurf88_S5, internal, instance=A_Gear-1
      [OMITTED]
783 *Elset, elset=__PickedSurf88_S4, internal, instance=A_Gear-1
      [OMITTED]
785 *Elset, elset=__PickedSurf88_S6, internal, instance=A_Gear-1
      [OMITTED]
787 *Surface, type=ELEMENT, name=_PickedSurf88, internal
    __PickedSurf88_S5, S5
789 __PickedSurf88_S4, S4
    __PickedSurf88_S6, S6
791 *Elset, elset=__PickedSurf89_S5, internal, instance=B_Gear-1
      [OMITTED]
793 *Elset, elset=__PickedSurf89_S6, internal, instance=B_Gear-1
      [OMITTED]
795 *Elset, elset=__PickedSurf89_S3, internal, instance=B_Gear-1, generate
      [OMITTED]
797 *Elset, elset=__PickedSurf89_S4, internal, instance=B_Gear-1
      [OMITTED]
799 *Surface, type=ELEMENT, name=_PickedSurf89, internal
    __PickedSurf89_S5, S5
801 __PickedSurf89_S6, S6
    __PickedSurf89_S4, S4
803 __PickedSurf89_S3, S3
    *Elset, elset=__PickedSurf90_S5, internal, instance=A_Gear-1
805   [OMITTED]
    *Elset, elset=__PickedSurf90_S3, internal, instance=A_Gear-1, generate
807   [OMITTED]
    *Elset, elset=__PickedSurf90_S4, internal, instance=A_Gear-1
809   [OMITTED]
    *Surface, type=ELEMENT, name=_PickedSurf90, internal
811 __PickedSurf90_S5, S5
    __PickedSurf90_S3, S3
813 __PickedSurf90_S4, S4
    *Elset, elset=__PickedSurf91_S5, internal, instance=B_Gear-1, generate
815   [OMITTED]
    *Elset, elset=__PickedSurf91_S3, internal, instance=B_Gear-1
817   [OMITTED]
    *Elset, elset=__PickedSurf91_S4, internal, instance=B_Gear-1
819   [OMITTED]
    *Elset, elset=__PickedSurf91_S6, internal, instance=B_Gear-1, generate
821   [OMITTED]
    *Surface, type=ELEMENT, name=_PickedSurf91, internal
823 __PickedSurf91_S5, S5
    __PickedSurf91_S3, S3
825 __PickedSurf91_S4, S4
    __PickedSurf91_S6, S6
827 *Elset, elset=__PickedSurf92_S3, internal, instance=A_Gear-1
      [OMITTED]
829 *Elset, elset=__PickedSurf92_S5, internal, instance=A_Gear-1
      [OMITTED]
831 *Elset, elset=__PickedSurf92_S4, internal, instance=A_Gear-1
      [OMITTED]
833 *Elset, elset=__PickedSurf92_S6, internal, instance=A_Gear-1, generate
      [OMITTED]
835 *Surface, type=ELEMENT, name=_PickedSurf92, internal
    __PickedSurf92_S3, S3
```

```
__PickedSurf92_S5, S5
__PickedSurf92_S4, S4
__PickedSurf92_S6, S6
*Elset, elset=__PickedSurf93_S3, internal, instance=B_Gear-1
  [OMITTED]
*Elset, elset=__PickedSurf93_S5, internal, instance=B_Gear-1, generate
  [OMITTED]
*Elset, elset=__PickedSurf93_S4, internal, instance=B_Gear-1
  [OMITTED]
*Surface, type=ELEMENT, name=_PickedSurf93, internal
__PickedSurf93_S3, S3
__PickedSurf93_S5, S5
__PickedSurf93_S4, S4
*Elset, elset=__PickedSurf94_S3, internal, instance=A_Gear-1
  [OMITTED]
*Elset, elset=__PickedSurf94_S4, internal, instance=A_Gear-1
  [OMITTED]
*Elset, elset=__PickedSurf94_S5, internal, instance=A_Gear-1
  [OMITTED]
*Surface, type=ELEMENT, name=_PickedSurf94, internal
__PickedSurf94_S3, S3
__PickedSurf94_S4, S4
__PickedSurf94_S5, S5
*Elset, elset=__PickedSurf95_S5, internal, instance=B_Gear-1
  [OMITTED]
*Elset, elset=__PickedSurf95_S3, internal, instance=B_Gear-1, generate
  [OMITTED]
*Elset, elset=__PickedSurf95_S4, internal, instance=B_Gear-1
  [OMITTED]
*Surface, type=ELEMENT, name=_PickedSurf95, internal
__PickedSurf95_S5, S5
__PickedSurf95_S3, S3
__PickedSurf95_S4, S4
*Elset, elset=__PickedSurf96_S5, internal, instance=A_Gear-1
  [OMITTED]
*Elset, elset=__PickedSurf96_S3, internal, instance=A_Gear-1
  [OMITTED]
*Elset, elset=__PickedSurf96_S6, internal, instance=A_Gear-1, generate
  [OMITTED]
*Elset, elset=__PickedSurf96_S4, internal, instance=A_Gear-1
  [OMITTED]
*Surface, type=ELEMENT, name=_PickedSurf96, internal
__PickedSurf96_S5, S5
__PickedSurf96_S3, S3
__PickedSurf96_S6, S6
__PickedSurf96_S4, S4
*Elset, elset=__PickedSurf97_S5, internal, instance=B_Gear-1
  [OMITTED]
*Elset, elset=__PickedSurf97_S3, internal, instance=B_Gear-1
  [OMITTED]
*Elset, elset=__PickedSurf97_S4, internal, instance=B_Gear-1
  [OMITTED]
*Surface, type=ELEMENT, name=_PickedSurf97, internal
__PickedSurf97_S5, S5
__PickedSurf97_S3, S3
__PickedSurf97_S4, S4
```

```
** Constraint: A_shaft
*Coupling, constraint name=A_shaft, ref node=A_RP, surface=A_inner
*Kinematic
** Constraint: B_shaft
*Coupling, constraint name=B_shaft, ref node=B_RP, surface=B_inner
*Kinematic
*End Assembly
*Amplitude, name=Instantaneous, time=TOTAL TIME
             0.,              0.,           1e-10,              1.,
            1.,              1.
**
** MATERIALS
**
*Material, name=Steel_Elastic
*Elastic
187000., 0.29
*Material, name=UMAT
*Depvar
      4,
*User Material, constants=3
187000.,  0.29, 1e+10
**
** INTERACTION PROPERTIES
**
*Surface Interaction, name=CoF
1.,
*Friction, slip tolerance=0.005
 0.05,
*Surface Behavior, pressure-overclosure=HARD
**
** BOUNDARY CONDITIONS
**
** Name: A_position Type: Displacement/Rotation
*Boundary
A_RP, 1, 1
A_RP, 2, 2
A_RP, 3, 3
A_RP, 4, 4
A_RP, 5, 5
** Name: B_position Type: Displacement/Rotation
*Boundary
B_RP, 1, 1
B_RP, 2, 2
B_RP, 3, 3
B_RP, 4, 4
B_RP, 5, 5
**
** INTERACTIONS
**
** Interaction: Int-1
*Contact Pair, interaction=CoF, type=SURFACE TO SURFACE, adjust=0.0
_PickedSurf30, _PickedSurf29
** Interaction: Int-2
*Contact Pair, interaction=CoF, type=SURFACE TO SURFACE, adjust=0.0
_PickedSurf32, _PickedSurf31
** Interaction: Int-3
```

```
*Contact Pair, interaction=CoF, type=SURFACE TO SURFACE
_PickedSurf34, _PickedSurf33
** Interaction: Int-4
*Contact Pair, interaction=CoF, type=SURFACE TO SURFACE
_PickedSurf36, _PickedSurf35
** Interaction: Int-5
*Contact Pair, interaction=CoF, type=SURFACE TO SURFACE
_PickedSurf38, _PickedSurf37
** Interaction: Int-6
*Contact Pair, interaction=CoF, type=SURFACE TO SURFACE
_PickedSurf41, _PickedSurf40
** Interaction: Int-7
*Contact Pair, interaction=CoF, type=SURFACE TO SURFACE
_PickedSurf43, _PickedSurf42
** Interaction: Int-8
*Contact Pair, interaction=CoF, type=SURFACE TO SURFACE
_PickedSurf45, _PickedSurf44
** Interaction: Int-9
*Contact Pair, interaction=CoF, type=SURFACE TO SURFACE
_PickedSurf47, _PickedSurf46
** Interaction: Int-10
*Contact Pair, interaction=CoF, type=SURFACE TO SURFACE
_PickedSurf49, _PickedSurf48
** Interaction: Int-11
*Contact Pair, interaction=CoF, type=SURFACE TO SURFACE
_PickedSurf51, _PickedSurf50
** Interaction: Int-12
*Contact Pair, interaction=CoF, type=SURFACE TO SURFACE
_PickedSurf53, _PickedSurf52
** Interaction: Int-13
*Contact Pair, interaction=CoF, type=SURFACE TO SURFACE
_PickedSurf55, _PickedSurf54
** Interaction: Int-14
*Contact Pair, interaction=CoF, type=SURFACE TO SURFACE
_PickedSurf57, _PickedSurf56
** Interaction: Int-15
*Contact Pair, interaction=CoF, type=SURFACE TO SURFACE
_PickedSurf59, _PickedSurf58
** Interaction: Int-16
*Contact Pair, interaction=CoF, type=SURFACE TO SURFACE
_PickedSurf61, _PickedSurf60
** Interaction: Int-17
*Contact Pair, interaction=CoF, type=SURFACE TO SURFACE
_PickedSurf63, _PickedSurf62
** Interaction: Int-18
*Contact Pair, interaction=CoF, type=SURFACE TO SURFACE
_PickedSurf65, _PickedSurf64
** Interaction: Int-19
*Contact Pair, interaction=CoF, type=SURFACE TO SURFACE
_PickedSurf67, _PickedSurf66
** Interaction: Int-20
*Contact Pair, interaction=CoF, type=SURFACE TO SURFACE
_PickedSurf69, _PickedSurf68
** Interaction: Int-21
*Contact Pair, interaction=CoF, type=SURFACE TO SURFACE
_PickedSurf71, _PickedSurf70
```

```
** Interaction: Int-22
*Contact Pair, interaction=CoF, type=SURFACE TO SURFACE
_PickedSurf73, _PickedSurf72
** Interaction: Int-23
*Contact Pair, interaction=CoF, type=SURFACE TO SURFACE
_PickedSurf75, _PickedSurf74
** Interaction: Int-24
*Contact Pair, interaction=CoF, type=SURFACE TO SURFACE
_PickedSurf77, _PickedSurf76
** Interaction: Int-25
*Contact Pair, interaction=CoF, type=SURFACE TO SURFACE
_PickedSurf79, _PickedSurf78
** Interaction: Int-26
*Contact Pair, interaction=CoF, type=SURFACE TO SURFACE
_PickedSurf81, _PickedSurf80
** Interaction: Int-27
*Contact Pair, interaction=CoF, type=SURFACE TO SURFACE
_PickedSurf83, _PickedSurf82
** Interaction: Int-28
*Contact Pair, interaction=CoF, type=SURFACE TO SURFACE
_PickedSurf85, _PickedSurf84
** Interaction: Int-29
*Contact Pair, interaction=CoF, type=SURFACE TO SURFACE
_PickedSurf87, _PickedSurf86
** Interaction: Int-30
*Contact Pair, interaction=CoF, type=SURFACE TO SURFACE
_PickedSurf89, _PickedSurf88
** Interaction: Int-31
*Contact Pair, interaction=CoF, type=SURFACE TO SURFACE
_PickedSurf91, _PickedSurf90
** Interaction: Int-32
*Contact Pair, interaction=CoF, type=SURFACE TO SURFACE
_PickedSurf93, _PickedSurf92
** Interaction: Int-33
*Contact Pair, interaction=CoF, type=SURFACE TO SURFACE
_PickedSurf95, _PickedSurf94
** Interaction: Int-34
*Contact Pair, interaction=CoF, type=SURFACE TO SURFACE
_PickedSurf97, _PickedSurf96
** ----------------------------------------------------------------
**
** STEP: Elastic_start1
**
*Step, name=Elastic_start1, nlgeom=YES, inc=100000
*Static
5e-05, 0.00125, 1.25e-08, 5e-05
**
** BOUNDARY CONDITIONS
**
** Name: B_velocity Type: Velocity/Angular velocity
*Boundary, type=VELOCITY
_PickedSet98, 6, 6, 157.08
**
** LOADS
**
** Name: A_load   Type: Moment
```

```
*Cload, amplitude=Instantaneous
A_RP, 6, 150000.
**
** CONTROLS
**
*Controls, reset
*Controls, analysis=discontinuous
*Controls, parameters=time incrementation
, , , , , , , 10, , ,
**
** OUTPUT REQUESTS
**
*Restart, write, overlay, frequency=25
**
** FIELD OUTPUT: F-Output-1
**
*Output, field, time interval=0.00025
*Node Output
RF, U
*Element Output, directions=YES
LE, S, SDV
*Contact Output
CFORCE, CSTRESS
*Output, history, frequency=0
*End Step
** ----------------------------------------------------------------
**
** STEP: UMAT_1
**
*Step, name=UMAT_1, nlgeom=YES, inc=100000
*Static
1e-05, 0.00375, 1e-09, 1e-05
**
** OUTPUT REQUESTS
**
*Restart, write, overlay, frequency=25
**
** FIELD OUTPUT: F-Output-1
**
*Output, field, time interval=0.0001
*Node Output
RF, U
*Element Output, directions=YES
LE, S, SDV
*Contact Output
CFORCE, CSTRESS
*Output, history, frequency=0
*End Step
** ----------------------------------------------------------------
**
** STEP: Elastic_finish1
**
*Step, name=Rest1, nlgeom=YES, inc=100000
*Static
7e-05, 0.035, 1e-09, 7e-05
**
```

```
** OUTPUT REQUESTS
**
*Restart, write, overlay, frequency=100
**
** FIELD OUTPUT: F-Output-1
**
*Output, field, time interval=0.0035
*Node Output
RF, U
*Element Output, directions=YES
LE, S, SDV
*Contact Output
CFORCE, CSTRESS
*Output, history, frequency=0
*End Step
** ----------------------------------------------------------------
**
** STEP: Elastic_start2
**
*Step, name=Elastic_start2, nlgeom=YES, inc=1000000
*Static
5e-05, 0.00125, 1.25e-08, 5e-05
**
** OUTPUT REQUESTS
**
*Restart, write, overlay, frequency=25
**
** FIELD OUTPUT: F-Output-1
**
*Output, field, time interval=0.00025
*Node Output
RF, U
*Element Output, directions=YES
LE, S, SDV
*Contact Output
CFORCE, CSTRESS
*Output, history, frequency=0
*End Step
** ----------------------------------------------------------------
**
** STEP: UMAT_2
**
*Step, name=UMAT_2, nlgeom=YES, inc=100000
*Static
1e-05, 0.00375, 1e-09, 1e-05
**
** OUTPUT REQUESTS
**
*Restart, write, overlay, frequency=25
**
** FIELD OUTPUT: F-Output-1
**
*Output, field, time interval=0.0001
*Node Output
RF, U
*Element Output, directions=YES
```

```
LE, S, SDV
*Contact Output
CFORCE, CSTRESS
*Output, history, frequency=0
*End Step
** ----------------------------------------------------------------
**
** STEP: Elastic_finish2
**
*Step, name=Rest2, nlgeom=YES, inc=1000000
*Static
7e-05, 0.035, 1e-09, 7e-05
**
** OUTPUT REQUESTS
**
*Restart, write, overlay, frequency=100
**
** FIELD OUTPUT: F-Output-1
**
*Output, field, time interval=0.0035
*Node Output
RF, U
*Element Output, directions=YES
LE, S, SDV
*Contact Output
CFORCE, CSTRESS
*Output, history, frequency=0
*End Step
** ----------------------------------------------------------------
**
** STEP: Elastic_start3
**
*Step, name=Elastic_start3, nlgeom=YES, inc=100000
*Static
5e-05, 0.00125, 1.25e-08, 5e-05
**
** OUTPUT REQUESTS
**
*Restart, write, overlay, frequency=25
**
** FIELD OUTPUT: F-Output-1
**
*Output, field, time interval=0.00025
*Node Output
RF, U
*Element Output, directions=YES
LE, S, SDV
*Contact Output
CFORCE, CSTRESS
*Output, history, frequency=0
*End Step
** ----------------------------------------------------------------
**
** STEP: UMAT_3
**
*Step, name=UMAT_3, nlgeom=YES, inc=100000
```

```
*Static
1e-05, 0.00375, 1e-09, 1e-05
**
** OUTPUT REQUESTS
**
*Restart, write, overlay, frequency=25
**
** FIELD OUTPUT: F-Output-1
**
*Output, field, time interval=0.0001
*Node Output
RF, U
*Element Output, directions=YES
LE, S, SDV
*Contact Output
CFORCE, CSTRESS
*Output, history, frequency=0
*End Step
** ----------------------------------------------------------------
**
** STEP: Elastic_finish3
**
*Step, name=Rest3, nlgeom=YES, inc=100000
*Static
7e-05, 0.035, 1e-09, 7e-05
**
** OUTPUT REQUESTS
**
*Restart, write, overlay, frequency=100
**
** FIELD OUTPUT: F-Output-1
**
*Output, field, time interval=0.0035
*Node Output
RF, U
*Element Output, directions=YES
LE, S, SDV
*Contact Output
CFORCE, CSTRESS
*Output, history, frequency=0
*End Step
** ----------------------------------------------------------------
**
** STEP: Elastic_start4
**
*Step, name=Elastic_start4, nlgeom=YES
*Static
5e-05, 0.00125, 1.25e-08, 5e-05
**
** OUTPUT REQUESTS
**
*Restart, write, overlay, frequency=25
**
** FIELD OUTPUT: F-Output-1
**
*Output, field, time interval=0.00025
```

```
*Node Output
RF, U
*Element Output, directions=YES
LE, S, SDV
*Contact Output
CFORCE, CSTRESS
*Output, history, frequency=0
*End Step
** ----------------------------------------------------------------
**
** STEP: UMAT_4
**
*Step, name=UMAT_4, nlgeom=YES, inc=100000
*Static
1e-05, 0.00375, 1e-09, 1e-05
**
** OUTPUT REQUESTS
**
*Restart, write, overlay, frequency=25
**
** FIELD OUTPUT: F-Output-1
**
*Output, field, time interval=0.0001
*Node Output
RF, U
*Element Output, directions=YES
LE, S, SDV
*Contact Output
CFORCE, CSTRESS
*Output, history, frequency=0
*End Step
** ----------------------------------------------------------------
**
** STEP: Elastic_finish4
**
*Step, name=Rest4, nlgeom=YES, inc=100000
*Static
7e-05, 0.035, 1e-09, 7e-05
**
** OUTPUT REQUESTS
**
*Restart, write, overlay, frequency=100
**
** FIELD OUTPUT: F-Output-1
**
*Output, field, time interval=0.0035
*Node Output
RF, U
*Element Output, directions=YES
LE, S, SDV
*Contact Output
CFORCE, CSTRESS
*Output, history, frequency=0
*End Step
** ----------------------------------------------------------------
**
```

```
** STEP: Elastic_start5
**
*Step, name=Elastic_start5, nlgeom=YES, inc=100000
*Static
5e-05, 0.00125, 1.25e-08, 5e-05
**
** OUTPUT REQUESTS
**
*Restart, write, overlay, frequency=25
**
** FIELD OUTPUT: F-Output-1
**
*Output, field, time interval=0.00025
*Node Output
RF, U
*Element Output, directions=YES
LE, S, SDV
*Contact Output
CFORCE, CSTRESS
*Output, history, frequency=0
*End Step
** ----------------------------------------------------------------
**
** STEP: UMAT_5
**
*Step, name=UMAT_5, nlgeom=YES, inc=100000
*Static
1e-05, 0.00375, 1e-09, 1e-05
**
** OUTPUT REQUESTS
**
*Restart, write, overlay, frequency=25
**
** FIELD OUTPUT: F-Output-1
**
*Output, field, time interval=0.0001
*Node Output
RF, U
*Element Output, directions=YES
LE, S, SDV
*Contact Output
CFORCE, CSTRESS
*Output, history, frequency=0
*End Step
** ----------------------------------------------------------------
**
** STEP: Elastic_finish5
**
*Step, name=Rest5, nlgeom=YES, inc=100000
*Static
7e-05, 0.035, 1e-09, 7e-05
**
** OUTPUT REQUESTS
**
*Restart, write, overlay, frequency=100
**
```

```
** FIELD OUTPUT: F-Output-1
**
*Output, field, time interval=0.0035
*Node Output
RF, U
*Element Output, directions=YES
LE, S, SDV
*Contact Output
CFORCE, CSTRESS
*Output, history, frequency=0
*End Step
** ----------------------------------------------------------------
**
** STEP: Elastic_start6
**
*Step, name=Elastic_start6, nlgeom=YES, inc=100000
*Static
5e-05, 0.00125, 1.25e-08, 5e-05
**
** OUTPUT REQUESTS
**
*Restart, write, overlay, frequency=25
**
** FIELD OUTPUT: F-Output-1
**
*Output, field, time interval=0.00025
*Node Output
RF, U
*Element Output, directions=YES
LE, S, SDV
*Contact Output
CFORCE, CSTRESS
*Output, history, frequency=0
*End Step
** ----------------------------------------------------------------
**
** STEP: UMAT_6
**
*Step, name=UMAT_6, nlgeom=YES, inc=100000
*Static
1e-05, 0.00375, 1e-09, 1e-05
**
** OUTPUT REQUESTS
**
*Restart, write, overlay, frequency=25
**
** FIELD OUTPUT: F-Output-1
**
*Output, field, time interval=0.0001
*Node Output
RF, U
*Element Output, directions=YES
LE, S, SDV
*Contact Output
CFORCE, CSTRESS
*Output, history, frequency=0
```

```
*End Step
** ----------------------------------------------------------------
**
** STEP: Elastic_finish6
**
*Step, name=Rest6, nlgeom=YES, inc=100000
*Static
7e-05, 0.035, 1e-09, 7e-05
**
** OUTPUT REQUESTS
**
*Restart, write, overlay, frequency=100
**
** FIELD OUTPUT: F-Output-1
**
*Output, field, time interval=0.0035
*Node Output
RF, U
*Element Output, directions=YES
LE, S, SDV
*Contact Output
CFORCE, CSTRESS
*Output, history, frequency=0
*End Step
** ----------------------------------------------------------------
**
** STEP: Elastic_start7
**
*Step, name=Elastic_start7, nlgeom=YES, inc=100000
*Static
5e-05, 0.00125, 1.25e-08, 5e-05
**
** OUTPUT REQUESTS
**
*Restart, write, overlay, frequency=25
**
** FIELD OUTPUT: F-Output-1
**
*Output, field, time interval=0.00025
*Node Output
RF, U
*Element Output, directions=YES
LE, S, SDV
*Contact Output
CFORCE, CSTRESS
*Output, history, frequency=0
*End Step
** ----------------------------------------------------------------
**
** STEP: UMAT_7
**
*Step, name=UMAT_7, nlgeom=YES, inc=100000
*Static
1e-05, 0.00375, 1e-09, 1e-05
**
** OUTPUT REQUESTS
```

```
**
*Restart, write, overlay, frequency=25
**
** FIELD OUTPUT: F-Output-1
**
*Output, field, time interval=0.0001
*Node Output
RF, U
*Element Output, directions=YES
LE, S, SDV
*Contact Output
CFORCE, CSTRESS
*Output, history, frequency=0
*End Step
** ----------------------------------------------------------------
**
** STEP: Elastic_finish7
**
*Step, name=Rest7, nlgeom=YES, inc=100000
*Static
7e-05, 0.035, 1e-09, 7e-05
**
** OUTPUT REQUESTS
**
*Restart, write, overlay, frequency=100
**
** FIELD OUTPUT: F-Output-1
**
*Output, field, time interval=0.0035
*Node Output
RF, U
*Element Output, directions=YES
LE, S, SDV
*Contact Output
CFORCE, CSTRESS
*Output, history, frequency=0
*End Step
** ----------------------------------------------------------------
**
** STEP: Elastic_start8
**
*Step, name=Elastic_start8, nlgeom=YES, inc=100000
*Static
5e-05, 0.00125, 1.25e-08, 5e-05
**
** OUTPUT REQUESTS
**
*Restart, write, overlay, frequency=25
**
** FIELD OUTPUT: F-Output-1
**
*Output, field, time interval=0.00025
*Node Output
RF, U
*Element Output, directions=YES
LE, S, SDV
```

```
*Contact Output
CFORCE, CSTRESS
*Output, history, frequency=0
*End Step
** ----------------------------------------------------------------
**
** STEP: UMAT_8
**
*Step, name=UMAT_8, nlgeom=YES, inc=100000
*Static
1e-05, 0.00375, 1e-09, 1e-05
**
** OUTPUT REQUESTS
**
*Restart, write, overlay, frequency=25
**
** FIELD OUTPUT: F-Output-1
**
*Output, field, time interval=0.0001
*Node Output
RF, U
*Element Output, directions=YES
LE, S, SDV
*Contact Output
CFORCE, CSTRESS
*Output, history, frequency=0
*End Step
** ----------------------------------------------------------------
**
** STEP: Elastic_finish8
**
*Step, name=Rest8, nlgeom=YES, inc=100000
*Static
7e-05, 0.035, 1e-09, 7e-05
**
** OUTPUT REQUESTS
**
*Restart, write, overlay, frequency=100
**
** FIELD OUTPUT: F-Output-1
**
*Output, field, time interval=0.0035
*Node Output
RF, U
*Element Output, directions=YES
LE, S, SDV
*Contact Output
CFORCE, CSTRESS
*Output, history, frequency=0
*End Step
** ----------------------------------------------------------------
**
** STEP: Elastic_start9
**
*Step, name=Elastic_start9, nlgeom=YES, inc=100000
*Static
```

```
5e-05, 0.00125, 1.25e-08, 5e-05
**
** OUTPUT REQUESTS
**
*Restart, write, overlay, frequency=25
**
** FIELD OUTPUT: F-Output-1
**
*Output, field, time interval=0.00025
*Node Output
RF, U
*Element Output, directions=YES
LE, S, SDV
*Contact Output
CFORCE, CSTRESS
*Output, history, frequency=0
*End Step
** ----------------------------------------------------------------
**
** STEP: UMAT_9
**
*Step, name=UMAT_9, nlgeom=YES, inc=100000
*Static
1e-05, 0.00375, 1e-09, 1e-05
**
** OUTPUT REQUESTS
**
*Restart, write, overlay, frequency=25
**
** FIELD OUTPUT: F-Output-1
**
*Output, field, time interval=0.0001
*Node Output
RF, U
*Element Output, directions=YES
LE, S, SDV
*Contact Output
CFORCE, CSTRESS
*Output, history, frequency=0
*End Step
** ----------------------------------------------------------------
**
** STEP: Elastic_finish9
**
*Step, name=Rest9, nlgeom=YES, inc=100000
*Static
7e-05, 0.035, 1e-09, 7e-05
**
** OUTPUT REQUESTS
**
*Restart, write, overlay, frequency=100
**
** FIELD OUTPUT: F-Output-1
**
*Output, field, time interval=0.0035
*Node Output
```

```
RF, U
*Element Output, directions=YES
LE, S, SDV
*Contact Output
CFORCE, CSTRESS
*Output, history, frequency=0
*End Step
** ----------------------------------------------------------------
**
** STEP: Elastic_start10
**
*Step, name=Elastic_start10, nlgeom=YES, inc=100000
*Static
5e-05, 0.00125, 1.25e-08, 5e-05
**
** OUTPUT REQUESTS
**
*Restart, write, overlay, frequency=25
**
** FIELD OUTPUT: F-Output-1
**
*Output, field, time interval=0.00025
*Node Output
RF, U
*Element Output, directions=YES
LE, S, SDV
*Contact Output
CFORCE, CSTRESS
*Output, history, frequency=0
*End Step
** ----------------------------------------------------------------
**
** STEP: UMAT_10
**
*Step, name=UMAT_10, nlgeom=YES, inc=100000
*Static
1e-05, 0.00375, 1e-09, 1e-05
**
** OUTPUT REQUESTS
**
*Restart, write, overlay, frequency=25
**
** FIELD OUTPUT: F-Output-1
**
*Output, field, time interval=0.0001
*Node Output
RF, U
*Element Output, directions=YES
LE, S, SDV
*Contact Output
CFORCE, CSTRESS
*Output, history, frequency=0
*End Step
```